Numerical damage analysis of aeronautical composite structures using multiscale methods

Ivančević, Darko

Doctoral thesis / Disertacija

2015

Degree Grantor / Ustanova koja je dodijelila akademski / stručni stupanj: **University of Zagreb, Faculty of Mechanical Engineering and Naval Architecture / Sveučilište u Zagrebu, Fakultet strojarstva i brodogradnje**

Permanent link / Trajna poveznica: https://urn.nsk.hr/urn:nbn:hr:235:606968

Rights / Prava: In copyright/Zaštićeno autorskim pravom.

Download date / Datum preuzimanja: **2025-03-29**

University of Zagreb

FACULTY OF MECHANICAL ENGINEERING
AND NAVAL ARCHITECTURE

Darko Ivančević

NUMERICAL DAMAGE ANALYSIS OF AERONAUTICAL COMPOSITE STRUCTURES USING MULTISCALE METHODS

DOCTORAL THESIS

Zagreb, 2015

University of Zagreb

FACULTY OF MECHANICAL ENGINEERING
AND NAVAL ARCHITECTURE

Darko Ivančević

NUMERICAL DAMAGE ANALYSIS OF AERONAUTICAL COMPOSITE STRUCTURES USING MULTISCALE METHODS

DOCTORAL THESIS

Supervisor:
Prof. DSc. Ivica Smojver

Zagreb, 2015

Sveučilište u Zagrebu

FAKULTET STROJARSTVA I BRODOGRADNJE

Darko Ivančević

NUMERIČKA ANALIZA OŠTEĆENJA KOMPOZITNIH ZRAKOPLOVNIH KONSTRUKCIJA PRIMJENOM VIŠERAZINSKIH METODA

DOKTORSKI RAD

Mentor:

Prof. dr. sc. Ivica Smojver

Zagreb, 2015

BIBLIOGRAPHY DATA

Preface

This Thesis has been written entirely by me and contains the results obtained during my work as research assistant at the Department of Aeronautical Engineering, Faculty of Mechanical Engineering and Naval Architecture, University of Zagreb.

The research activities have been performed employing the knowledge obtained during my undergraduate, graduate and postgraduate studies at the Faculty of Mechanical Engineering and Naval Architecture and using the cited references.

Zagreb, March 2015 Darko Ivančević

Contents

List of Figures

List of Tables

List of Symbols

Abbreviations

Summary

The research is focused on multiscale methodology application at impact damage modelling of composite structures. Application of multiscale principles on complex composite structures necessitates computationally efficient micromechanical models. Efficient alternatives to FE-based micromechanical models are analytical and semi-analytical micromechanical theories. Consequently, modelling of composite structures has been in this Thesis performed employing the semi-analytical High Fidelity Generalized Method of Cells (HFGMC) micromechanical model. The application of micromechanical models enables modelling of damage processes and physical phenomena which are specific to fibre reinforced composite structures. Micromechanical damage initiation and progression theories have been employed in this research as to model composite damage and failure modes at the structural scale. The micromechanical damage initiation and damage propagation models have been validated with available experimental results, whereas results of the multiscale methodology have been compared to available experimental results and to the results obtained employing ply level failure theories. The modified Bodner-Partom viscoplasticity theory has been employed in this research as to model the strain rate effects of epoxy-based composites at high strain rates. The results of the micromechanical strain rate dependent theory have been compared with available experimental results.

Keywords: High Fidelity Generalized Method of Cells, composite structures, micromechanics, impact damage, multiscale analysis.

Prošireni sažetak

Nosivi dijelovi konstrukcija kojima je jedan od najvažnijih zahtjeva što manja masa u posljednjim se desetljećima sve češće izrađuju upotrebom vlaknima ojačanih kompozitnih materijala. Unatoč brojnim prednostima, kompozitni materijali se tek u najnovijim konstrukcijama koriste za izradu primarnih nosivih dijelova zrakoplova. Jedan od razloga zbog kojih se tek u novije vrijeme kompozitni materijali koriste za izradu glavnih nosivih elemenata u zrakoplovstvu je povećanje pouzdanosti metoda proračuna popuštanja konstrukcija izrađenih od višeslojnih kompozitnih materijala.

Uobičajeni pristup proračunu kompozitnih konstrukcija je upotreba kriterija popuštanja primijenjenih na razini kompozitnog sloja, pri čemu se popuštanje promatranog sloja određuje usporedbom stanja naprezanja ili deformacija u homogeniziranom materijalu s čvrstoćom, odnosno dopuštenom deformacijom materijala. Nedostaci postojećih kriterija popuštanja postali su očiti tijekom održavanja *World Wide Failure Exercise* (WWFE) [Hinton et al., 2002]. Rezultati WWFE otkrili su da postojeće teorije popuštanja pri određenim kombinacijama naprezanja slabije procjenjuju opterećenje pri kojem dolazi do oštećenja, a problem je posebno izražen u slučaju složenijih rasporeda slojeva u laminatu.

Budući da su načini popuštanja kompozitnih materijala povezani s procesima unutar samog materijala, pouzdanost predviđanja popuštanja može se povećati modeliranjem oštećenja na razini mikrostrukture heterogenog materijala. Primjena mikromehaničkih modela za rješavanje inženjerskih problema u suvremenoj numeričkoj mehanici zahtijeva pristup modeliranja na više razina (engl. *multiscale*). Ovim se pristupom problem proračuna kompozitnih konstrukcija razmatra na dvije razine – makrorazini, koja rješava globalni problem, te mikrorazini, gdje se određuje stanje naprezanja i deformacija unutar

heterogenog materijala. Važan dio mikromehaničkih teorija je koncept jedinične ćelije (engl. *Repeating Unit Cell* - RUC). Jedinična ćelija je temeljni "gradivi element" koji svojim periodičnim ponavljanjem karakterizira nehomogeni materijal. Ovaj koncept pretpostavlja pojednostavljenu i savršeno uređenu periodičnu mikrostrukturu materijala uz rubne uvjete periodičnosti na vanjskim granicama jedinične ćelije.

Prednost modeliranja heterogenih materijala na mikrorazini je što se pri modeliranju kompozitnih konstrukcija uzimaju u obzir procesi unutar mikrostrukture. Time je omogućeno modeliranje fizikalnih pojava koje određuju homogenizirana mehanička svojstva vlaknima ojačanih kompozitnih materijala. Primjena višerazinskog pristupa pri proračunu realnih konstrukcija zahtijeva vrlo visoku računalnu učinkovitost mikromehaničkih modela. Pregledom literature ustanovljeno je da se po primjeni u višerazinskom okruženju i po rasponu primjene ističe metoda ćelija velike točnosti (*High Fidelity Generalized Method of Cells* - HFGMC) [Aboudi et al., 2003], [Aboudi et al., 2012], [Pineda et al., 2012a], [Bednarcyk et al., 2004].

HFGMC spada u skupinu polu-analitičkih mikromehaničkih modela nastalih iz metode ćelija (*Method of Cells* - MOC) [Aboudi, 1988]. U izvornoj teoriji je jedinična ćelija diskretizirana korištenjem jedne podćelije za vlakno, dok preostale tri podćelije predstavljaju matricu. Polje pomaka unutar podćelija određeno je polinomom prvog reda u njihovom lokalnom koordinatnom sustavu, a postavljanjem uvjeta dvostruke periodičnosti na rubove MOC modela omogućeno je modeliranje jednousmjerenih kompozitnih materijala. Važno poboljšanje teorije uvedeno je razvojem poopćene metode ćelija (*Generalized Method of Cells* - GMC) [Paley and Aboudi, 1992]. Jedinična ćelija je u ovom mikromehaničkom modelu podijeljena na proizvoljan broj pravokutnih podćelija. Korištenjem većeg broja podćelija omogućena je točnija raspodjela polja deformacija i naprezanja u heterogenom materijalu. GMC se uglavnom koristio za određivanje ekvivalentnih neelastičnih svojstava kompozitnih materijala s metalnom matricom [Paley and Aboudi, 1992], [Arnold et al., 1996]. U [Pindera and Bednarcyk, 1999] je izvedena preformulirana verzija GMC-a s većom računalnom učinkovitošću koja je primijenjena na fino diskretizirane mikromodele (100×100 podćelija). Povećanje računalne učinkovitosti omogućilo je modeliranje mehaničkih sustava s više vlakana unutar jedinične ćelije, eliptičnih vlakana i drugih morfoloških sustava. Iako je osnovna teorija ovog mikromodela razvijena još 1992. godine, GMC se, upravo zbog njegove dobre računalne učinkovitosti koristi i u novije vrijeme, pogotovo u višerazinskom okruženju [Kurnatowski

et al., 2012], [May et al., 2014]. Također, razvijaju se nove formulacije na temelju ovog mikromodela [Kurnatowski and Matzenmiller, 2012] kao i modeli odvajanja vlakna od matrice [Matzenmiller and Köster, 2007].

Točnost ovih mikromehaničkih modela povećana je uvođenjem diskretizacije polja pomaka unutar podćelija polinomom drugog reda. Ova numerička formulacija nazvana je HOTFGM (*Higher Order Theory of Functionally Graded Materials*) [Aboudi et al., 1999], a proširivanje HOTFGM modela na periodične mikrostrukture rezultiralo je HFGMC mikromehaničkim modelom [Aboudi et al., 2003]. Po uzoru na prethodne verzije ovih mikromehaničkih modela, i HFGMC se primjenjivao za modeliranje širokog raspona složenih pojava u kompozitnim materijalima - plastičnost metalne matrice, termo-elastičnost i termoplastičnost matrice, odvajanje vlakna od matrice, te na legure s efektom prisjetljivosti oblika (engl. *Shape Memory Alloys*) [Aboudi et al., 2003], [Khatam and Pindera, 2009], [Freed and Aboudi, 2009].

Istraživanja oštećivanja primjenom mikromehanike uglavnom su bila usmjerena prema kompozitnim materijalima s metalnom matricom, a tek se u novijim istraživanjima mikromehanički principi koriste za proučavanje procesa oštećivanja kompozitnih materijala s polimernim matricama [Moncada et al., 2008], [Pineda, 2012]. Jedan od zaključaka rezultata WWFE-a je spoznaja da se za točnije modeliranje procesa oštećivanja kompozitnih materijala s polimernom matricom u obzir mora uzeti proces postupnog smanjivanja mehaničkih svojstava koji je posljedica nastanka oštećenja na mikroskopskom nivou [Hinton et al., 2002]. Uobičajeni pristup kojim se modelira postupno smanjivanje mehaničkih svojstava je primjena principa mehanike oštećenja kontinuuma (engl. *Continuum Damage Mechanics* - CDM) na homogenizirana svojstva kompozitnog materijala [Voyiadjis and Kattan, 1999].

Analiziranjem postupka oštećivanja na mikromehaničkom nivou, kriteriji popuštanja se primjenjuju na razini jedinica diskretizacije mikromehaničkog modela, odnosno podćelija ako se radi o HFGMC modelu. Na temelju prvih rezultata, u kojima su se mehanička svojstva podćelija postavljala na vrlo niske vrijednosti nakon postizanja uvjeta popuštanja [Moncada, 2012], [Tang and Zhang, 2012], zaključeno je da se principi mehanike oštećenja kontinuuma moraju primijeniti i na mikromehaničkoj razini kako bi se moglo modelirati postupno smanjivanje mehaničkih svojstava homogeniziranog kompozitnog materijala. Principi mehanike oštećenja kontinuuma počeli su se primjenjivati tek u novijim istraživanjima u sklopu HFGMC modela, a uključuju složenije modele koji

uzimaju u obzir višeosnu prirodu oštećenja kompozitnih materijala [Bednarcyk et al., 2010], [Pineda, 2012].

Mikromehanički model

U ovom istraživanju korištena je modificirana verzija HFGMC-a, koju odlikuje znatno poboljšana računalna učinkovitost [Bansal and Pindera, 2006]. Glavna karakteristika mikromehaničkih modela temeljenih na metodi ćelija je diskretizacija jedinične ćelije heterogenog materijala koristeći $N_\beta \times N_\gamma$ pravokutnih podćelija koje, u najjednostavnijem obliku ovog modela, mogu biti popunjene materijalom matrice ili materijalom vlakna. Ukupan broj različitih materijalnih modela (tj. faza), te broj i dimenzije podćelija su proizvoljni.

Primijenjena verzija HFGMC [Bansal and Pindera, 2005], [Bansal and Pindera, 2006] razlikuje se od originalne [Aboudi et al., 2003] po načinu postavljanja i rješavanja sustava jednadžbi kojim se određuje polje pomaka unutar jedinične ćelije. Rješavanje mikromehaničkog problema temelji se na formulaciji lokalnih matrica krutosti podćelija, koje povezuju komponente pomaka i sila na granicama podćelija. Uvođenjem rubnih uvjeta na spojevima pojedinih podćelija, te na rubovima jedinične ćelije, formira se globalni sustav jednadžbi. Na spojevima podćelija zadani su uvjeti kontinuiteta osrednjenih sila i pomaka, dok su na rubovima jedinične ćelije zadani rubni uvjeti periodičnosti. Sprječavanje pomaka jedinične ćelije kao krutog tijela riješeno je fiksiranjem pomaka rubnih podćelija u kutovima jedinične ćelije. Krajnji rezultat HFGMC modela je određivanje tenzora koncentracije deformacija (engl. *Strain Concentration Tensor*), koji povezuje polje deformacija svake pojedine podćelije sa homogeniziranim stanjem deformacije.

Implementacija u višerazinsku metodologiju

HFGMC model se u okviru opisane metodologije koristi kao mikromehanički model unutar okruženja analiza na više razina. Problem na makro-razini se pri tome rješava korištenjem MKE programa Abaqus/Explicit, koji je povezan sa HFGMC programom korištenjem potprograma za implementaciju korisničkih konstitutivnih jednadžbi - VU-MAT. HFGMC je zbog toga programiran u Fortran programskom jeziku kao dodatan potprogram, te se poziva za svaku pojedinu materijalnu točku modela konačnih elemenata.

U svrhu poboljšanja računalne učinkovitosti razvijene metodologije, HFGMC model se u razvijenoj metodologiji poziva samo za materijalne točke modela konačnih elemenata, u kojima se može očekivati nastajanje oštećenja. Pri tome se koriste vrijednosti kriterija popuštanja, definiranih na razini kompozitnih slojeva, za inicijaciju mikromehaničkih analiza u višerazinskom okruženju. Veza između VUMAT potprograma i korištenog mikromehaničkog modela ostvarena je korištenjem 44 SDV-a (engl. *Solution Dependent State Variable*) i 47 COMMON bloka, koji omogućuju prijenos podataka, strukturiranih u matrice i vektore, iz trenutnog vremenskog inkrementa eksplicitne analize u sljedeći. SDV se u razvijenoj metodologiji koriste za vizualizaciju maksimalnih vrijednosti parametara mikromehaničkih kriterija popuštanja i modela oštećivanja, te za vizualizaciju parametara koji su zajednički za sve podćelije jedinične ćelije poput homogeniziranih vrijednosti elastičnih konstanti materijala.

Mikromehanički kriteriji popuštanja i oštećivanja

U mikromehaničkim analizama kriteriji popuštanja se definiraju na razini konstituenata kompozitnog materijala. Za predviđanje popuštanja vlakna koriste se jednostavni kriteriji poput maksimalnih dopuštenih naprezanja ili deformacija u smjeru vlakna, dok su kriteriji inicijacije oštećenja matrice složenije definirani. U istraživanju su korištena četiri mikromehanička kriterija popuštanja. To su trodimenzionalni oblik Tsai-Hill kriterija za matricu koji se koristi sa kriterijem maksimalnih deformacija za vlakno, prema [Pineda et al., 2009]. Kriteriji koji su korišteni u sklopu MCT (engl. *MultiContinuum Theory*), prema [Mayes and Hansen, 2004], za inicijaciju oštećenja u vlaknu i matrici čine drugu skupinu kriterija koji su implementirani u metodologiju. Treći kriterij čini MMCDM teorija oštećivanja mikromehaničkog modela [Bednarcyk et al., 2010], a četvrti čini kriterij maksimalnih glavnih vrijednosti naprezanja [Pineda, 2012]. Rezultati usporedbe pokazuju velike razlike među njima. Zaključeno je da će se za mikromehaničko modeliranje oštećivanja morati koristiti principi mehanike oštećenja kontinuuma i na mikromehaničkoj razini. Zbog toga su u metodologiju implementirana dva pristupa kojima se oštećenja kompozitnih materijala modeliraju na razini mikromehanike. To su MMCDM model, prema [Bednarcyk et al., 2010], i Crack Band model oštećivanja, prema [Pineda, 2012]. Modeli oštećivanja su verificirani usporedbom s dostupnim rezultatima WWFE.

Rezultati

Mikromehanički modeli oštećivanja verificirani su usporedbom s dostupnim eksperimentalnim rezultatima za Silenka E-glass 1200tex/ MY750/HY917/DY063 Epoxy te T300/BSL914C CFRP kompozite. Višerazinska metodologija je primijenjena na MKE modelima konstrukcijskih dijelova zrakoplovnih konstrukcija. Prvi primjer je kompozitni panel ojačan uzdužnim nosačima. Rezultati analiza poslužili su za odabir parametara za inicijaciju mikromehaničkih analiza u višerazinskim analizama. Sukladno tome, velika je pozornost tijekom razvijanja mikromehaničke metodologije posvećena usporedbi mikromehaničkih kriterija popuštanja i kriterija popuštanja na razini kompozitnih slojeva.

Drugu skupinu primjera predstavljaju udarne analize u kompozitne ploče. Numerički modeli reproduciraju eksperimentalne uvjete u kojima su kompozitne ploče izložene udarima želatinskim udaračima pri brzinama od 200-280 m/s. Budući da su dostupni rezultati eksperimentalnih ispitivanja vrlo oskudni, višerazinska metodologija je verificirana i usporedbom s Abaqus-ovim modelom oštećivanja za vlaknima ojačane kompozitne materijale.

MMCDM model oštećivanja prilagođen je jednousmjerenim kompozitnim materijalima s epoksidnom matricom te omogućuje modeliranje višeosne prirode oštećivanja ovih materijala. Posljedično, primjena ovog modela u višerazinskim analizama omogućuje točnije modeliranje procesa oštećivanja. Evaluacijom mikromehaničkih teorija oštećivanja pokazala je da bi se kriterij inicijacije oštećivanja primijenjen u Crack Band modelu oštećivanja morao modificirati kako bi se omogućilo predviđanje/modeliranje homogeniziranog ponašanja kompozitnog materijala pri smičnom opterećenju u ravnini sloja. U nastavku istraživanja će se koristiti Crack Band model oštećivanja jer omogućuje modeliranje oštećenja u složenijim jediničnim ćelijama, koje će biti nužnost za mikromehaničke analize naprednih kompozitnih materijala.

Zaključak

HFGMC mikromehanički model je u okviru ove disertacije korišten za razvoj višerazinske metodologije, koja omogućuje primjenu mikromehaničkih kriterija popuštanja i teorija oštećivanja u numeričkim proračunima kompozitnih konstrukcija. Namjena razvijene višerazinske metodologije je predviđanje udarnih oštećenja u kompozitnim konstrukcijama,

s namjerom korištenja razvijene metodologije na naprednim kompozitnim konstrukcijama u budućim istraživanjima.

Mikromehanički pristupi oštećivanja kompozitnih materijala, u usporedbi s homogeniziranim pristupima, omogućuju modeliranje procesa oštećivanja na razini konstituenata materijala. Za modeliranje inicijacije oštećenja razmatrano je nekoliko kriterija popuštanja. Kako je pokazano, postoje velike razlike u rezultatima dobivenih primjenom različitih kriterija, koje se očituju kako u predviđanju opterećenja pri kojem dolazi do inicijacije oštećenja, tako i u fizikalnoj interpretaciji dobivenih rezultata (interakcija između načina popuštanja kompozitnog materijala). Nadalje, za modeliranje nelinearnog ponašanja kompozitnih slojeva potrebno je u mikromehaničke konstitutivne jednadžbe ugraditi i modele oštećivanja.

Primjena mikromehaničkog pristupa modeliranju oštećivanja kompozitnog materijala omogućuje unaprjeđenje proračuna popuštanja kompozitnih slojeva. No, da bi mikromehaničke analize rezultirale točnim predviđanjima, moraju se koristiti fizikalno točna mehanička svojstva konstituenata na mikromehaničkoj razini (engl. *in-situ* svojstva). Zbog toga je razvijena metodologija primijenjena na Silenka GFRP i T300/914 CFRP kompozitne materijale, čija su svojstva dobro dokumentirana u literaturi jer su bili proučavani u okviru WWFE.

Višerazinska primjena MMCDM teorije pokazala je da metodologija pouzdano predviđa načine popuštanja kompozitne ploče. Pritom je ustanovljen značajan stupanj korelacije mikromehaničkog modela oštećivanja i Puck-ovog kriterija inicijacije oštećenja te modela progresivnog oštećivanja za vlaknima ojačane kompozitne materijale u Abaqus-u. Unatoč tome, bili bi potrebni detaljniji eksperimentalni rezultati za dodatnu validaciju višerazinske metodologije. Nadalje, podudaranje rezultata dobivenih Puck-ovim kriterijem popuštanja (na razini kompozitnih slojeva) s rezultatima MMCDM modela oštećivanja rezultiralo je upotrebom Puck-ovog kriterija za inicijaciju mikromehaničkih analiza u višerazinskim analizama.

Mogući izvor razlika između rezultata numeričkih analiza (višerazinskih, kao i homogeniziranih) i rezultata eksperimenata danih u [Hou and Ruiz, 2007] je utjecaj velikih brzina deformacije na mehanička svojstva kompozita. Mehanička svojstva vlaknima ojačanih kompozitnih materijala s epoksidnim matricama pokazuju izraženu ovisnost o brzini deformacije. Efekti povećane brzine deformacije modelirani su primjenom modificiranog Bodner-Partom viskoplastičnog modela za podćelije matrice. Iako korišteni

viskoplastični model može predvidjeti nelinearno ponašanje matrice pri povećanim brzinama deformacije, dodatno se mora uključiti i model oštećivanja kako bi se mogao modelirati homogenizirani odziv kompozitnog materijala pri većim deformacijama, što je u skladu s rezultatima sličnih istraživanja u literaturi [Zheng, 2006], [Taibei et al., 2002]. Primijenjeni pristup modeliranju utjecaja brzine deformacije na elastična svojstva kompozitnog materijala rezultira prihvatljivim rezultatima, uzimajući u obzir veliko rasipanje dostupnih eksperimentalnih podataka.

Cilj i hipoteza istraživanja

Cilj predloženog istraživanja je unaprjeđenje numeričkih postupaka modeliranja procesa oštećenja višeslojnih kompozitnih konstrukcija pod udarnim opterećenjem primjenom računalno učinkovitih formulacija HFGMC mikromehaničkog modela. Materijalne modele razvijene primjenom pristupa višerazinskih analiza, kao i modele popuštanja i određivanja ekvivalentnih mehaničkih svojstava kompozitnog materijala moguće je uspješno primijeniti na zrakoplovne konstrukcije.

Višerazinske analize omogućuju modeliranje efekata koje nije moguće modelirati homogeniziranim pristupom, poput modeliranja utjecaja povećanih brzina deformiranja na konstitutivne modele i načine popuštanja kompozitnih materijala s epoksidnom matricom.

Hipoteza:

Primjenom mikromehaničkih principa na numeričke analize udarnih oštećenja kompozitnih konstrukcija moguće je modelirati specifične efekte koji ovise o mikrostrukturi heterogenog materijala čime se znatno povećava točnost modeliranja udarnih oštećenja te proširuje područje primjene razvijene metodologije.

Pregled rada

Prvo poglavlje sadrži uvod u područje istraživanja te objašnjava motivaciju i postavljene ciljeve istraživanja. U ovom poglavlju sadržan je i pregled dosadašnjih istraživanja koji dodatno pojašnjava motivaciju i ciljeve istraživanja.

U drugom poglavlju dan je pregled višerazinskih pristupa s naglaskom na primjenu u kompozitnim materijalima. U ovom poglavlju detaljno je objašnjena polu-analitička

modificirana HFGMC mikromehanička metoda, koja je korištena u ovom istraživanju. Uz pregled temeljnih izraza korištene mikromehaničke teorije opisana je i implementacija HFGMC mikromehaničkog modela u višerazinsko okruženje korištenjem Abaqus-ovih korisničkih potprograma.

U trećem poglavlju dan je pregled korištenih kriterija popuštanja. Uz mikromehaničke kriterije popuštanja, korištene u višerazinskim analizama, dan je i pregled kriterija popuštanja i modela oštećivanja definiranih na razini kompozitnih slojeva koji su korišteni za validaciju višerazinske metodologije.

U četvrtom poglavlju dan je pregled korištenih mikromehaničkih modela oštećivanja koji su implementirani u mikromehanički model u okviru ove disertacije. Dobiveni rezultati su uspoređeni s dostupnim eksperimentalnim rezultatima.

U petom poglavlju je primijenjena višerazinska metodologija u numeričkim simulacijama na primjerima iz zrakoplovstva. Prva primjena vrijedi za statičko opterećenje kompozitnog panela ojačanog uzdužnim nosačima, a drugu skupinu primjera čine analize udarnog oštećenja koje oponašaju eksperimentalne uvjete udara mekog tijela (engl. *soft body impact*) u kompozitne ploče. Budući da su u literaturi vrlo oskudno dostupni eksperimentalni rezultati ovakvih pokusa, višerazinska metodologija je verificirana i usporedbom s rezultatima kriterija popuštanja i modela oštećivanja postavljenih na razini kompozitnih slojeva.

U šestom poglavlju su modelirani efekti, koji nastaju pri velikim brzinama deformacije, implementacijom modificiranog Bodner-Partom viskoplastičnog materijalnog modela u konstitutivne jednadžbe podćelija matrice u HFGMC mikromehaničkom modelu. Mikromehanička metodologija korištena je u ovom poglavlju za predviđanje homogeniziranog ponašanja IM7/977-2 CFRP kompozitnog materijala pri povećanim brzinama deformacije, uzimajući u obzir nelinearno ponašanje matrice kao i ovisnost modula elastičnosti o brzini deformacije.

U posljednjem poglavlju dan je pregled dobivenih zaključaka kao i preporuke za buduća istraživanja u području višerazinskih pristupa modeliranju oštećenja u kompozitnim konstrukcijama.

Izvorni znanstveni doprinos

1. Razvijena višerazinska metodologija primijenjena je na relativno velikim i složenim numeričkim modelima. Doprinos se pritom očituje kroz kritičku evaluaciju mikromehaničkih modela inicijacije oštećenja te teorija oštećivanja, i kriterija popuštanja kompozitnih materijala definiranih na razini kompozitnih slojeva, koji su korišteni u okviru razvijene metodologije za pokretanje mikromehaničkih analiza. Kao rezultat ovog pristupa, znatno je povećana računalna učinkovitost metodologije.

2. Validacija primijenjenih mikromehaničkih kriterija popuštanja i modela oštećivanja ostvarena je i) usporedbom rezultata modela s dostupnim eksperimentalnim rezultatima iz WWFE, ii) usporedbom rezultata mikromehaničkih kriterija popuštanja s kriterijima popuštanja na razini homogeniziranih kompozitnih slojeva u višerazinskim analizama, te iii) primjenom mikromehaničkih modela oštećivanja za modeliranje oštećenja na makro-razini.

   U usporedbi sa sličnim višerazinskim analizama udarnih oštećenja, u kojima je korišten GMC mikromehanički model, u razvijenoj metodologiji je korišten točniji HFGMC mikromehanički model. Dodatno, u metodologiju su implementirani složeniji mikromehanički modeli oštećivanja, koji omogućuju modeliranje mikromehaničkih procesa oštećivanja koji određuju nelinearno ponašanje kompozitnih slojeva.

3. U ovoj disertaciji ostvareno je modeliranje utjecaja povećanih brzina deformacije implementacijom modificiranog Bodner-Partom viskoplastičnog modela u HFGMC mikromehanički model. Uz viskoplastični konstitutivni model, koji određuje nelinearno ponašanje homogeniziranog kompozitnog materijala, u model je dodan i pristup koji određuje utjecaj brzine deformacije na elastična svojstva kompozitnog materijala. Doprinos u ovom dijelu disertacije očituje se u uspješnoj implementaciji opisanog modela u HFGMC mikromehanički model, omogućujući pouzdano modeliranje homogeniziranog ponašanja kompozitnog materijala pri povećanim brzinama deformacije.

Ključne riječi: High Fidelity Generalized Method of Cells, kompozitne konstrukcije, mikromehanika, udarna oštećenja, višerazinska analiza.

1 | Introduction

The use of fibre reinforced composite materials in highly loaded lightweight structures is in constant increase. Despite many advantages as for example specific strength, application of composite materials for highly loaded structural items has not reached its full potential. The increased cost of composite structures, susceptibility to impact damage, difficult maintenance and complicated certification procedures belong to the disadvantages of composite materials. These disadvantages have postponed the use of composite materials for applications in primary structural elements of aeronautical structures in the past.

Application of composite materials in aeronautical structures has been initiated in the 1970s in military aviation due to high demands on performances of these structures. As shown in Figure 1.1, the constant increase in fuel prices has resulted in the demand for more efficient aeronautical structures in commercial aviation. Composite materials application in these structures leads to significant weight savings which subsequently result in fuel savings. Application of composites in the most recent commercial aircraft types surpassed their military counterparts in the composite application, as shown in Figure 1.1. Extreme demands on military aircraft structures, which arise from e.g. high temperatures due to aerothermodynamic effects at supersonic velocities, currently prevent higher levels of composite material application in military aircraft types.

Composite materials have long been employed for secondary structural items of the aircraft, e.g. high-lift devices and control surfaces. Only the most recent aircraft types employ composites for primary structural applications. Examples of the advanced application of composite structures are the wing box structure of the Airbus A380, main
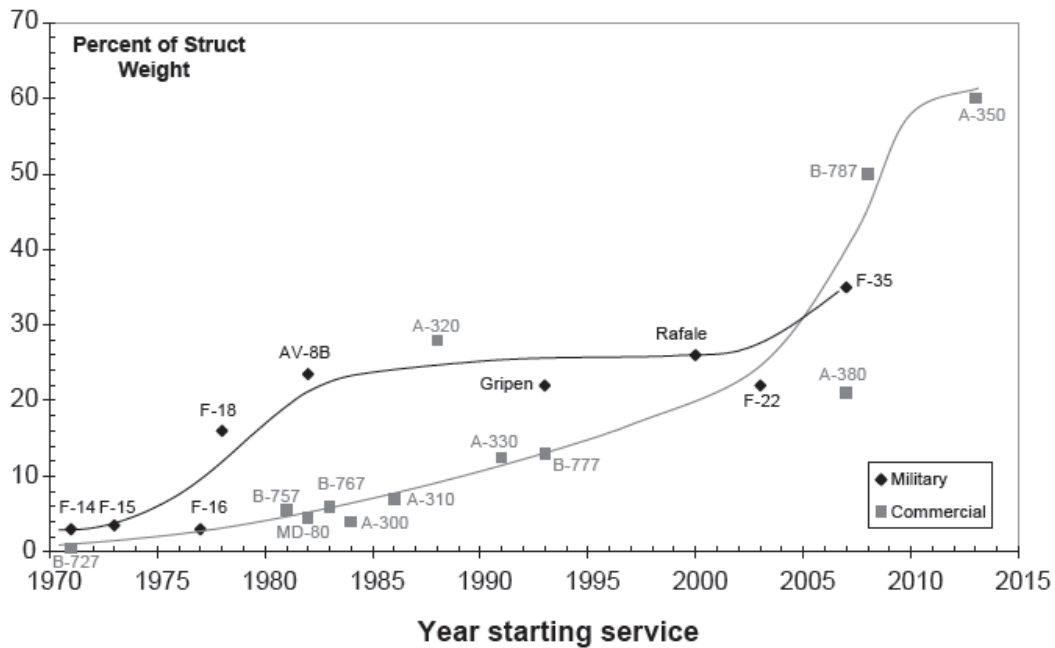
Figure 1.1: Weight percentage of composite materials in aeronautical structures [Kassapoglou, 2010].

spar of the A400M and the complete fuselages and wings of the Boeing 787 and Airbus A350 [Kassapoglou, 2010]. The weight percentage of composites in the Boeing 787 is approximately 50%, whereas the newest Airbus A350 aircraft has approximately 60% of composites in the structural weight. As to illustrate the composite structural components in a modern aircraft structure, Figure 1.2 shows the layout of structural materials in the Airbus A350 airframe.

Enhanced reliability of numerical procedures employed in the design of composite structures is one of the factors which enabled advanced application of composite materials. Additionally, the increase of reliability of numerical methods used in the structural analyses has been necessary to fulfil the certification requirements of aeronautical structures [Georgiadis et al., 2007], [Guida et al., 2013].

One of the drawbacks of composite materials is the susceptibility to impact damage. Impact at low impacting velocities and kinetic energies causes a specific type of damage specific for laminated composite structures - Barely Visible Impact Damage (BVID) which is a great concern for the maintenance of aeronautical composite structures. As opposed to this damage mode, high energy impacts usually result in the perforation of

Figure 1.2: Airbus A350 structural materials [McConnell, 2011].

the impacted structure due to brittle damage mechanisms of the composite material.

The research conducted in this Thesis presents a continuation of previously performed research activities in which a numerical birdstrike damage prediction methodology has been developed. Results of these research activities have been published in e.g. [Smojver and Ivančević, 2010], [Smojver and Ivančević, 2011], [Ivančević and Smojver, 2011]. The multiscale method has been developed in this Thesis as to improve the damage prediction approach for composite structures and to enable modelling of advanced composite materials in the further research.

1.1   Motivation

The failure modes of composite materials are a result of the material heterogeneous microstructure. Consequently, the most common composite failure modes include fibre breakage, matrix failure, fibre pullout and delamination. The conventional approach to the sizing of composite structures is the application of failure criteria which are employed at the level of a composite ply. These criteria compare the ply stress state to the strength or allowable strain of the ply material. Some of the commonly employed ply-level failure theories involve e.g. the Tsai-Wu, Hashin, Puck and Cuntze criterion [Hinton et al., 2002], [Hinton et al., 2004]. Failure criteria for composite materials are grouped into

phenomenological and physics based criteria [Schücker, 2006]. The first group consists of criteria developed from yield criteria of isotropic materials. Consequently, these criteria are unable to determine the failure modes of composite materials. The derivation of physics based criteria begins by considering the different failure mechanisms of composite materials (e.g. Puck and Hashin criteria).

The shortcomings of existing failure criteria became evident during the World Wide Failure Exercise (WWFE) [Hinton et al., 2002], [Hinton et al., 2004]. The WWFE results revealed that the problem of failure and damage prediction of composite structures has not been solved completely, which is especially the case for more complex composite laminates. Another important conclusion is that physics based criteria better predict the failure loads of composite structures since the failure modes of fibre reinforced composite materials are implicitly taken into account. Although many complex ply-level failure criteria have been developed, their application in engineering practice is limited, as shown in Figure 1.3.
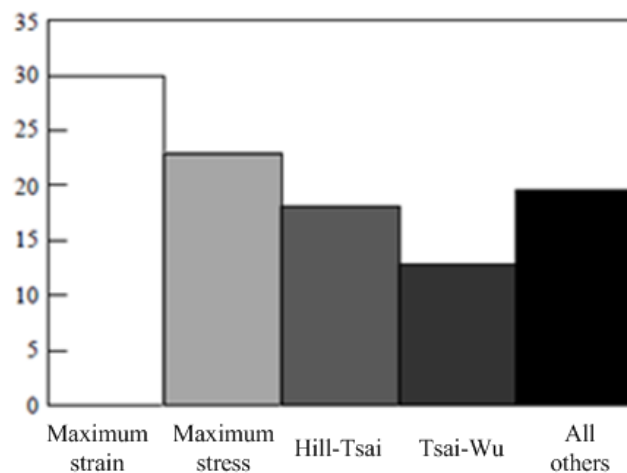
Figure 1.3: Engineering application of failure criteria, after [Sun et al., 1996].

As the failure modes are an immediate result of processes within the material, the accuracy of numerical failure prediction methods can be increased by modelling of the damage processes at the microstructural level of the heterogeneous material. Micromechanical methods can be applied to engineering problems using multiscale methods, as shown schematically in Figure 1.4.

The multiscale approach separates the analysed problem on two length scales - the macro-scale, which solves the problem on the engineering level usually employing the

finite element method, and the micro-scale, at which the stress and strain fields within the microstructure have been determined. An important feature of micromechanical methods is the Repeating Unit Cell (RUC) concept. The unit cell is a basic "building element" which characterises the evaluated heterogeneous material. Another important concept is the Representative Volume Element (RVE). The RVE micro model is a statistically representative sample of the heterogeneous material which has the same volume fractions of material phases and statistical distribution of inclusions, while homogeneous boundary conditions are applied to the boundaries of the RVE. The RUC concept assumes a simplified and perfectly arranged periodic microstructure with periodic boundary conditions on RUC boundaries.
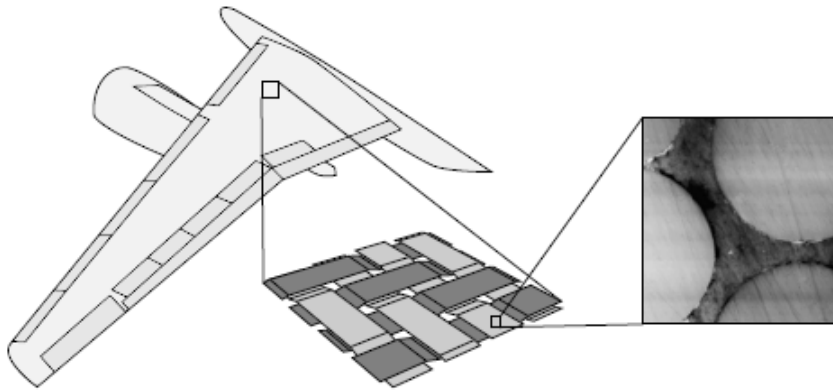
Figure 1.4: Schematic representation of the length scales in micromechanical structural analyses [Schwab et al., 2014].

An advantage of the multiscale damage modelling approach using micromechanical models is that the processes within the unit cell of the composite material are explicitly taken into account in the analysis of composite structures. Consequently, modelling of effects which determine homogenised mechanical properties of fibre reinforced composite materials, e.g. the unit cell morphology and fibre/matrix interphase effects, has been enabled.

When modelling of high strain rate problems, e.g. bird strike on aeronautical structures, the effects of the elevated strain rates on constitutive behaviour have to be taken into account. High strain rates have different implications on the fibre and matrix material models, as these effects influence only the matrix constituent [Goldberg et al., 2003a]. These effects can be modelled using micromechanical models. Consequently, the homogenised composite response, calculated using properties of the constituents, can be

predicted by these models.

A further benefit of micromechanical approaches is the ability to model advanced composite systems. The unit cells of such materials consist of several constituents of different sizes and functions. Thus, the very high computational cost of multiscale analyses requires the use of computationally efficient micromechanical models. Literature review on micromechanical methods revealed the High Fidelity Generalized Method of Cells (HFGMC) to be a computationally efficient procedure which has been applied to a very broad range of composite materials physical phenomena [Aboudi et al., 2003], [Aboudi et al., 2012], [Pineda et al., 2012a], [Bednarcyk et al., 2004].

1.2   Literature review

The HFGMC model belongs to the group of semi-analytical micromechanical models developed from the Method of Cells – MOC [Aboudi, 1988]. The original theory discretizes the composite RUC into three matrix and one fibre subcell. The displacement field within the subcell has been predicted using a first-order polynomial in the local coordinate system, whereas periodicity conditions at RUC boundaries enabled modelling of unidirectional composite materials. Although today MOC is an outdated theory, it has been employed for complex physical phenomena e.g. thermoplasticity effects in Metal Matrix Composites (MMC) and for modelling of the effect of fibre/matrix interface on composite mechanical properties [Aboudi, 1988].

A significant improvement has been introduced by the Generalized Method of Cells (GMC) [Paley and Aboudi, 1992]. In this model, the RUC has been discretized using an arbitrary number of subcells. Application of finer RUC discretization enabled more accurate modelling of the stress and strain fields within the heterogeneous material. The GMC model has been mostly employed for modelling of homogenised properties of MMCs with elasto-plastic effects [Paley and Aboudi, 1992], [Arnold et al., 1996]. The three-dimensional GMC model has been introduced in [Aboudi, 1995] and has been employed for modelling of three-dimensional woven composites. The reformulated GMC theory, with enhanced computational properties, has been applied for very fine GMC models (e.g. 100×100 subcells) in [Pindera and Bednarcyk, 1999]. The enhanced computational properties of this model enabled modelling of RUCs with several fibres, complex fibre shapes and RUC morphologies. Although the basic GMC theory dates back

to 1992, it is still being used in current researches, primarily due to its computational effectiveness which makes the model suitable for multiscale applications [Kurnatowski et al., 2012], [May et al., 2014]. Furthermore, new GMC formulations are being developed [Kurnatowski and Matzenmiller, 2012], as well as new interface models for fibre/matrix debonding [Matzenmiller and Köster, 2007].

Accuracy of the models has been improved by the introduction of a second-order displacement field. This theory has been named Higher Order Theory for Functionally Graded Materials (HOTFGM), and has been developed for modelling of Functionally Graded Materials (FGM) [Aboudi et al., 1999]. Expansion of the theory on periodic microstructures resulted in the HFGMC model [Aboudi et al., 2003]. Computational efficiency of HFGMC is a result of the application of traction continuity condition on subcell boundaries, which enables sufficiently accurate results employing relatively coarse RUC discretization [Aboudi et al., 2012]. The second order displacement field results in lower computational efficiency compared to GMC. Consequently, the HFGMC has been applied in the multiscale framework only in recent literature e.g. in [Pineda et al., 2012a], [Pineda et al., 2013].

Similarly to preceding micromechanical theories, HFGMC has been applied to a broad range of complex physical phenomena in composite materials – e.g. matrix plasticity, thermoelasticity and thermoplasticity of metal matrices, fibre/matrix debonding and shape memory alloys [Aboudi et al., 2003], [Aboudi et al., 2012], [Pineda et al., 2012a], [Bednarcyk et al., 2004], [Khatam and Pindera, 2009], [Freed and Aboudi, 2009].

Application of modified boundary conditions on RUC boundaries enabled modelling of localised effects in the composite, e.g. breakage of a single fibre or localised cracks in the matrix [Aboudi and Ryvkin, 2012], [Ryvkin and Aboudi, 2012]. Furthermore, various micromechanical models have been derived from the HFGMC. Among these, the reformulated HFGMC or Finite Volume Direct Averaging Micromechanics (FVDAM) theory [Bansal and Pindera, 2006] is particularly attractive due to its 60% increase in computational efficiency compared to the original model. A further interesting extension of the theory is the parametric FVDAM, which enables discretization of the composite RUC employing arbitrarily shaped subcells [Khatam and Pindera, 2009], [Calvacante and Marques, 2014], [Calvacante et al., 2008]. Consequently, more complex unit cell morphologies can be discretized employing fewer subcells. However, the additional computational cost presents a disadvantage of the parametric FVDAM approaches.

Research on micromechanical damage modelling has been mainly focused on fibre/matrix debonding in MMC, whereas micromechanical principles have been employed only in recent researches on damage modelling of polymeric composites [Bednarcyk et al., 2010], [Pineda et al., 2012a], [Pineda, 2012], [Moncada, 2012]. One of the important conclusions drawn from the WWFE is that the progressive nature of damage in the material has to be taken into account in order to obtain accurate results [Hinton et al., 2002]. The gradual degradation is a result of the damage initiation at the microstructural level. Progressive degradation of composite mechanical properties is usually modelled employing Continuum Damage Mechanics (CDM) principles on homogenised composite properties [Lapczyk and Hurtado, 2007], [Voyiadjis and Kattan, 1999], [Georgiadis et al., 2007].

Micromechanical approach in damage modelling applies failure criteria on the level of discretization of the micromechanical model, which is a single subcell in the HFGMC model. Based on initial results of micromechanical theories, in which subcell mechanical properties have been completely degraded when the failure initiation criterion has been reached, it has been concluded that CDM principles also need to be included at the micromechanical level [Tang and Zhang, 2012], [Moncada, 2012], [Bednarcyk and Arnold, 2009]. Advanced applications of multiscale approaches are provided in e.g. [Moncada, 2012] and [May et al., 2014], where the GMC model has been employed in impact damage analyses. The CDM principles have been used within HFGMC models only in recent researches, and include models which capture the multiaxial nature of damage in composite materials [Bednarcyk et al., 2010]. In the focus of the most recent research is the problem of dimensional dependence of damage processes in the multiscale framework [Pineda et al., 2012a], [Pineda et al., 2013].

1.3   Objectives and Thesis hypothesis

The objective of the research is improvement of numerical damage modelling procedures of impact loaded laminated composite structures. This has been achieved by implementation of the HFGMC micromechanical model with enhanced computational properties. The application of the multiscale methodology enables the further development of constitutive models, as well as damage models and material homogenisation of the composite material, to be applied on aeronautical structures. Furthermore, multiscale

analyses allow modelling of effects specific to fibre reinforced materials e.g. composite damage modes and high strain rate effects on constitutive models and failure modes of composites with epoxy matrices.

Thesis hypothesis:

Application of micromechanical models in the numerical impact simulations at composite structures enables modelling of specific effects which depend on the microstructure of the heterogeneous material. Consequently, the accuracy of the damage process simulation will be significantly improved, and the application domain expanded.

1.4   Thesis outline

Chapter 1

The first Chapter provides the introduction to the Thesis, in which the motivation and Thesis objectives have been defined. The literature review provided in this Chapter additionally clarifies the motivation and objectives of the Thesis.

Chapter 2

The second Chapter provides an overview of the multiscale approaches with a particular focus on application in composite materials. The semi-analytical reformulated High Fidelity Generalized Method of Cells model, which has been employed in the multiscale methodology developed in this Thesis, has been thoroughly explained. In addition to the description of the micromechanical theory, this Chapter provides the description of the HFGMC implementation into the Abaqus/Explicit FE framework. In addition to the multiscale application, a standalone HFGMC application, employed for implementation and validation of micromechanical failure theories, has been developed as described in this Chapter.

Chapter 3

Chapter 3 provides an overview of failure and damage theories applied in the design of composite structures. Four micromechanical damage initiation theories have been evaluated in this Thesis. These failure initiation theories have been validated using the

standalone HFGMC application in this Chapter.

Chapter 4

In Chapter 4, two progressive degradation theories, applied at the micromechanical scale, have been validated and compared to the experimental results available in the literature. The results demonstrated in this Chapter show that the micromechanical model and the applied failure theories can simulate the microdamage mechanisms causing nonlinear behaviour in matrix-dominated load cases, as well as the failure state of composite materials.

Chapter 5

The multiscale methodology has been employed in Chapter 5 as to model quasi-static tensile loading of a stringer reinforced composite panel and on soft body impact analyses on composite plates. The numerical simulations in this Chapter replicate gas gun experimental testing available in the literature. However, as experimental evidence of such experimental testing is very limited in the literature, the multiscale methodology has been validated by comparison with ply-level composite failure and damage theories.

Chapter 6

Chapter 6 provides an overview of the constitutive modelling specifics which are necessary to consider in the high strain rate modelling of composite materials with epoxy matrices. The nonlinear effects have been modelled in this Thesis employing the modified Bodner-Partom viscoplasticity theory. The HFGMC micromechanical model has been applied in this Chapter as to predict the homogenised composite behaviour of the IM7/977-2 composite at elevated strain rate considering the nonlinear matrix behaviour and the effect on the elasticity modulus.

Chapter 7

The final Chapter summarises the obtained results and provides recommendations for further research.

2 | Multiscale methodology

2.1 Multiscale approaches

Multiscale methods encompass a very wide field of techniques which have been employed as to solve a problem in which the structural behaviour depends on physical phenomena at smaller length scales. The number of scales investigated in multiscale approaches depends on the number of microstructural features that are inherent in the investigated physical phenomena. The type of coupling, or method of establishing interactions between different length scales, defines the type of the multiscale approach. The types of multiscale approaches are grouped, in general, into hierarchical, concurrent and synergistic approaches, after [Sullivan and Arnold, 2010]. A schematic representation of the relations between the computational efficiency and the exactness with which the physical phenomena have been modelled (fidelity) using multiscale methods, has been shown in Figure 2.1. The micromechanical approaches employed in the relevant multiscale methods have been also summarised in this Figure, as discussed in the following Section.

Hierarchical, or sequential, approaches employ coupling in strictly one direction, which depending on the direction of the change of scale, is up-scaling (homogenisation) or down-scaling (localisation). The term localisation refers to the transition from the larger to a subsequent lower scale, where the local variables e.g. microstructural stresses and strains are calculated based on the microstructural arrangement of constituents and their mechanical properties under the applied macroscopic loading. The transition in the opposite direction, from the micro-scale to the structural scale, is referred to as homogenisation. The equivalent mechanical properties of the heterogeneous material have been determined in this process.
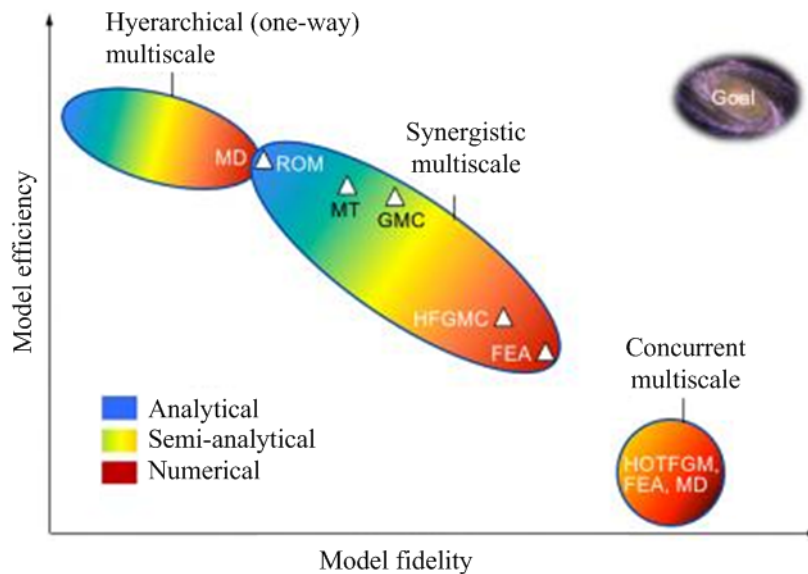
Figure 2.1: Micromechanical models used in multiscale approaches [Aboudi et al., 2012].

The hierarchical approach is employed in applications where the interactions of the investigated physical phenomena on the separate length scales are weak. Coupling between the scales has been established by either application of boundary conditions (down-scaling) or as prediction of effective properties (up-scaling) [Sullivan and Arnold, 2010].

Physical processes with strong interaction between the investigated scales have to be treated using concurrent multiscale methods as to model the phenomenon accurately. The investigated scales have been analysed simultaneously in these approaches, at a significant computational cost. An example of the application of concurrent multiscaling in the analysis of composite structures has been presented in [Smilauer et al., 2011], where triaxially braided composites have been investigated.

Synergistic multiscale approaches present a compromise between the computationally inefficient concurrent multiscaling approaches and the simple hierarchical approaches. The coupling strategy employed in this Thesis belongs to the synergistic approaches, as the interaction between the two scales has been established in the upscaling and downscaling directions, as shown in Figure 2.2.

In the analysis of fibre reinforced materials, the smallest scale of interest is the length scale of the fibre and matrix constituents. Most of the multiscale approaches employed on composite materials belong to synergistic approaches, after [Sullivan and Arnold,

2010]. The term "multiscale" in these approaches generally refers to two scales - the microstructural and the macroscopic or structural scale. Meso-scale computations, which have been employed as to calculate the laminate scale, have been performed in this Thesis by the multi-layered shell finite element in Abaqus.

Analytical, semi-analytical and numerical micromechanical models have been employed for micromechanical computations in multiscale analyses of composite structures throughout the literature, as shown in Figure 2.1.
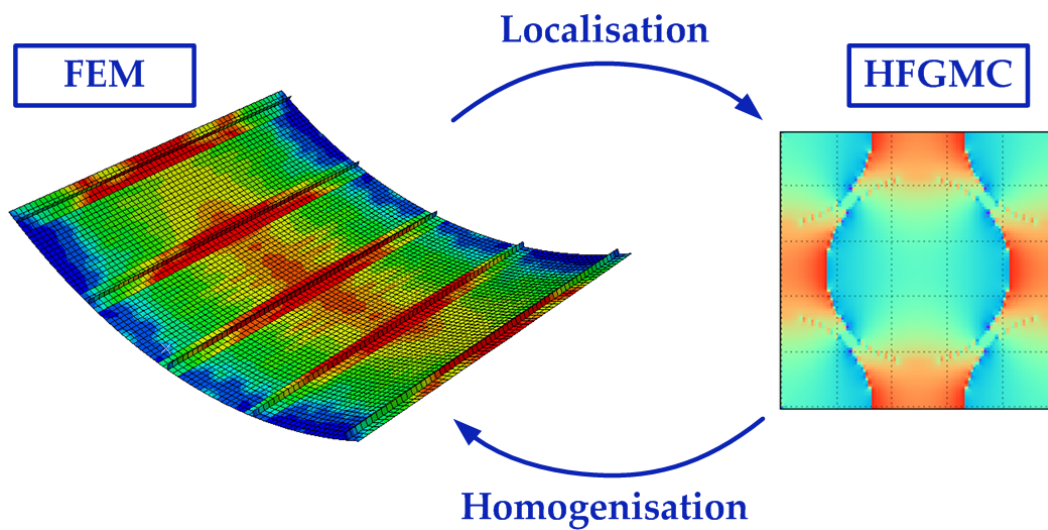
Figure 2.2: Two-scale methodology applied in this Thesis.

2.2   Micromechanics of composite materials

A very wide range of analytical, semi-analytical and numerical micromechanical models has been developed throughout the literature with the focus on modelling of the homogenised composite elasticity properties based on the properties and microstructural arrangements of the constituents. Simple micromechanical models as e.g. the Rule of Mixtures (ROM), predict the composite properties based on the volume fractions and mechanical properties of the constituents. More refined theories, e.g. Concentric Cylinder Assemblage (CCA) model assume that the composite consists of a distribution of cylindrical inclusions providing more accurate predictions of composite stiffness.

In addition to the prediction of the equivalent composite elasticity properties, advanced micromechanical theories enable modelling of the local fields within the heterogeneous

material which allows modelling of failure and damage processes. Mori-Tanaka (designated as MT in Figure 2.1) theory, for example, predicts the average fields in the fibre inclusion embedded in an infinite matrix assuming that the matrix fields are equal to the applied far fields. The Eshelby Equivalent Inclusion Method predicts concentration matrices for the average fields in the constituents by assuming the presence of an eigenstrain in an ellipsoidal inclusion. As the constituent level fields have been predicted, microdamage and failure mechanisms can be modelled by these theories. In addition to the traditional analytical models for prediction of the homogenised composite properties, special analytical models have been developed for modelling of specific composite failure modes, as for example formation of fibre kink bands in [Pimenta et al., 2009].

Figure 2.1 shows some of the micromechanical approaches employed in the three groups of multiscale approaches. Numerical methods (Finite Element, Boundary Element and Mesh-Free Methods) offer increased accuracy of the determination of the local fields but are computational demanding. Among the numerical methods applied in composite micromechanics models, the Finite Element Method has been employed for two and three-dimensional micromechanical models including complex damage and cohesive models for modelling of micromechanical damage processes. Examples of the applications on composite materials have been provided in e.g. [Fish and Shek, 2000], [Sun et al., 2001], [Verpoest and Lomov, 2005].

Analytical micromechanical models can predict only the constituent-averaged values of the local fields. Therefore, semi-analytical methods (Green's function, Fourier series approach, Transformation series approach, MOC based theories, after [Pineda, 2012]), offer the advantage of modelling spatially varying local fields at significantly lower computational cost compared to the fully numerical micromechanics models. Semi-analytical models are therefore a compromise between the numerical and analytical models. This Chapter focuses on the development of the HFGMC micromechanical theory, employed throughout this research. As shown in the various applications throughout the literature, the HFGMC model presents a good compromise between accuracy and computational effectiveness.

Heterogeneous microstructures have been represented by RVE and RUC concepts in the micromechanical models. The Representative Volume Element (RVE) has been typically defined as a volume of material whose effective behaviour is representative of the material as a whole. The RVE should be large enough as to statistically capture the

micro fluctuations of the heterogeneous material, enabling the prediction of the effective properties [Aboudi et al., 2012].

The RVE is a statistically representative sample of the heterogeneous material which has the same volume fractions of material phases and statistical distribution of inclusions. In contrast, the Representative Unit Cell (RUC) concept assumes a simplified and perfectly arranged periodic microstructure with periodic boundary conditions on RUC boundaries. The RVE and RUC terms have been often used interchangeably in the literature as discussed in e.g. [Pindera et al., 2009] and [Matzenmiller and Kurnatowski, 2009].

Figure 2.3 shows an illustration of the RUC concept. The right-hand side image shows an RUC discretized using rectangular subvolumes (subcells in the MOC-based micromechanical models). As the application and methods of micromechanics are very wide, only the MOC-based micromechanical models will be discussed in this Thesis, whereas detailed overviews of the micromechanical approaches have been presented in e.g. [Aboudi et al., 2012].
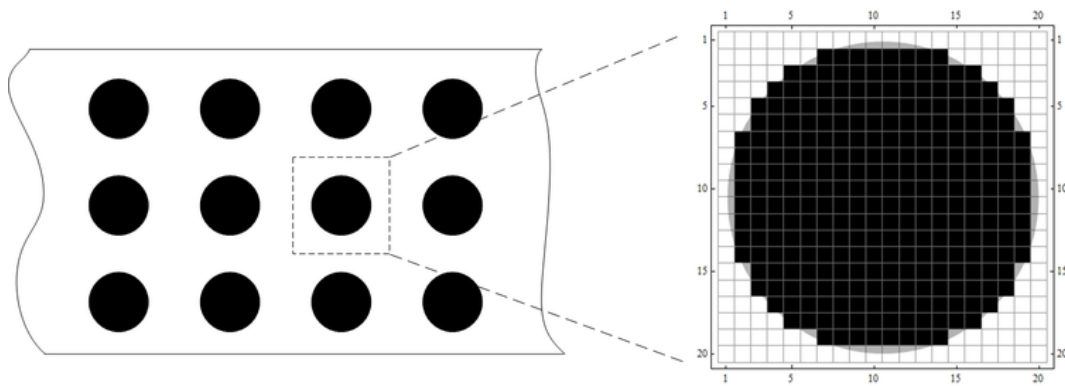
Figure 2.3: RUC concept.

2.3   Method of Cells micromechanical models

The Method of Cells micromechanical model discretizes a two-phase composite assuming perfect arrangement of fibres [Aboudi, 1988]. Consequently, the RUC concept has been employed in this micromechanical model. The MOC representative cell of the unidirectional composite has been discretized into four rectangular subcells in the original MOC model. One of the subcells represents the fibre constituent, whereas the

matrix has been represented by the remaining three subcells, as shown in Figure 2.4, where the MOC discretization scheme has been shown. The fibres are continuous and extend in the x_1 direction, whereas the fibre arrangement is periodic in the x_2 and x_3 directions. Dimensions of the RUC have been denoted by h and l, whereas the individual subcells have been denoted by the upper indexes β in the x_2 direction and γ in the x_3 direction. The local (subcell) coordinate systems have been designated using $\bar{y}_2, \bar{y}_3$, as shown in Figure 2.4. This designation convention has been employed throughout this Thesis for the more advanced micromechanical models.

Discretization using rectangular subcells would suggest that the circular fibre has been replaced by a rectangular inclusion. However, the governing interfacial equilibrium conditions have been applied at the boundaries of the individual subcells in an average sense. Consequently, the exact shape of the fibre inclusion has not been taken into account by the MOC as only the mechanical effect of the circular fibre inclusion in an average sense has been included into the model. A further implication of the applied interface-averaged boundary conditions is that the stress concentrations which would occur on the corners of the fibre inclusion are not present in the model. These features also apply for the more complex MOC-based micromechanical models.
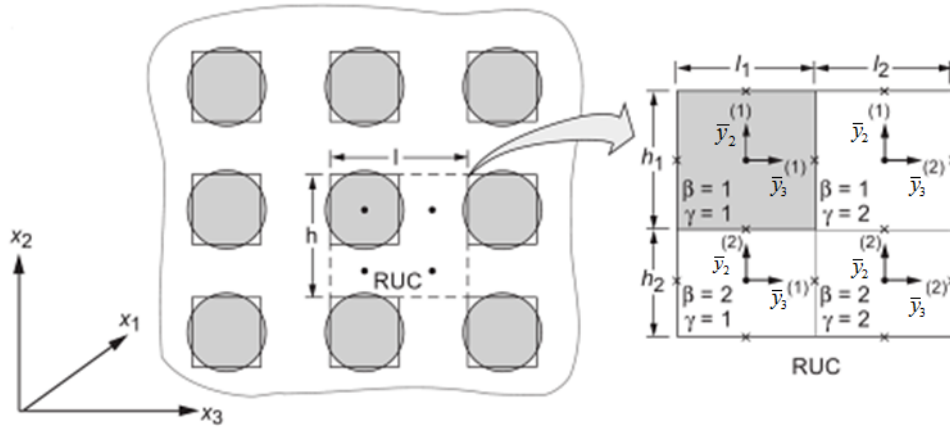
Figure 2.4: RUC discretization by MOC, after [Aboudi et al., 2012].

The first order displacement expansion in the subcell coordinates has been employed in the original MOC, which has been written as

$$u_i^{(\beta,\gamma)} = w_i^{(\beta,\gamma)} + \bar{y}_2^{(\beta)}\phi_i^{(\beta,\gamma)} + \bar{y}_3^{(\gamma)}\psi_i^{(\beta,\gamma)}, \qquad i = 1, 2, 3. \tag{2.1}$$

The term $w_i^{(\beta,\gamma)}$ in Equation 2.1 denotes the subcell centre displacement vector, whereas $\phi_i^{(\beta,\gamma)}$ and $\psi_i^{(\beta,\gamma)}$ are variables which determine the displacement field based on the local coordinates. The subcell strain components have been predicted using the strain-displacement relation in the subcell coordinate system

$$\varepsilon_{ij}^{(\beta,\gamma)} = \frac{1}{2}\left[\frac{\partial u_i^{(\beta,\gamma)}}{\partial \bar{y}_j^{(\beta)}} + \frac{\partial u_j^{(\beta,\gamma)}}{\partial \bar{y}_i^{(\gamma)}}\right]. \tag{2.2}$$

The micromechanical solution has been obtained by application of interfacial traction and displacement continuity conditions at the inner interfaces as well as on the outer RUC boundaries assuming periodicity conditions. Consequently, a system of four linear algebraic equations has been obtained in terms of the unknown displacement variables ϕ_i and ψ_i, where $i = 2, 3$. Solution of the system determines the RUC strain field, whereas application of the local (subcell) constitutive laws determines the stress field within the RUC.

As discussed in the literature review in Section 1.2, the MOC has been applied to a very wide range of thermoinelastic problems in MMC throughout the literature. These approaches have been summarised in [Aboudi et al., 2012].

An extension of the original MOC model has been derived in the form of the Generalized Method of Cells (GMC) [Paley and Aboudi, 1992]. This model allows the composite material RUC to be represented by an arbitrary number of subcells, thereby enabling modelling of more complex unit cells of the heterogeneous material. Consequently, the total number of subcells in the x_2 direction has been denoted by N_β, while the total number of subcells in the x_3 direction is N_γ. The improved RUC refinement enhances the accuracy of the prediction of the local fields within the heterogeneous material.

The GMC theory applies the same first order subcell displacement expansion as the MOC in Equation 2.1. Consequently, the subcell displacement components depend on the unknown variables in the same form as for the original MOC

$$\begin{aligned}
\varepsilon_{11}^{(\beta,\gamma)} &= \frac{\partial w_1^{(\beta,\gamma)}}{\partial x_1}, \\
\varepsilon_{22}^{(\beta,\gamma)} &= \phi_2^{(\beta,\gamma)}, \\
\varepsilon_{33}^{(\beta,\gamma)} &= \psi_3^{(\beta,\gamma)}, \\
\varepsilon_{23}^{(\beta,\gamma)} &= \tfrac{1}{2}(\phi_3^{(\beta,\gamma)} + \psi_2^{(\beta,\gamma)}), \\
\varepsilon_{13}^{(\beta,\gamma)} &= \tfrac{1}{2}(\psi_1^{(\beta,\gamma)} + \frac{\partial w_3^{(\beta,\gamma)}}{\partial x_1}), \\
\varepsilon_{12}^{(\beta,\gamma)} &= \tfrac{1}{2}(\phi_1^{(\beta,\gamma)} + \frac{\partial w_2^{(\beta,\gamma)}}{\partial x_1}).
\end{aligned} \tag{2.3}$$

The solution to the GMC micromechanical model has been predicted following the same principle as in the MOC. Therefore, application of traction and displacement continuity conditions at the subcell interfaces and the periodicity conditions at the RUC boundary allows assembly of the GMC system of equations. The interfacial boundary conditions have again been applied in the integral, average sense. The final form of the GMC system of equations has been obtained in the form

$$\boldsymbol{\varepsilon}^{(\beta,\gamma)} = \left[\begin{array}{c} \mathbf{A_M} \\ \mathbf{A_G} \end{array}\right]^{-1} \left[\begin{array}{c} \mathbf{0} \\ \mathbf{J} \end{array}\right] \bar{\boldsymbol{\varepsilon}}. \tag{2.4}$$

The submatrices $\mathbf{J}$ and $\mathbf{A_G}$ have been obtained after application of the displacement continuity conditions, whereas the submatrix $\mathbf{A_M}$ contains elements obtained after application of the traction continuity conditions. The relation between the subcell local strains $\boldsymbol{\varepsilon}^{(\beta,\gamma)}$ and the averaged homogenised strains $\bar{\boldsymbol{\varepsilon}}^{(\beta,\gamma)}$ has been established by the strain concentration tensors, which have been obtained by algebraic operations on the matrices in Equation 2.4.

There are several drawbacks which limit the applicability of the GMC model in composite damage prediction analyses, as addressed in [Bednarcyk et al., 2004] and [Bansal and Pindera, 2006]. The most important has been denoted throughout the literature as lack of normal-shear coupling. This term indicates a deficiency which results from the application of the first order displacement field. Consequently, application of macroscopic normal strains/stresses results in only normal subcell strains/stresses although each subcell is isotropic, transversely orthotropic or orthotropic. Accordingly, macroscopic shear strains/stresses results in only averaged shear subcell strains/stresses. The effect of the lack of normal shear coupling on the local RUC fields has been shown in Figure 2.5.
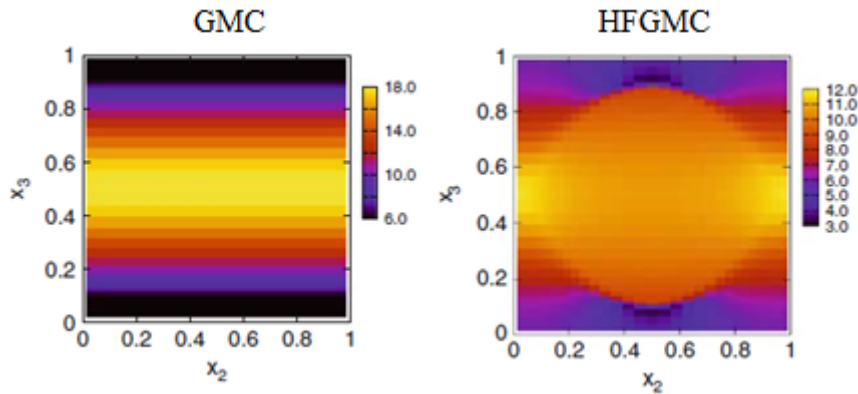
Figure 2.5: Comparison of GMC and HFGMC - contours of σ_{22} under prescribed $\bar{\varepsilon}_{22} = 1$, after [Matzenmiller and Kurnatowski, 2009].

As stated in [Bansal and Pindera, 2006], this deficiency can potentially result in very inaccurate results in the presence of cracks, disbonds or porosities. A further drawback of the GMC theory is that the displacement field within the unit cell is linear, making it unsuitable for e.g. wave propagation analyses, as stated in [Aboudi, 1988].

The GMC model has been widely used as it enables relatively accurate micro-scale analyses with significantly shorter computational times compared to FE micromechanical models, as stated in [Gan et al., 2000]. In recent publications, the GMC has been used as a micro-scale model in multiscale analyses as e.g. in [Pineda et al., 2009], [Moncada, 2012], [May et al., 2014]. The GMC theory has been also evaluated for implementation into the methodology developed in this Thesis. However, the described disadvantages and the intention of establishing a multiscale methodology for advanced composite materials in the further research motivated the implementation of more refined micromechanical methods. As shown in [Pineda et al., 2012b], GMC is not refined as to capture the local stress/strain fields in complex unit cell morphologies accurately.

2.4 High Fidelity Generalized Method of Cells

The deficiencies caused by the linear displacement field approximation in GMC have been solved by the High Fidelity Generalized Method of Cells as explained in [Aboudi et al., 2003] and [Arnold et al., 2004]. HFGMC employs a second-order Legendre type polynomial to approximate the displacement field within the subcell, leading to fundamental differences between the HFGMC and GMC, although they share the same

concept of unit cell discretization. Comparison of the results and computational aspects of the GMC and HFGMC micromechanical analyses has been provided in e.g. [Bednarcyk et al., 2004] and [Bansal and Pindera, 2006].

The micromechanical model employed this Thesis is based on reformulated HFGMC model, which has been initially introduced in [Bansal and Pindera, 2002]. The fundamental HFGMC equations [Aboudi et al., 2003] have been reformulated in order to enhance the computational efficiency of the model. The basic principle of the rearrangement of micromechanical equations has been introduced in [Bansal and Pindera, 2002] for the Higher Order Theory for Functionally Graded Materials (HOTFGM) model. The same approach has been applied on periodic microstructures in [Bansal and Pindera, 2005]. The reformulation introduces a local/global stiffness matrix approach which eliminates the need to satisfy various moments of the stress tensor, as explained in [Bansal and Pindera, 2005]. The result of this approach is an improvement of the computational efficiency by 60% compared to the original HFGMC model, as demonstrated in [Bansal and Pindera, 2006]. The reformulated HFGMC model has been later renamed as Finite Volume Direct Averaging Micromechanics (FVDAM) model [Bansal and Pindera, 2006].

Despite the fact that rearrangement of the solution procedure has resulted in significant computational efficiency benefits, the term HFGMC has been also employed for the reformulated version of the model throughout this Thesis. The applied naming convention can be justified by the fact that fundamental aspects of the models, as for example subcell displacement expansion, unit cell discretization, employed boundary conditions, are equal. More detailed explanation and discussion on the original and reformulated HFGMC models have been provided in [Arnold et al., 2004], [Haj-Ali and Aboudi, 2012] and [Aboudi et al., 2012].

The unit cell discretization is shown in Figure 2.6. The model for the unidirectional fibre-reinforced material is based on the previously defined assumption that fibres extend in the x_1 direction and are arranged in a doubly periodic array in the x_2 and x_3 directions. The coordinate system used for the HFGMC model corresponds to the material coordinate system of the composite ply, as x_1 is aligned with the fibre direction, x_2 lies in the ply plane and x_3 is perpendicular to the ply plane. The unit cell, having dimensions $l \times h$, is discretized into $N_\beta \times N_\gamma$ rectangular subcells. The constitutive behaviour of the (β, γ) subcell is governed by the elasticity tensor $\mathbf{C}^{(\beta,\gamma)}$. Consequently, the number of material phases in the HFGMC micromechanical model is limited only by the number
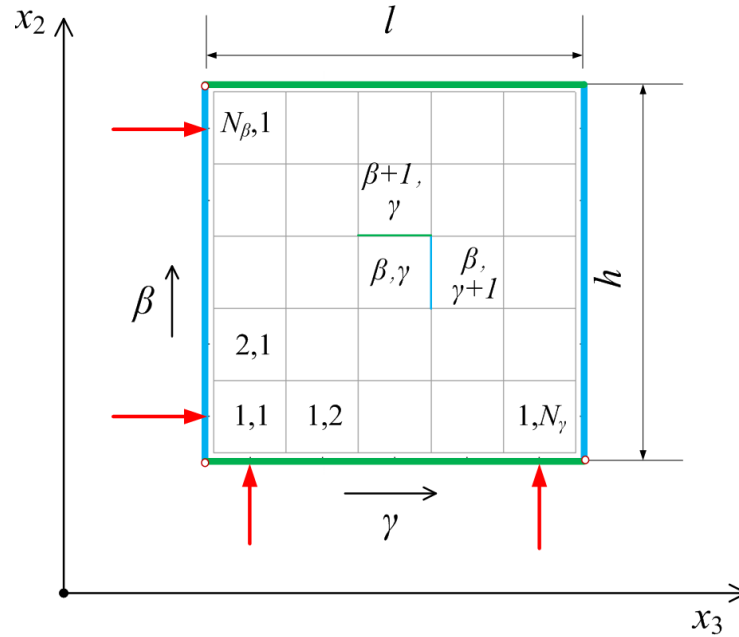
Figure 2.6: HFGMC discretization.

of subcells in the RUC. In the most simple HFGMC model for composite materials the RUC consists only of fibre and matrix material phases, while the unit cell has been discretized using a single fibre in the unit cell centre, as shown in the right-hand side image in Figure 2.3.

The final aim of micromechanical theories is to determine the strain concentration tensors $A_{ijkl}^{(\beta,\gamma)}$, which relate the microstructural strain field $\bar{\varepsilon}^{(\beta,\gamma)}$ based on the applied homogenised strain state $\bar{\varepsilon}$

$$\varepsilon_{ij}^{(\beta,\gamma)} = A_{ijkl}^{(\beta,\gamma)} \bar{\varepsilon}_{kl}. \tag{2.5}$$

The HFGMC theory assumes the displacement field within the subcells in the form

$$u_i^{(\beta,\gamma)} = \bar{\varepsilon}_{ij} x_j + u_i^{'(\beta,\gamma)}, \quad i = 1, 2, 3, \tag{2.6}$$

where the first term on the right side $(\bar{\varepsilon}_{ij} x_j)$ represents the contribution of the homogenised (averaged) strain, while $u_i^{'(\beta,\gamma)}$ represents the fluctuating displacement field.

The fluctuating displacement field has been approximated using a second-order Legendre-type polynomial expansion in the local subcell coordinates $(\bar{y}_2, \bar{y}_3)$, after [Aboudi et al., 2003]

$$
\begin{aligned}
u_i^{'(\beta,\gamma)} &= W_{i(00)}^{(\beta,\gamma)} + \bar{y}_2^{(\beta)} W_{i(10)}^{(\beta,\gamma)} + \bar{y}_3^{(\gamma)} W_{i(01)}^{(\beta,\gamma)} \\
&+ \tfrac{1}{2}\left(3\bar{y}_2^{(\beta)2} - \tfrac{h_\beta^2}{4}\right) W_{i(20)}^{(\beta,\gamma)} + \tfrac{1}{2}\left(3\bar{y}_3^{(\gamma)2} - \tfrac{l_\gamma^2}{4}\right) W_{i(02)}^{(\beta,\gamma)}, \qquad i = 1, 2, 3.
\end{aligned}
\tag{2.7}
$$

The $W_{i(mn)}^{(\beta,\gamma)}$ variables in Equation 2.7 are microvariables which define the fluctuating displacement field within each subcell. These microvariables have to be determined in order to calculate the strain field within the unit cell. The microscopic strain tensor has been calculated by using the relation

$$
\varepsilon_{ij}^{(\beta,\gamma)} = \bar{\varepsilon}_{ij} + \frac{1}{2}\left(\frac{\partial u_i^{'(\beta,\gamma)}}{\partial \bar{y}_j^{(\beta,\gamma)}} + \frac{\partial u_j^{'(\beta,\gamma)}}{\partial \bar{y}_i^{(\beta,\gamma)}}\right).
\tag{2.8}
$$

The solution of the micromechanical system of equations determines the unknown microvariables $W_{i(mn)}^{(\beta,\gamma)}$ in Equation 2.7. The resulting relations for the subcell strain tensor components are

$$
\begin{aligned}
\varepsilon_{11}^{(\beta,\gamma)} &= \bar{\varepsilon}_{11}, \\
\varepsilon_{22}^{(\beta,\gamma)} &= \bar{\varepsilon}_{22} + W_{2(10)}^{(\beta,\gamma)} + 3\bar{y}_2^{(\beta)} W_{2(20)}^{(\beta,\gamma)}, \\
\varepsilon_{33}^{(\beta,\gamma)} &= \bar{\varepsilon}_{33} + W_{3(01)}^{(\beta,\gamma)} + 3\bar{y}_2^{(\beta)} W_{3(02)}^{(\beta,\gamma)}, \\
\varepsilon_{12}^{(\beta,\gamma)} &= \bar{\varepsilon}_{12} + \tfrac{1}{2}\left[W_{1(10)}^{(\beta,\gamma)} + 3\bar{y}_2^{(\beta)} W_{1(20)}^{(\beta,\gamma)}\right], \\
\varepsilon_{13}^{(\beta,\gamma)} &= \bar{\varepsilon}_{13} + \tfrac{1}{2}\left[W_{1(01)}^{(\beta,\gamma)} + 3\bar{y}_3^{(\gamma)} W_{1(02)}^{(\beta,\gamma)}\right], \\
\varepsilon_{23}^{(\beta,\gamma)} &= \bar{\varepsilon}_{23} + \tfrac{1}{2}\left[W_{2(01)}^{(\beta,\gamma)} + 3\bar{y}_3^{(\gamma)} W_{2(02)}^{(\beta,\gamma)} + W_{3(10)}^{(\beta,\gamma)} + 3\bar{y}_2^{(\beta)} W_{3(20)}^{(\beta,\gamma)}\right].
\end{aligned}
\tag{2.9}
$$

Figure 2.7 shows the naming convention for the subcell averaged displacement and traction components employed throughout this Chapter. The traction and displacement components in the reformulated micromechanical formulation have been averaged along the subcell boundaries, as opposed to volume averaged quantities in the original model, after [Bansal and Pindera, 2006]. Consequently, the averaged displacement components have been defined as

$$
u_i^{2\pm(\beta,\gamma)} = \frac{1}{l_\gamma} \int\limits_{-l_\gamma/2}^{l_\gamma/2} u_i^{(\beta,\gamma)}\left(\pm\frac{h_\beta}{2}, \bar{y}_3^{(\gamma)}\right) d\bar{y}_3^{(\gamma)},
\tag{2.10}
$$
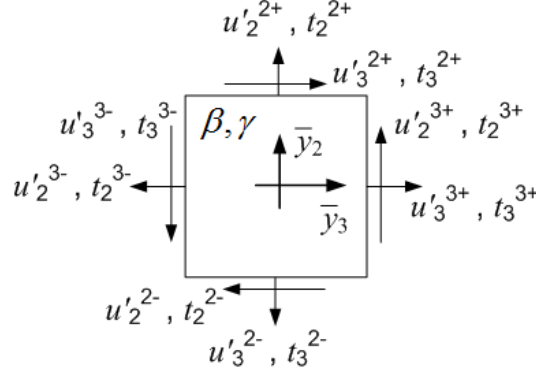
Figure 2.7: Subcell displacement and traction components.

$$u_i^{3\pm(\beta,\gamma)} = \frac{1}{h_\beta} \int\limits_{-h_\beta/2}^{h_\beta/2} u_i^{(\beta,\gamma)} \left(\bar{y}_2^{(\beta)}, \pm\frac{l_\gamma}{2} \right) d\bar{y}_2^{(\beta)}, \qquad i = 1, 2, 3. \tag{2.11}$$

Accordingly, the surface averaged traction components have been obtained as

$$t_i^{2\pm(\beta,\gamma)} = \frac{1}{l_\gamma} \int\limits_{-l_\gamma/2}^{l_\gamma/2} \sigma_{ij}^{(\beta,\gamma)} n_j^{(\beta,\gamma)} \left(\pm\frac{h_\beta}{2}, \bar{y}_3^{(\gamma)} \right) d\bar{y}_3^{(\gamma)}, \tag{2.12}$$

$$t_i^{3\pm(\beta,\gamma)} = \frac{1}{h_\beta} \int\limits_{-h_\beta/2}^{h_\beta/2} \sigma_{ij}^{(\beta,\gamma)} n_j^{(\beta,\gamma)} \left(\bar{y}_2^{(\beta)}, \pm\frac{l_\gamma}{2} \right) d\bar{y}_2^{(\beta)}, \qquad i = 1, 2, 3. \tag{2.13}$$

Equations 2.10 - 2.13 have been defined in the subcell local coordinate system $\bar{y}_2, \bar{y}_3$. The traction components in Equations 2.12 and 2.13 have been generated by the normal stress components at subcell interfaces.

The reformulated HFGMC model introduces local (subcell) stiffness matrices, which relate surface averaged traction components t_i of each subcell to the averaged fluctuating displacements u_i' at subcell boundaries and the macroscopic strain components which have been applied to the RUC. The tractions in the axial (*1*) direction are independent of tractions in the transverse directions (*2* and *3*), enabling separation of the stiffness matrix into axial and transverse local matrices. The subcell fluctuating displacement field in Equation 2.7 has been completely defined by the 15 unknown microvariables $W_{i(mn)}^{(\beta,\gamma)}$. The subcell local stiffness matrices relate 12 averaged displacement to 12 averaged traction components. Consequently, additional three equations are necessary as to obtain

the solution for the unknown microvariables. These relations have been introduced by satisfying the equilibrium equations at subcell boundaries

$$\int_{S_{\beta\gamma}} t_i^{n^{(\beta,\gamma)}} dS_{\beta\gamma} = 0, \qquad i = 1,2,3. \tag{2.14}$$

For the two-dimensional HFGMC model Equation 2.14 can be written as

$$\begin{aligned}
l_\gamma \left[t_1^{2+} + t_1^{2-} \right]^{(\beta,\gamma)} + h_\beta \left[t_1^{3+} + t_1^{3-} \right]^{(\beta,\gamma)} &= 0, \\
l_\gamma \left[t_2^{2+} + t_2^{2-} \right]^{(\beta,\gamma)} + h_\beta \left[t_2^{3+} + t_2^{3-} \right]^{(\beta,\gamma)} &= 0, \\
l_\gamma \left[t_3^{2+} + t_3^{2-} \right]^{(\beta,\gamma)} + h_\beta \left[t_3^{3+} + t_3^{3-} \right]^{(\beta,\gamma)} &= 0.
\end{aligned} \tag{2.15}$$

Application of several algebraic manipulation on Equations 2.10 - 2.15 leads to the 3 unknown microvariables. The complete derivation of the microvariables has been provided in the original papers of the reformulated HFGMC theory [Bansal and Pindera, 2002], [Bansal and Pindera, 2006]. The zero order microvariables $(W_{i(00)})$ have been defined as

$$\begin{aligned}
W_{1(00)}^{(\beta,\gamma)} &= \frac{C_{66}^{(\beta,\gamma)}}{2\bar{C}_{11}^{(\beta,\gamma)}} \left(u_1'^{2+} + u_1'^{2-} \right)^{(\beta,\gamma)} + \frac{h_\beta^2 C_{55}^{(\beta,\gamma)}}{2l_\gamma^2 \bar{C}_{11}^{(\beta,\gamma)}} \left(u_1'^{3+} + u_1'^{3-} \right)^{(\beta,\gamma)}, \\
W_{2(00)}^{(\beta,\gamma)} &= \frac{C_{22}^{(\beta,\gamma)}}{2\bar{C}_{22}^{(\beta,\gamma)}} \left(u_2'^{2+} + u_2'^{2-} \right)^{(\beta,\gamma)} + \frac{h_\beta^2 C_{44}^{(\beta,\gamma)}}{2l_\gamma^2 \bar{C}_{22}^{(\beta,\gamma)}} \left(u_2'^{3+} + u_2'^{3-} \right)^{(\beta,\gamma)}, \\
W_{3(00)}^{(\beta,\gamma)} &= \frac{l_\gamma^2 C_{44}^{(\beta,\gamma)}}{2h_\beta^2 \bar{C}_{33}^{(\beta,\gamma)}} \left(u_3'^{2+} + u_3'^{2-} \right)^{(\beta,\gamma)} + \frac{C_{33}^{(\beta,\gamma)}}{2\bar{C}_{33}^{(\beta,\gamma)}} \left(u_3'^{3+} + u_3'^{3-} \right)^{(\beta,\gamma)},
\end{aligned} \tag{2.16}$$

where the $\bar{C}$ variables are dependent on the elasticity tensor components and subcell dimensions as

$$\begin{aligned}
\bar{C}_{11}^{(\beta,\gamma)} &= C_{66}^{(\beta,\gamma)} + \frac{h_\beta^2}{l_\gamma^2} C_{55}^{(\beta,\gamma)}, \\
\bar{C}_{22}^{(\beta,\gamma)} &= C_{22}^{(\beta,\gamma)} + \frac{h_\beta^2}{l_\gamma^2} C_{33}^{(\beta,\gamma)}, \\
\bar{C}_{33}^{(\beta,\gamma)} &= C_{33}^{(\beta,\gamma)} + \frac{l_\gamma^2}{h_\beta^2} C_{55}^{(\beta,\gamma)}.
\end{aligned} \tag{2.17}$$

The first and second order microvariables $(W_{i(10)}, W_{i(01)}, W_{i(20)}, W_{i(02)})$ have been defined as

$$
\begin{bmatrix} W_{1(10)} \\ W_{1(20)} \\ W_{1(01)} \\ W_{1(02)} \end{bmatrix}^{(\beta,\gamma)} = \begin{bmatrix} \frac{1}{h_\beta} & -\frac{1}{h_\beta} & 0 & 0 \\ \frac{2}{h_\beta^2} & \frac{2}{h_\beta^2} & 0 & 0 \\ 0 & 0 & \frac{1}{l_\gamma} & -\frac{1}{l_\gamma} \\ 0 & 0 & \frac{2}{l_\gamma^2} & \frac{2}{l_\gamma^2} \end{bmatrix} \begin{bmatrix} \bar{u}_1'^{2+} \\ \bar{u}_1'^{2-} \\ \bar{u}_1'^{3+} \\ \bar{u}_1'^{3-} \end{bmatrix}^{(\beta,\gamma)} - \begin{bmatrix} 0 \\ \frac{4}{h_\beta^2} \\ 0 \\ \frac{4}{l_\gamma^2} \end{bmatrix} W_{1(00)}^{(\beta,\gamma)}, \qquad (2.18)
$$

$$
\begin{bmatrix} W_{2(10)} \\ W_{2(20)} \\ W_{3(10)} \\ W_{3(20)} \end{bmatrix}^{(\beta,\gamma)} = \begin{bmatrix} \frac{1}{h_\beta} & -\frac{1}{h_\beta} & 0 & 0 \\ \frac{2}{h_\beta^2} & \frac{2}{h_\beta^2} & 0 & 0 \\ 0 & 0 & \frac{1}{h_\beta} & -\frac{1}{h_\beta} \\ 0 & 0 & \frac{2}{h_\beta^2} & \frac{2}{h_\beta^2} \end{bmatrix} \begin{bmatrix} \bar{u}_2'^{2+} \\ \bar{u}_2'^{2-} \\ \bar{u}_3'^{2+} \\ \bar{u}_3'^{2-} \end{bmatrix}^{(\beta,\gamma)} - \begin{bmatrix} 0 & 0 \\ \frac{4}{h_\beta^2} & 0 \\ 0 & 0 \\ 0 & \frac{4}{h_\beta^2} \end{bmatrix} \begin{bmatrix} W_{2(00)} \\ W_{3(00)} \end{bmatrix}^{(\beta,\gamma)},
$$

$$
(2.19)
$$

$$
\begin{bmatrix} W_{2(01)} \\ W_{2(02)} \\ W_{3(01)} \\ W_{3(02)} \end{bmatrix}^{(\beta,\gamma)} = \begin{bmatrix} \frac{1}{l_\gamma} & -\frac{1}{l_\gamma} & 0 & 0 \\ \frac{2}{l_\gamma^2} & \frac{2}{l_\gamma^2} & 0 & 0 \\ 0 & 0 & \frac{1}{l_\gamma} & -\frac{1}{l_\gamma} \\ 0 & 0 & \frac{2}{l_\gamma^2} & \frac{2}{l_\gamma^2} \end{bmatrix} \begin{bmatrix} \bar{u}_2'^{3+} \\ \bar{u}_2'^{3-} \\ \bar{u}_3'^{3+} \\ \bar{u}_3'^{3-} \end{bmatrix}^{(\beta,\gamma)} - \begin{bmatrix} 0 & 0 \\ \frac{4}{l_\gamma^2} & 0 \\ 0 & 0 \\ 0 & \frac{4}{l_\gamma^2} \end{bmatrix} \begin{bmatrix} W_{2(00)} \\ W_{3(00)} \end{bmatrix}^{(\beta,\gamma)}.
$$

$$
(2.20)
$$

The local HFGMC equations can be decoupled for the axial and the transversal components. Consequently, the subcell governing equations can be written as

$$
\begin{Bmatrix} \bar{t}_1^{2+} \\ \bar{t}_1^{2-} \\ \bar{t}_1^{3+} \\ \bar{t}_1^{3-} \end{Bmatrix}^{(\beta,\gamma)} = \begin{bmatrix} L_{11} & L_{12} & L_{13} & L_{14} \\ L_{21} & L_{22} & L_{23} & L_{24} \\ L_{31} & L_{32} & L_{33} & L_{34} \\ L_{41} & L_{42} & L_{43} & L_{44} \end{bmatrix}^{(\beta,\gamma)} \begin{Bmatrix} \bar{u}_1'^{2+} \\ \bar{u}_1'^{2-} \\ \bar{u}_1'^{3+} \\ \bar{u}_1'^{3-} \end{Bmatrix}^{(\beta,\gamma)} + 2 \begin{bmatrix} C_{66} & 0 \\ -C_{66} & 0 \\ 0 & C_{55} \\ 0 & -C_{55} \end{bmatrix}^{(\beta,\gamma)} \begin{Bmatrix} \bar{\varepsilon}_{12} \\ \bar{\varepsilon}_{13} \end{Bmatrix},
$$

$$
(2.21)
$$

$$
\left\{\begin{array}{c} \bar{t}_2^{2+} \\ \bar{t}_2^{2-} \\ \bar{t}_3^{2+} \\ \bar{t}_3^{2-} \\ \bar{t}_2^{3+} \\ \bar{t}_2^{3-} \\ \bar{t}_3^{3+} \\ \bar{t}_3^{3-} \end{array}\right\}^{(\beta,\gamma)} = \left[\begin{array}{cccccccc} K_{11} & K_{12} & 0 & 0 & K_{15} & K_{16} & K_{17} & K_{18} \\ K_{21} & K_{22} & 0 & 0 & K_{25} & K_{26} & K_{27} & K_{28} \\ 0 & 0 & K_{33} & K_{34} & K_{35} & K_{36} & K_{37} & K_{38} \\ 0 & 0 & K_{43} & K_{44} & K_{45} & K_{46} & K_{47} & K_{48} \\ K_{51} & K_{52} & K_{53} & K_{54} & K_{55} & K_{56} & 0 & 0 \\ K_{61} & K_{62} & K_{63} & K_{64} & K_{65} & K_{66} & 0 & 0 \\ K_{71} & K_{72} & K_{73} & K_{74} & 0 & 0 & K_{77} & K_{78} \\ K_{81} & K_{82} & K_{83} & K_{84} & 0 & 0 & K_{87} & K_{88} \end{array}\right]^{(\beta,\gamma)} \left\{\begin{array}{c} \bar{u}_2'^{2+} \\ \bar{u}_2'^{2-} \\ \bar{u}_3'^{2+} \\ \bar{u}_3'^{2-} \\ \bar{u}_2'^{3+} \\ \bar{u}_2'^{3-} \\ \bar{u}_3'^{3+} \\ \bar{u}_3'^{3-} \end{array}\right\}^{(\beta,\gamma)}
$$

$$
+ \left[\begin{array}{cccc} C_{12} & C_{22} & C_{23} & 0 \\ -C_{12} & -C_{22} & -C_{23} & 0 \\ 0 & 0 & 0 & 2C_{44} \\ 0 & 0 & 0 & -C_{44} \\ 0 & 0 & 0 & 2C_{44} \\ 0 & 0 & 0 & -2C_{44} \\ C_{13} & C_{23} & C_{33} & 0 \\ -C_{13} & -C_{23} & -C_{33} & 0 \end{array}\right]^{(\beta,\gamma)} \left\{\begin{array}{c} \bar{\varepsilon}_{11} \\ \bar{\varepsilon}_{22} \\ \bar{\varepsilon}_{33} \\ \bar{\varepsilon}_{23} \end{array}\right\}.
$$

$$(2.22)$$

The components of the axial (in Equation 2.21) and transverse (in Equation 2.22) subcell stiffness matrices are defined in [Bansal and Pindera, 2002], and have been provided in Appendix A. One component of the axial and transverse subcell stiffness matrices has been provided in Equation 2.23 for completeness of this text as

$$
\begin{aligned}
L_{11}^{(\beta,\gamma)} = L_{22}^{(\beta,\gamma)} &= \frac{C_{66}^{(\beta,\gamma)}}{h_\beta}\left(4 - 3\frac{C_{66}^{(\beta,\gamma)}}{\bar{C}_{66}^{(\beta,\gamma)}}\right), \\
K_{12}^{(\beta,\gamma)} = K_{21}^{(\beta,\gamma)} &= \frac{C_{22}^{(\beta,\gamma)}}{h_\beta}\left(2 - 3\frac{C_{22}^{(\beta,\gamma)}}{\bar{C}_{22}^{(\beta,\gamma)}}\right).
\end{aligned}
$$

$$(2.23)$$

Components of the elasticity tensor in Equations 2.21 - 2.23 refer to the subcell elasticity tensor in the subcell local coordinate system which coincides with the material coordinate system of the composite material for the 2-D micromechanical model. The strain tensor components in Equations 2.21 and 2.22 refer to the homogenised strain state, which has been imposed on the boundaries of the RUC.

As to determine the displacement field within the composite unit cell, the global RUC stiffness matrices have to be assembled from the local stiffness matrices. Three

types of boundary conditions have been applied to the subcell interfaces as to assemble the global HFGMC equations.

The traction and displacement continuity conditions between the adjoining subcells have been applied in the integral form using average interface traction and displacement values. The traction continuity condition imposes mechanical equilibrium at the subcell interfaces, which for the traction components in the x_2 and the x_3 directions has been defined as

$$
\begin{aligned}
\bar{t}_i^{2+(\beta,\gamma)} + \bar{t}_i^{2-(\beta+1,\gamma)} &= 0, \\
\bar{t}_i^{3+(\beta,\gamma)} + \bar{t}_i^{3-(\beta,\gamma+1)} &= 0, \qquad i = 1, 2, 3.
\end{aligned}
\tag{2.24}
$$

The displacement continuity condition imposes the equivalence of displacements of common interfaces in the surface averaged sense. For subcell displacement components in the x_2 and the x_3 directions, this condition has been defined as

$$
\begin{aligned}
\bar{u}_i^{'2+(\beta,\gamma)} &= \bar{u}_i^{'2-(\beta+1,\gamma)} = \bar{u}_i^{'2(\beta+1,\gamma)}, \\
\bar{u}_i^{'3+(\beta,\gamma)} &= \bar{u}_i^{'3-(\beta,\gamma+1)} = \bar{u}_i^{'3(\beta,\gamma+1)}, \quad i = 1, 2, 3.
\end{aligned}
\tag{2.25}
$$

The upper indexes in Equation 2.25 refer to subcell interfaces which are counted from the unit cell outer boundaries. This nomenclature has been employed in the following text, while the β and γ indexes range from $1, ..., N_\beta - 1$ and $1, ..., N_\gamma - 1$.

Application of the traction and displacement continuity conditions on the interfaces within the unit cell completes the assembly of the global system of equations. The global HFGMC can also be decoupled into an axial and transverse systems, in accordance with the principle employed in the derivation of local stiffness matrices. Application of traction and displacement boundary conditions at subcell interfaces enables formulation of the equilibrium equations for each of the β, γ interfaces, which define the relation between the surface averaged displacements within the unit cell and the applied macro-scale strain state. The axial system of equations defines the relationship between displacement components in the *1* direction to the homogenised strain components $\bar{\varepsilon}_{12}$ and $\bar{\varepsilon}_{13}$. As an example of the global axial system of equations, the relation for the applied strain component $\bar{\varepsilon}_{12}$ has been defined as

$$L_{12}^{(\beta,\gamma)}\bar{u}_1^{'2(\beta,\gamma)} + (L_{11}^{(\beta,\gamma)} + L_{22}^{(\beta+1,\gamma)})\bar{u}_1^{'2(\beta+1,\gamma)} + L_{21}^{(\beta+1,\gamma)}\bar{u}_1^{'2(\beta+2,\gamma)} + L_{14}^{(\beta,\gamma)}\bar{u}_1^{'3(\beta,\gamma)}$$
$$+L_{13}^{(\beta,\gamma)}\bar{u}_1^{'3(\beta,\gamma+1)} + L_{24}^{(\beta+1,\gamma)}\bar{u}_1^{'3(\beta+1,\gamma)} + L_{23}^{(\beta+1,\gamma)}\bar{u}_1^{'3(\beta+1,\gamma+1)} = 2\left(C_{66}^{(\beta+1,\gamma)} - C_{66}^{(\beta,\gamma)}\right)\bar{\varepsilon}_{12},$$

$$(2.26)$$

while a similar relation can be written for $\bar{\varepsilon}_{13}$, as shown in [Bansal and Pindera, 2006]. The global system of equations for the displacement components in the $x_2 - x_3$ plane and the relation with the $\bar{\varepsilon}_{11}$, $\bar{\varepsilon}_{22}$, $\bar{\varepsilon}_{33}$ and $\bar{\varepsilon}_{23}$ strain components is defined in the transversal system of equations. As an Example of the transversal system of global equations, the relation of displacement components and the macroscopic normal strains $\bar{\varepsilon}_{11}$, $\bar{\varepsilon}_{22}$ and $\bar{\varepsilon}_{33}$ is defined as

$$K_{12}^{(\beta,\gamma)}\bar{u}_2^{'2(\beta,\gamma)} + \left(K_{11}^{(\beta,\gamma)} + K_{22}^{(\beta+1,\gamma)}\right)\bar{u}_2^{'2(\beta+1,\gamma)} + K_{21}^{(\beta+1,\gamma)}\bar{u}_2^{'2(\beta+2,\gamma)} + K_{16}^{(\beta,\gamma)}\bar{u}_2^{'3(\beta,\gamma)}$$
$$+K_{15}^{(\beta,\gamma)}\bar{u}_2^{'3(\beta,\gamma+1)} + K_{26}^{(\beta+1,\gamma)}\bar{u}_2^{'3(\beta+1,\gamma)} + K_{25}^{(\beta+1,\gamma)}\bar{u}_2^{'3(\beta+1,\gamma+1)} + K_{18}^{(\beta,\gamma)}\bar{u}_3^{'3(\beta,\gamma)}$$
$$+K_{17}^{(\beta,\gamma)}\bar{u}_3^{'3(\beta,\gamma+1)} + K_{28}^{(\beta+1,\gamma)}\bar{u}_3^{'3(\beta+1,\gamma)} + K_{27}^{(\beta+1,\gamma)}\bar{u}_3^{'3(\beta+1,\gamma+1)} =$$
$$\left(C_{12}^{(\beta+1,\gamma)} - C_{12}^{(\beta,\gamma)}\right)\bar{\varepsilon}_{11} + \left(C_{22}^{(\beta+1,\gamma)} - C_{22}^{(\beta,\gamma)}\right)\bar{\varepsilon}_{22} + \left(C_{23}^{(\beta+1,\gamma)} - C_{23}^{(\beta,\gamma)}\right)\bar{\varepsilon}_{33}.$$

$$(2.27)$$

The remaining relations, needed to assemble the global system of the HFGMC equations have been provided in [Bansal and Pindera, 2006]. The axial and transversal systems of equations can be written in the more convenient matrix form as

$$\begin{bmatrix} \mathbf{L}_{11} & \mathbf{L}_{12} \\ \mathbf{L}_{21} & \mathbf{L}_{22} \end{bmatrix} \begin{Bmatrix} \bar{\mathbf{u}}_1^{'2} \\ \bar{\mathbf{u}}_1^{'3} \end{Bmatrix} = \begin{bmatrix} \mathbf{\Delta c}_{11} & \mathbf{0} \\ \mathbf{0} & \mathbf{\Delta c}_{22} \end{bmatrix} \begin{Bmatrix} \bar{\varepsilon}_{12} \\ \bar{\varepsilon}_{13} \end{Bmatrix}, \qquad (2.28)$$

$$\begin{bmatrix} \mathbf{K}_{11} & \mathbf{0} & \mathbf{K}_{13} & \mathbf{K}_{14} \\ \mathbf{0} & \mathbf{K}_{22} & \mathbf{K}_{23} & \mathbf{K}_{24} \\ \mathbf{K}_{31} & \mathbf{K}_{32} & \mathbf{K}_{33} & \mathbf{0} \\ \mathbf{K}_{41} & \mathbf{K}_{42} & \mathbf{0} & \mathbf{K}_{44} \end{bmatrix} \begin{Bmatrix} \bar{\mathbf{u}}_2^{'2} \\ \bar{\mathbf{u}}_3^{'2} \\ \bar{\mathbf{u}}_2^{'3} \\ \bar{\mathbf{u}}_3^{'3} \end{Bmatrix} = \begin{bmatrix} \mathbf{\Delta C}_{11} & \mathbf{\Delta C}_{12} & \mathbf{\Delta C}_{13} & \mathbf{0} \\ \mathbf{0} & \mathbf{0} & \mathbf{0} & \mathbf{\Delta C}_{24} \\ \mathbf{0} & \mathbf{0} & \mathbf{0} & \mathbf{\Delta C}_{34} \\ \mathbf{\Delta C}_{41} & \mathbf{\Delta C}_{42} & \mathbf{\Delta C}_{43} & \mathbf{0} \end{bmatrix} \begin{Bmatrix} \bar{\varepsilon}_{11} \\ \bar{\varepsilon}_{22} \\ \bar{\varepsilon}_{33} \\ \bar{\varepsilon}_{23} \end{Bmatrix}.$$

$$(2.29)$$

Similarly as in the local stiffness matrices, the macroscopic strain state is at the right-hand side of Equations 2.28 and 2.29. The size of the axial system in Equation 2.28 is $[2N_\beta N_\gamma + (N_\beta + N_\gamma)] \times [2N_\beta N_\gamma + (N_\beta + N_\gamma)]$, whereas the transversal system in Equation 2.29 has $[4N_\beta N_\gamma + 2(N_\beta + N_\gamma)] \times [4N_\beta N_\gamma + 2(N_\beta + N_\gamma)]$ components. The submatrices in Equations 2.28 and 2.29 are provided in Appendix A, while one diagonal

and one off-diagonal component of transverse system are provided here as to promote clarity of this text. The axial global submatrices have identical structure. The component $\mathbf{K}_{11}$ has the form

$$
\mathbf{K}_{11} = \begin{bmatrix}
\mathbf{A}_{11}^{(1)} & 0 & 0 & 0 & 0 & 0 \\
0 & \mathbf{A}_{11}^{(2)} & 0 & 0 & 0 & 0 \\
0 & 0 & \mathbf{A}_{11}^{(3)} & 0 & 0 & 0 \\
0 & 0 & 0 & . & 0 & 0 \\
0 & 0 & 0 & 0 & . & 0 \\
0 & 0 & 0 & 0 & 0 & \mathbf{A}_{11}^{(N_\gamma)}
\end{bmatrix}, \tag{2.30}
$$

where the submatrix $\mathbf{A}_{11}^{(\gamma)}$ has been assembled from subcell stiffness matrices as

$$
\mathbf{A}_{11}^{(\gamma)} = \begin{bmatrix}
K_{22}^{(1,\gamma)} & K_{21}^{(1,\gamma)} & 0 & . & 0 & 0 & 0 \\
K_{12}^{(1,\gamma)} & K_{11}^{(1,\gamma)} + K_{22}^{(2,\gamma)} & K_{21}^{(2,\gamma)} & 0 & . & 0 & 0 & 0 \\
0 & K_{12}^{(1,\gamma)} & K_{11}^{(2,\gamma)} + K_{22}^{(3,\gamma)} & K_{21}^{(3,\gamma)} & . & 0 & 0 & 0 \\
0 & 0 & 0 & . & . & 0 & 0 & 0 \\
0 & 0 & 0 & . & . & . & 0 & 0 \\
0 & 0 & 0 & 0 & . & . & 0 & 0 \\
0 & 0 & 0 & 0 & . & K_{12}^{(N_\beta-1,\gamma)} & K_{11}^{(N_\beta-1,\gamma)} + K_{22}^{(N_\beta,\gamma)} & K_{21}^{(N_\beta,\gamma)} \\
0 & 0 & 0 & 0 & . & 0 & K_{12}^{(N_\beta,\gamma)} & K_{11}^{(N_\beta,\gamma)}
\end{bmatrix},
$$

$$\tag{2.31}$$

for $\gamma = 1, ..., N_\gamma$. The structure of the off-diagonal components in Equation 2.29 is defined as

$$
K_{13} = \begin{bmatrix}
B_{13}^{(1,1)} & B_{13}^{(1,2)} & . & . & . & B_{13}^{(1,N_\beta)} \\
B_{13}^{(2,1)} & B_{13}^{(2,2)} & . & . & . & B_{13}^{(2,N_\beta)} \\
. & . & . & . & . & . \\
. & . & . & . & . & . \\
. & . & . & . & . & . \\
B_{13}^{(N_\gamma,1)} & B_{13}^{(N_\gamma,2)} & . & . & . & B_{13}^{(N_\gamma,N_\beta)}
\end{bmatrix}, \tag{2.32}
$$

where the submatrix $B_{13}^{(\beta,\gamma)}$ has been assembled from components of subcell local stiffness matrices as

$$B_{13}^{(\beta,\gamma)} = \begin{bmatrix}
 & \gamma \to & 1 & 2 & . & . & \gamma & \gamma+1 & . & . & N_\gamma+1 \\
\beta \downarrow & & & & & & & & & & \\
1 & & 0 & 0 & . & . & 0 & 0 & . & . & 0 \\
2 & & 0 & 0 & . & . & 0 & 0 & . & . & 0 \\
. & & . & . & . & . & . & . & . & . & . \\
. & & . & . & . & . & . & . & . & . & . \\
\beta & & 0 & 0 & . & . & K_{26}^{(\beta,\gamma)} & K_{25}^{(\beta,\gamma)} & . & . & 0 \\
\beta+1 & & 0 & 0 & . & . & K_{16}^{(\beta,\gamma)} & K_{15}^{(\beta,\gamma)} & . & . & 0 \\
. & & . & . & . & . & . & . & . & . & . \\
. & & . & . & . & . & . & . & . & . & . \\
N_\beta+1 & & 0 & 0 & . & . & 0 & 0 & . & . & 0
\end{bmatrix}. \qquad (2.33)$$

Periodicity conditions in the x_2 and x_3 directions have been imposed on traction and displacement components at outer unit cell boundaries. These boundary conditions are defined as

$$\begin{aligned}
\bar{t}_i^{2(1,\gamma)} + \bar{t}_i^{2(N_\beta+1,\gamma)} &= 0, \\
\bar{t}_i^{3(\beta,1)} + \bar{t}_i^{3(\beta,N_\gamma+1)} &= 0, \\
\bar{u}_i^{'2(1,\gamma)} &= \bar{u}_i^{'2(N_\beta+1,\gamma)}, \\
\bar{u}_i^{'3(\beta,1)} &= \bar{u}_i^{'3(\beta,N_\gamma+1)}, \qquad i = 1,2,3.
\end{aligned} \qquad (2.34)$$

Application of the periodicity conditions introduces two new relations to the axial global system in Equation 2.28 and four additional relations to the transverse global system in Equation 2.29. The additional relations have been introduced by replacing the subcell indexes in the global equations (for example Equations 2.26 and 2.27) as

$$\begin{aligned}
\beta \to N_\beta, \quad \beta+1 \to 1, \quad \beta+2 \to 2, \\
\gamma \to N_\gamma, \quad \gamma+1 \to 1, \quad \gamma+2 \to 2.
\end{aligned} \qquad (2.35)$$

Consequently, the number of equations has been reduced to $[2N_\beta N_\gamma] \times [2N_\beta N_\gamma]$ for the axial system of equations and $[4N_\beta N_\gamma] \times [4N_\beta N_\gamma]$ for the transverse system. The global stiffness matrices **L** and **K** in Equations 2.28 and 2.29 are singular. In order to prevent rigid body motion of the unit cell, four displacement components at the corners of the unit cell have to be prevented. These fixed displacement components have been highlighted by the red arrows in Figure 2.6. As periodicity conditions are imposed at

the unit cell boundaries, the four fixed displacement components have been transferred to the opposite displacement components, thereby preventing rigid body motion of the complete unit cell.

Finally, solution of the global HFGMC equations for the unknown displacement components enables calculation of the microvariables in Equations 2.16 and 2.18 - 2.20, which determine the strain field within the unit cell, as defined in Equation 2.9.

2.5   Application of HFGMC micromechanical model

Solution of the micromechanical equations enables the determination of the strain concentration tensors $A_{ijkl}^{(\beta,\gamma)}$ in Equation 2.5, which relate the strain state in the β, γ subcell to the applied homogenised strain state. The localisation equation, in which the strain tensors have been written in Voigt notation, can be defined in a matrix form as

$$\boldsymbol{\varepsilon}^{(\beta,\gamma)} = \mathbf{A}^{(\beta,\gamma)}\bar{\boldsymbol{\varepsilon}}. \tag{2.36}$$

The numerical procedure for determination of the strain concentration tensors has been explained in [Aboudi et al., 2012]. Within this procedure, the unit cell has been first loaded with a unit macroscopic deformation in the 11 direction $\bar{\varepsilon}_{11} = 1.0$, while the remaining macroscopic strain tensor components are equal to zero. The solution of the defined global system of equation (Equations 2.28 and 2.29) defines a microscopic strain state in each of the β, γ subcells. This strain state, written in Voigt notation, forms the first column in the $\mathbf{A}^{(\beta,\gamma)}$ matrix. In the following iteration, the HFGMC systems of equations have been solved for the macroscopic strain component $\bar{\varepsilon}_{22} = 1.0$, while the resulting strain states form the second columns of the $\mathbf{A}^{(\beta,\gamma)}$ matrices. This procedure continues for the remaining four strain components, thereby completing the strain concentration tensor calculation.

The stress field within the unit cell has been calculated using subcell constitutive relations, after

$$\sigma_{ij}^{(\beta,\gamma)} = C_{ijkl}^{(\beta,\gamma)}\varepsilon_{kl}^{(\beta,\gamma)}. \tag{2.37}$$

The unit cell macroscopic stresses can be obtained by averaging the microscopic stresses over the unit cell as

$$\bar{\boldsymbol{\sigma}} = \frac{1}{hl} \sum_{\gamma=1}^{N_\gamma} \sum_{\beta=1}^{N_\beta} h_\beta l_\gamma \mathbf{C}^{(\beta,\gamma)} \mathbf{A}^{(\beta,\gamma)} \bar{\boldsymbol{\varepsilon}}, \tag{2.38}$$

while the equivalent elasticity tensor, which governs the constitutive response of the composite material, has been calculated as

$$\mathbf{C}^* = \frac{1}{hl} \sum_{\gamma=1}^{N_\gamma} \sum_{\beta=1}^{N_\beta} h_\beta l_\gamma \mathbf{C}^{(\beta,\gamma)} \mathbf{A}^{(\beta,\gamma)}. \tag{2.39}$$

Micromechanical analyses enable investigation of the effects at the microstructural level which determine the composite mechanical properties at the macro-level. These effects include the unit cell morphology (spatial arrangement of the constituents in the unit cell), volume fractions of the constituents, as well as constituents' constitutive models. HFGMC has been employed in this Section as to predict equivalent composite properties. Validation of the micromechanical analyses has been performed using FE analysis of a CFRP composite unit cell provided in [Hyer, 2009] with a 60% fibre volume fraction. The constituent mechanical properties for this analysis have been listed in Table 2.1.

Table 2.1: Constituent properties after [Hyer, 2009]

Carbon fibre properties					
E_1 [GPa]	$E_2 = E_3$ [GPa]	$\nu_{12} = \nu_{13}$ [$-$]	ν_{23} [$-$]	$G_{12} = G_{13}$ [GPa]	G_{23} [GPa]
230.	23.1	0.2	0.4	8.96	8.27
Epoxy matrix properties					
E [GPa]	ν [-]				
4.62	0.36				

As shown in Table 2.1, matrix subcells have been modelled as isotropic materials, whereas orthotropic elasticity constitutive relations have been assigned to the fibre subcells. As to evaluate the effect of unit cell morphology on the effective composite properties predicted by HFGMC, three types of unit cells have been analysed in this example. The evaluated RUC morphologies are shown in Figure 2.8. The first unit cell consists of a single fibre at the unit cell centre (designated as type 1 or square unit cell morphology throughout this Thesis). The second unit cell discretizes the composite material with four fibres at the unit cell corners (type 2 unit cell morphology). The third
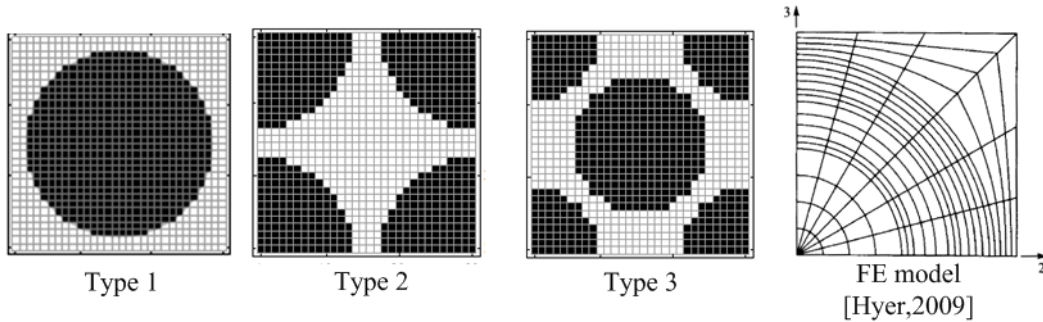
Figure 2.8: Evaluated RUC morphologies.

unit cell is a combination of the first and second unit cells, with fibre centers at unit cell corners and a single fibre located at the unit cell centre (type 3 unit cell morphology throughout this Thesis, referred to as diamond unit cell morphology in the literature). All unit cells represent unidirectional composites with 60% fibre volume fraction. The RUC morphology in the referent FE model employs the square morphology with applied symmetry boundary conditions which enable modelling of one-quarter of the unit cell. More details about the referent FE micromechanical model can be found in [Hyer, 2009]. The results of the micromechanical analyses have been summarised in Table 2.2.

Table 2.2: Comparison of HFGMC predicted composite properties with FEM results provided in [Hyer, 2009].

Micromodel:	30 x 30 HFGMC			FEM [Hyer, 2009]
RUC type:	1	2	3	1
E_1 [GPa]	141.688	141.688	140.675	141.7
$E_2 = E_3$ [GPa]	12.434	12.435	10.376	12.38
$G_{12} = G_{13}$ [GPa]	4.131	4.133	4.138	4.05
G_{23} [GPa]	3.408	3.408	4.329	2.94
$\nu_{12} = \nu_{13}$ [-]	0.257	0.257	0.257	0.256
ν_{23} [-]	0.419	0.419	0.513	0.421
Discretized V_f [-]	0.5999	0.5999	0.5956	0.6000

The HFGMC unit cells have been discretized using 30×30 equally sized subcells for this analysis. As the HFGMC model employs rectangular subcells, the discretized fibre volume fraction (V_f) differs from the referent value (0.6). This difference is most pronounced for the third unit cell type used in this analysis.

Evaluation of the effect of unit cell refinement has been performed using three levels of refinement - 10×10, 20×20 and 30×30 subcells for modelling of the equivalent

composite properties. The square unit cell morphology has been used in this study while the evaluated composite material is CFRP T300/5208 with 70% fibre volume fraction. The standardised constituent properties, after [Kollar and Springer, 2003], have been provided in Table 2.3, while the results of the micromechanical analyses have been summarised in Table 2.4.

Table 2.3: T300/5208 properties [Kollar and Springer, 2003].

T300 fibre				
E_1 [GPa]	$E_2 = E_3$ [GPa]	$\nu_{12} = \nu_{13}$ [-]	ν_{23} [-]	$G_{12} = G_{13}$ [GPa]
258.57	18.69	0.2	0.4	19.68
5208 matrix				
E [GPa]	ν [-]			
3.4	0.35			

The effective mechanical properties predicted by the HFGMC models converge with increased unit cell refinement if the unit cell discretization accurately predicts the fibre volume fraction. The last column in Table 2.4 shows experimentally determined composite properties, after [Kollar and Springer, 2003]. As shown, relatively large differences occur in the prediction of the in-plane shear modulus and the Poisson's coefficients.

Table 2.4: Effect of unit cell refinement on the computed composite properties.

N_β x N_γ	10 x 10	20 x 20	30 x 30	Ply properties
V_f [-]	68.00%	69.00%	70.20%	70.00%
E_1 [GPa]	176.96	179.49	182.61	181.00
$E_2 = E_3$ [GPa]	11.34	11.03	11.29	10.30
G_{12} [GPa]	9.02	5.56	6.10	7.17
$\nu_{12} = \nu_{13}$ [-]	0.236	0.239	0.237	0.28
ν_{23} [-]	0.394	0.388	0.391	0.59

Significant discrepancies between micromechanically calculated and experimentally observed properties have been often encountered in micromechanical studies. These differences emerge from the assumption that the constituent properties of a composite material are equal to the original (neat) constituent properties. Therefore, micromechanical analyses employ modified constituent mechanical properties, which have been defined as to match the predicted homogenised properties to the experimentally obtained results. These modified properties are referred to as in-situ properties throughout the literature.

The differences between the in-situ and the neat constituent properties have been caused by the curing process, by the effect of microstructural fibre arrangement in the composite, and by size effects, as discussed in e.g. [Camanho et al., 2007], [Ng et al., 2010]. The dependence of transverse tensile and in-plane shear strengths of a composite ply on the ply thickness is an example of the size effect on composite mechanical properties.

2.6   Multiscale implementation of HFGMC

Application of the multiscale damage prediction methodology in this Thesis has been focused on the high-velocity impact problems where highly nonlinear phenomena are expected to occur. These nonlinear phenomena include e.g. extremely large structural deformations, material degradation, structural failure and complex contact conditions. Application of implicit FE methods for the solution of these nonlinear problems would result in significant convergence difficulties. Consequently, explicit finite element codes have been employed for solution of the described problems. Examples of physical phenomena for which explicit procedures are more appropriate, compared to implicit methods, include high-speed dynamic events, complex contact problems, complex post-buckling problems, highly nonlinear quasi-static problems and material degradation and failure, after [Abaqus, 2010].

Structural-scale numerical analyses have been performed in this Thesis using the commercial FE code Abaqus/Explicit. The link between the structural-scale FE analysis and the HFGMC micromechanical computations has been achieved using the VUMAT subroutine for user defined constitutive models in Abaqus/Explicit. The VUMAT has been written in FORTRAN programming language. The complete architecture of the subroutine is structured in a two-state arrangement, where the states refer to the Cauchy stress and parameters of the constitutive model at the beginning and end of the current time increment.

The strain increment, obtained with Hughes-Winget formula, is passed into VUMAT as to define the new strain state, after [Abaqus, 2010]. All material point computations in the VUMAT have to be programmed in the vector form as to employ computational advantages of vector processing. Consequently, utility subroutines (e.g. UEXTER-NALDB), which would facilitate implementation of complex constitutive models as is the case in the implementation of the HFGMC model into VUMAT, are not available for

Abaqus/Explicit. Constitutive equations in the VUMAT subroutine have been written in the main material coordinate system, which is aligned with the HFGMC basic coordinate system. Therefore, no additional transformations of stresses, strain, elasticity and compliance tensors are necessary during coupling of the macro and micro-scales. The HFGMC model has been programmed in FORTRAN language as subroutine which is called for each material point in the VUMAT, as shown by the simplified flowchart in Figure 2.9.
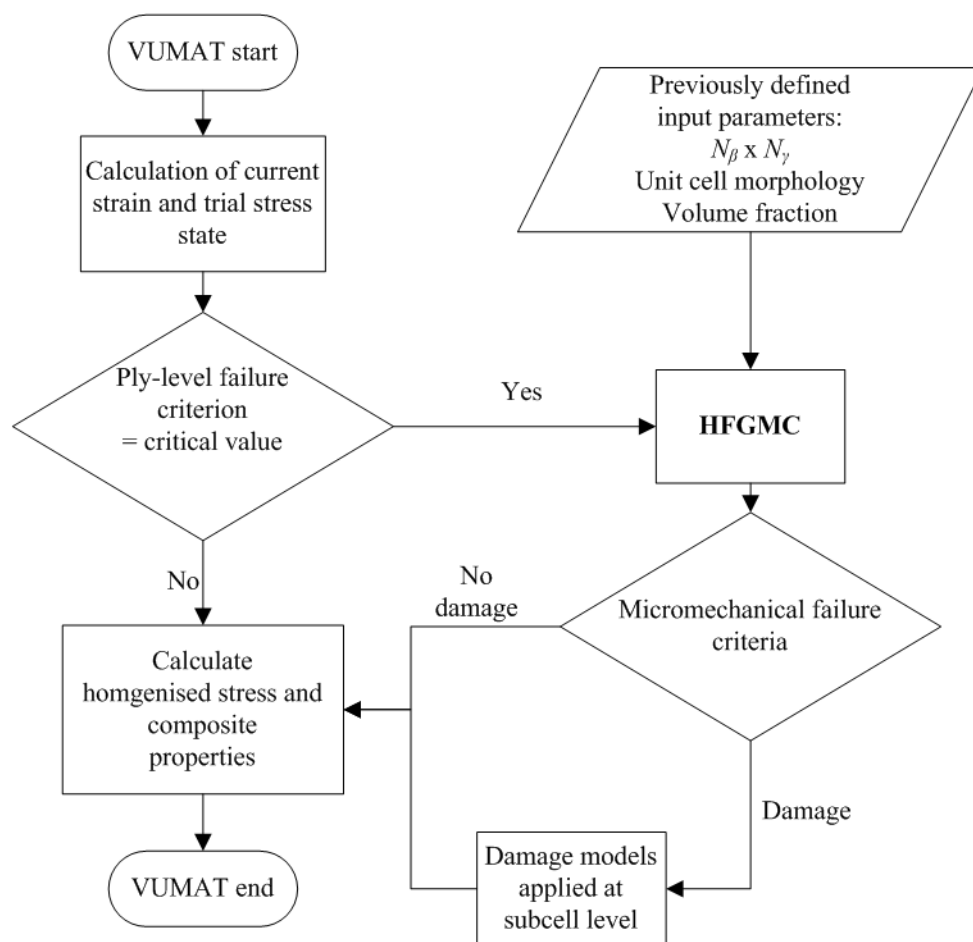
Figure 2.9: Simplified VUMAT-HFGMC flowchart.

Ply-level composite failure criteria, predicted by the trial stress state, have been employed in the methodology as to initiate micromechanical computations only for the material points where damage progression at the subcell level can be expected, as shown in Figure 2.9. Consequently, the computational performance of the multiscale methodology has been enhanced. Comparison of the evaluated micromechanical failure

criteria with the ply-level composite failure criteria has been performed in Section 5.2.

The constitutive model of the material at the macro-scale has been determined by the HFGMC model. Therefore, the Cauchy stress state at the end of the increment, as predicted by the user-defined constitutive law governed by the HFGMC model, has to be defined in the VUMAT subroutine. This task has been achieved by the application of the damage laws on the subcell level, whereas the effect of microdamage mechanisms on the homogenised mechanical properties has been subsequently included by application of the homogenisation employing Equation 2.38.

As the constitutive laws in the multiscale methodology have been applied on the subcell level, a very large number of data has to be stored and transferred from the current to the following time increment throughout the explicit analysis. The variables of the micromechanical model have been programmed in vector and matrix form as to simplify mathematical procedures necessary to solve the micromechanical analysis. The transfer of micro-scale state variables, associated to each material point in the FE model, in vector and matrix form throughout the time dependent analysis has been achieved using COMMON blocks in VUMAT. Examples of matrix-formated variables of the HFGMC subroutine are e.g. subcell strain concentration tensors $\mathbf{A}^{(\beta,\gamma)}$, subcell elasticity tensors $\mathbf{C}^{(\beta,\gamma)}$ and parameters of the damage models. The link between the macro-scale VUMAT and the HFGMC subroutine has been achieved using a total of 44 Solution Dependent state Variables (SDV) and 47 Common blocks.

At the start of the explicit analysis (stepTime = 0.0), the VUMAT subroutine solves a linear elastic stress update. The elasticity properties for this step have been predicted by the HFGMC subroutine prior to the FE analyses. The arrangement of the VUMAT subroutine utilises an approach where the total number of material points in the FE model has been divided into blocks of an inconsistent size. The problem becomes even more complicated when parallel processing has been applied in the simulation. Consequently, particular attention has to be given to the identification of each material point. This problem has been solved in the methodology by application of material point identifiers which have to be stored as COMMON variables.

The more refined flowchart of the HFGMC subroutine has been shown in Figure 2.10. The macroscopic strain state of the currently investigated material point at the current time increment, as provided by the explicit FE analysis, has been used as applied load for the HFGMC micromechanical model (Equations 2.28 and 2.29).
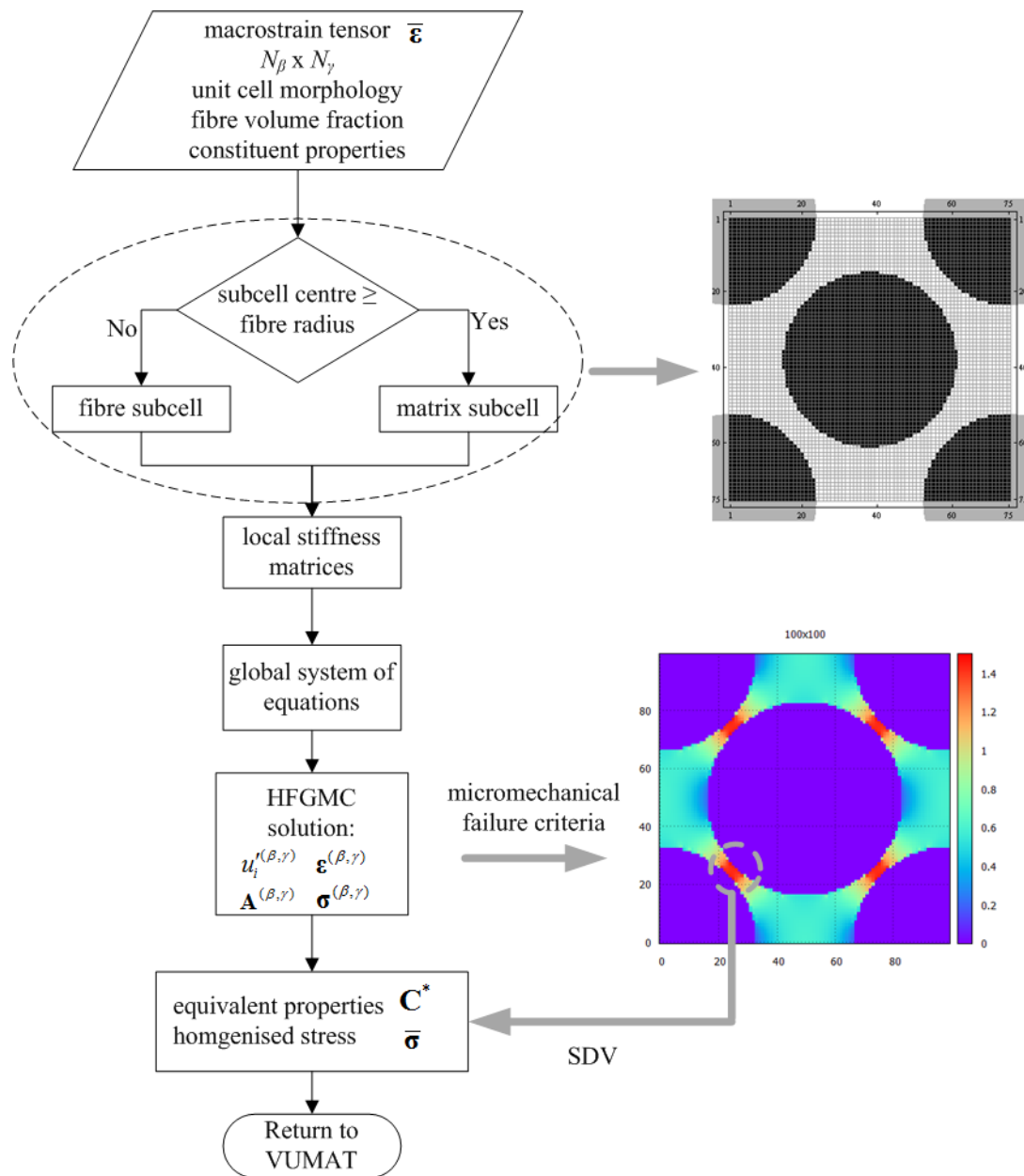
Figure 2.10: HFGMC flowchart.

Additional input parameters are variables which define the micromechanical model discretization refinement, unit cell morphology, as well as parameters which define properties of the composite material – fibre and matrix mechanical properties and fibre volume fraction. The preprocessor module discretizes the unit cell by assigning subcell fibre or matrix properties based on the distance of subcell centres to the fibre centres defined by unit cell morphology, as shown in Figure 2.11.
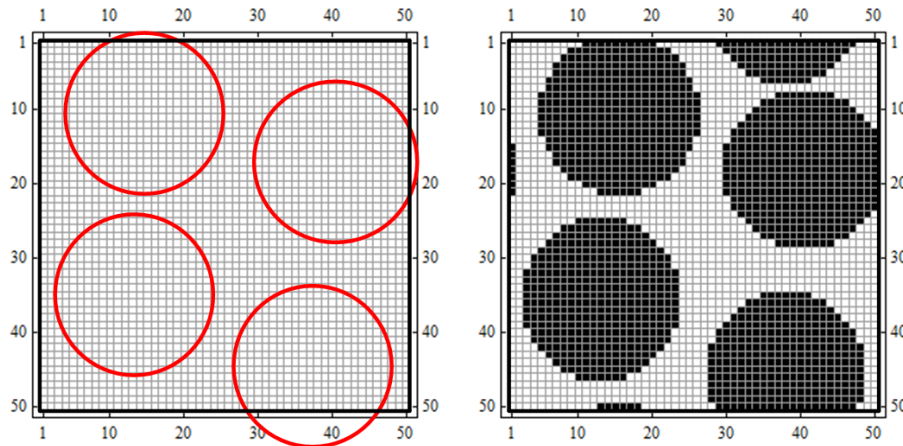
Figure 2.11: HFGMC preprocessor.

The SDVs have been employed as to visualise the maximal values of the micromechanical quantities within the RUC applied to the material point. For example, the maximal values of micromechanically calculated failure criteria, effective composite properties and similar variables have been visualised by the SDVs in the multiscale HFGMC application.

The discretization of the unit cell in the HFGMC model employs rectangular shaped subcells, as explained in Section 2.4. Generally, the HFGMC theory places no restrictions on the shapes of the unit cell and refinement (N_β and N_γ).

The sparse structure of the global system of equations (Equations 2.28 and 2.29) allowed implementation of a sparse system solver in the methodology. Benefits of the sparse implementation are finer unit cell discretization as well as a significant improvement in computational effectiveness. As to illustrate the sparsity of the HFGMC equations, the left-hand side image in Figure 2.12 shows the nonzero elements in the transverse global stiffness matrix discretized using 5×5 subcells, whereas the right-hand side image shows the dependence of the matrix sparsity on the employed RUC discretization. The MKL Direct Sparse Solver has been employed as to solve the HFGMC systems of equations.

Solution of the HFGMC systems of equations enables calculation of output variables e.g. homogenised mechanical properties, strain concentration tensors and failure indexes of the micromechanical failure criteria, which are returned to the VUMAT subroutine.

In addition to the multiscale HFGMC application, a standalone HFGMC application has been developed with the primary intent to enable comparison of the failure theories and evaluate the micromechanical damage models. The homogenised strain state has
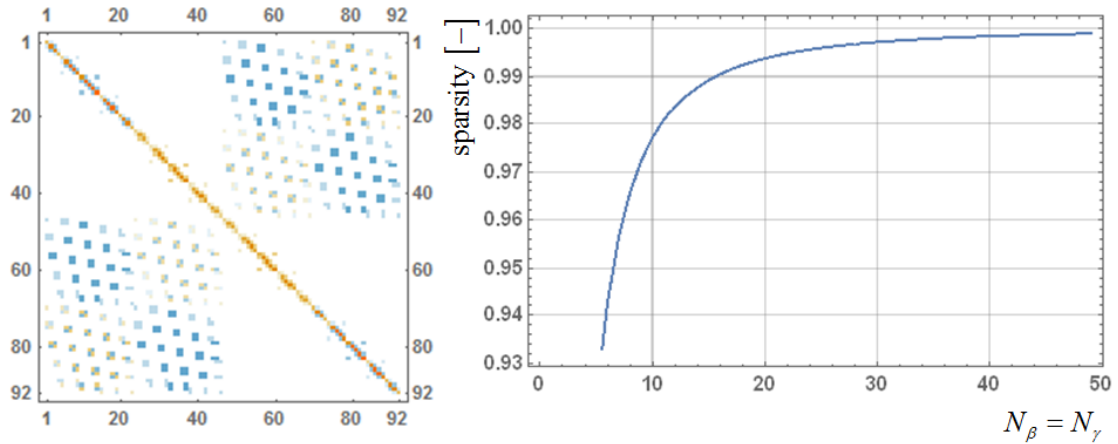
Figure 2.12: Sparsity of the transverse global stiffness matrix.

been simulated in the HFGMC standalone application for various macroscopic load cases. As the structure of HFGMC subroutines is equal for the standalone application and the multiscale environment, the secondary role of the standalone application is testing and debugging of HFGMC subroutines.

Visualisation of the results of the micromechanical model in the transverse plane (x_2-x_3) has throughout this Thesis been done using x_2 as the vertical axis as to comply with the usual visualisation approach used throughout the literature e.g. [Herakovich, 1998], [Aboudi et al., 2012], [Haj-Ali and Aboudi, 2009].

The solution in explicit FE analyses has been obtained in a very large number of extremely small time increments. Abaqus/Explicit employs a central difference time integration rule in which each increment is relatively computationally inexpensive when compared to the direct-integration dynamic analysis procedures in implicit FE analyses. Details of the implementation of the central difference scheme for the solution of the dynamic finite element system of equations have been provided in [Abaqus, 2010].

The central difference operator for the forward Euler scheme is conditionally stable, where the critical size of the increment has been determined by the highest frequency of the system. In practice, explicit FE codes employ a conservative approximation of the stable time increment which is defined as the smallest transit time of a dilatational wave through the finite elements in the mesh

$$\Delta t \approx \frac{L_{\min}}{c_d}, \tag{2.40}$$

where c_d is the dilatational wave speed in the material and L_{min} is the shortest dimension of the finite element. The value of the wave speed depends on the material properties, which for isotropic materials has been calculated as

$$c_d = \sqrt{\frac{\lambda + 2\mu}{\rho}}. \tag{2.41}$$

In order to ensure the accuracy of the micromechanical solution, the stable time increment of the explicit simulation has been further reduced in the high-velocity impact analyses where the micromechanical progressive damage models have been employed. Therefore, the initially predicted value of approximately 6. $\times 10^{-7}$ s for the FE model employed in Section 5.6, has been reduced, depending on the analysed impact case, to approximately 2. $\times 10^{-8}$ s as the applied strain increment has exceeded the stable strain increment. The value of the strain increment at which the applied HFGMC solution scheme results in accurate results has been determined using the standalone application and comparison of the results obtained using the evaluated micromechanical damage models with experimental composite failure curves and nonlinear behaviour.

Applications of Abaqus/Explicit on soft body impact analyses on aeronautical structures has been demonstrated in e.g. [Ivančević and Smojver, 2011], [Smojver and Ivančević, 2011]. Typical values of time increment sizes have been approximately $10^{-7} - 10^{-8}$ s, depending on the particular FE model, while a total time of 2 ms had to be simulated in these analyses as to predict the final damage state. This simplified evaluation of the computational efforts employed in impact analyses illustrates the necessity for efficient micromechanical models if the multiscale approach has been employed for the solution of similar impact analyses.

2.7 Conclusion

The intent of this Chapter has not been to provide a complete overview of the MOC micromechanical models and multiscale methods, as this task would be out of scope of this Thesis. Therefore, only the most important relations and concepts, which have lead to the implementation of the employed micromechanical theory, have been illustrated, whereas a detailed overview of the reformulated HFGMC model has been presented

in this Chapter. Applications of the HFGMC as a micromechanical model have been presented in the examples where the effective composite properties have been predicted.

A detailed overview of the HFGMC model implementation has been presented, where the computational aspects of the multiscale HFGMC implementation, employed in this Thesis, have been discussed. The developed standalone HFGMC application has been a valuable asset in the development of the multiscale methodology since the employed micromechanical failure and damage models have been evaluated in the standalone application. These analyses provided insight into the micromechanical effects of the evaluated damage models on the homogenised composite material models, as discussed in Chapter 4.

More refined MOC-based micromechanical models exist, e.g. the parametric FVDAM models as discussed in the literature review. Still, due to the emphasis on computational efficiency these models have not been included in the methodology. However, these models could be evaluated in the further research activities.

3 | Damage initiation modelling

3.1 Introduction

Complexities encountered in damage modelling of composite structures arise from the microstructural level heterogeneities of the composite material. The problem of failure modelling of laminated composite structures becomes even more complicated due to the fact that aeronautical composite structures consist of several composite plies which are oriented at different lay-up angles as to optimise the structural performance. Failure is defined as the state of a material system in which the structure is not able to further perform its design function [Talreja and Singh, 2007]. However, complete failure of a structure does not coincide with the onset of damage processes in the material. Consequently, significant damage could be accumulated in the structure prior to the loss of structural integrity.

The microstructural heterogeneity determines the emergence of the failure mode of
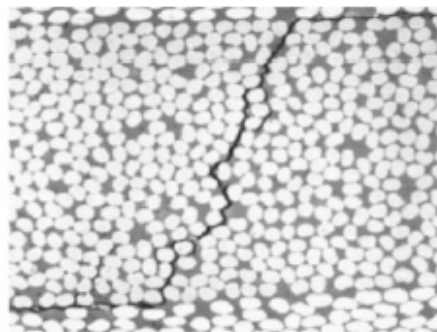
Figure 3.1: Interference of matrix cracks and delamination [Talreja and Singh, 2007].

the composite material - the physical mechanism in which damage has been manifested in the heterogeneous material. Composite failure modes associated with failure of the composite ply (intra-ply failure) are fibre fracture, fibre buckling (kinking), fibre splitting, fibre pullout, fibre-matrix debonding, matrix cracking and radial cracks, after [Herakovich, 1998]. Damage processes are initiated as matrix microcracks, which localise into larger defects between and along the fibres in plies oriented transverse to the primary load direction. Matrix cracks cause many of the intra-ply failure modes. Propagation of these transverse matrix cracks may lead to delamination - a failure mode of the composite lamina in which the plies physically separate from each other. An example of the interferences of transverse matrix cracks and delamination at the $+45°/90°/-45°$ interfaces has been shown in Figure 3.1. Although matrix cracks in a single ply do not disrupt the structural integrity, significant degradation in material stiffness and more severe failure modes could be caused by this failure mode.

Fibre failure in tensile loading occurs in those load cases when the stress or strain in the laminate is higher than the fibre strength or allowable fibre strain. Fibre kinking is the fibre failure mode observed in compressive loading. As discussed in [Talreja and Singh, 2007], fibre failure modes are always accompanied by other failure modes. Consequently, the real reason for the ultimate ply failure is often not evident. The interference of the failure modes associated with fibre failure has been shown in Figure 3.2.

Ply-level failure criteria are generally applied in the structural analyses of composites. Therefore, several ply-level criteria have been employed throughout this Thesis for
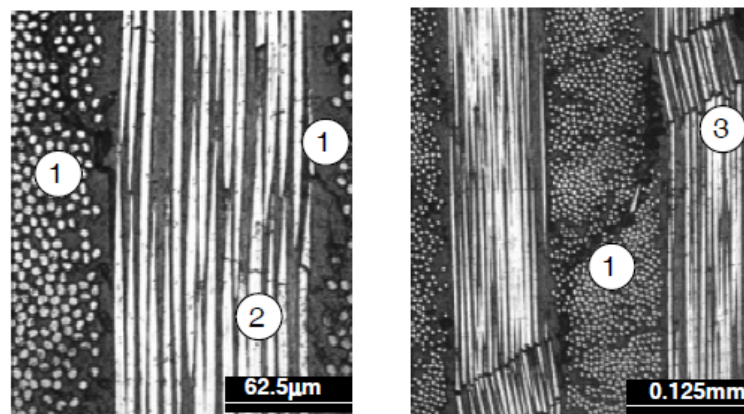
Figure 3.2: Fibre and matrix failure modes, designation of failure modes: 1) matrix cracking 2) fibre breaking 3) kink band [Pinho et al., 2006].

validation of the employed micromechanical theories. These failure criteria have been programmed in the multiscale VUMAT subroutine as to enable simultaneous evaluation of the stress state using micromechanical and ply-level failure theories. Details of these criteria have been summarised in Section 3.2. Additionally, the Abaqus built-in progressive damage model for fibre reinforced composites has also been employed for the methodology validation. Details of this model have been provided in Section 3.3.

Micro level modelling of the failure processes enables many advantages compared to the homogenised approach, as discussed in Chapter 1. Failure initiation has been studied in this Thesis using four theories which have been employed for this purpose in the literature. Details of the employed micromechanical failure theories have been provided in Section 3.4. The micromechanical failure initiation theories have been evaluated in this Chapter by visualisation in the homogenised stress space and by analyses of the effects within the RUC.

3.2   Ply-level failure initiation criteria

Homogenised composite failure criteria predict initiation of damage processes in composite materials by comparing the stress or strain states with allowable stress or strain values of the composite plies. The ply-level criteria are defined in the composite material main material coordinate system. However, significant discrepancies exist between the failure loads predicted using different failure theories, as discussed in Section 1.1. Consequently, the estimation of the structural response of the damaged structure will depend on the applied failure theory in the progressive damage analyses.

Four ply-level failure theories have been evaluated in this research - the Tsai-Wu, Tsai-Hill, Hashin and Puck's failure models. Only the final forms and basic properties of these criteria have been provided in this Thesis while derivation of the criteria and more information are provided in e.g. [Puck et al., 2002], [Hinton et al., 2004].

1) Tsai-Wu criterion
The Tsai-Wu criterion, also known as the quadratic failure criterion, has the form

$$F_i\sigma_i + F_{ij}\sigma_i\sigma_j = 1, \tag{3.1}$$

where the F_{ij} and F_i are variables dependent on composite ply strengths. The stress components in Equation 3.1 are written in Voigt notation.

2) Tsai - Hill criterion

The Tsai-Hill criterion has been developed by expanding the Von Mises criterion on orthotropic material models [Hyer, 2009]. The criterion is defined as

$$
\begin{aligned}
&[(G+H)\sigma_1^2 + (F+H)\sigma_2^2 + (F+G)\sigma_3^2 - 2H\sigma_1\sigma_2 \\
&-2G\sigma_1\sigma_3 - 2F\sigma_2\sigma_3 + 2L\tau_{23}^2 + 2M\tau_{13}^2 + 2N\tau_{12}^2 < 1].
\end{aligned}
\tag{3.2}
$$

The parameters denoted by F through N in Equation 3.2 are dependent on ply strengths while their values are determined in analyses of simple uniaxial stress states [Smojver, 2007]. The Tsai-Wu and Tsai-Hill criteria have similar properties - both belong to the group of interactive failure criteria, as they consider the interaction of stress components at the failure state. A common disadvantage of Tsai-Wu and Tsai-Hill criteria is the fact that they are not able to predict the failure mode of the composite material.

3) Hashin criterion

The Hashin's failure criterion distinguishes between four failure modes which is a significant improvement over the Tsai-Wu and Tsai-Hill criteria. The criterion is intended for unidirectional composites in plane stress state. The four failure modes are
a) Tensile fibre failure

$$
\left(\frac{\sigma_{11}}{X_t}\right)^2 + \frac{\tau_{12}^2}{S^2} = 1,
\tag{3.3}
$$

b) Compressive fibre failure

$$
\left(\frac{\sigma_{11}}{X_c}\right)^2 = 1,
\tag{3.4}
$$

c) Tensile matrix failure

$$
\frac{\sigma_{22}^2}{Y_t^2} + \frac{\tau_{12}^2}{S^2} = 1,
\tag{3.5}
$$
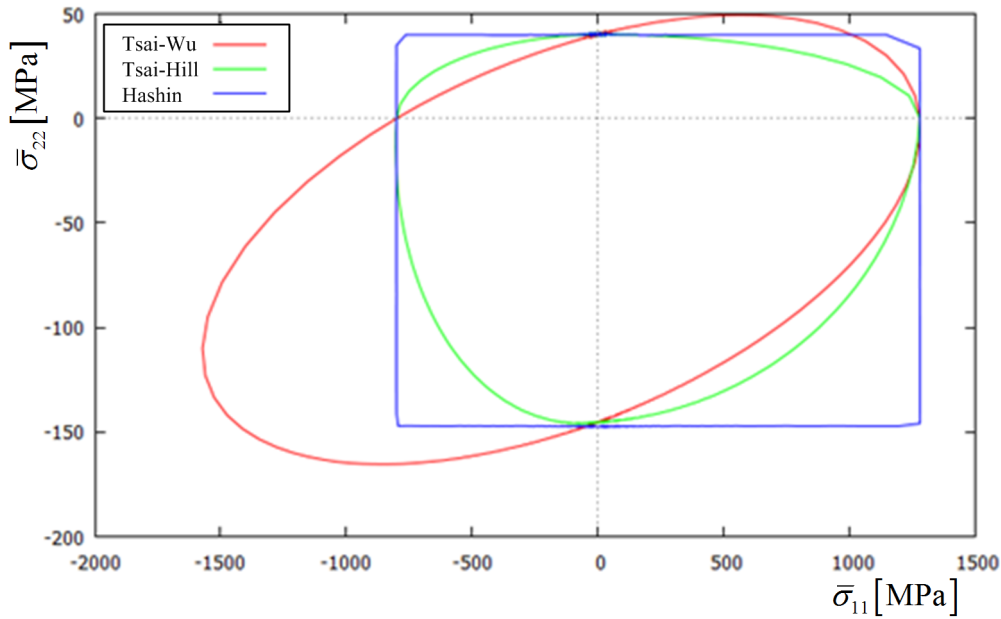
Figure 3.3: Comparison of Tsai-Wu, Tsai-Hill and Hashin criteria in the $\bar{\sigma}_{11} - \bar{\sigma}_{22}$ stress space.

d) Compressive matrix failure

$$\left[\left(\frac{Y_c}{2S}\right)^2 - 1\right]\left(\frac{\sigma_{22}}{Y_c}\right) + \frac{(\sigma_{22})^2}{4S^2} + \frac{\tau_{12}^2}{S^2} = 1. \tag{3.6}$$

Comparison of failure curves predicted by the Tsai-Wu, Tsai-Hill and Hashin criteria in the $\bar{\sigma}_{11} - \bar{\sigma}_{22}$ stress space has been shown in Figure 3.3. These failure curves have been predicted using composite ply strengths of the GFRP material which been summarised in Table 3.1, after [Soden et al., 1998].

4) Puck criterion

Puck's failure theory has been specifically designed for fibre reinforced materials. Similarly to the Hashin criterion, the Puck's criterion separates fibre failure (FF) and matrix failure, which in Puck's theory is denoted as inter-fibre failure (IFF). Fibre failure has been predicted using a simple criterion based on the ply strengths (tensile or

Table 3.1: GFRP ply strengths, after [Soden et al., 1998].

X_t [MPa]	X_c [MPa]	Y_t [MPa]	Y_c [MPa]	S [MPa]
1280.	800.	40.	145.	73.

compressive) in the fibre direction, after [Puck and Schürmann, 1998]

$$\left(\frac{\sigma_{11}}{X}\right)^2 = 1 \quad \begin{cases} X = X_t & \text{for} \quad \sigma_{11} > 0, \\ X = X_c & \text{for} \quad \sigma_{11} < 0. \end{cases} \tag{3.7}$$

Matrix failure has been predicted as brittle failure in the action plane, which is aligned with the fibre direction and inclined by the angle θ with regard to the ply plane (x_1, x_2) as shown in Figure 3.4. Similarly to the Mohr's failure theory, failure is predicted to initiate due to the stresses in the action plane, which is defined as the plane with the lowest resistance to the applied stress state. The stress components acting in the action plane can be transformed from the stress tensor in the main material coordinate system using the relations

$$\sigma_n = \sigma_{22}\cos^2\theta,$$
$$\tau_{nt} = -\sigma_{22}\sin\theta\cos\theta, \tag{3.8}$$
$$\tau_{n1} = \tau_{21}\cos\theta.$$

Complete derivation of the criterion is provided in [Puck and Schürmann, 1998], while only the final relations of the failure theory in the ply material principal coordinate system have been summarised in this Section. The Puck's IFF theory for the plane stress case (Puck-2D) defines three failure modes, which are dependent on the stress state in the material. The first failure mode (Mode A) is defined for $\sigma_{22} \geq 0$ and $\theta = 0$ as
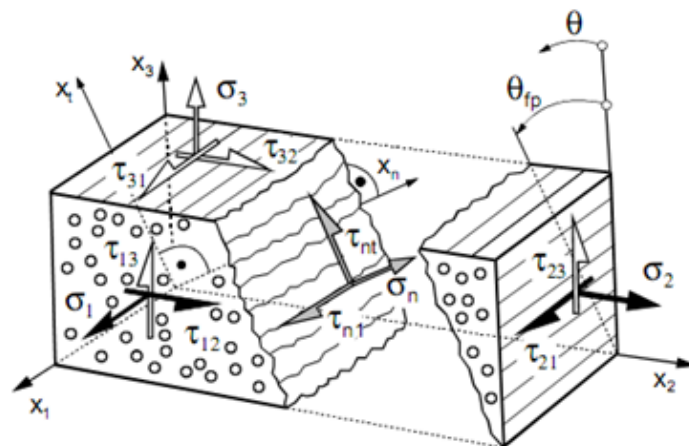
Figure 3.4: Stress components in Puck's action plane [Puck and Schürmann, 1998].

$$\sqrt{\left(\frac{1}{R_{22}^t} - \frac{p_{12}^t}{R_{12}}\right)^2 \sigma_{22}^2 + \left(\frac{\sigma_{12}}{R_{12}}\right)^2} + \frac{p_{12}^t}{R_{12}}\sigma_{22} = 1. \tag{3.9}$$

Matrix failure Mode B is caused by compressive values of σ_{22} and $\theta = 0$. Additionally, the stress state needs to satisfy the relation $0 \leq \left|\frac{\sigma_{22}}{\sigma_{12}}\right| \leq \frac{|R_{23}^A|}{\tau_c}$. Mode B is defined as

$$\sqrt{\left(\frac{p_{12}^c}{R_{12}}\right)^2 \sigma_{22}^2 + \left(\frac{\sigma_{12}}{R_{12}}\right)^2} + \frac{p_{12}^c}{R_{12}}\sigma_{22} = 1, \tag{3.10}$$

where R_{23}^A and τ_c are calculated as

$$R_{23}^A = \frac{R_{12}}{2p_{12}^c}\left(\sqrt{1 + 2p_{12}^c\frac{R_{22}^c}{R_{12}}} - 1\right), \tag{3.11}$$

$$\tau_c = R_{12}\sqrt{1 + 2p_{23}^c}. \tag{3.12}$$

The final IFF failure mode is Mode C, which is also defined for compressive σ_{22} values, while $\cos\theta_{fp} = \sqrt{\frac{R_{23}^A}{-\sigma_{22}}}$ and $0 \leq \left|\frac{\sigma_{22}}{\sigma_{12}}\right| \leq \frac{R_{23}^A}{|\tau_c|}$. Mode C is defined as

$$\left[\left(\frac{\sigma_{12}}{2(1 + p_{23}^c)R_{12}}\right)^2 + \left(\frac{\sigma_{22}}{R_{22}^c}\right)^2\right]\frac{R_{22}^c}{-\sigma_{22}} = 1. \tag{3.13}$$

The parameters denoted by R in Equations 3.9 - 3.13 are ply strengths, whereas the p parameters in these equations denote the slopes of the failure surface, as explained in [Puck et al., 2002].

3.3   Progressive damage and failure model in Abaqus

The Continuum Damage Mechanics based progressive damage model in Abaqus employs Hashin's failure initiation criterion (Section 3.2), after [Abaqus, 2010]. Consequently, damage initiation has been predicted using the failure criteria and damage modes defined by Hashin's theory. Upon damage onset, degradation of the composite ply properties has been modelled using damage parameters, which modify the initial undamaged elasticity matrix. Fibre (d_f), matrix (d_m) and shear (d_s) damage parameters reflect the current state of damage, having values ranging from 0 for an undamaged state, to 1 for a completely degraded material. The damaged elasticity matrix has the form

$$\mathbf{C_d} = \frac{1}{D} \begin{bmatrix} (1 - d_f)\, E_1 & (1 - d_f)\,(1 - d_m)\, \nu_{21} E_1 & 0 \\ (1 - d_f)\,(1 - d_m)\, \nu_{12} E_2 & (1 - d_m)\, E_2 & 0 \\ 0 & 0 & (1 - d_s)\, G_{12} D \end{bmatrix}, \quad (3.14)$$

where $D = 1 - (1 - d_f)(1 - d_m)\nu_{12}\nu_{21}$, after [Abaqus, 2010]. The mechanical properties in Equation 3.14 are unidirectional ply material properties defined in the main material coordinate system.
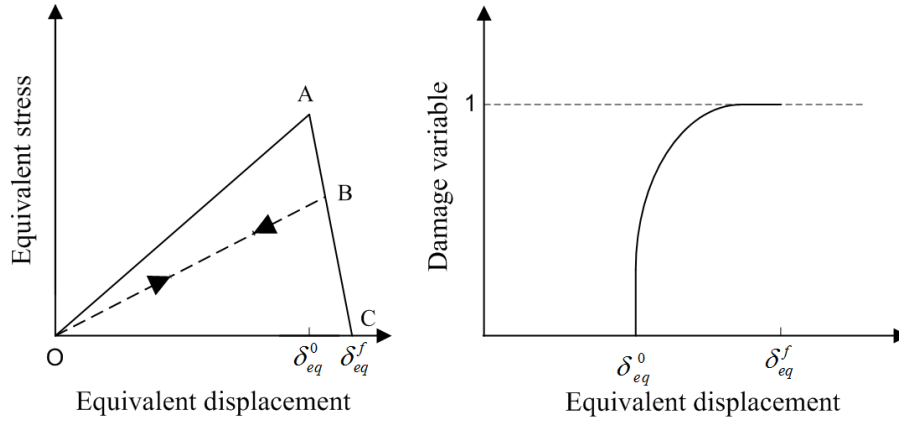
Figure 3.5: Equivalent displacement and evolution of damage variables in Abaqus damage model [Abaqus, 2010].

In order to avoid mesh dependency during material softening, a constitutive law expressed as a stress - equivalent displacement relation has been employed, as shown in Figure 3.5. Linear elastic behaviour prior to damage initiation is represented by the positive slope (OA) of the stress-displacement curve in Figure 3.5, left-hand side image. If Hashin's damage initiation criterion has been reached, damage parameters modify the stiffness matrix (Equation 3.14), thereby simulating degradation of mechanical properties. This part of stress – equivalent displacement curve is represented by the negative slope curve (AC) in Figure 3.5. Unloading and reloading from a partially damaged state occurs along a linear path represented by the line BO (or OB for reloading). The area of the triangle OAC is equal to the energy dissipated due to damage. The fracture energies in the four failure modes are the input parameters of the model. After damage initiation, damage parameter of a particular failure mode evolves as

$$d = \frac{\delta_{eq}^f(\delta_{eq} - \delta_{eq}^0)}{\delta_{eq}\left(\delta_{eq}^f - \delta_{eq}^0\right)}, \tag{3.15}$$

where δ_{eq}^0 is the initial equivalent displacement at which Hashin's damage initiation criterion has been reached and δ_{eq}^f is the displacement at which the material is completely damaged according to this failure mode. Equation 3.15 has been graphically presented in Figure 3.5, right-hand side image. An element is removed from the mesh when all material points reach the critical damage value in fibre failure modes, as to prevent infinite straining of elements with degraded stiffness properties. More information about the damage model have been provided in [Abaqus, 2010], [Barbero et al., 2013] and [Lapczyk and Hurtado, 2007].

3.4 Damage initiation at the micromechanical level

Micromechanical failure theories predict failure initiation at the subcell level in MOC-based micromechanical models employing constituent-level damage initiation criteria. Consequently, simple failure criteria, as e.g. the maximal stress or the maximal strain in the fibre direction criteria, have been applied for fibre subcells, whereas more complex criteria have been employed for matrix subcells. In order to obtain the failure initiation curves of the composite material using micromechanical principles, fibre and matrix failure modes have to be taken into account simultaneously, as damage onset in the constituents occurs under different loading conditions.

Ply-level failure theories which account for damage effects prior to complete ply failure performed better in the failure theory evaluation, as concluded in the aftermath of the WWFE, after [Bednarcyk et al., 2010]. These microdamage effects cause nonlinearities in the in-plane shear and transverse compressive constitutive behaviour of the composite plies, where the matrix properties govern the homogenised material response. Figure 3.6 shows the microdamage effects on the constitutive response in transverse compression and in-plane shear for the Silenka E-glass 1200tex/ MY750/HY917/DY063 Epoxy composite, after [Soden et al., 1998]. This composite material has been referred to as Silenka GFRP throughout this Thesis.

Progressive damage mechanics principles need also to be included in the micromechanical theories as to improve the prediction of failure onset and complete failure of the
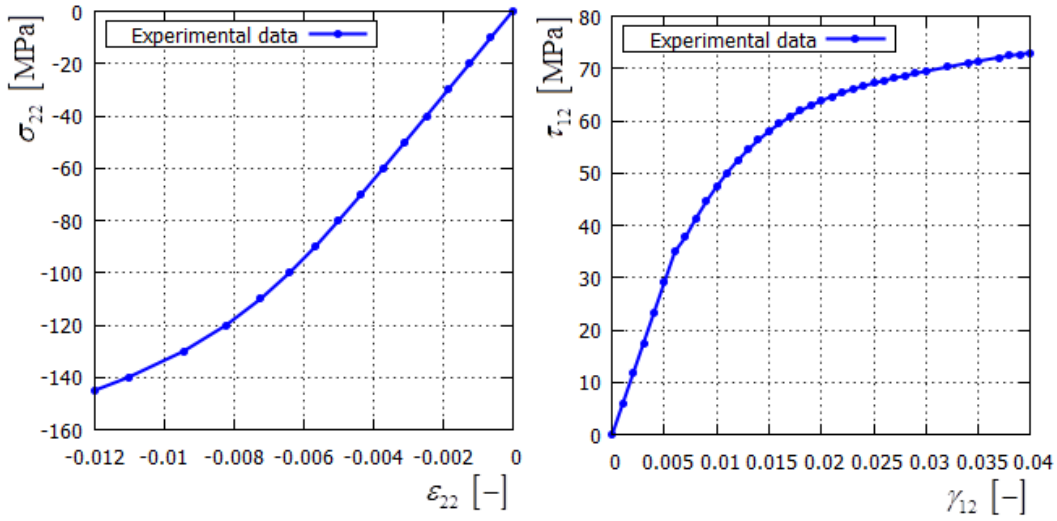
Figure 3.6: Nonlinear behaviour of Silenka E-glass 1200tex/ MY750/HY917/DY063 Epoxy composite in transverse compression (left-hand side image) and in-plane shear (right-hand side image), after [Soden et al., 1998].

composite material, as discussed in the following Chapter. Consequently, micromechanical failure theories have been evaluated in this Chapter employing the in-situ properties in Table 3.2. These values have been defined in [Bednarcyk et al., 2010] and result in micromechanical damage initiation using the MMCDM theory (Section 4.2) at the homogenised stress and strain levels at which the Silenka GFRP material shows onset of the ply-level nonlinearities. The elasticity properties in Table 3.2 are in-situ properties and differ slightly from the values provided in [Soden et al., 1998]. The approximate composite ply stress values, at which onset of nonlinear behaviour becomes evident in Figure 3.6, are summarised in Table 3.3. The HFGMC simulations have been performed using the 30 × 30 model. Literature review has resulted in four micromechanical damage

Table 3.2: Silenka GFRP properties for validation of micromechanical failure criteria, after [Bednarcyk et al., 2010] and [Mayes and Hansen, 2004].

Silenka E-glass 1200tex fibre				
E [GPa]	$\nu[-]$	X_t [MPa]	X_c [MPa]	S_{12f} [MPa]
74.	0.2	2109.	1287.6	95.2
MY750/HY917/DY063 Epoxy matrix				
E [GPa]	$\nu[-]$	X_t [MPa]	X_c [MPa]	S [MPa]
3.7	0.35	46.25	106.19	60.71

Table 3.3: Approximate composite ply stresses at which nonlinear behaviour has been observed for the Silenka GFRP composite.

$+\bar{\sigma}_{22}$ [MPa]	$-\bar{\sigma}_{22}$ [MPa]	$\bar{\tau}_{12}$ [MPa]
40.	90.	35.

initiation models which have been selected for evaluation and implementation into the methodology. Details of these models have been presented in this Section.

1) Three-dimensional Tsai-Hill criterion

Matrix microcracking has been modelled by application of the GMC theory in the multiscale framework in [Pineda et al., 2009]. The three-dimensional Tsai-Hill criterion has been applied in this reference for prediction of transverse cracking in the matrix, whereas the maximal strain in fibre direction criterion has been used for fibre breakage prediction.

According to the 3D Tsai–Hill criterion, microdamage in the subcell has been initiated when the stress state satisfies the relation

$$
\frac{\left(\sigma_{11}^{(\beta,\gamma)}\right)^2+\left(\sigma_{22}^{(\beta,\gamma)}\right)^2+\left(\sigma_{33}^{(\beta,\gamma)}\right)^2}{Y^2}+\frac{\sigma_{11}^{(\beta,\gamma)}\sigma_{22}^{(\beta,\gamma)}+\sigma_{11}^{(\beta,\gamma)}\sigma_{33}^{(\beta,\gamma)}+\sigma_{22}^{(\beta,\gamma)}\sigma_{33}^{(\beta,\gamma)}}{Y^2}+
$$
$$
\frac{\left(\sigma_{12}^{(\beta,\gamma)}\right)^2+\left(\sigma_{13}^{(\beta,\gamma)}\right)^2+\left(\sigma_{23}^{(\beta,\gamma)}\right)^2}{T^2}=1. \tag{3.16}
$$

The parameter Y in Equation 3.16 denotes the matrix transverse strength, while T is the matrix shear strength. The value of transverse matrix strength can be the tensile or compressive, based on the type of the applied homogenised transverse stress $\bar{\sigma}_{22}$

$$
\begin{aligned}
Y &= Y_c \quad \text{for} \quad \bar{\sigma}_{22} < 0, \\
Y &= Y_t \quad \text{for} \quad \bar{\sigma}_{22} > 0,
\end{aligned} \tag{3.17}
$$

after [Pineda et al., 2009]. The fibre breakage criterion employed in addition to the 3D Tsai-Hill criterion compares the strain in fibre direction to the ultimate fibre material strain in fibre direction ε_f^U,

$$
\left(\frac{\varepsilon_{11}^{(\beta,\gamma)}}{\varepsilon_f^U}\right)^2 \geq 1. \tag{3.18}
$$

Failure initiation curves of the neat matrix material with properties listed in Table 3.2 using the 3D Tsai-Hill criterion in the $\bar{\sigma}_{11}-\bar{\sigma}_{22}$ and the $\bar{\sigma}_{22}-\bar{\sigma}_{33}$ stress space are
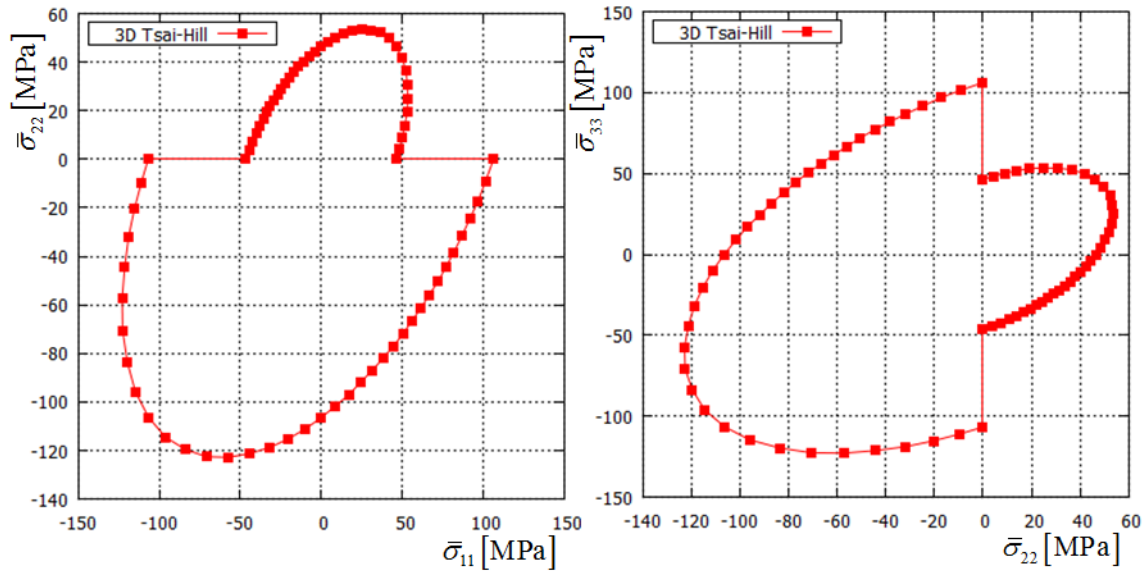
Figure 3.7: 3D Tsai-Hill failure curves in the $\bar{\sigma}_{11} - \bar{\sigma}_{22}$ and $\bar{\sigma}_{22} - \bar{\sigma}_{33}$ stress spaces for the MY750 matrix.

shown in Figure 3.7, whereas damage initiation curves of the Silenka GFRP material have been shown in Figure 3.8. As shown in these Figures, the 3D Tsai-Hill failure curves show discontinuities which occur when the $\bar{\sigma}_{22}$ stress component changes its tensile/compressive character due to the differences in tensile and compressive strength values, as defined in Equations 3.16 and 3.17.

2) MultiContinuum Theory

The MultiContinuum Theory (MCT), after [Mayes and Hansen, 2004], is an FE micromechanics-based failure theory which was analysed in the WWFE. The fibre and matrix failure initiation criteria, employed in the MCT, have been evaluated for the prediction of microdamage initiation within HFGMC micromechanical models in this Thesis.

As opposed to the original application, the MCT constituent-based failure criteria have been applied at the subcell level, consequently taking into account stress variations within the unit cell instead of dealing with averaged constituent values. The deviation from the original application has been motivated by the idea to evaluate the MCT failure initiation criteria as a basis for damage models, where the composite damage processes would be governed by the local fields within the RUC.
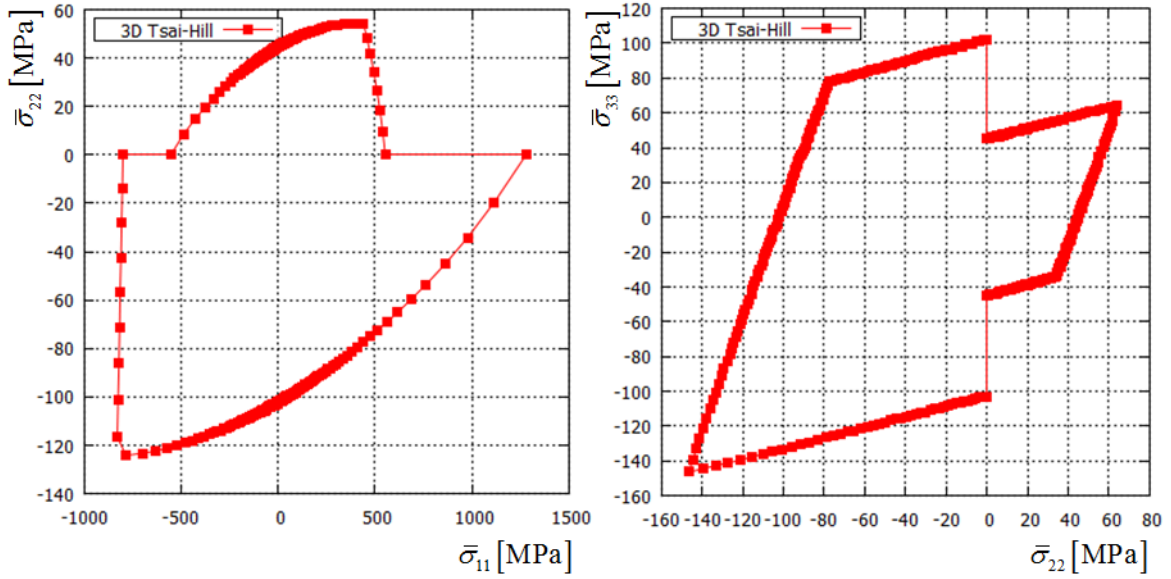
Figure 3.8: 3D Tsai-Hill failure curves in the $\bar{\sigma}_{11} - \bar{\sigma}_{22}$ and $\bar{\sigma}_{22} - \bar{\sigma}_{33}$ stress spaces for the Silenka GFRP composite.

The MCT failure initiation criteria have been derived from the quadratic interaction failure theory by implementation of specific behaviour of the constituents in composite failure process. Contrary to the approach employed in the derivation of e.g. Tsai-Wu and Hashin criteria, these specifics have been employed at the constituent level in the MCT theory.

Only the final forms of the criteria have been presented in this Thesis, whereas the complete derivation has been provided in [Mayes and Hansen, 2004]. Failure initiation in the matrix is predicted if the stress state satisfies the relation

$$K_{3m}I_3 + K_{4m}I_4 = 1, \tag{3.19}$$

where

$$K_{3m} = \frac{1}{S_{22m}^2 + S_{33m}^2}, \tag{3.20}$$

and

$$K_{4m} = \frac{1}{S_{12m}^2}. \tag{3.21}$$

S_{22} and S_{33} are matrix strengths in the *2* and *3* directions, which are dependent on

the tensile/compressive character of the loading in the 2 direction, after [Mayes and Hansen, 2004]. Fibre failure is predicted using the equation

$$K_{1f}I_1^2 + K_{4f}I_4 = 1, \tag{3.22}$$

where

$$K_{1f} = \frac{1}{S_{11f}^2}, \tag{3.23}$$

and

$$K_{4f} = \frac{1}{S_{12f}^2}. \tag{3.24}$$

The S_{11f} term denotes the strength in fibre direction, which can be tensile or compressive, while S_{12f} is the fibre shear strength. Equations 3.19 and 3.22 include the transversally isotropic stress invariants, expressed as

$$\begin{aligned} I_1 &= \sigma_{11}, \\ I_2 &= \sigma_{22} + \sigma_{33}, \\ I_3 &= \sigma_{22}^2 + \sigma_{33}^2 + 2\sigma_{23}^2, \\ I_4 &= \sigma_{12}^2 + \sigma_{13}^2, \end{aligned} \tag{3.25}$$

after [Mayes and Hansen, 2004].

The matrix failure curve of the MultiContinuum Theory for loading in the $\bar{\sigma}_{22} - \bar{\sigma}_{33}$ stress space, obtained using Equation 3.19 and epoxy matrix properties defined in Table 3.2, has been shown in Figure 3.9. The different values of matrix strengths in the 2 and 3 directions in tensile and compressive loading states cause discontinuities in the failure curves, similarly to the 3D Tsai-Hill failure curve in Figure 3.7. The MCT theory failure curves of the Silenka GFRP material in the $\bar{\sigma}_{11} - \bar{\sigma}_{22}$ and $\bar{\sigma}_{22} - \bar{\sigma}_{33}$ stress spaces have been shown in Figure 3.10.

3) Mixed-Mode Continuum Damage Mechanics failure criteria

The Mixed-Mode Continuum Damage Mechanics model (MMCDM), introduced in [Bednarcyk et al., 2010], has been implemented into the multiscale damage modelling
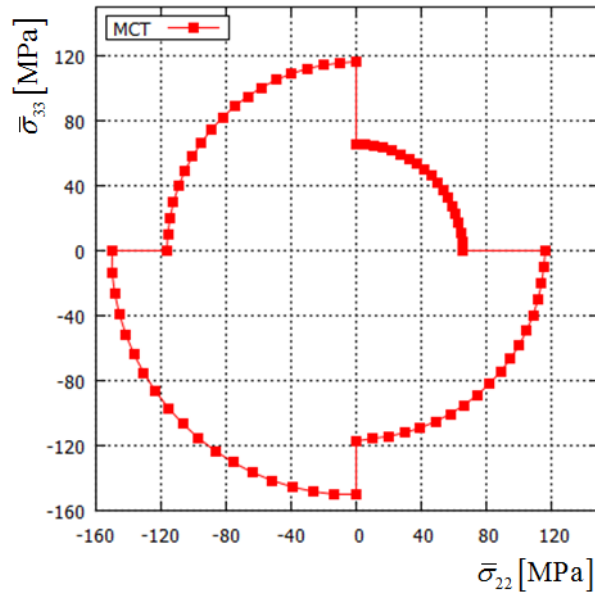
Figure 3.9: MCT failure curve for the MY750 matrix in the $\bar{\sigma}_{22} - \bar{\sigma}_{33}$ stress space.
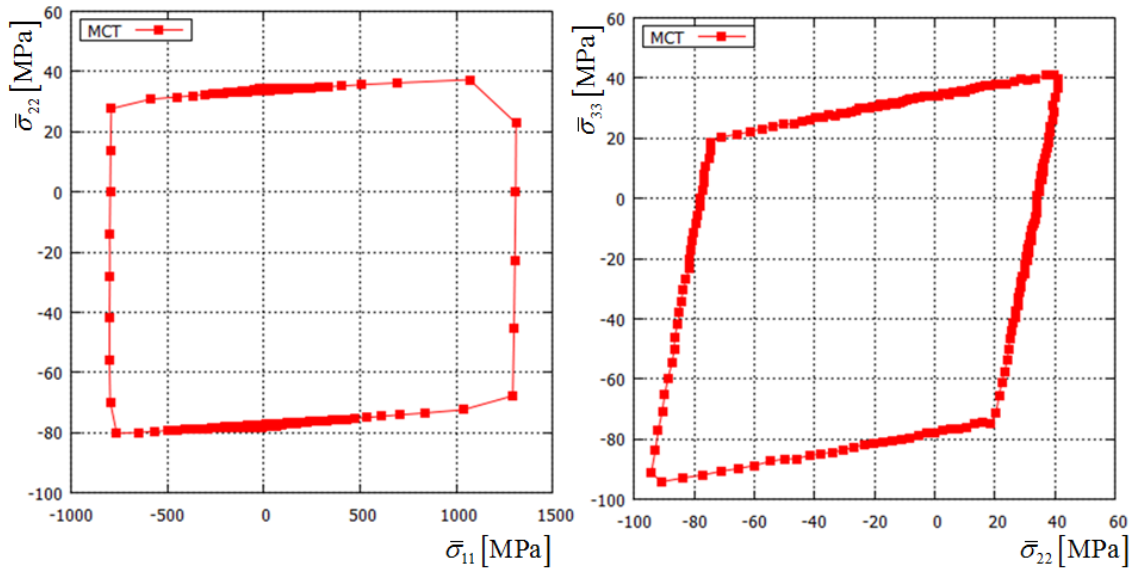
Figure 3.10: MCT failure curves for the Silenka GFRP composite in the $\bar{\sigma}_{11} - \bar{\sigma}_{22}$ and $\bar{\sigma}_{22} - \bar{\sigma}_{33}$ stress spaces.

methodology in this Thesis. The microdamage initiation criteria employed in the MMCDM theory have been presented in this Section, whereas details of the associated damage model have been provided in Section 4.2.

The MMCDM model employs the 3D Hashin-type strain based failure criterion for the matrix in combination with the maximal stress criterion for the fibre. The matrix
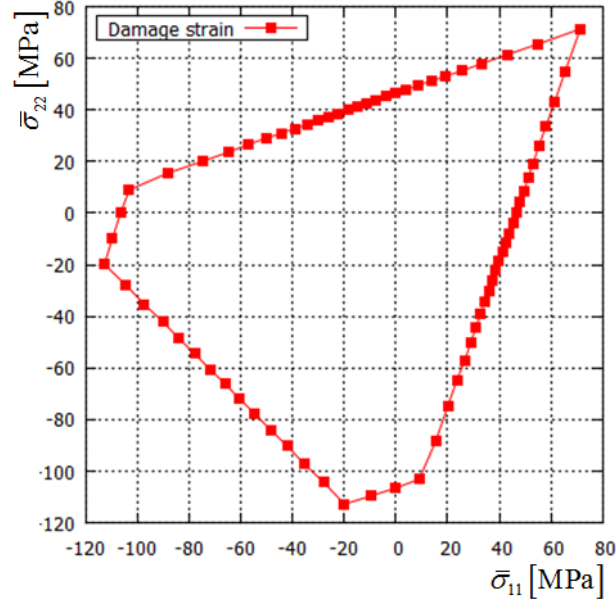
Figure 3.11: MMCDM damage initiation curve for the evaluated MY750 matrix in the $\bar{\sigma}_{11} - \bar{\sigma}_{22}$ stress space.

damage initiation model introduces damage strains, which are written in the form of the three-dimensional Hashin failure criterion in terms of strain instead of stress components. The damage strains, which account for the multiaxial nature of damage initiation in the matrix, are defined as

$$\varepsilon_1^D = \sqrt{\left(\frac{\varepsilon_{11}}{X_\varepsilon}\right)^2 + \left(\frac{\gamma_{13}}{R_\varepsilon}\right)^2 + \left(\frac{\gamma_{12}}{S_\varepsilon}\right)^2}, \tag{3.26}$$

$$\varepsilon_2^D = \sqrt{\left(\frac{\varepsilon_{22}}{Y_\varepsilon}\right)^2 + \left(\frac{\gamma_{23}}{Q_\varepsilon}\right)^2 + \left(\frac{\gamma_{12}}{S_\varepsilon}\right)^2}, \tag{3.27}$$

$$\varepsilon_3^D = \sqrt{\left(\frac{\varepsilon_{33}}{Z_\varepsilon}\right)^2 + \left(\frac{\gamma_{23}}{Q_\varepsilon}\right)^2 + \left(\frac{\gamma_{13}}{R_\varepsilon}\right)^2}, \tag{3.28}$$

where X_ε, Y_ε, Z_ε variables are damage initiation strains in the normal directions whereas R_ε, Q_ε and S_ε are engineering shear damage initiation strains. The values of normal damage initiation strains for epoxy matrices depend on the tensile/compressive character of the corresponding normal stresses. Values for the evaluated MY750 epoxy matrix have been provided in Table 4.1, after [Bednarcyk et al., 2010].
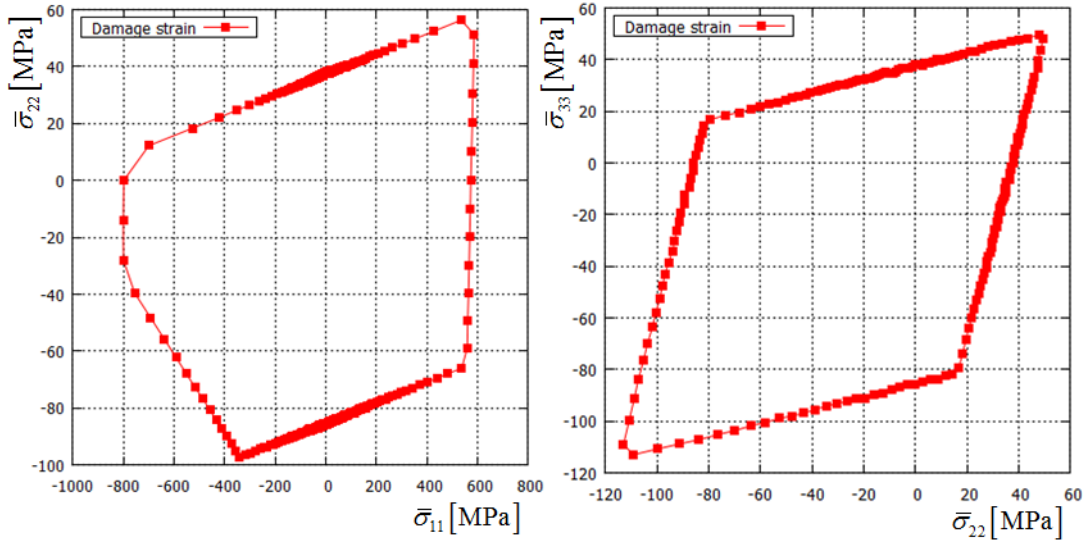
Figure 3.12: MMCDM damage initiation curves for the Silenka GFRP composite.

Application of the damage strain based failure theory follows the standard approach in using failure criteria, as the theory predicts onset of nonlinearities if the right-hand side terms in Equations 3.26 - 3.28 reach values above one.

The fibre failure criterion, which has been employed along with the MMCDM theory, predicts failure in fibre subcells if the local stress component in fibre direction exceeds the fibre strength

$$\left(\frac{\sigma_{11}^{(\beta,\gamma)}}{\sigma_f^U}\right)^2 \geq 1, \tag{3.29}$$

where σ_f^U is the fibre strength, which usually has different values in tensile and compressive loading.

The MMCDM damage initiation curve for the neat matrix material, employing mechanical properties defined in Table 3.2, is shown in Figure 3.11, whereas application of the MMCDM theory on the composite material modelled with the HFGMC has been presented in Figure 3.12.

4) Maximal principal stress criterion

The micromechanical Crack Band theory, introduced in [Pineda, 2012], has been evaluated in this Thesis for the application in the multiscale framework. Damage initiation

has in this model been modelled by means of two failure modes, which evolve depending on the stress state in the relevant matrix subcell. Failure mode of the relevant subcell has in this approach been determined based on the tensile/compressive character of the principal stress with the largest magnitude $\left|\sigma_I^{(\beta,\gamma)}\right| > \left|\sigma_{II}^{(\beta,\gamma)}\right| > \left|\sigma_{III}^{(\beta,\gamma)}\right|$. Consequently, Mode I failure refers to crack band opening which occurs at stress states with tensile maximal absolute values of the principal stress in the subcell.

The failure initiation criterion for Mode I failure has been defined as

$$\frac{\sigma_I^{(\beta,\gamma)}}{\sigma_C^{(\beta,\gamma)}} = 1, \quad \sigma_I^{(\beta,\gamma)} \geq 0. \tag{3.30}$$

$\sigma_C^{(\beta,\gamma)}$ in Equation 3.30 is the cohesive strength of the material. The Mode I failure criterion, as well as the associated progressive degradation model (Section 4.3), have been defined in the principal stress coordinate system. In the opposite stress condition $(\sigma_I^{(\beta,\gamma)} < 0)$, crack band growth under compressive principal stresses occurs. Experimental evidence shows that monolithic materials under compressive loading fail with crack bands aligned to the plane of maximum shear stress $\bar{\tau}^{(\beta,\gamma)}$, after [Pineda, 2012]. Consequently, a Mohr-Coulomb type failure criterion has been employed to indicate damage onset in these conditions. The criterion has been defined as

$$\frac{\tau_E^{(\beta,\gamma)}}{\tau_C^{(\beta,\gamma)}} = 1, \quad \sigma_I^{(\beta,\gamma)} < 0, \tag{3.31}$$

where $\tau_E^{(\beta,\gamma)}$ is the effective shear stress which includes the contribution of the traction normal to the crack band (σ_n)

$$\tau_E^{(\beta,\gamma)} = \left|\tau^{(\beta,\gamma)}\right| + \mu_i \sigma_n^{(\beta,\gamma)}, \tag{3.32}$$

where μ_i is the internal friction coefficient calculated as

$$\mu_i = \tan\left\{\sin^{-1}\left[\frac{\left(2\tau_C^{(\beta,\gamma)}\right)^2 - \left(\sigma_C^{(\beta,\gamma)}\right)^2}{\left(2\tau^{(\beta,\gamma)}\right)^2 + \left(\sigma_C^{(\beta,\gamma)}\right)^2}\right]\right\}. \tag{3.33}$$

As the fibre failure initiation criterion has not been specified in [Pineda, 2012], the maximal stress in the fibre direction criterion has been employed for failure initiation in fibre subcells as defined in Equation 3.29. Figure 3.13 shows the failure curves for
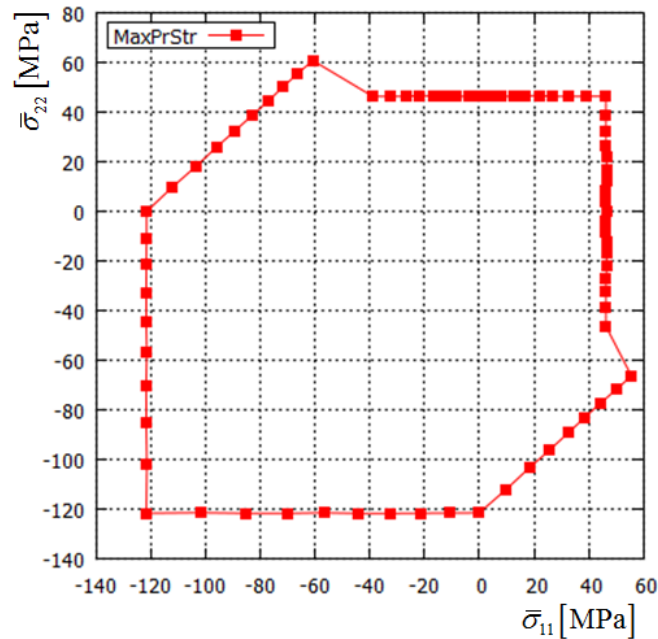
Figure 3.13: Maximal principal stress damage initiation curves for MY750 matrix matrix.

the evaluated epoxy matrix with properties defined in Table 3.2 in the $\bar{\sigma}_{11} - \bar{\sigma}_{22}$ stress space. The failure curve shows discontinuities due to a change in the failure mode. The damage initiation curves of the Silenka GFRP material in the $\bar{\sigma}_{11} - \bar{\sigma}_{22}$ and $\bar{\sigma}_{22} - \bar{\sigma}_{33}$ stress spaces, predicted using the maximal principal stress criterion for matrix subcells and the maximal stress criterion for fibre subcells, are shown in Figure 3.14.

3.5   Evaluation of micromechanical failure criteria

The standalone HFGMC application has in this Section been employed as to evaluate the micromechanical damage initiation theories. The 30×30 single-fibre RUC with mechanical properties of the constituents at which microdamage mechanisms have been initiated in the evaluated Silenka GFRP material has been employed in the analyses.

The results in Figures 3.15 - 3.18 show the failure curves obtained using the micromechanical failure theories on the composite material in various bi-axial stress states. The failure curves visualise the homogenised applied stress state at which the relevant failure theories predict damage initiation in the first subcell within the HFGMC model. Visualisation of the micromechanical failure curves in the homogenised $\bar{\sigma}_{11} - \bar{\sigma}_{22}$ stress plane has been shown in Figure 3.15.
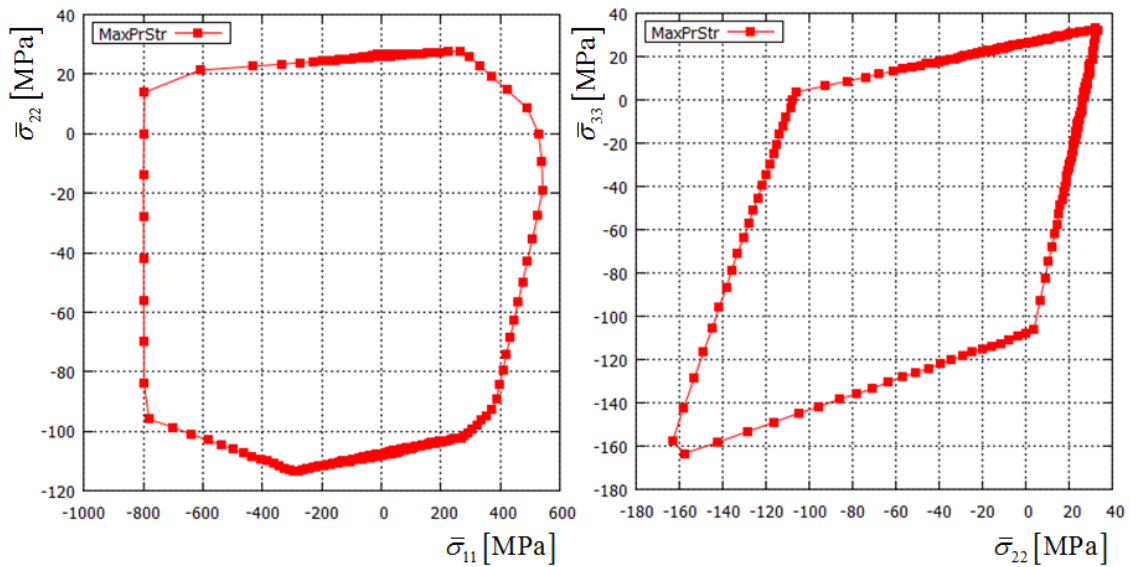
Figure 3.14: Maximal principal stress damage initiation curves for the Silenka GFRP composite.
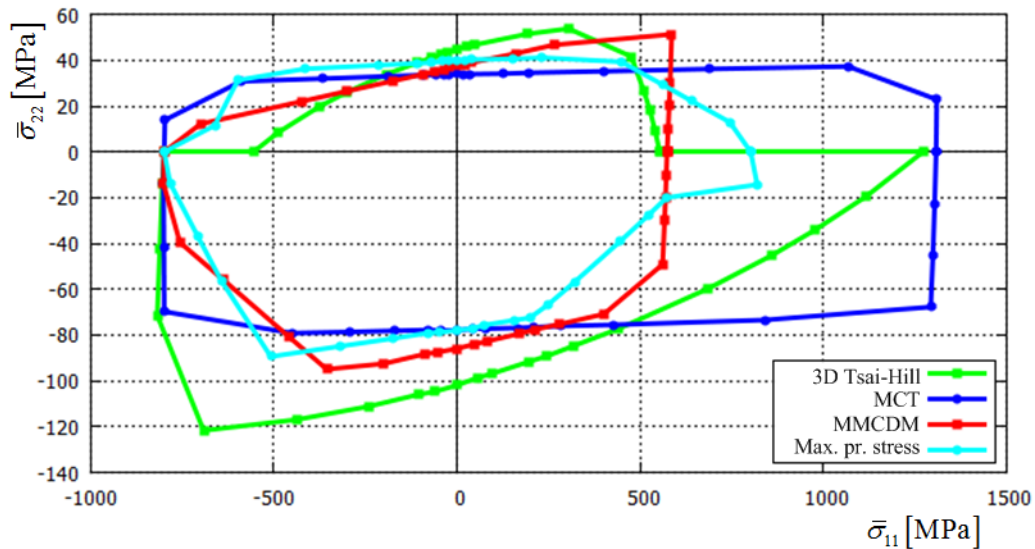
Figure 3.15: Comparison of the evaluated micromechanical failure criteria for the Silenka GFRP composite in the $\bar{\sigma}_{11} - \bar{\sigma}_{22}$ stress space.

Various failure modes have to be accounted for by the micromechanical failure criteria in the composite RUC. Consequently, discontinuities in the failure curves arise from the switch of matrix failure modes or by the change of the constituent which initiates failure. The 3D Tsai-Hill criterion shows most pronounced discontinuities due to the application of the tensile/compressive matrix strengths as discussed in Section 3.4.

As shown in Figure 3.15, the largest discrepancies between the evaluated failure theories in the physical interpretation of microdamage mechanisms exist in the prediction of the tensile fibre failure mode. The 3D Tsai-Hill criterion indicates two damage initiation stresses for this loading condition. The one calculated using the lower, tensile transverse strength predicts initiation of degradation processes at approximately the same loading at which the MMCDM theory indicates damage initiation. Otherwise, the response predicted using the compressive transverse strengths predicts the subcell damage onset at $\bar{\sigma}_{11}$ loading which is close to the value at which the associated maximal strain for the fibre criterion would predict tensile fibre failure. Therefore, physical interpretation of the 3D Tsai-Hill criterion is that the theory predicts matrix microdamage in the fibre dominated loading only if the applied $\bar{\sigma}_{22}$ stress is tensile, whereas almost no matrix microdamage occurs in the compressive transverse loading.

The MCT theory is the only evaluated micromechanical failure theory which predicts fibre breakage without previous damage onset in the matrix subcells, as this characteristic has been implemented into the derivation of the MCT failure initiation criteria. In compressive fibre-oriented loading, all micromechanical theories predict the same physical behaviour of the composite - compressive fibre failure at the homogenised stress state which is equal to the compressive strength of the composite ply. This part of the failure curves has been equally predicted by all evaluated micromechanical damage initiation theories.

Table 3.4: Comparison of damage initiation stresses [MPa].

	3D Tsai-Hill	MCT	MMCDM	Max. principal stress
$+\bar{\sigma}_{22}$	44.4	33.7	37.2	39.4
$-\bar{\sigma}_{22}$	-101.4	-77.3	-85.1	-77.3
$\bar{\tau}_{12}$	34.8	34.8	34.8	20.1

The applied homogenised stresses at which micromechanical failure theories initiate damage in transverse and in-plane shear loading are summarised in Table 3.4. The micromechanical failure theories indicate damage initiation with noticeable differences along the applied homogenised $\bar{\sigma}_{22}$ loading. Along this load path, the MCT matrix criterion is the first to initiate the nonlinear processes, whereas the 3D Tsai-Hill criterion overestimates even the composite transverse tensile ply strength (40 MPa). The MMCDM damage strains and maximal principal stress criteria predict subcell damage initiation at
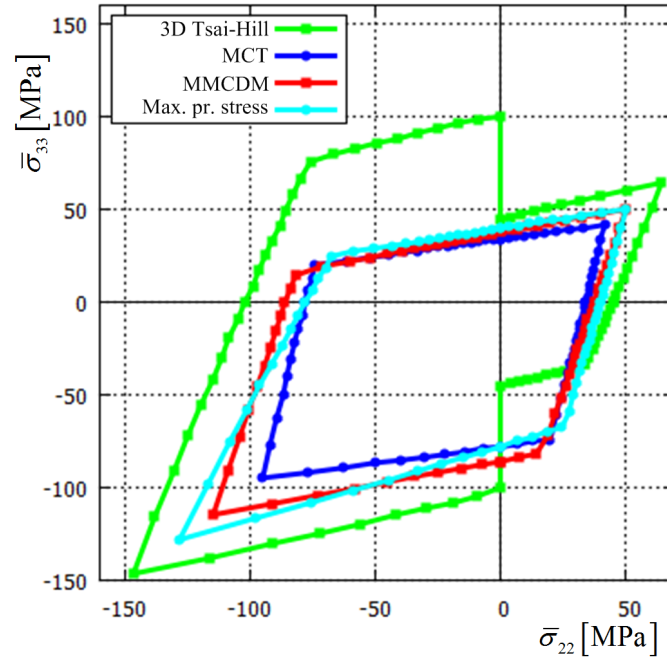
Figure 3.16: Comparison of the evaluated micromechanical failure criteria for the Silenka GFRP composite in the $\bar{\sigma}_{22} - \bar{\sigma}_{33}$ stress space.

$\bar{\sigma}_{22}$ values slightly lower than the composite transverse tensile strength. In compressive transverse $\bar{\sigma}_{22}$ loading direction the Mohr-Coulomb criterion and the MCT criterion predict damage onset at approximately the same load increment, whereas the 3D Tsai-Hill overestimates onset of the nonlinear behaviour.

Comparison of micromechanical failure curves in the $\bar{\sigma}_{22} - \bar{\sigma}_{33}$ for the composite material is shown in Figure 3.16. All the evaluated failure theories predict failure curves having the same shape in the $\bar{\sigma}_{22} - \bar{\sigma}_{33}$ stress space, with similar values at the axes. An exception is the 3D Tsai-Hill criterion, which shows discontinuities and significant deviations from the other evaluated failure theories due to the employed approach for selection of the transverse matrix subcell strength value in this criterion.

Evaluation of the micromechanical failure theories in the $\bar{\sigma}_{22} - \bar{\tau}_{12}$ stress space has been shown in Figure 3.17. Under these loading conditions, the 3D Tsai-Hill, MCT and MMCDM damage strain criteria show excellent agreement, except the differences in the transverse stresses which has been discussed earlier. The maximal principal stress criterion shows initiation at the lowest load in the pure shear loading ($\bar{\sigma}_{22} = 0$) and in the stress states in which shear stresses are accompanied with compressive transverse
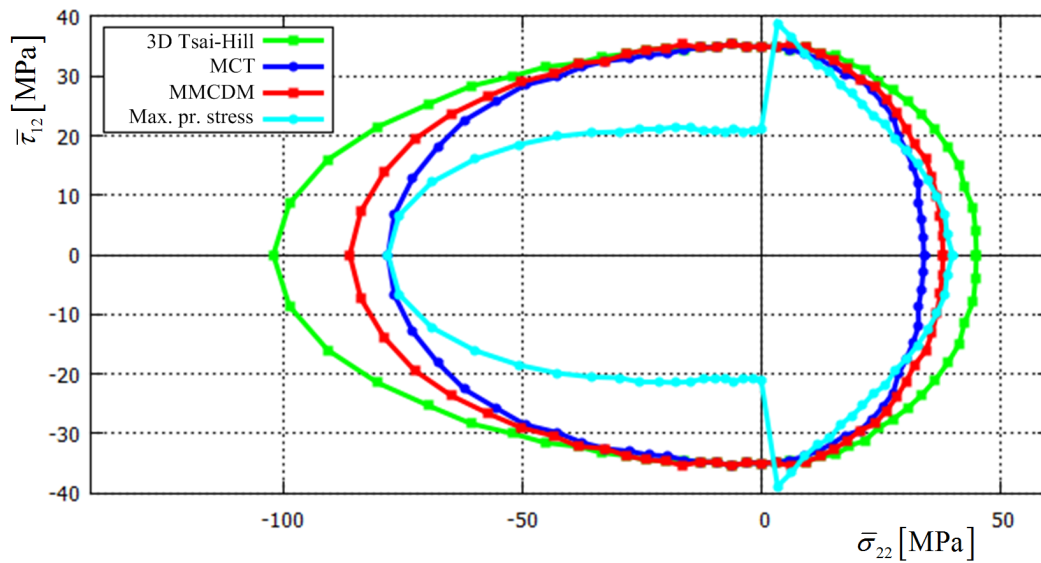
Figure 3.17: Comparison of the evaluated micromechanical failure criteria for the Silenka GFRP composite in the $\bar{\sigma}_{22} - \bar{\tau}_{12}$ stress space.

stresses. The discontinuity in the failure curve has been caused by the change from matrix Mode I to Mode II failure initiation.
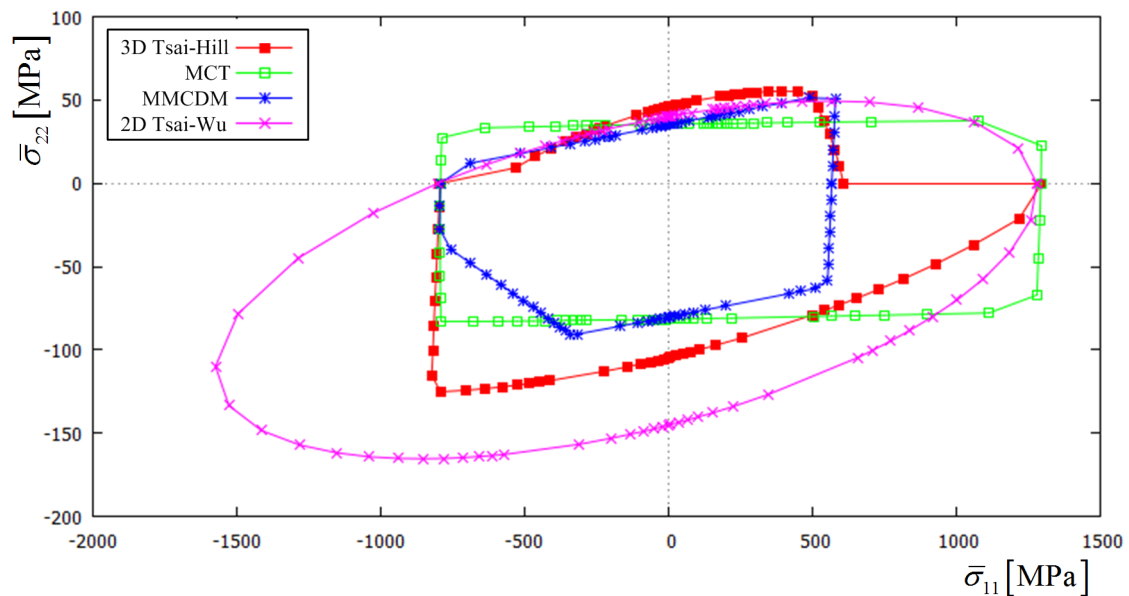
Figure 3.18: Comparison of micromechanical criteria with ply-level Tsai-Wu criterion in the $\bar{\sigma}_{11} - \bar{\sigma}_{22}$ stress space [MPa].

The distinction between the application of ply-level failure theories and the microme-chanical damage initiation theories has been illustrated by the comparison of the failure

curves predicted by the ply-level Tsai-Wu failure criterion and the micromechanical theories. Results of the comparison are shown in Figure 3.18 for the $\bar{\sigma}_{11} - \bar{\sigma}_{22}$ stress space. The Tsai-Wu failure curve has been predicted employing the ply strengths of the evaluated Silenka GFRP composite material which are defined in Table 3.1. As shown in Figure 3.18, the micromechanical failure criteria are more restrictive as they are related to the composite stress states at which nonlinear behaviour, caused by microdamage, becomes evident in the response of the homogenised composite ply. Comparison of the sizes and shapes of the failure curves predicted using the evaluated failure theories provides insight into the stress states at which microdamage mechanisms are present in the material although not included in the analysis using the Tsai-Wu ply-level criterion. The differences between the micromechanical criteria and the ply-level Tsai-Wu criterion are more pronounced in compressive regions of the homogenised $\bar{\sigma}_{11} - \bar{\sigma}_{22}$ stress space.

The micromechanical failure curves visualise the homogenised stress loading at which the local fields within the RUC initiate damage in the first subcell within the RUC. The damage initiation within the RUC has been studied in this Section as to expand the micromechanical failure theory evaluation and to provide more details about the failure initiation process predicted using different failure theories. Distribution of the failure criteria within the RUC, at the tensile $\bar{\sigma}_{22}$ loading at which damage initiates, as predicted by the relevant failure theories, has been shown in Figure 3.19.
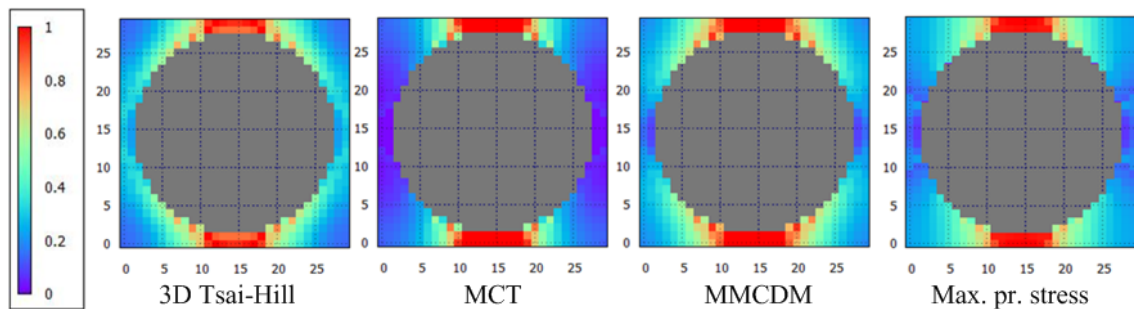
Figure 3.19: Distribution of failure criteria within the unit cell at the homogenised tensile $\bar{\sigma}_{22}$ loading defined in Table 3.4.

Comparison of the RUC failure criteria distribution indicates that the theories predict damage initiation at the same location and approximately the same size of the RUC, due to the simple unit cell morphology analysed in this analysis. The contours of the MMCDM criterion refer to values of ε_2^D, as this component takes the highest values in

this load case. Accordingly, the contours which are shown for the maximal principal stress criterion refer to Mode I damage initiation.

Figure 3.20 shows the RUC distribution of the failure criteria in the transverse compressive load case. Failure onset has been predicted with large discrepancies in this load case, as indicated by the values in Table 3.4. The contours for the MMCDM damage strains refer to ε_2^D, whereas Mode II is the predominant failure mode predicted by the maximal principal stress criterion.
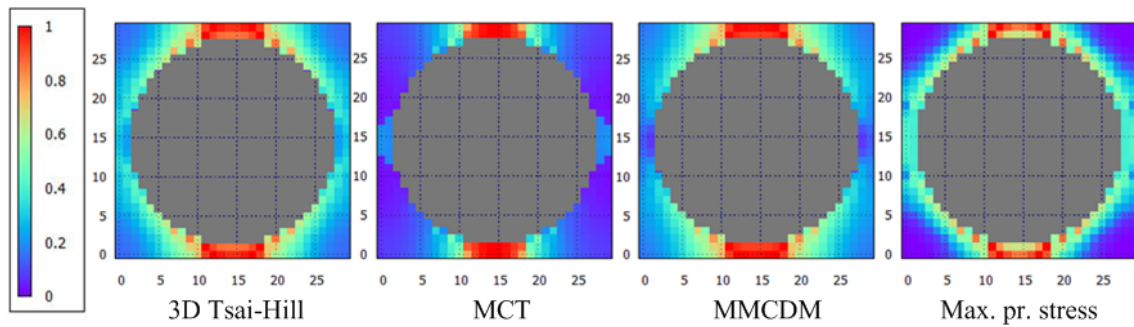
Figure 3.20: Distribution of failure criteria within the unit cell at the homogenised compressive $\bar{\sigma}_{22}$ loading defined in Table 3.4.

RUC distribution of the failure criteria in the in-plane shear loading at the subcell damage initiation, as defined in Table 3.4, has been shown in Figure 3.21. The MMCDM damage strains in this Figure refer to ε_1^D. In addition, ε_2^D values are approximately equal to the values of ε_1^D in this load case. As shown by the values in Table 3.4, the micromechanical failure theories predict damage onset at comparable $\bar{\tau}_{12}$ stresses with the exception of the maximal principal stress criterion, which underestimates the microdamage initiation in shear loading. The nonphysical distribution of the maximal principal stress criteria in Figure 3.21 has been caused by varying values of the friction coefficient in the definition of the Mohr-Coulomb damage initiation criterion and by variations of Mode I and Mode II damage initiation within the RUC.

3.6   Effects of unit cell discretization and morphology

The RUC morphology and discretization affect the homogenised composite properties, as discussed in Section 2.5. Therefore, influence of these parameters on the microdamage
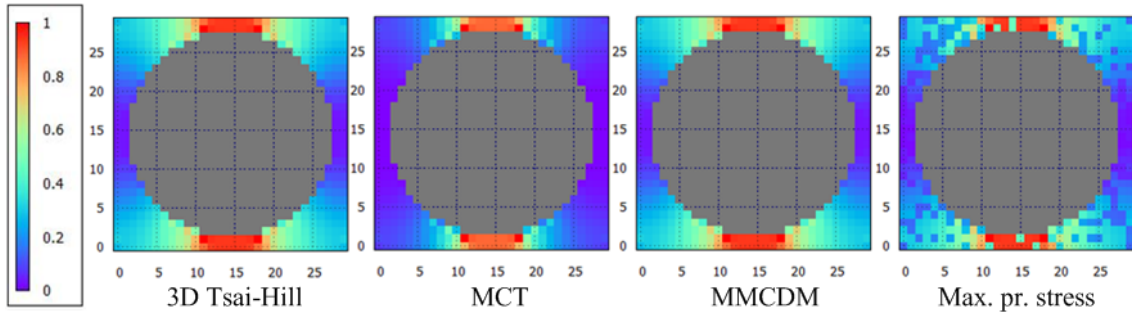
Figure 3.21: Distribution of failure criteria within the unit cell at the homogenised shear $\bar{\tau}_{12}$ loading defined in Table 3.4.

initiation has been evaluated in this Section. These effects have been assessed on damage initiation at tensile $\bar{\sigma}_{22}$ loading conditions. MOC-based micromechanical theories enable modelling of the nonlinear behaviour of heterogeneous materials employing relatively coarse unit cell discretization which has been demonstrated by numerous examples throughout the literature, as discussed in Section 2.4.
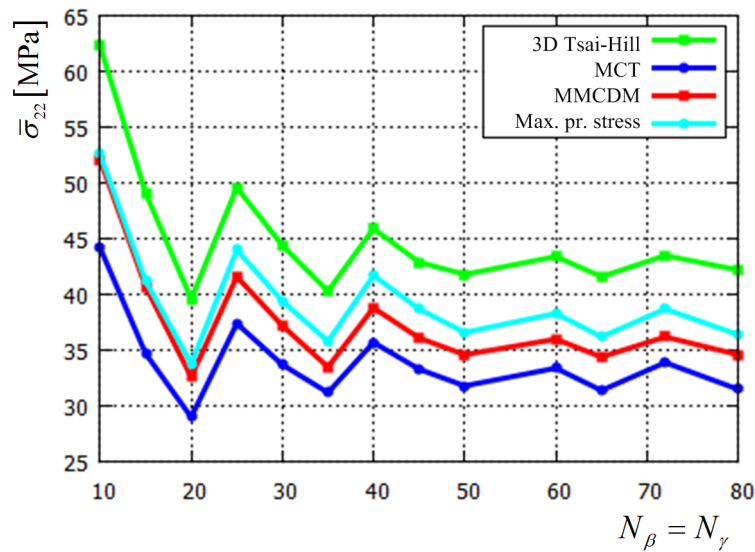
Figure 3.22: Effect of unit cell discretization on the applied transverse tensile stress at which the criteria indicate onset of damage processes.

The RUC preprocessor, employed in this Thesis, discretizes the composite material using an automated procedure as explained in Section 2.6. The effect of the applied unit cell discretization on the $\bar{\sigma}_{22}$ loading at which the failure theories predict onset of subcell nonlinearities has been shown in Figure 3.22. Large jumps and non-smooth convergence
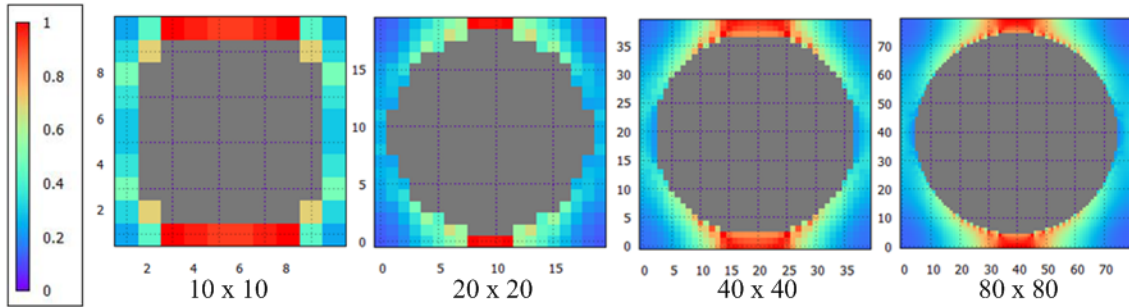
Figure 3.23: Effect of unit cell discretization on distribution of 3D Tsai-Hill criterion within the single-fibre unit cell.

are evident in the results of the convergence analysis, especially for the coarser RUC discretization levels. This effect has been caused by the different discretizations of the fibre inclusion, which also affect the composite properties, as discussed in Section 2.5.

Figure 3.23 shows the effect of automatic RUC discretization on the distribution of the failure criteria within the unit cell. As shown, the discretization determines the shapes and sizes of the fibre constituent which consequently affects the local RUC stress and strain fields. Besides the fibre volume fraction, which naturally has a detrimental effect on the composite properties, additional attention has to be attributed to the process of RUC generation and subsequent determination of in-situ properties applied in the micromechanical damage modelling procedure.

Furthermore, discrepancies between the damage initiation stresses are noticeable also in the finer RUC discretizations. The effect of the portion of the unit cell at which the failure criterion initiates damage processes determines the homogenised composite behaviour and needs to be accounted for in the derivation of the damaging laws. This effect has been discussed in Section 4.3.

The RUC morphology affects the local fields within the RUC, causing differences in the composite properties predicted by micromechanical theories, as discussed in Section 2.5. The local fields also affect the homogenised load state at which the failure theories initiate damage processes. As to illustrate this effect, Figure 3.24 shows the comparison between the ε_2^D MMCDM damage strains in the RUC morphologies defined in Figure 2.8. These results have been predicted for an applied homogenised loading of $\bar{\sigma}_{22} = 38$ MPa. Micromechanical computations performed on the unit cell morphology with fibres at unit cell corners (RUC type 2) result in identical results to the results shown in Section

3.5, as this type of unit cell morphology is equal to the morphology with the single fibre in unit cell centre. As shown by the right-hand side image in Figure 3.24, the unit cell with diamond morphology (RUC type 3) predicts damage initiation at slightly higher applied $\bar{\sigma}_{22}$ loading (37.6 vs. 37.2 MPa). The differences in the distribution of the failure criteria values are clearly illustrated in Figure 3.24.
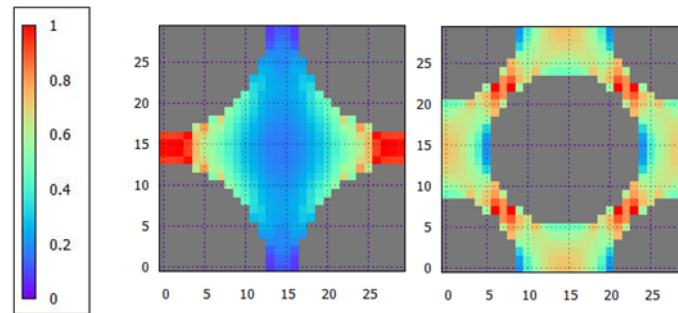
Figure 3.24: Distribution of ε_2^D damage strains (MMCDM) in the type 2 and type 3 unit cell morphologies at $\bar{\sigma}_{22} = 38$ MPa.

Differences in the RUC distributions of the micromechanical failure criteria are more pronounced in cases where the composite material is modelled using more complex RUC morphologies, as shown in Figure 3.25. This unit cell represents a composite material with 60% fibre volume fraction, discretized using 50×50 unit cells and loaded with $\bar{\sigma}_{22}$ stresses at which the criteria indicate damage initiation. The values at which damage has been initiated by the evaluated failure theories are approximately 20% lower compared to the values provided in Table 3.4, due to the stress concentration caused by the thin matrix areas between the fibres. All failure theories predict damage onset in the same part of the unit cell, where the small distance between two neighbouring fibres causes stress concentration. Distribution of the MCT criterion is more localised compared to other theories, whereas values of the three-dimensional Tsai-Hill criterion take high values also in other parts of the RUC.

3.7   Conclusion

The presented results have been obtained in the initial research phase of this Thesis in which various constituent level micromechanical failure theories have been evaluated as to model damage in polymer-based reinforced composites using HFGMC. Evaluation of the micromechanical failure theories revealed significant discrepancies between the
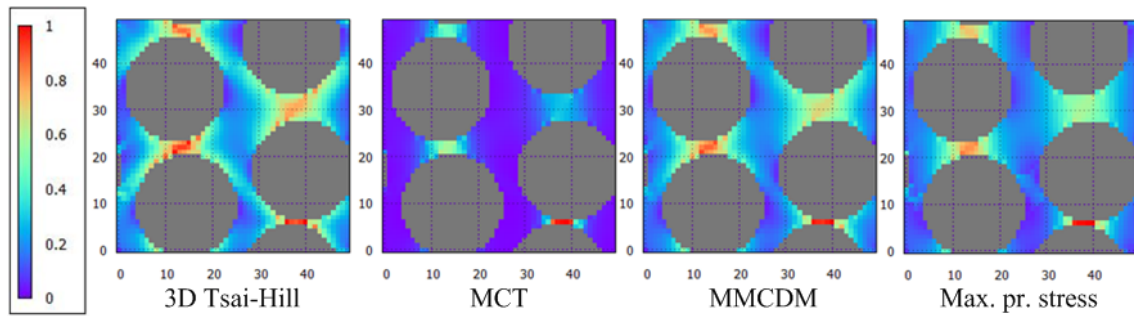
Figure 3.25: Application of micromechanical failure theories on a complex RUC.

failure theories. These differences are evident in the values of the applied loading which initiates microdamage in the composite, as well as in the physical interpretation of the damage processes at the microstructural level. Consequently, the interference of composite failure modes has been differently predicted by the failure theories. This effect is the most evident in the case of the MCT failure initiation criteria and the application of the 3D Tsai-Hill criterion. The 3D Tsai-Hill criterion shows non-physical behaviour in some loading conditions and a generally overestimated load state at which microdamage mechanisms have been initiated in the composite material.

An important conclusion from the performed evaluation is that microdamage has not been caused by local peak values of the micromechanical failure criteria. Therefore, damaged subcells are present in a large portion of the unit cell at the applied RUC loading which results in micromechanical damage onset. Consequently, implementation of damage laws at the subcells level plays a detrimental role in the prediction of the nonlinearities which influence composite material's response at the ply scale. The complex nature of microdamage mechanisms and specific behaviour of the composite material at the macro-scale has to be included in the damage laws applied to the subcells in the RUC. Furthermore, in-situ strength properties have to be used in the micromechanical failure theories, as application of the neat constituent values can lead to significant discrepancies in the prediction of composite ply strengths. Considering all observations, the next methodology development phase has been focused on application of progressive degradation models on the subcell mechanical properties as to simulate the damage processes of composite materials using HFGMC. The damage theories employed in this Thesis have been discussed in the following section.

4 | Micromechanical progressive degradation models

4.1 Introduction

Micromechanical damage has been modelled by the instantaneous degradation of subcell mechanical properties in the first applications of MOC-based micromechanical models for prediction of composite laminate failure. Results of these early applications have been published in e.g. [Moncada et al., 2008] and [Tang and Zhang, 2012], where the GMC micromechanical model has been used for this purpose. In these approaches, initiation of micromechanical damage has been predicted employing failure criteria at the subcell level, considering the different homogenised stress states at which damage has been initiated in the individual constituents. Consequently, matrix failure has been predicted using e.g. the Tsai-Wu and Tsai-Hill criteria whereas the maximal stress and strain in fibre direction criteria have been employed for the fibre subcells.

In these early applications, damage has been modelled by degradation of mechanical properties to very low values (0.01% of the undamaged values) for subcells which reach the failure state employing the relevant failure theory. The subsequent application of the homogenisation procedure over the RUC, which includes the completely degraded subcells, results in progressive degradation of the composite mechanical properties. However, the obtained effect of progressive degradation on the homogenised properties has not been sufficient as to enable modelling of the pronounced nonlinear behaviour of epoxy-based composite plies at in-plane shear and transverse compression prior to complete failure of the material, as discussed in [Bednarcyk et al., 2010].

Conclusions drawn from these studies highlighted the importance of the application of the more refined constituent level damage approaches at the micromechanical level.

Therefore, the microdamage mechanisms have been included into the developed multiscale damage modelling approach using the progressive degradation models which have been summarised in this Chapter. The micromechanical progressive degradation models apply Continuum Damage Mechanics principles to the constituent level constitutive models. Two Continuum Damage Mechanics based damage models, which have been applied in MOC-based micromechanical models in the literature, have been evaluated in this Thesis for the implementation into the developed methodology. The first model is the Mixed-Mode Continuum Damage Mechanics Model presented in Section 4.2, whereas the second model relies on the application of the Crack Band theory to model the progressive degradation effects, as shown in Section 4.3. Results of these models have been compared and validated for the application in the developed multiscale framework. The methodology has been validated using available experimental results.

4.2   Mixed-Mode Continuum Damage Mechanics (MMCDM) model

The MMCDM theory, introduced in [Bednarcyk et al., 2010], implemented two main improvements over the micromechanical damage modelling approaches employed in e.g. [Moncada, 2012], [Tang and Zhang, 2012]. These improvements consist of the inclusion of progressive degradation principles, applied to the subcell mechanical properties, and explicit modelling of the multiaxial behaviour of the composite material damage processes. The multiaxiality of the damage model enables enhanced modelling of the composite nonlinearities observed in matrix dominated loading conditions. Consequently, interactions and differences in the responses observed in tensile, compressive and shear loading of the composite material have been implemented into the constitutive law governed by the micromechanical model.

The MMCDM overview in this Thesis summarises the final relations and fundamental aspects of the damage model, whereas details and the complete background of the theory have been provided in [Bednarcyk et al., 2010], [Pineda et al., 2014], [Aboudi et al., 2012]. As explained in Section 3.4, the damage strains, defined in Equations 3.26 - 3.28, act as damage initiation criteria within the MMCDM theory. The particular formulation of the damage strains accounts for the interactions between the strain components and introduces multiaxiality into the modelling of microdamage initiation. Furthermore,

values of the damage strains govern the damage evolution equations based on the constituent uniaxial stress-strain responses, after [Bednarcyk et al., 2010]. Microdamage processes have been initiated in matrix subcells if any of the damage strains takes values above 1.0. Afterwards, maximal values of the damage strains ($\varepsilon_{i\,max}^{D}$) have been employed as the critical values for indication of damage progression in subsequent load increments.

Scalar damage variables have been used in the MMCDM theory as to model anisotropic elastic damage in the matrix subcell constitutive model. Accordingly, evolution of damage progression in the subcells has been tracked employing tensile and compressive damage variables $D_{i}^{T/C}$ in each of the three normal directions. Consequently, multiaxial nature of damage progression has been modelled by the MMCDM theory employing six separate and mutually independent scalar damage variables.

Damage progression has to be modelled if the applied RUC loading results in the increase of the maximal value of any of the damage strains ($\varepsilon_{i}^{D} > \varepsilon_{i\,max}^{D}$). The incremental changes of damage variables, which control degradation of mechanical properties during a load increment, have been derived based on the stress-strain curves for uniaxial loading of the constituents as

$$dD_i = (1 - D_i - k_i')\frac{d\varepsilon_i^D}{\varepsilon_i^D}, \quad i = 1, 2, 3, \tag{4.1}$$

where $d\varepsilon_i^D$ is the damage strain increment, while k_i' is the normalized instantaneous slope parameter calculated as

$$k_i' = Ae^{-\varepsilon_i^D/B}, \quad i = 1, 2, 3. \tag{4.2}$$

The parameters A and B in Equation 4.2 are the post-damage slope parameters, which define the constitutive behaviour of the damaged matrix material. These post-damage slope parameters take different values in tensile and compressive loading conditions. The normalized instantaneous slope parameter is related to the initial elastic modulus E^0 and the tangent modulus k_i as

$$k_i' = \frac{k_i}{E^0}, \quad i = 1, 2, 3. \tag{4.3}$$

Incremental changes of damage variables are accumulated into the total damage variables depending on the tensile/compressive character of normal stresses in the applied load increment

$$
\begin{aligned}
D_i^T &= D_{i\ old}^T + dD_i \quad \text{for} \quad \sigma_{ii} > 0, \\
D_i^C &= D_{i\ old}^C + dD_i \quad \text{for} \quad \sigma_{ii} < 0.
\end{aligned}
\tag{4.4}
$$

The matrix subcell elasticity properties have been degraded employing

$$
E_i = d_i E^0 \quad \text{for} \quad i = 1, 2, 3,
\tag{4.5}
$$

and

$$
\nu_{ij} = d_i \nu^0 \quad \text{for} \quad i, j = 1, 2, 3.
\tag{4.6}
$$

E^0 and ν^0 in Equations 4.5 and 4.6 are elastic constants of the initially isotropic matrix material. As the damage modelling approach in the MMCDM theory is anisotropic, the initially isotropic constitutive model of matrix subcells transfers into an orthotropic model. The secondary damage variables d_i in these equations have been calculated as

$$
d_i = \begin{cases} 1 - b_{ii}^T D_i^T & \text{for} \quad \sigma_{ii} > 0, \\ 1 - b_{ii}^C D_i^C & \text{for} \quad \sigma_{ii} < 0, \end{cases}
\tag{4.7}
$$

where b_{ii} parameters are scaling parameters, which take different values in tensile and compressive loading. Accordingly, the shear stiffness components have been degraded employing the appropriate damage variables as

$$
\begin{aligned}
G_{23} &= \left(1 - b_{42} D_2^{T/C} - b_{43} D_3^{T/C}\right) G^0, \\
G_{13} &= \left(1 - b_{51} D_1^{T/C} - b_{53} D_3^{T/C}\right) G^0, \\
G_{12} &= \left(1 - b_{61} D_1^{T/C} - b_{62} D_2^{T/C}\right) G^0,
\end{aligned}
\tag{4.8}
$$

where G^0 is the undamaged matrix shear modulus. The T/C upper indexes in Equation 4.8 refer to the tensile or compressive values of the damage variables D_i. As shown in [Bednarcyk et al., 2010], application of the degradation laws, defined in Equations 4.5, 4.6 and 4.8, preserves symmetries of the elasticity and compliance tensors. If the

maximal values of damage strains remain constant in the applied load increment, no further damage evolves in the material. Consequently, in unloading load increments, the mechanical response of the model is linearly elastic since plasticity has been neglected in the MMCDM theory.

Final failure of matrix subcells, as the state in which the material loses its load carrying ability, has been predicted by the model if any of the subcell stiffness components becomes very low. This condition has been achieved if the secondary damage variables, defined in Equation 4.7, become equal to or less than 0.01%. Additionally, the MMCDM theory employs damage energy principles to predict final subcell failure. Separate final failure criteria have for this purpose been employed in tensile and compressive loading conditions. Accordingly, a strain energy release rate criterion has been used in the tensile loading, whereas failure in compressive load cases has been predicted using the total released energy. The increment in released strain energy density dW has been calculated using the relation

$$dW = \frac{1}{2} \left\{ \sigma \left(\varepsilon + d\varepsilon \right) - \varepsilon \left(\sigma + d\sigma \right) \right\}, \tag{4.9}$$

which has been derived by considering the stress/strain relations in Figure 4.1 for the uniaxial load case assuming a piecewise linear response throughout the load increments.

Mode-specific criteria have been employed in the final failure modelling of matrix subcells based on the three loading modes (Mode I - opening, Mode II - in-plane shear and Mode III - out of plane shear). The mode-specific strain energy density release rates, which have been derived employing analogy with a macroscopically cracked body in [Bednarcyk et al., 2010], are

$$
\begin{aligned}
dW_I^1 &= dW_1; & dW_{II}^1 &= \frac{dD_1}{dD_1+dD_2}dW_6; & dW_{III}^1 &= \frac{dD_1}{dD_1+dD_3}dW_5; \\
dW_I^2 &= dW_2; & dW_{II}^2 &= \frac{dD_2}{dD_2+dD_3}dW_4; & dW_{III}^2 &= \frac{dD_2}{dD_1+dD_2}dW_6; \\
dW_I^3 &= dW_3; & dW_{II}^3 &= \frac{dD_3}{dD_1+dD_3}dW_5; & dW_{III}^3 &= \frac{dD_3}{dD_2+dD_3}dW_4.
\end{aligned}
\tag{4.10}
$$

The associated strain energy release rates, which are used to model failure of matrix subcells, are
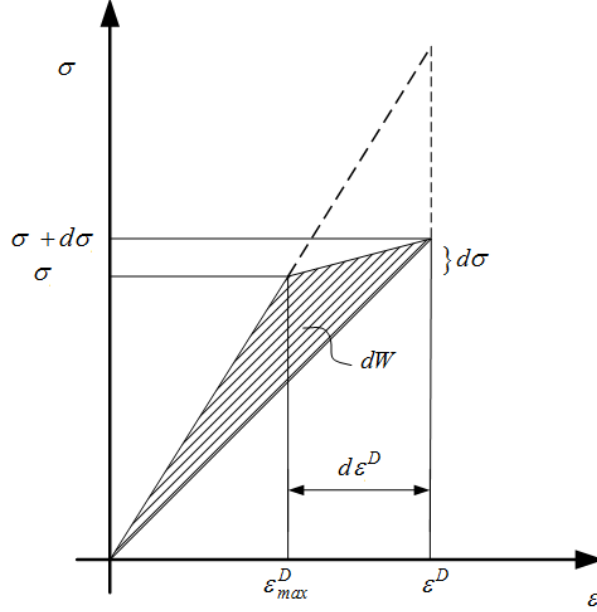
Figure 4.1: Graphical representation of the dissipated strain energy density.

$$G_I^1 = \frac{l_1}{b_{11}^T} \frac{dW_I^1}{dD_1}; \quad G_{II}^1 = \frac{l_1}{b_{61}} \frac{dW_{II}^1}{dD_1}; \quad G_{III}^1 = \frac{l_1}{b_{51}} \frac{dW_{III}^1}{dD_1};$$
$$G_I^2 = \frac{l_2}{b_{22}^T} \frac{dW_I^2}{dD_2}; \quad G_{II}^2 = \frac{l_2}{b_{42}} \frac{dW_{II}^2}{dD_2}; \quad G_{III}^2 = \frac{l_2}{b_{62}} \frac{dW_{III}^2}{dD_2}; \qquad (4.11)$$
$$G_I^3 = \frac{l_3}{b_{33}^T} \frac{dW_I^3}{dD_3}; \quad G_{II}^3 = \frac{l_3}{b_{53}} \frac{dW_{II}^3}{dD_3}; \quad G_{III}^3 = \frac{l_3}{b_{43}} \frac{dW_{III}^3}{dD_3},$$

where b_{ij} denote scaling parameters, while l_i is the material length in the normal directions. Complete degradation of matrix subcells properties in tensile loading modes has been predicted to occur if the mode-specific strain energy release rates reach the materials' critical strain energy release rate,

$$G_M^i \geq G_M^C, \quad M = I, II, III. \qquad (4.12)$$

Failure in compressive loading modes has been predicted by the MMCDM model using a criterion based on the total dissipated energy. The criterion has been formulated as

$$(W_I^i + W_{II}^i + W_{III}^i) V = W_S^C, \quad i = 1, 2, 3, \qquad (4.13)$$

where V is the volume of the material and W_S^C is the critical compressive strain energy.

Complete failure of a matrix subcell has been modelled by the application of very low values to the elasticity properties (0.01% of the undamaged values) of the failed subcells.

Degradation of fibre mechanical properties prior to complete failure has been neglected in this model, as no apparent nonlinearity has been observed in the fibre oriented loading in epoxy-based composites. Consequently, fibre subcells reach the failure state at the loading in which the failure initiation criterion, specified in Equation 3.29, reaches the critical state. Consequently, if the axial stress component in fibre subcells takes values higher than the fibre strength, failure occurs which instantaneously reduces fibre elastic properties to a very low value (0.01% of the undamaged value), thereby simulating complete subcell failure.

4.3   Smeared Crack Band damage model

The previously described MMCDM theory has been especially developed as to model matrix microdamage mechanisms in unidirectionally reinforced composite materials. The particular behaviour of epoxy composites, with significant pre-peak nonlinearity at in-plane shear and transverse compressive loading, has been accounted for by this theory.

As to expand the application domain of the developed multiscale approach, the Smeared Crack Band theory has been implemented into the methodology. The Crack Band theory is a well-known numerical technique developed as to alleviate the problem of length scale dependence of numerical damage modelling approaches. The fundamental relations of the Smeared Crack Band model (referred to as Crack Band theory in the further text) have been provided in this Chapter, whereas more details about the model and mesh objective theories can be found in e.g. [Bažant and Cedolin, 2010]. Implementation of the theory in this Thesis followed the particular version of this model which has been modified as to enable implementation into HFGMC, after [Pineda, 2012]. The Crack Band theory has in this reference been employed for micromechanical modelling of microdamage mechanisms in polymer-based composites (transverse tensile cracking and compressive shear banding), whereas validation in the multiscale framework has been performed in e.g. [Pineda et al., 2012a] and [Pineda et al., 2013].

More complex heterogeneous materials, consisting of several constituents in complex unit cell morphologies, could be modelled using this approach. This capability is especially attractive for further research activities which will be focused on advanced composite

materials (e.g. self-healing materials). The implementation of the theory is directly applicable to the three-dimensional extension of the micromechanical methodology. A major advantage of the described model is the inclusion of a discretization objective continuum damage model into the HFGMC framework.
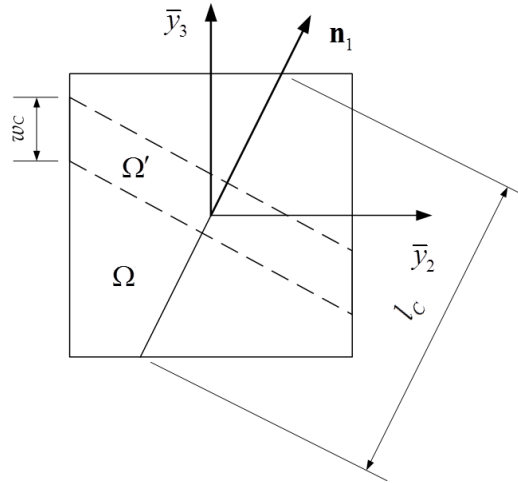
Figure 4.2: Crack band within subcell, after [Pineda, 2012].

The fundamental premise applied in the Crack Band theory is that the microscopic damage processes occur in the crack band - a narrow region in the continuum where several microcracks exist. The subcell crack band is designated by Ω' in Figure 4.2, while w_c is the frontal width of the crack. The characteristic length l_C, applied in the Crack Band concept, has been determined as the dimension across the subcell which is perpendicular to the crack band, as shown in Figure 4.2. The coordinate system $\mathbf{n_1}, \mathbf{n_2}, \mathbf{n_3}$ is aligned with the principal stress coordinate system. The normal $\mathbf{n_1}$ is associated with the maximal absolute principal stress as defined in Equation 3.30, which is perpendicular to the crack band.

Microdamage onset has in the approach been modelled using two failure modes, after [Pineda, 2012]. Initiation of these failure modes has been discussed in Chapter 3.4. The damaging mode has been determined based on the tensile/compressive character of the principal stress with the maximal absolute value. Consequently, Mode I damage occurs in stress states at which the principal stress value with the highest magnitude is tensile, whereas the Mode II failure has been predicted in the opposite case. Upon the initiation of damage in the HFGMC subcell, the crack band orientation remains constant throughout further load increments of the unit cell, after [Pineda, 2012].

Mesh objectivity has been enforced by scaling of the post-peak softening slope of the subcell stress-strain constitutive law. The dissipated energy density thus becomes a function of the characteristic length of the damaging continuum. The Crack Band theory has been implemented in the HFGMC model by application on the constitutive laws of the subcells. Consequently, mesh objectivity has been preserved by modification of the post-peak softening slope of the stress-strain curve depending on the characteristic length of the damaging subcell.
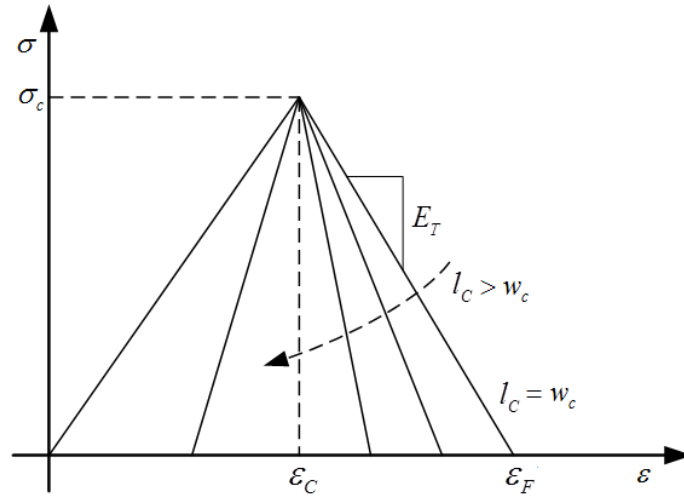
Figure 4.3: Illustration of Crack Band theory.

Application of the Crack Band theory on the constitutive model has been shown in Figure 4.3. The critical strain energy release rate G_C is related to the energy density dissipated during complete failure of the material W_F as

$$G_C = w_c W_F.$$

(4.14)

The critical strain energy release rate corresponds to the area under the one-dimensional traction separation law and, therefore, governs the cohesive response during crack propagation. For the one-dimensional loading case, Equation 4.14, can be further extended into

$$G_C = wc \left(\frac{\sigma_c{}^2}{2} \right) \left(\frac{1}{E^0} - \frac{1}{E_T} \right).$$

(4.15)

Since G_C is a material property, the post-peak softening slope E_T and the failure strain ε_F have to be modified considering the characteristic length scale of the subcell. The Crack Band theory relations, applied to the subcell, have been consequently defined as

$$\varepsilon_F^{(\beta,\gamma)} = \frac{2G_{IC}^{(\beta,\gamma)}}{\sigma_C^{(\beta,\gamma)} l_C^{(\beta,\gamma)}} \tag{4.16}$$

and

$$E_{IT}^{(\beta,\gamma)} = \left(\frac{1}{E_{11}^0} - \frac{\varepsilon_F^{(\beta,\gamma)}}{\sigma_C^{(\beta,\gamma)}} \right)^{-1}, \tag{4.17}$$

where $E_{IT}^{(\beta,\gamma)}$ is the tangent modulus predicted by Mode I damage, while E_{11}^0 designates the undamaged elastic modulus in *1* axis of the maximal principal stress coordinate system. As to prevent non-physical snap back of the tangent modulus, a limit has been placed on the maximum subcell dimension

$$l_C^{(\beta,\gamma)} < \frac{2G_{IC}^{(\beta,\gamma)} E_{11}^0}{\left(\sigma_C^{(\beta,\gamma)} \right)^2}. \tag{4.18}$$

Damage processes under Mode I conditions have been modelled in the principal coordinate system. Therefore, the subcell elasticity tensor has to be transformed into the principal coordinate system using relations for 3D transformations of elasticity and compliance tensors. The damage evolution law has been derived from the equivalence of the degradation law and the constitutive law defined by the Crack Band theory. Consequently, the damage evolution law for Mode I failure employing the linear degradation model can be analytically obtained as

$$D_I^{(\beta,\gamma)} = \frac{1 - \frac{\varepsilon_c^{(\beta,\gamma)}}{\varepsilon_I^{(\beta,\gamma)}}}{1 - \frac{\varepsilon_C^{(\beta,\gamma)}}{\varepsilon_f^{(\beta,\gamma)}}}, \tag{4.19}$$

after [Jirasek, 2011]. $\varepsilon_C^{(\beta,\gamma)}$ in Equation 4.19 is the strain component in $\mathbf{n_1}$ direction when Mode I damage has been initiated.

Application of the scalar damage parameter defined in Equation 4.19 follows the standard principle in damage mechanics, in which damage parameter values lower than

zero indicate absence of degradation, whereas values equal to one indicate complete degradation of the material. Subcell failure has been predicted if the damage variables (D_I for Mode I and D_{II} for Mode II) take very low values (0.01%), after which no further damage can be accumulated in the material. The damage parameters modify the subcell compliance tensor as

$$
\mathbf{S}^{(\beta,\gamma)} =
\begin{bmatrix}
\frac{S_{1111}^{0(\beta,\gamma)}}{1-D_I^{(\beta,\gamma)}} & S_{1122}^{0(\beta,\gamma)} & S_{1133}^{0(\beta,\gamma)} & 0 & 0 & 0 \\
S_{1122}^{0(\beta,\gamma)} & S_{2222}^{0(\beta,\gamma)} & S_{2233}^{0(\beta,\gamma)} & 0 & 0 & 0 \\
S_{1133}^{0(\beta,\gamma)} & S_{2233}^{0(\beta,\gamma)} & S_{3333}^{0(\beta,\gamma)} & 0 & 0 & 0 \\
0 & 0 & 0 & S_{2323}^{0(\beta,\gamma)} & 0 & 0 \\
0 & 0 & 0 & 0 & \frac{S_{1313}^{0(\beta,\gamma)}}{1-D_I^{(\beta,\gamma)}} & 0 \\
0 & 0 & 0 & 0 & 0 & \frac{S_{1212}^{0(\beta,\gamma)}}{1-D_I^{(\beta,\gamma)}}
\end{bmatrix},
\tag{4.20}
$$

after [Pineda, 2012]. Similarly to the MMCDM theory, application of the damaging law defined in Equation 4.20 introduces anisotropic constitutive laws to the initially isotropic matrix subcells.

Mode II failure initiation has been predicted employing the Mohr-Coulomb failure theory, as discussed in Section 3.4. According to [Pineda, 2012], the Crack Band model for Mode II failure follows the same principles as illustrated for Mode I with the main difference that all relations defined by the Crack Band theory have been applied in the coordinate system aligned with the maximal shear stress coordinate system. Consequently, the relations for Mode II failure resulting from the degradation law are

$$
\gamma_F^{(\beta,\gamma)} = \frac{2G_{IIC}^{(\beta,\gamma)}}{\tau_C^{(\beta,\gamma)} l_C^{(\beta,\gamma)}}
\tag{4.21}
$$

and

$$
E_{IIT}^{(\beta,\gamma)} = \left(\frac{1}{G_{12}^0} - \frac{\gamma_F^{(\beta,\gamma)}}{\tau_C^{(\beta,\gamma)}} \right)^{-1},
\tag{4.22}
$$

where G_{12}^0 is the undamaged shear modulus in the maximal shear stress coordinate system, while τ_C is the cohesive shear strength.

As shown in [Pineda, 2012], the shear strain in the maximal shear stress coordinate system is work conjugate to the effective shear stress derived from the Mohr-Coulomb
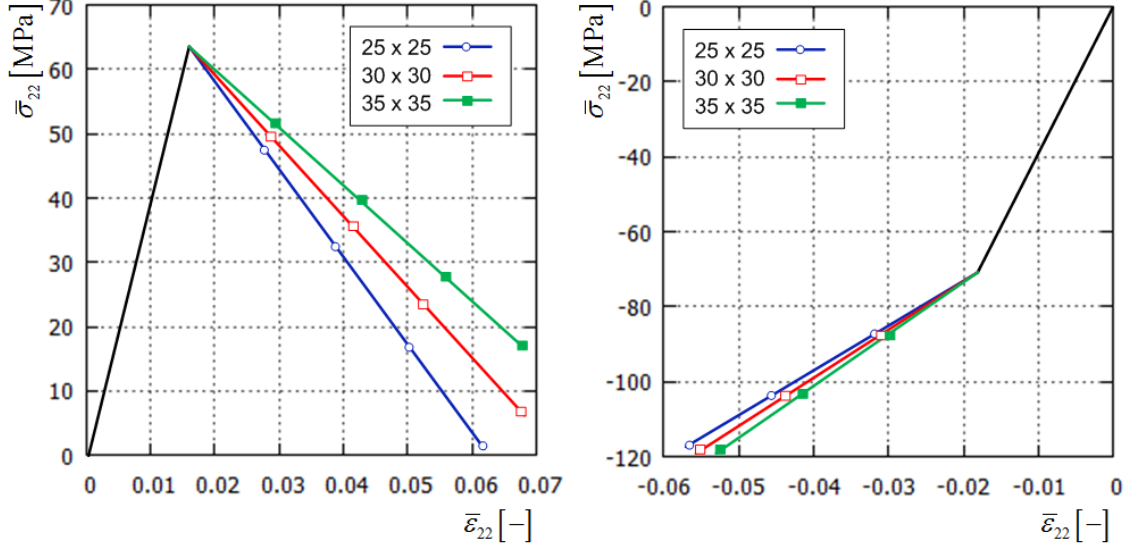
Figure 4.4: Effect of unit cell discretization on the matrix constitutive model under Mode I (left-hand side image) and Mode II damage (right-hand side image).

theory. Consequently, the Mode II damage parameter is defined as

$$D_{II}^{(\beta,\gamma)} = \frac{1 - \frac{\gamma_c^{(\beta,\gamma)}}{\gamma_I^{(\beta,\gamma)}}}{1 - \frac{\gamma_c^{(\beta,\gamma)}}{\gamma_F^{(\beta,\gamma)}}}. \tag{4.23}$$

Degradation due to damage effects has been modelled by modification of the compliance matrix in the maximal shear stress coordinate system using damage parameters defined in Equation 4.23 as

$$\mathbf{S}^{(\beta,\gamma)} = \begin{bmatrix} S_{1111}^{0(\beta,\gamma)} & S_{1122}^{0(\beta,\gamma)} & S_{1133}^{0(\beta,\gamma)} & 0 & 0 & 0 \\ S_{1122}^{0(\beta,\gamma)} & S_{2222}^{0(\beta,\gamma)} & S_{2233}^{0(\beta,\gamma)} & 0 & 0 & 0 \\ S_{1133}^{0(\beta,\gamma)} & S_{2233}^{0(\beta,\gamma)} & S_{3333}^{0(\beta,\gamma)} & 0 & 0 & 0 \\ 0 & 0 & 0 & S_{2323}^{0(\beta,\gamma)} & 0 & 0 \\ 0 & 0 & 0 & 0 & \frac{S_{1313}^{0(\beta,\gamma)}}{1-D_{II}^{(\beta,\gamma)}} & 0 \\ 0 & 0 & 0 & 0 & 0 & \frac{S_{1212}^{0(\beta,\gamma)}}{1-D_{II}^{(\beta,\gamma)}} \end{bmatrix}. \tag{4.24}$$

Similarly to the Mode I criterion, a limit has been applied to the maximal subcell size. This limit has been enforced using the relation

$$l_C^{(\beta,\gamma)} < \frac{2G_{IC}^{(\beta,\gamma)}G_{12}^0}{\left(\tau_C^{(\beta,\gamma)}\right)^2}. \tag{4.25}$$

Following the application of the subcell constitutive damaging laws, the final step in the application of the theory consists of the transformation of the damaged compliance and updated stress tensors from the principal stress or the maximal shear stress coordinate systems to the subcell local coordinate system. Once the damage laws have been applied at the subcell level for the current load increment, the homogenisation procedure has been employed as to predict the updated strain concentration tensors of the HFGMC, equivalent mechanical properties and the homogenised stress tensor of the unit cell, as explained in Section 2.6.

According to the micromechanical Crack Band theory application, dimensions of the subcell influence the post-peak tangent modulus of the constitutive laws applied to matrix subcells. Consequently, the discretization refinement, used to discretize the composite RUC in the micromechanical model, affects the slope of the tangent stiffness tensor in the post-peak regime of matrix subcells. This effect has been shown in the left-hand side image in Figure 4.4 for Mode I damage on the MY750 matrix, whereas transverse compression under Mode II damage has been shown in the right-hand side image in this Figure. Shear loading of the matrix results in a shear stress-shear strain constitutive model governed by Mode II damage similar to the illustration for Mode I damage Figure 4.4.

4.4   Application of MMCDM theory

Validation of the MMCDM theory implementation into the multiscale methodology developed in this Thesis has been performed by the application of the model on experimental data provided in [Soden et al., 1998] and [Hinton et al., 2002]. The HFGMC micromechanical model has been intended to be used to govern the constitutive model within the Abaqus/Explicit analyses. Therefore, validation of the implementation has been performed only on the available experimental data of unidirectional composite laminates using the standalone HFGMC application. The evaluated composite materials are the Silenka GFRP and the T300/BSL914C epoxy composite (referred to as T300/914 throughout this Thesis).

Validation of the MMCDM implementation into the HFGMC model has been performed by comparison with experimental data of composite ply failure envelopes provided as part of the WWFE [Hinton et al., 2002]. Additionally, available experimental data of the nonlinear matrix dominated behaviour of the composite material, after [Soden et al., 1998], have been used as to validate the model.

Table 4.1: MY750 matrix damage properties for the MMCDM model [Bednarcyk et al., 2010]

Property	Symbol	Unit	Value
Tensile damage initiation strain	$X_\varepsilon^T = Y_\varepsilon^T = Z_\varepsilon^T$	[-]	0.0125
Compressive damage initiation strain	$X_\varepsilon^C = Y_\varepsilon^C = Z_\varepsilon^C$	[-]	0.0287
Engineering shear damage initiation strain	$R_\varepsilon = Q_\varepsilon = S_\varepsilon$	[-]	0.0443
Mode I critical SERR	G_I^C	[J/m^2]	800.
Mode II and III critical SERR	$G_{II}^C = G_{III}^C$	[J/m^2]	2400.
Critical compressive strain energy	W_S^C	[J]	1.86×10^{-6}
Material length	l_i	[m]	9.0×10^{-5}

MMCDM damage parameters for the MY750 epoxy matrix, which have been employed in [Bednarcyk et al., 2010] as to model the damage/failure curves of the Silenka GFRP material, are shown in Table 4.1. The mechanical properties of the E-glass fibre and the MY750 matrix have already been provided in the previous Chapter in Table 3.2.

Table 4.2: MY750 post-damage slope and scaling parameters [Bednarcyk et al., 2010]

Post-damage slope parameters [-]			
$A^T = 0.70$	$A^C = 1.90\ (2.00)$	$B^T = 0.82$	$B^C = 1.20\ (0.96)$
Scaling parameters [-]			
$b_{ii}^T = b_{ii}^C = 1.32$		$b_{4i} = b_{5i} = b_{6i} = 0.50$	

Besides the damage initiation strains, Table 4.1 contains the parameters for the subcell failure prediction. Constitutive response of the matrix within the MMCDM theory has been governed by the post-damage slope and scaling parameters, which are summarised in Table 4.2 for the MY750 matrix. These values have been taken from [Bednarcyk et al., 2010]. However, the compressive post-damage slope parameters A^C and B^C have been adjusted as to obtain better correlation with experimental results in transverse compression. The values in the parentheses in Table 4.2 are the original values provided in [Bednarcyk et al., 2010].

Application of the MMCDM damage model, with parameters defined in Tables 4.1
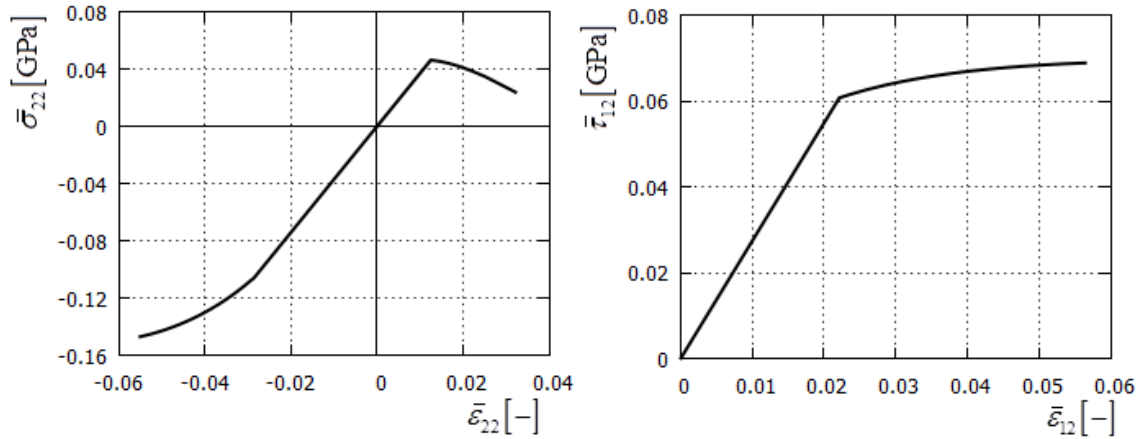
Figure 4.5: Nonlinear behaviour of the neat MY750 matrix modelled by the MMCDM model - transverse tensile/compressive loading (left-hand side image) and in-plane shear (right-hand side image) responses.

and 4.2, on the constitutive behaviour of the neat MY750 matrix has been shown in Figure 4.5, in the transverse tensile and compressive loading $\bar{\sigma}_{22} - \bar{\varepsilon}_{22}$ and the in-plane shear loading $\bar{\tau}_{12} - \bar{\varepsilon}_{12}$. The results illustrate the in-situ three-axial constitutive model, governed by the MMCDM anisotropic damaging laws, which has been applied in the matrix subcells as to predict the nonlinear response of the composite ply.

The progressive degradation effects on the damage initiation and final failure curves of the MY750 epoxy matrix material in the $\bar{\sigma}_{11} - \bar{\sigma}_{22}$ stress space, modelled with the MMCDM model, are shown in Figure 4.6. The differences between the damage initiation curves, predicted by the stress states at which the damage strains indicate microdamage initiation, and the final failure curve as the state in which the material loses its load carrying ability, indicate the extent of accumulated microdamage in the matrix material prior the state in which subcells begin to fail. As shown, a significant amount of microdamage has been accumulated by the matrix material prior to final failure under certain loading conditions. This effect is more pronounced in compressive transverse loading.

The damage analyses of the composite material have been performed in this Chapter using the 30×30 HFGMC unit cell with a single fibre in the unit cell centre. This particular unit cell has been employed as a compromise between the fidelity of determination of the local stress/strain fields within the RUC and computational performance, which is a significant factor for the multiscale application of the methodology. The microdamage
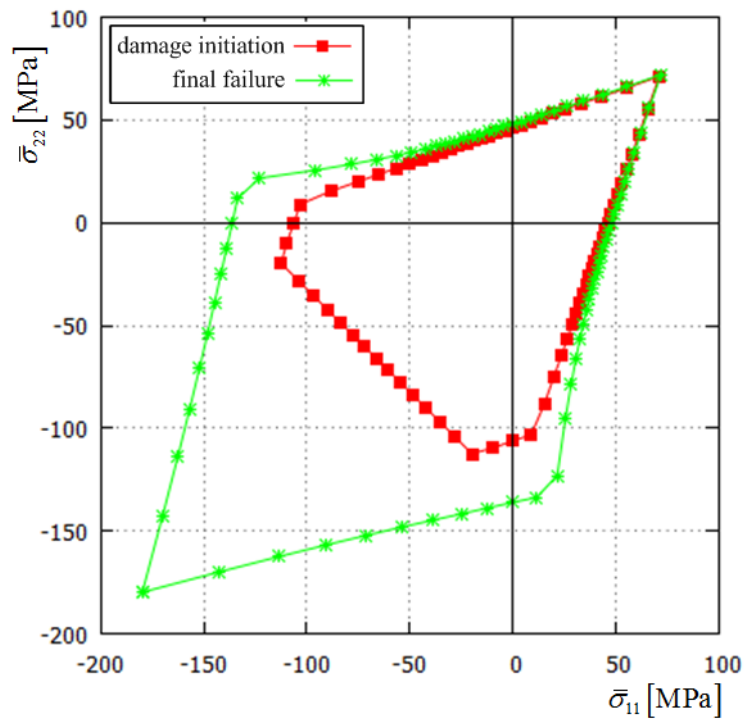
Figure 4.6: MMCDM damage initiation and final failure for the neat MY750 matrix in the $\bar{\sigma}_{11} - \bar{\sigma}_{22}$ stress space.
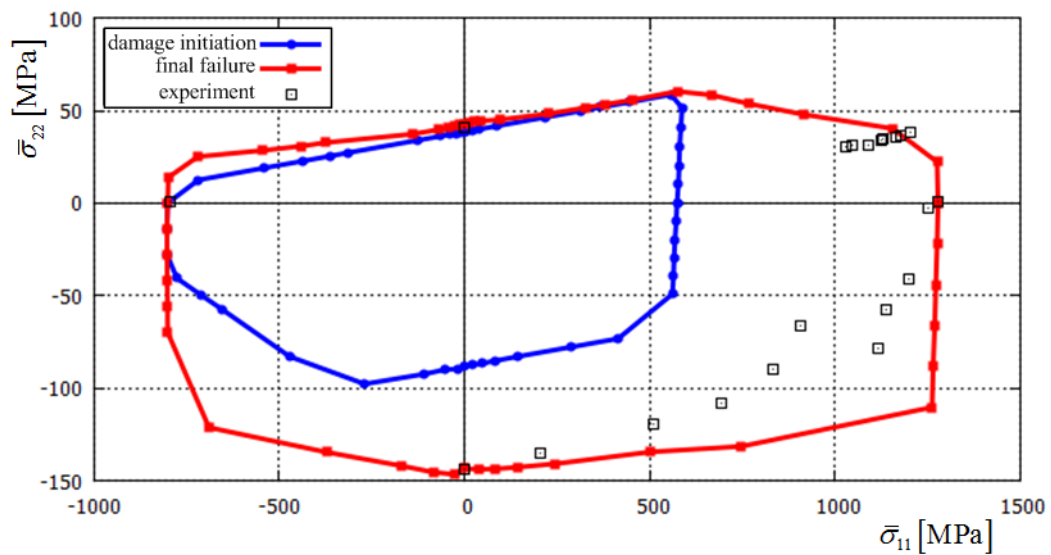
Figure 4.7: Damage initiation and final failure curves in the $\bar{\sigma}_{11} - \bar{\sigma}_{22}$ stress space for the Silenka GFRP composite, comparison with experimental data provided in [Hinton et al., 2002].

initiation and final failure curves in the biaxial $\bar{\sigma}_{11} - \bar{\sigma}_{22}$ stress space for the Silenka GFRP composite material, as predicted by the HFGMC model, are shown in Figure 4.7. Along with the HFGMC results, the experimental ply failure data, as provided in [Hinton et al., 2002], are shown in this Figure. A reasonable fit of the experimental data has been predicted by the model.

The composite microdamage mechanisms in the constitutive response of the Silenka GFRP composite are most pronounced in the $\bar{\sigma}_{22} - \bar{\tau}_{12}$ stress space, since the composite material exhibits significant pre-peak nonlinearity in the in-plane shear and transverse compressive loading, as previously discussed in Section 3.4 and shown in Figure 3.6. Validation using the experimental data in the $\bar{\sigma}_{22} - \bar{\tau}_{12}$ stress space for the Silenka GFRP composite, provided in [Hinton et al., 2002], has been shown in Figure 4.8. The microdamage mechanisms will be evident in all loading directions of the $\bar{\sigma}_{22} - \bar{\tau}_{12}$ stress space. Excellent agreement between the micromechanical model and the experimental data has been achieved in the evaluated load case.
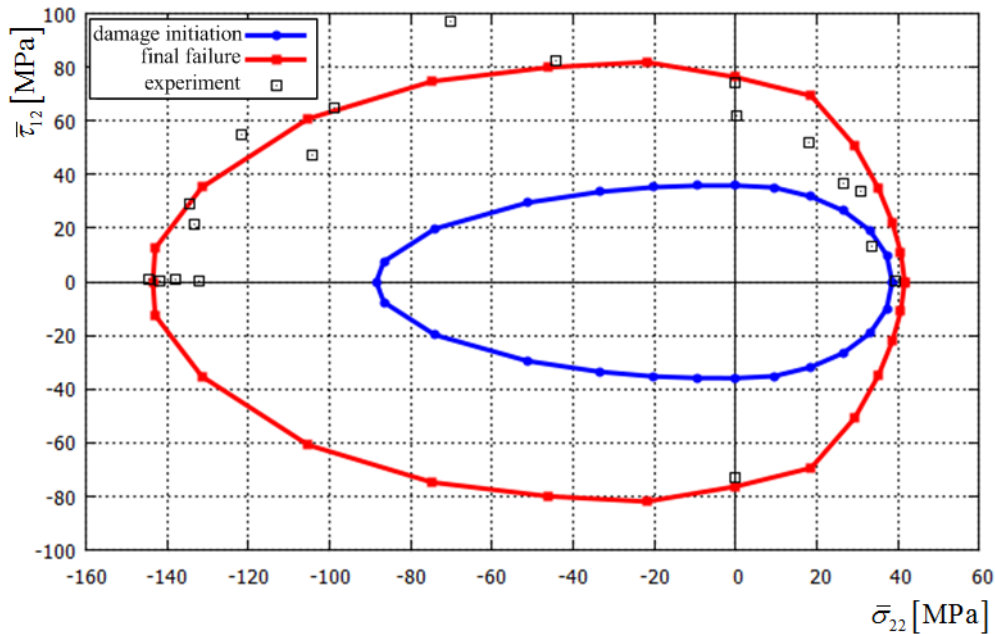
Figure 4.8: Damage initiation and final failure curves in the $\bar{\sigma}_{22} - \bar{\tau}_{12}$ stress space for the Silenka GFRP composite, comparison with experimental data provided in [Hinton et al., 2002].

The MMCDM theory has been applied in the multiscale framework in this Thesis. Therefore, evaluation of the MMCDM theory results within the RUC has been performed

as to assess the micromechanical effects of the progressive degradation model on the composite behaviour. Analyses of the local MMCDM parameters at various homogenised load cases provide the link between the local fields and the homogenised composite response. Results of these analyses have been essential for the interpretation of the MMCDM multiscale application since the SDVs, employed to visualise results of the micromechanical analysis in the multiscale framework, show only the maximal values of an individual parameter within the RUC, as explained in Section 2.6.

Evolution of the MMCDM model parameters within the Silenka GFRP composite RUC for the transverse tensile load case has been shown in Figure 4.9. For the transverse tensile load case only one data point, which specifies the transverse tensile strength of the GFRP material, has been provided in [Soden et al., 1998], indicating brittle behaviour of the composite. The transverse strength, as well as the brittle behaviour, have been accurately captured by the model.
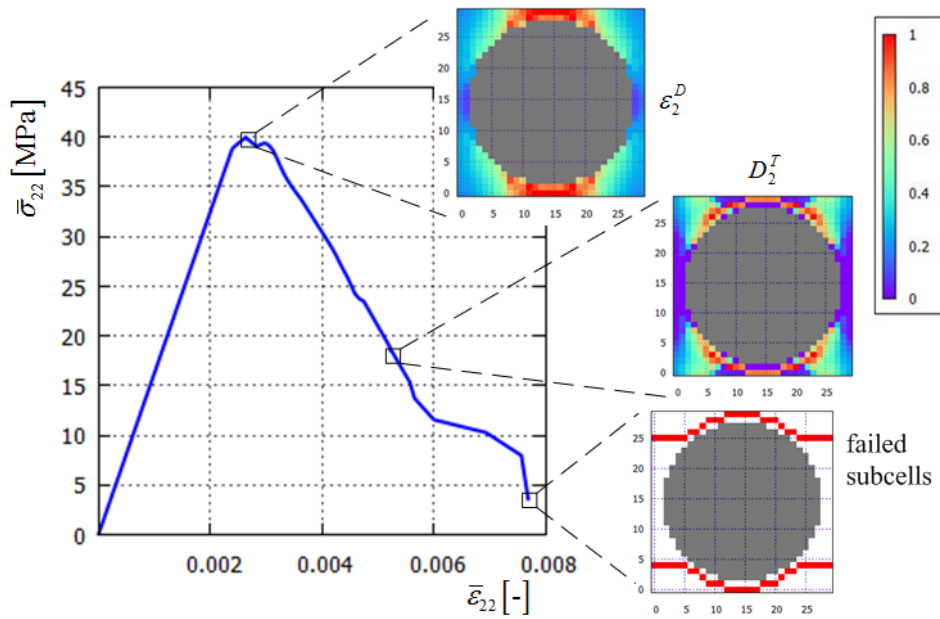
Figure 4.9: Evolution of MMCDM damage model parameters at transverse tensile loading of the Silenka GFRP composite.

At transverse tensile load conditions ε_2^D is the critical failure mode of the RUC. The RUC distribution of the ε_2^D damage strains for the peak loading, at which the first subcells reach the failure state, has been shown in Figure 4.9. Damage processes in the transverse tensile load case have been initiated at the applied $\bar{\sigma}_{22}$ stress which is slightly lower than the transverse tensile strength of the composite. Further application

of the loading results in the gradual increase of damage and the fraction of failed matrix subcells in the RUC. As a result, the homogenised properties have been significantly degraded by the failed subcells. The evolution of damage has been illustrated by the D_2^T damage parameter in Figure 4.9, whereas the final failure state of the RUC has been depicted by the contours of failed subcells in this Figure.

Evaluation of the damage model within the RUC revealed a relation between the fraction of failed matrix subcells and the completely degraded effective properties of the composite material in the matrix dominated failure modes. Consequently, the state in which the composite material becomes unable to further carry any significant loads in the matrix dominated loadings has been approximated to occur in the load cases in which 15% of matrix subcells have failed, as shown in Figure 4.9. A similar observation has been obtained performing micromechanical analyses employing the Crack Band model in Section 4.5.
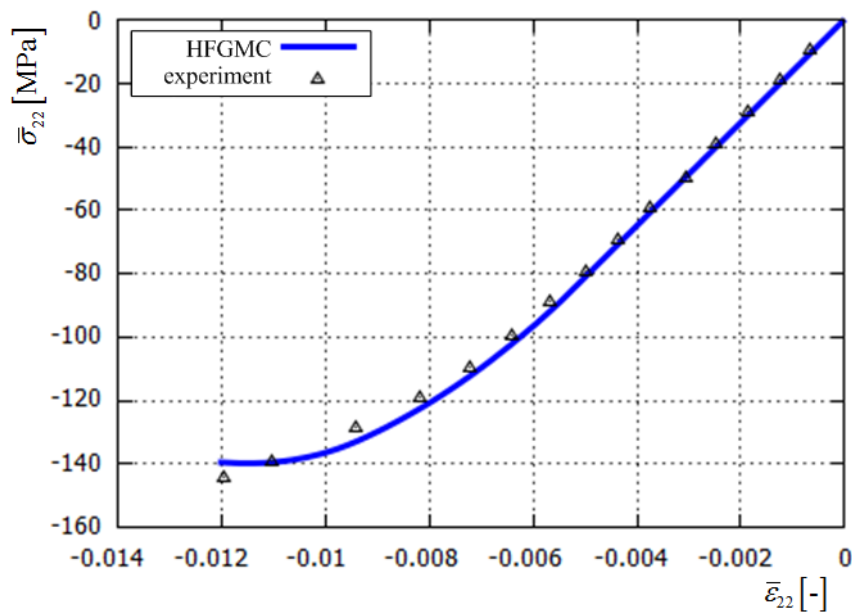
Figure 4.10: Transverse compressive loading - comparison of the model with experimental results for the Silenka GFRP composite.

This condition corresponds to the change of damaging mode from matrix microdamage to transverse matrix cracking. The approach to relate the portion of failed subcells in the unit cell with the complete matrix failure mode of the composite ply can be justified by the observation that transverse microcracks form almost instantaneously through the

ply specimen thickness, after [Talreja and Singh, 2007].

Constitutive behaviour in transverse compression of the Silenka GFRP material, simulated using HFGMC and the MMCDM model, has been shown in Figure 4.10. The experimental data, provided in [Soden et al., 1998], have been employed as to correlate the required compressive post-damage slope and scaling parameters as previously explained. As shown in Figure 4.10, the model simulates the nonlinear behaviour in the $\bar{\sigma}_{22} - \bar{\varepsilon}_{22}$ loading reasonably well. The relative difference between the predicted compressive strength and the value provided in [Soden et al., 1998] is 4.14% while the model has accurately predicted the transverse compressive failure strain.
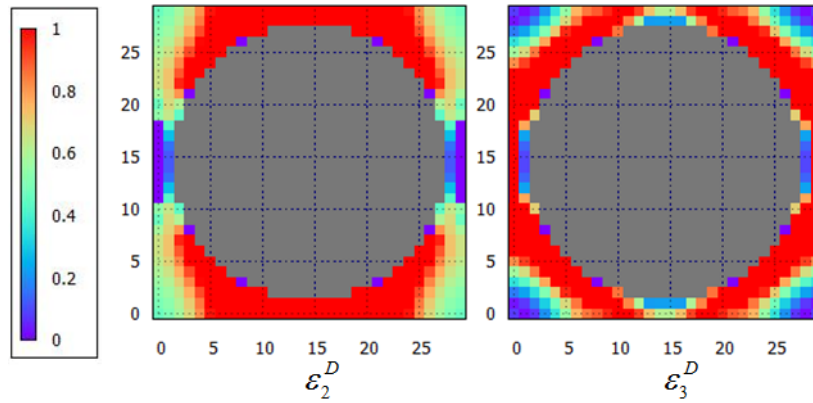
Figure 4.11: Damage strains for peak loading in transverse compressive loading.

Transverse compressive microdamage mechanisms of the composite have been dictated by ε_2^D as well as by the ε_3^D damage strains. Distribution of these damage strains within the RUC for the peak loading in transverse compression of the Silenka GFRP composite has been shown in Figure 4.11. Microdamage mechanisms evolve in the portions of the RUC where the damage strains take values above 1.0.

The RUC distribution of D_2^C and the D_3^T damage variables for the peak transverse compressive loading has been shown in Figure 4.12. Complete failure od the subcell in the MMCDM model has been controlled by the dissipated energy as shown in Equations 4.12 and 4.13. Consequently, subcell failure conditions can be fulfilled prior to the state in which damage variables reach the critical value (1.0). The contours of the failed subcells for transverse compressive loading are shown in the right-hand side image in Figure 4.12.

Comparison of the predicted in-plane shear response for the Silenka GFRP composite
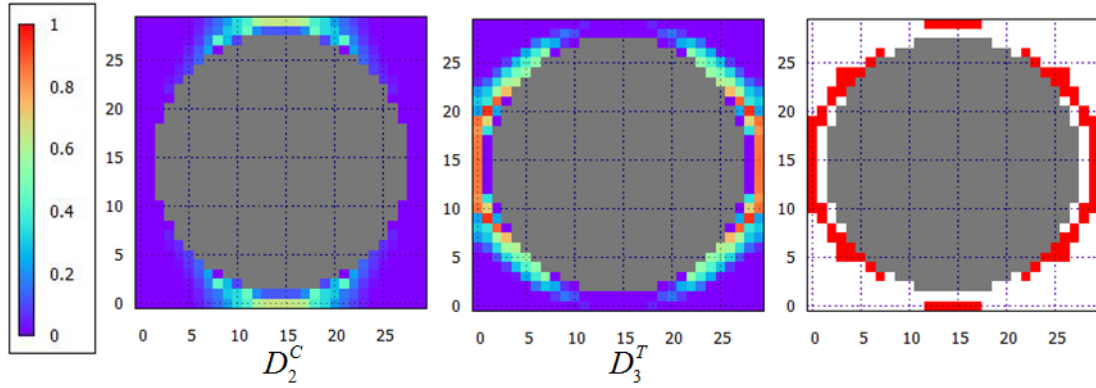
Figure 4.12: D_2^C and D_3^T damage variables and contours of failed subcells (right-hand side image) for peak transverse compressive loading of the Silenka GFRP composite.
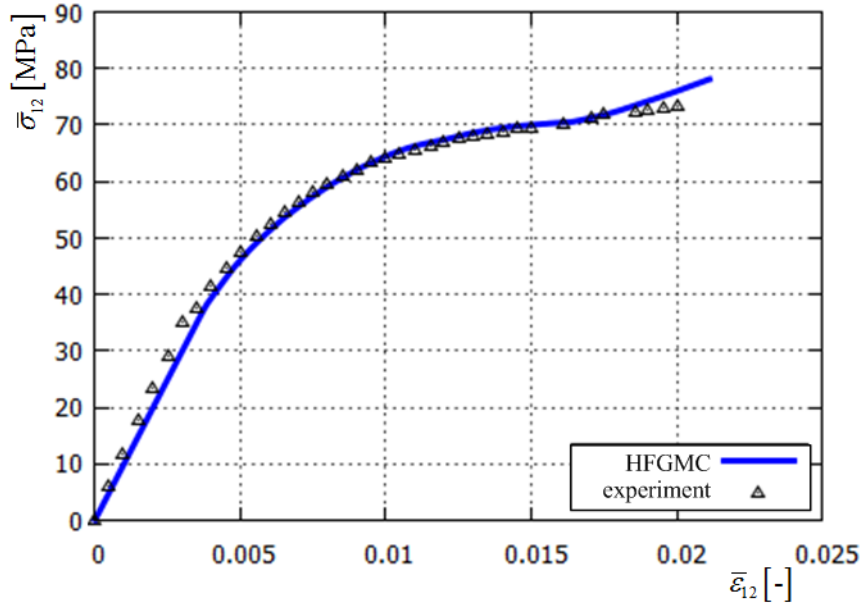
Figure 4.13: In-plane shear loading - comparison of the model with experimental results for the Silenka GFRP composite.

with the experimental results provided in [Soden et al., 1998] has been shown in Figure 4.13. The shear strength and the failure strain of the composite material have been slightly overestimated by the model, whereas the overall nonlinear behaviour in the in-plane shear loading has been predicted with acceptable accuracy.

Initiation of the in-plane shear nonlinearities has been determined simultaneously by ε_1^D and ε_2^D damage strains, as discussed in the Section 3.5. The nonlinear composite behaviour has been dictated for in-plane shear loading by the D_1^T and D_2^T damage
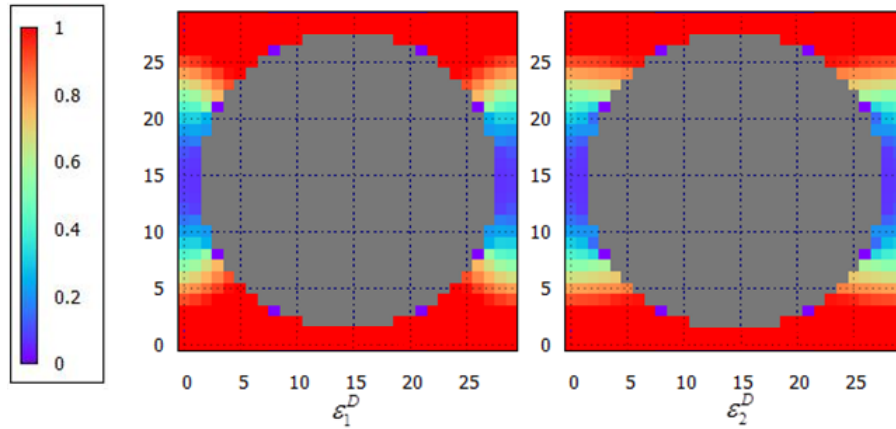
Figure 4.14: Damage strains for in-plane shear response at the critical load.

variables, which have similar distribution within the unit cell. Therefore, only the D_2^T damage variable RUC distribution has been shown in the left-hand side image in Figure 4.15. Contours of the failed subcells in the in-plane shear loading at peak load are shown in the right-hand side image in Figure 4.15.
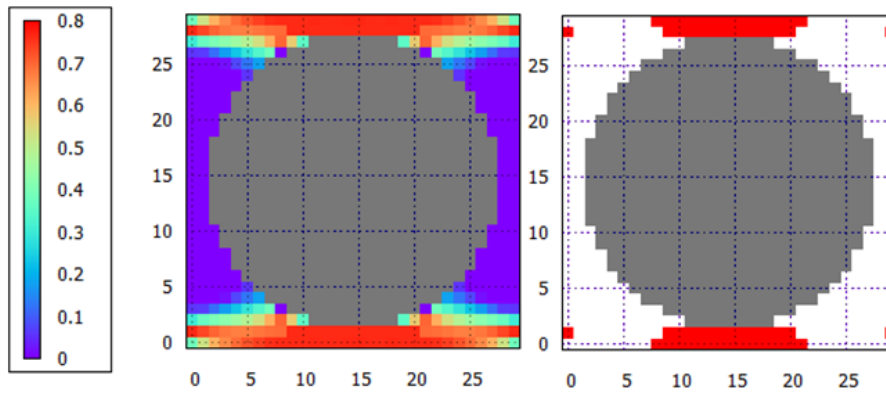
Figure 4.15: D_2^T damage variables for in-plane shear response (left-hand side image) and contours of failed subcells (right-hand side image) at the critical load for the Silenka GFRP composite.

The T300/914 composite has been applied in the multiscale soft body impact analyses in the following Chapter. The post-damage slope parameters of the MMCDM model for this composite material have been determined using the nonlinear in-plane shear response of the T300/914 composite provided in [Soden et al., 1998]. The predicted parameters, which have been used throughout the performed multiscale analyses in this Thesis for the T300/914 composite, are shown in Table 4.4. The in-situ constituent

Table 4.3: Mechanical properties employed in the analysis of the T300/914 composite.

T300 fibre				
E_1 [GPa]	$E_2 = E_3$ [GPa]	$G_{12} = G_{13}$ [GPa]	G_{23} [GPa]	ν_{23} [-]
230.0	18.5	19.0	12.0	0.4
$\nu_{12} = \nu_{13}$ [-]	X_t [GPa]	X_c [GPa]		
0.2	2.5	1.5		
914 matrix				
E [GPa]	ν [-]	$X_\varepsilon^T, Y_\varepsilon^T, Z_\varepsilon^T$ [-]	$X_\varepsilon^C, Y_\varepsilon^C, Z_\varepsilon^C$ [-]	$R_\varepsilon, Q_\varepsilon, S_\varepsilon$ [-]
4.6	0.35	0.0059	0.032	0.034

mechanical properties, employed in the micromechanical analyses as to predict the T300/914 composite ply properties provided in [Soden et al., 1998], are presented in Table 4.3.

As shown in Table 4.3, orthotropic mechanical properties have been employed for the T300 carbon fibre while an isotropic constitutive model (with an increased elasticity modulus compared to the values provided in [Soden et al., 1998]) has been applied for the matrix subcells.

Table 4.4: MMCDM damage model properties for the 914 matrix.

Post-damage slope parameters [-]			
$A^T = 0.70$	$A^C = 1.0$	$B^T = 1.10$	$B^C = 1.0$
Scaling parameters [-]			
$b_{ii}^T = b_{ii}^C = 1.32$		$b_{4i} = b_{5i} = b_{6i} = 0.50$	

The parameters of the final subcell failure model used in the MMCDM theory are not available for the 914 matrix and have therefore been assumed equal to the values provided in Table 4.2 for the MY750 matrix. This assumption has been justified by the fact that both matrices are epoxy polymers.

Figure 4.16 shows the response of the HFGMC analysis using the MMCDM model with properties defined in Table 4.4. The nonlinear response at shear loading has been accurately captured by the MMCDM model with the applied damage parameters. As the nonlinear response at transverse compressive loading has not been provided in [Soden et al., 1998], the relevant post-damage slope parameters have been selected to depict only limited nonlinearity prior to the final failure in this loading condition.

Validation of the model implementation for the T300/914 composite has been per-
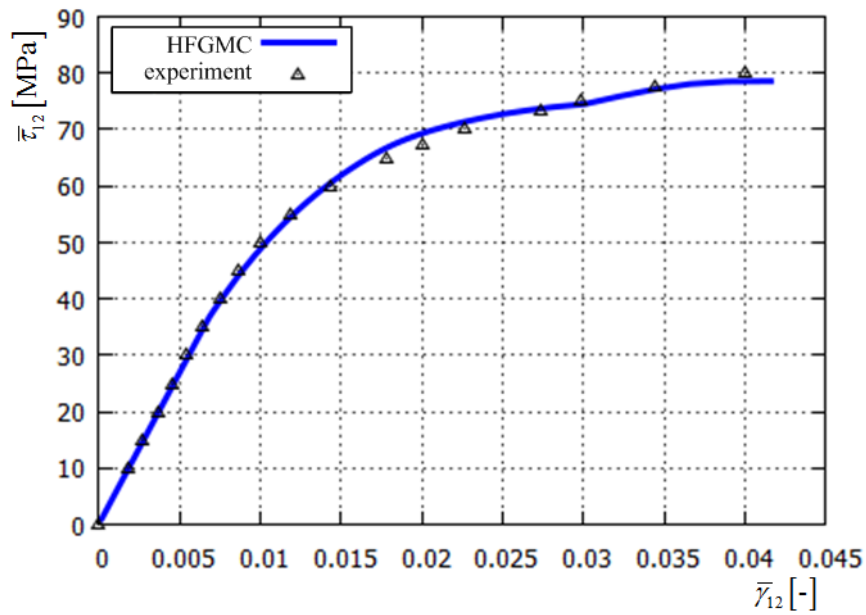
Figure 4.16: Modelling of the in-plane shear response of T300/914, experimental data have been provided in [Soden et al., 1998].
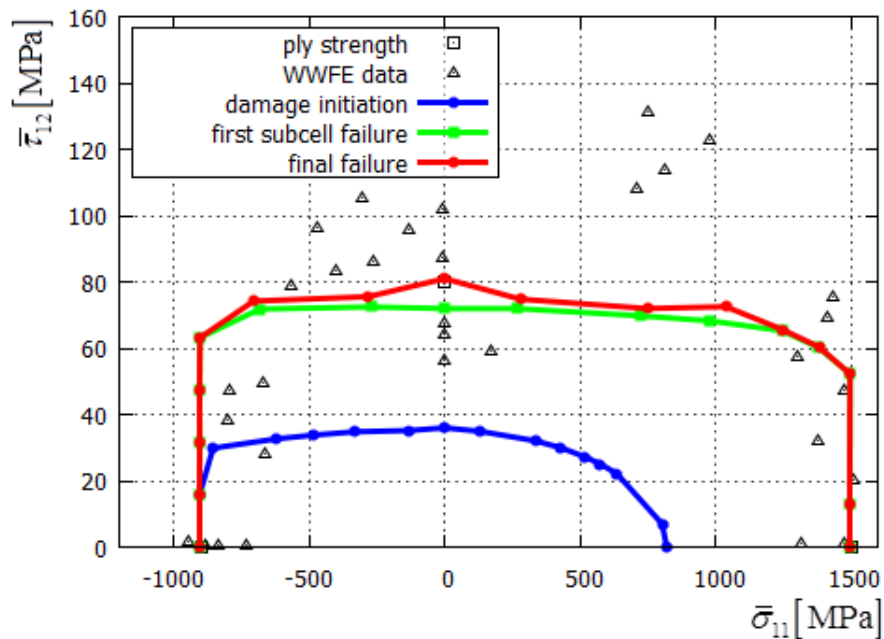
Figure 4.17: Damage initiation, first subcell failure and final failure curves of the T300/914 composite in the $\bar{\sigma}_{11} - \bar{\tau}_{12}$ stress space, experimental data have been provided in [Hinton et al., 2002].

formed by comparison with the experimental data in the $\bar{\sigma}_{11} - \bar{\tau}_{12}$ stress space, which have been provided in [Hinton et al., 2002]. Comparison of the damage initiation and the final failure curves with the experimental data has been shown in Figure 4.17. The experimental results in Figure 4.17 show large scatter of the failure shear stresses. Consequently, it is difficult to evaluate the physical correctness of the results and illustrates difficulties of the estimation of the required in-situ properties of the micromechanical damage models. Besides the damage initiation and final failure curve, the results in Figure 4.17 show the load states at which the first subcells in the RUC reach the failure state. The differences between the first subcell load condition and the peak load are most evident for the pure in-plane shear loading case.
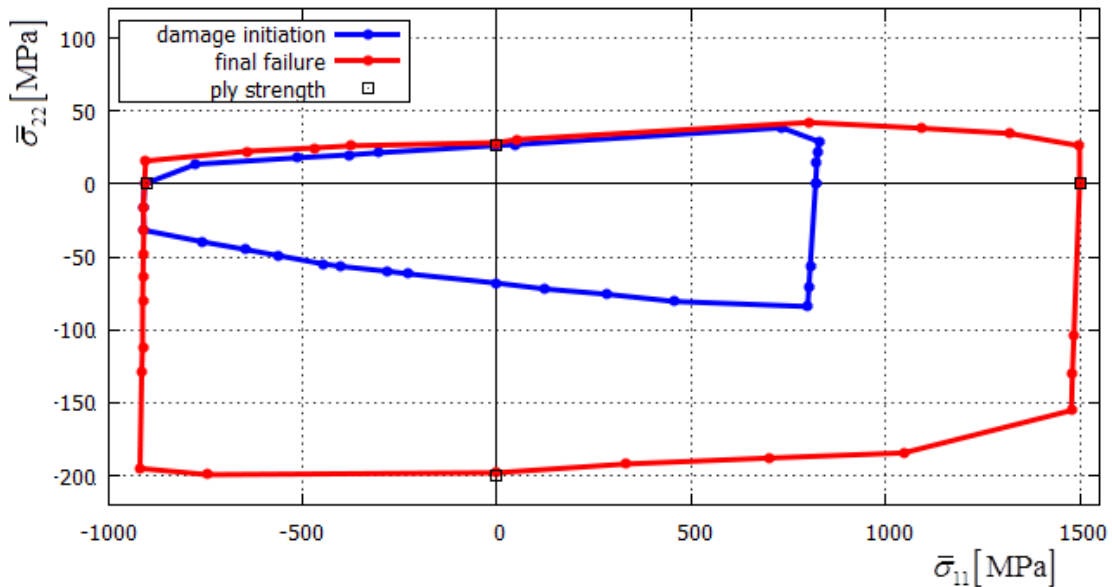
Figure 4.18: Damage initiation and final failure curves in the $\bar{\sigma}_{11} - \bar{\sigma}_{22}$ stress space for T300/914 composite, comparison with the ply strengths provided in [Soden et al., 1998].

Figure 4.18 shows the MMCDM damage initiation and final failure curves in the $\bar{\sigma}_{11} - \bar{\sigma}_{22}$ stress space for the T300/914 composite. The failure curves resemble the results provided for the evaluated GFRP material, with different values on the axes, representing the differences between the ply strengths. All conclusions obtained in the RUC observation of the micromechanical analyses obtained by the application of the model for the Silenka GFRP material are valid also for the evaluated CFRP material.

4.5   Application of the Crack Band damage model

Implementation of the Crack Band theory into the multiscale methodology developed in this Thesis has been validated by comparison with results provided in [Pineda, 2012] and [Pineda et al., 2012b]. The micromechanical Crack Band damaging model has been employed in these references within the HFGMC model as to model the microdamage mechanisms in the Silenka GFRP material.

The GFRP constituent mechanical properties have been previously defined in Table 4.1. Parameters of the Crack Band damage model are provided in Table 4.5. The subcell damage initiation strains (ε_c and γ_c) have been obtained by correlation with the experimental onset of nonlinear behaviour, as discussed in Section 3.5. The critical strain energy release rates in Table 4.5 have been taken from [Pineda, 2012]. These values have been obtained by correlation of the micromechanical damage model with experimental data.

Table 4.5: Crack Band damage model properties for the MY750 matrix.

ε_c [−]	γ_c [−]	G_{Ic} [J/m^2]	G_{IIc} [J/m^2]
0.0194	0.0256	0.00076	0.00435

The single-fibre RUC discretized with 30×30 subcells has been employed for micromechanical analyses in this Section as to enable comparison with the RUC distributions of the MMCDM damage model parameters. Dimensions of the unit cell have been adjusted with regard to the physical dimension of the fibre in this example (5 μm, as provided in [Pineda, 2012]) and the fibre volume fraction defined as 58%. Consequently, the RUC dimensions have been defined as 5.76×5.76 μm. The constitutive $\bar{\sigma}_{22} - \bar{\varepsilon}_{22}$ response in transverse tensile loading of the RUC has been shown in Figure 4.19.

As for the tensile transverse loading case only a single data point, specifying the composite elasticity properties and transverse tensile strength, has been provided in [Soden et al., 1998], the predicted post-peak response has been compared to the numerical results provided in [Pineda et al., 2012b]. These referent numerical analyses have been performed as to validate the Crack Band theory implementations using HFGMC, GMC and FE micromechanical models. A complex RUC morphology which consists of 13 randomly distributed fibres has been employed for this purpose. Results of the evaluation have been also presented for the single fibre RUC in [Pineda et al., 2012b]. These results
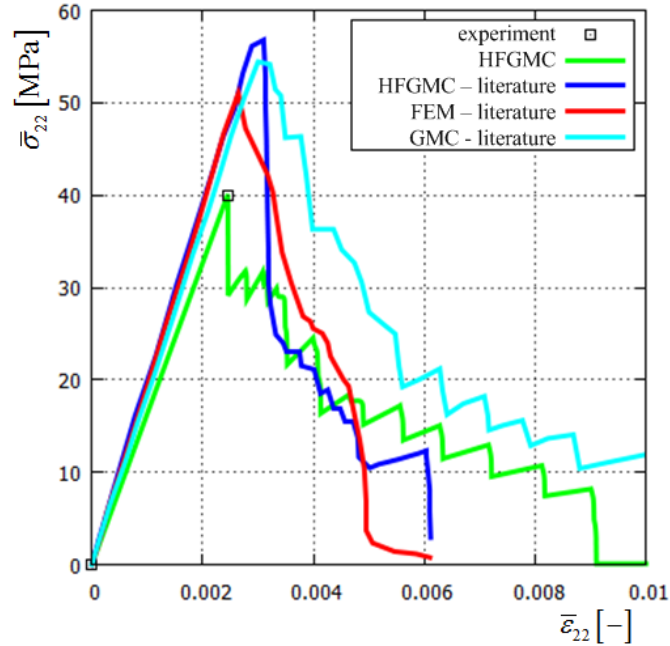
Figure 4.19: Transverse tensile loading of the Silenka GFRP composite in $\bar{\sigma}_{22} - \bar{\varepsilon}_{22}$, comparison with experimental results and the data provided in [Pineda et al., 2012b].

have been employed in this Thesis for evaluation of the methodology implementation.

The referent numerical results overpredict the transverse elastic modulus of the composite as well as the tensile strength of the composite ply, as shown in Figure 4.19. In-situ mechanical properties applied in the referent micromechanical models have been predicted for the 13-fibre unit cell. Application of these parameters on the single-fibre unit cell results in the inaccurate prediction of the tensile strength and the transverse elasticity properties of the composite. These inaccuracies have been generated by the stress concentrations caused by the thin matrix channels in the complex RUC, as discussed in Section 3.5.

The model captures accurately the peak strength which is followed by a sharp drop of the homogenised $\bar{\sigma}_{22}$ stress. The instant decrease of the transverse stresses has been caused by strain localisation in the failing subcells. A moderate match with the post-peak regime of the HFGMC and FEM results has been obtained, as shown in Figure 4.19. Consequently, the differences between the obtained results and the referent values (obtained using HFGMC, GMC and FEM) have been caused by differences in the RUC discretization and the slightly different in-situ constituent properties. Distribution of the maximal principal stress criterion at damage initiation is shown on the left-hand side
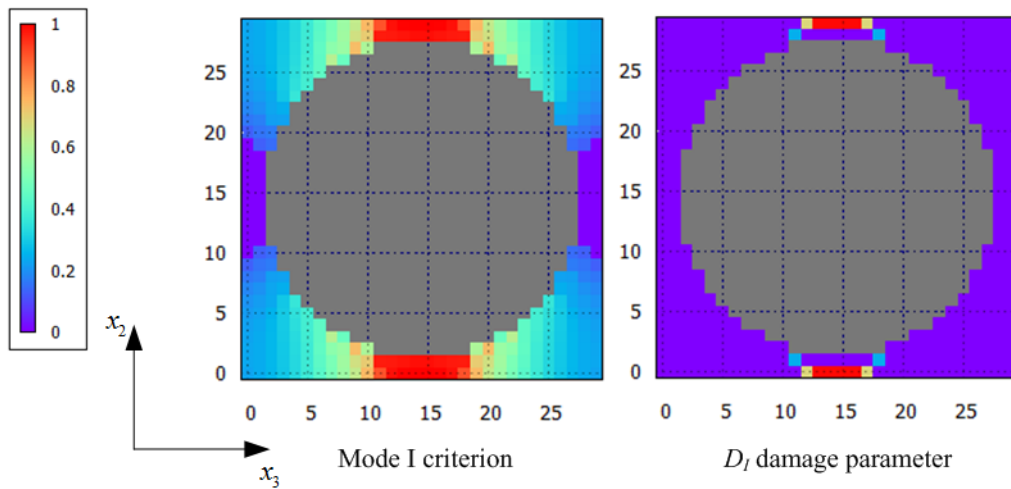
Figure 4.20: Maximal principal stress criterion and D_I damage parameter distribution for tensile loading of Silenka GFRP composite at peak stress.

image of Figure 4.20. The corresponding D_I damage parameters have been shown in the right-hand side image in Figure 4.20. Load redistribution due to the subcell failure has been shown in the left-hand side image in Figure 4.21.

Distribution of the damage parameter D_I has been shown for various states of the applied tensile transverse strain in the right-hand side images of Figures 4.20 and 4.21 and in both images in Figure 4.22. As shown in these images, at the loading in which
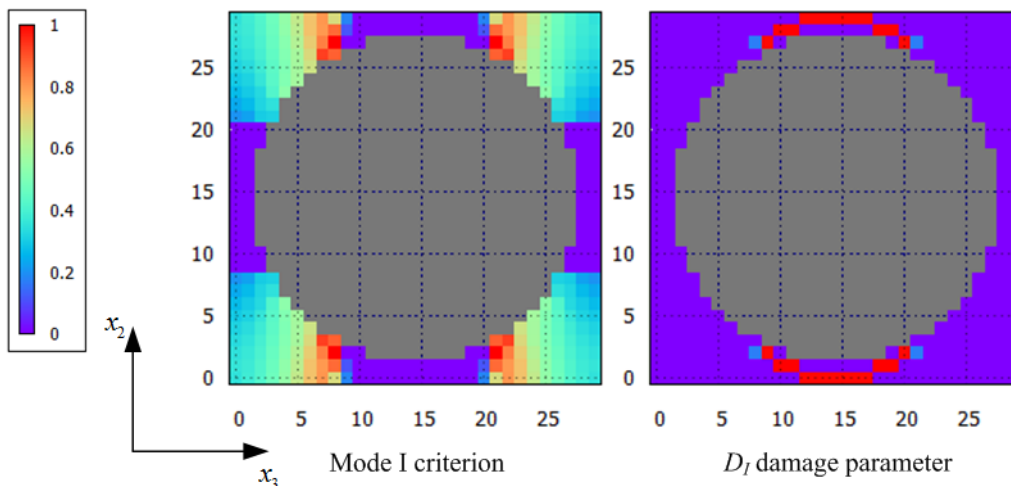
Figure 4.21: Maximal principal stress criterion and damage parameter distribution for tensile loading of Silenka GFRP composite at $\bar{\varepsilon}_{22} = 0.0039982$ (7.2% failed matrix subcells).

damage has advanced entirely through the unit cell, a state of complete loss of load carrying capability of the unit cell has been reached. This observation is in accordance with the conclusions of the MMCDM theory application where the state of complete loss of the composite mechanical properties, in matrix dominated loadings, has been achieved for load states in which approximately 15% of the matrix subcells have failed completely.
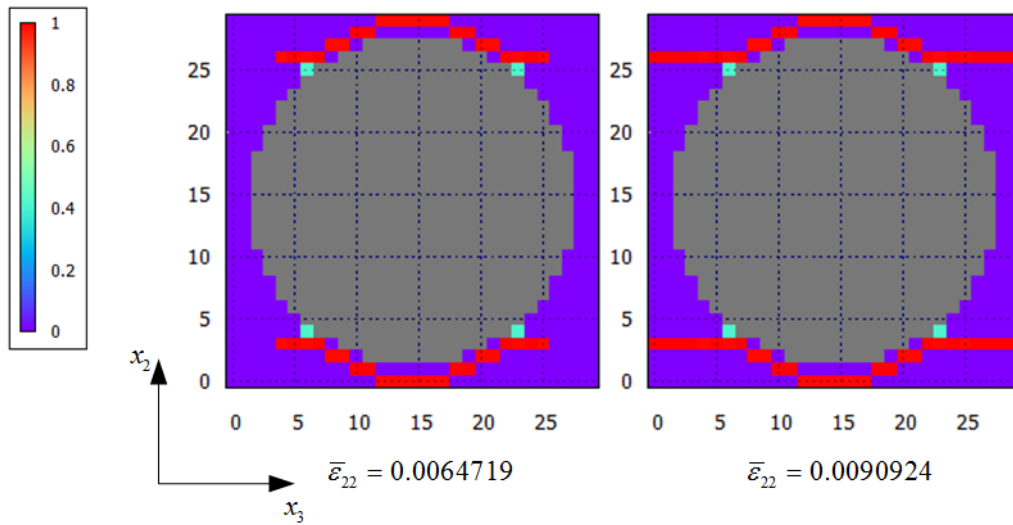
Figure 4.22: Damage parameter distribution for tensile loading (Mode I damage) of Silenka GFRP composite at $\bar{\varepsilon}_{22} = 0.0064719$ (12.2% failed matrix subcells) and $\bar{\varepsilon}_{22} = 0.0090924$ (16.6% failed subcells).

Nonlinear response in transverse compression has been used to validate the Mode II damage mode. The response of the composite RUC, along with the experimental results provided in [Soden et al., 1998], has been shown in Figure 4.23. The numerical results presented in [Pineda et al., 2012b] have been shown in this Figure for comparison. The numerical results, which have been illustrated in Figure 4.23, overestimate the transverse elasticity modulus as explained earlier in this Section. Microdamage onset in the Mode II conditions has been predicted by the 30×30 unit cell at the homogenised strain loading of 0.47%, which corresponds to a stress state of approximately -73 MPa in the homogenised composite material.

Figure 4.24 shows contours of Mode I and Mode II failure initiation criteria for the Mode II damage initiation load state. Damage processes have been initiated under Mode II conditions in the subcells located along the x_2 unit cell axis, as shown in the left-hand side image in Figure 4.24, whereas matrix subcells located along the x_3 axis are loaded
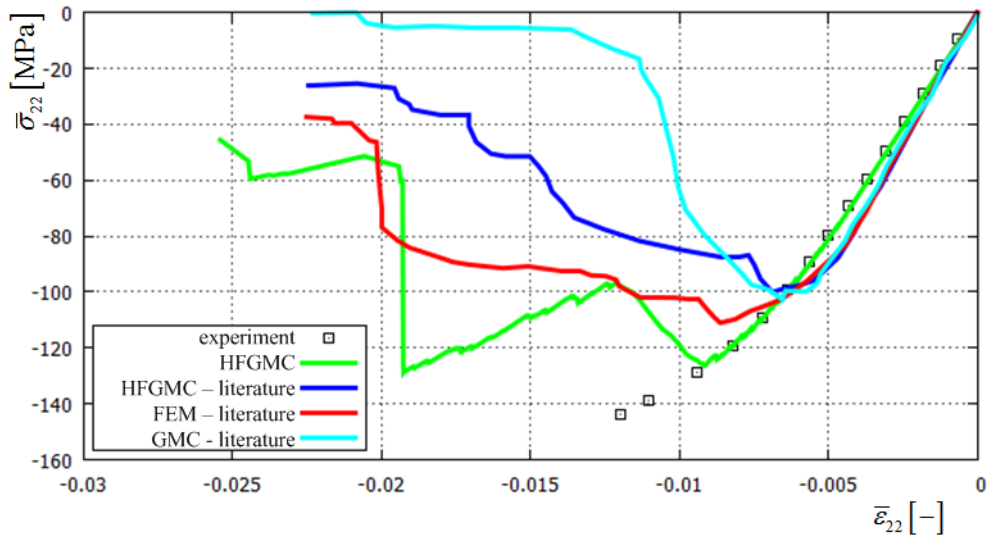
Figure 4.23: Transverse compressive $\bar{\sigma}_{22} - \bar{\varepsilon}_{22}$ loading of the Silenka GFRP composite, comparison with experimental and numerical results provided in [Pineda et al., 2012b].

under Mode I conditions, as shown in the right-hand side image in Figure 4.24. Maximal values of Mode I criterion at the Mode II damage initiation load are approximately 0.4.

Load redistribution, caused by damage processes in the RUC, results in the increase of Mode I damage initiation criteria. The nonlinear response of the composite material has been accurately predicted until the peak stress, which occurs at lower values compared
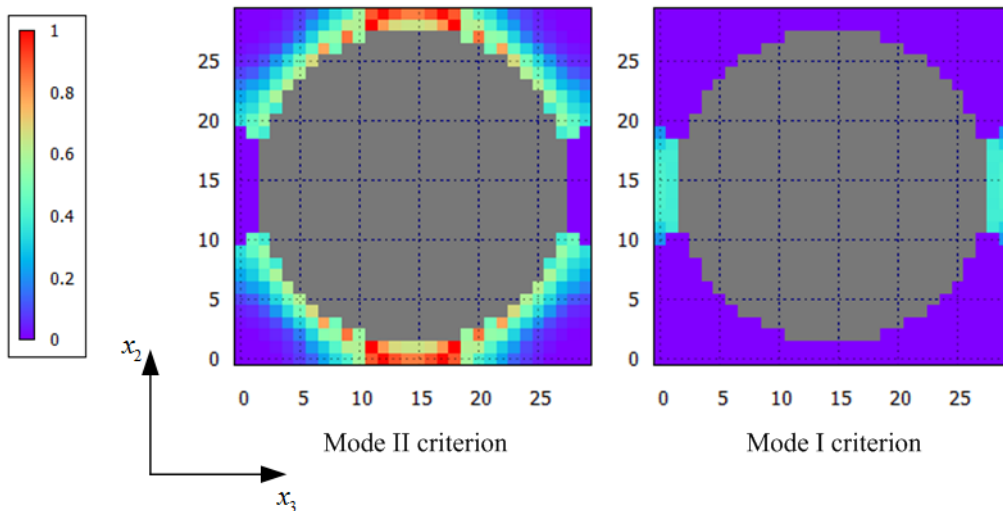
Figure 4.24: RUC distribution of Mode II and Mode I damage initiation criteria at initiation of damage processes in compressive loading.
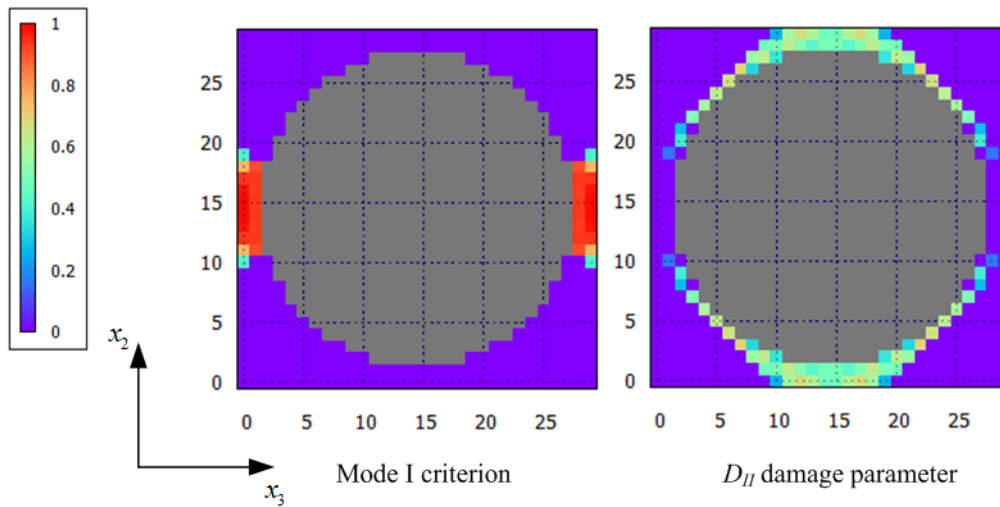
Figure 4.25: Mode I failure criterion and D_{II} damage parameter at initiation of Mode I damage processes at compressive loading.

to the experiments (approximately 128 MPa compared to 145 MPa) as shown in Figure 4.23.

The sudden drop in the homogenised stress in Figure 4.23 has been induced by Mode I damage processes at the applied transverse compressive strain of 0.9%. The left-hand side image in Figure 4.25 shows the Mode I failure criterion distribution at the Mode I damage initiation. The right-hand side image in Figure 4.25 shows contours of the D_{II} damage parameter for this load state. The maximal D_{II} damage parameter values are approximately 0.7. The underestimation of the composite ply transverse compressive strength, caused by Mode I damage processes, is in close agreement with the results provided in [Pineda, 2012]. As suggested in this reference, better match of experimental results could be achieved by suppressing Mode I damage in the transverse compressive load case.

The first subcells reach the failure state (Mode I failure) at an applied transverse strain of approximately -1.2%. The subsequent RUC load redistribution results in the continuation of the damage processes governed by Mode II damage. This part of the constitutive response is parallel to the curve prior to Mode I damage initiation. Consequently, if Mode I would be prevented, the applied model would predict the nonlinear response of the GFRP accurately.

Subcell failure under Mode II occurs at applied transverse strain of approximately
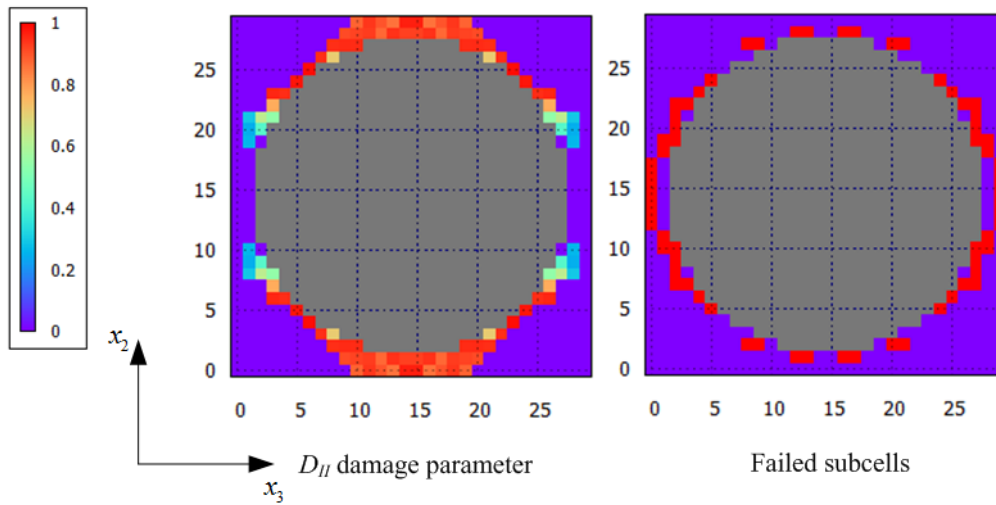
Figure 4.26: D_{II} damage parameter at applied transverse compressive strain of 0.019 (left-hand side image) and contours of failed subcells at the unit cell failure state.

1.9%. The sudden drop in transverse stress has been caused by the simultaneous failure of several subcells under Mode II failure.

D_{II} damage parameters for this load state are shown in Figure 4.26, left-hand side image, while the contours of completely failed subcells are shown in the right-hand side image in Figure 4.26. These contours are in close agreement with the referent results predicted by the FEM and HFGMC model using the single fibre unit cell in [Pineda et al., 2012b].

Damage initiation and final failure curves for the Silenka GFRP composite in the $\bar{\sigma}_{11} - \bar{\sigma}_{22}$ stress space are shown in Figure 4.27. As discussed previously, the model underestimates the compressive transverse strength of the composite ply by approximately 10%. The transverse tensile strength, as well as longitudinal tensile and compressive strengths, have been accurately predicted by the model. The obtained final failure curves using the Crack Band theory are very similar to the MultiContinuum Theory failure curve in Chapter 3.4. The predicted form of final failure in the transverse compressive region is very similar to the MMCDM model. Discontinuities in the damage initiation curve have been caused by the change in the matrix damage mode under the applied strain loadings.

The Crack Band damage model has not been applied as to simulate the in-plane shear behaviour of the composite. As discussed in [Pineda, 2012], a detailed three-dimensional
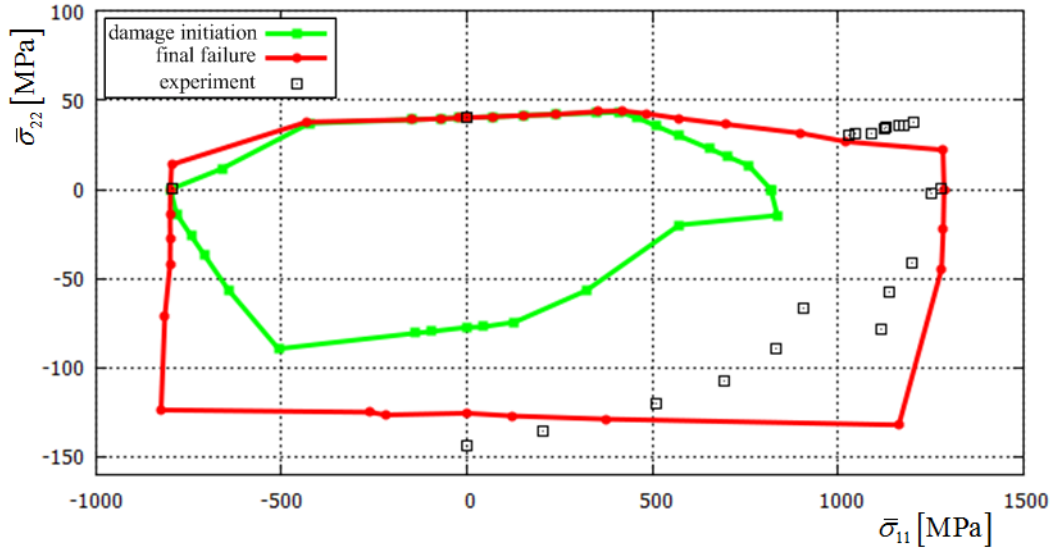
Figure 4.27: Damage initiation and final failure of the Silenka GFRP composite in the $\bar{\sigma}_{11} - \bar{\sigma}_{22}$ stress space, comparison with experimental results [Hinton et al., 2002].

micromechanical model would have to be employed as to capture the microcracks along the fibre which lead to the nonlinear behaviour of the composite material in in-plane shear loading. As shown in the analyses performed in Section 3.5, the employed damage initiation criterion would also have to be modified for this loading case.

4.6   Conclusion

Two micromechanical damage models have been evaluated in this Chapter. Implementation of the MMCDM model into the developed methodology has been validated by comparison with available experimental data. Good correlation with the experimental data has been achieved for the Silenka GFRP composite, whereas only moderate correlation with experimental data has been achieved in the application of the MMCDM model on the T300/914 composite as large scatter of experimental data prevents better correlation.

The MMCDM model enables modelling of composite ply nonlinearities in matrix dominated loading. Therefore, implementation of the model in the multiscale methodology offers increased accuracy over the previous applications of micromechanical failure criteria in the multiscale framework [Moncada, 2012], [Pineda et al., 2009]. Effects of the micromechanical degradation models on the damage processes within the RUC have

been studied as to establish a link between the local RUC results and the homogenised composite response. Evaluation of the micromechanical degradation models within the RUC resulted in similar conclusions for the two validated theories. However, application of the Crack Band damage model allows modelling only of the transverse cracking damage mode whereas the MMCDM model allows simulation of more complex RUC loadings. Further validation of the methodology could be performed by addition of lamination theory to the standalone HFGMC micromechanical model as to simulate failure curves of more complex layups.

Results obtained with the application of the Crack Band model are in close agreement with the referent results from the literature. The emphasis of the implementation of the Crack Band theory in this Thesis has been set on the further development of the methodology and application on more complex unit cells. The method will allow micromechanical investigations on advanced composite materials with complex microstructures. These research activities should be performed concurrently with experimental investigations in order to develop applicable micromechanical failure theories and determine the constituent in-situ properties, as the main difficulties in the micromechanical analyses.

5 | Multiscale failure analyses

5.1 Introduction

The micromechanical damage prediction methodology has been in this Chapter applied for structural-scale FE analyses. The standalone HFGMC application has been employed in the preceding Chapters as to validate the implemented micromechanical failure and damage theories. The conclusions gained from these analyses have been applied in this Chapter in the multiscale framework. Consequently, the micromechanical damage models, which enable modelling of microdamage mechanisms causing pre-peak nonlinearity, as well as the micromechanical failure criteria for prediction of the in-plane failure modes have been applied to structural-scale analyses.

The methodology has been applied in this Thesis on two FE structural problems representing typical applications in aeronautical structures. Aeronautical composite structures are generally manufactured as laminated structures, in which the ply orientations have been optimised for structural performance. Consequently, structural discretization using shell finite elements is appropriate for many applications in aeronautical structures. Therefore, the composite shell section has been employed in the numerical models as to model the composite laminate, whereas the HFGMC model has been applied as the constitutive model in the FE framework.

The first model on which the multiscale methodology has been tested in this Thesis represents a stringer reinforced composite panel, a typical structural element of aircraft structures.

Analyses on this, for multiscale applications very large numerical model, have been performed in the second research phase in this Thesis. The emphasis in these studies

---

has been set on validation of the micromechanical failure theories at the structural scale. Important factors which affect the applicability of the methodology in structural scale analyses, as e.g. computational times and programming aspects, have been evaluated here.

Evaluation of the micromechanical damage modelling approaches has been performed by application of the multiscale methodology on simulation of high-velocity soft body impact on a composite plate. Validation of the multiscale methodology has been performed by comparison with the available experimental data in the literature. The applicable experimental data is very limited in the literature and consists only of visually inspected damage states and descriptive interpretations of the final damaged states. Consequently, further validation of the multiscale methodology has been performed by comparison with the ply-level failure criteria and the Abaqus built-in progressive damage model for fibre reinforced composite materials.

5.2 Tensile loading of stringer reinforced composite panel

The multiscale methodology has been applied to a structural-scale numerical model representing a stringer reinforced composite panel loaded with a tensile load. Results of the analyses presented in this Section have been obtained in the research phase in which the link between the micromechanical HFGMC model and the FE macro-scale analyses has been established. Therefore, computational aspects, as e.g. performance and interactions between the different subroutines have been investigated. The results revealed that the methodology is computationally too costly for realistic structural applications considering the currently available hardware. Consequently, approaches which would improve the computational aspects have been implemented into the procedure.

Implicit FE simulations are more suitable for the tensile load cases analysed in this Section. However, the numerical benchmark analyses have been performed using Abaqus/Explicit with the aim of establishing guidelines for the adaptive multiscale approach. Within this approach, the HFGMC micromechanical computations in a given material point would be performed only for the load increments in which damage onset or progression are probable.

The results of the evaluated ply-level failure theories have been employed as to initiate

micromechanical computations in the methodology, as explained in Section 2.6 and shown in the flowchart in Figure 2.9. Therefore, evaluation of micromechanical failure theories against the ply-level failure theories has been performed. The results and conclusions are provided in this Section.
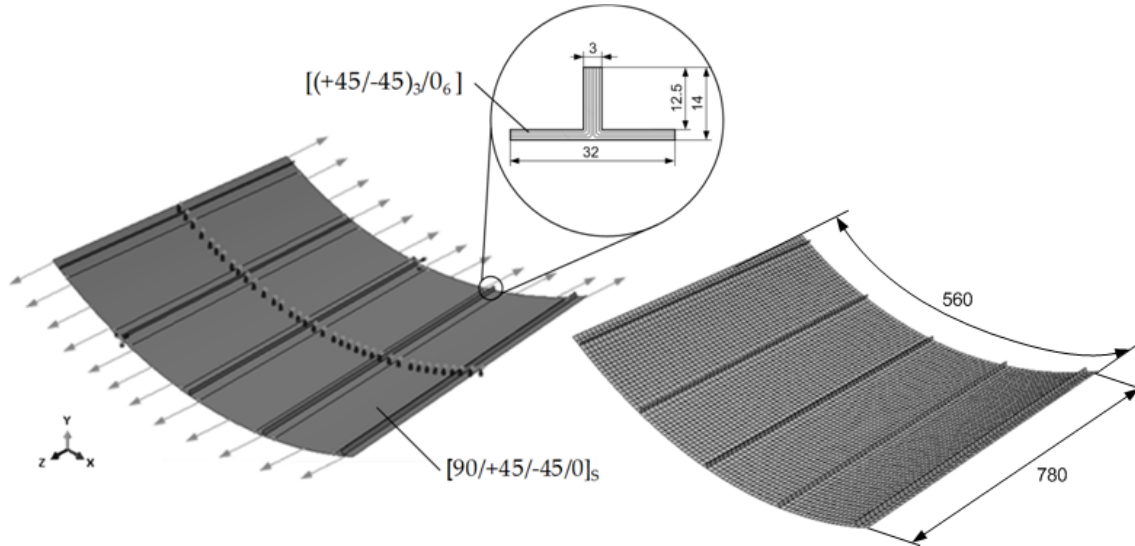
Figure 5.1: Numerical model of the stringer-stiffened composite panel, dimensions are in [mm].

The numerical FE model employed in the benchmark analyses is shown in Figure 5.1. The model represents a composite panel with stringer reinforcements, a typical structural component of aeronautical structures. Dimensions and laminate lay-up of the panel have been taken from [Degenhardt et al., 2008]. Length and arc length of the panel are 0.78 m and 0.56 m, respectively. The panel is made up of unidirectional plies with single ply thicknesses of 0.125 mm. Laminating sequence of the panel skin is $[90/+45/-45/0]_S$, where the orientation of unidirectional plies is measured with regard to the panel length direction (z axis in Figure 5.1). The stringer reinforcements are composed of two sets of $[(+45/-45)_3/0_6]$ laminates, while the stringers are of a T profile as shown in Figure 5.1. Details of the finite element model have been provided in Table 5.1.

Table 5.1: Details of the aeronautical panel numerical model.

Number of S4R elements	5270
Number of nodes	5418
Degrees of freedom	32508

Two tensile load cases, in which the panel has been loaded along the reinforcements

as shown schematically in Figure 5.1, have been analysed in this Section. The first analysed load case employs the Silenka GFRP constituent properties in the HFGMC model, whereas the T300/914 properties have been used in the second load case. The FE analyses of both load cases have been performed on the same FE model with the earlier defined composite layup. Only the material model and the imposed load have been varied as to account for the different elasticity and strength properties of the two composites.

Magnitudes of the imposed forces in the two load cases have been defined as to induce failure initiation in a relatively large part of the composite panel, as predicted by the ply-level failure criteria. The loading has been applied in the explicit analysis by gradually increasing magnitudes as to minimise the effects of the inertial forces. A total time of 0.009 s has been analysed whereas the load increases in the first 0.008 s and has been kept constant afterwards. HFGMC micromechanical computations have been performed only in the final 0.001 s, in which the stresses and strains in the FE model reached the equilibrium state. The computational times for the benchmark examples have been approximately 8 hours, highlighting the importance of the numerically efficient computations in the multiscale analyses.

Boundary conditions have been selected as to replicate experimental conditions used in the axial testing of similar stiffened panels, e.g. [Degenhardt et al., 2008]. Therefore, nodes at the half-length along the panel z axis have restricted degrees of freedom in the axial direction (z) and rotational degrees of freedom regarding the y direction, as shown in the left-hand side image in Figure 5.1. Additionally, nodes at the loaded ends of the panel have rigid body constraints, as to simulate the effect of the clamps used to load panels in experiments. All micromechanical computations in the multiscale analyses have been performed using the 30×30 HFGMC model with the square RUC morphology.

Loading on the Silenka GFRP reinforced panel has been simulated by the application

Table 5.2: Silenka GFRP strength properties and parameters for Puck's failure criterion after [Soden et al., 1998], [Puck et al., 2002].

X_t [MPa]	X_c [MPa]	Y_t [MPa]	Y_c [MPa]	S [MPa]
1280.	800.	40.	145.	73.
p_{12}^t [$-$]	p_{12}^c [$-$]	p_{23}^t [$-$]	p_{23}^c [$-$]	
0.3	0.25	0.22	0.22	

of tensile axial force of 96.8 kN (1100 N per node). The homogenised ply elasticity properties for the benchmark numerical model have been calculated by the HFGMC model using the Silenka GFRP constituent mechanical properties, as defined in Section 3.4. Constituent level properties have been specified in Table 3.2, whereas the HFGMC predicted composite elasticity properties have been summarised in Table 5.7.

Structural-scale validation of micromechanical and ply-level failure criteria has been performed using the ply-level Hashin, Puck, Tsai-Wu and Tsai-Hill failure theories. The ply-level failure theories have been programmed in the VUMAT subroutine as to enable application of the predicted failure indexes for initiation of the micromechanical computations. Composite ply strengths and parameters for the Puck criterion, needed for calculation of ply-level failure criteria, have been taken from [Soden et al., 1998], [Puck et al., 2002]. These properties are summarised in Table 5.2.
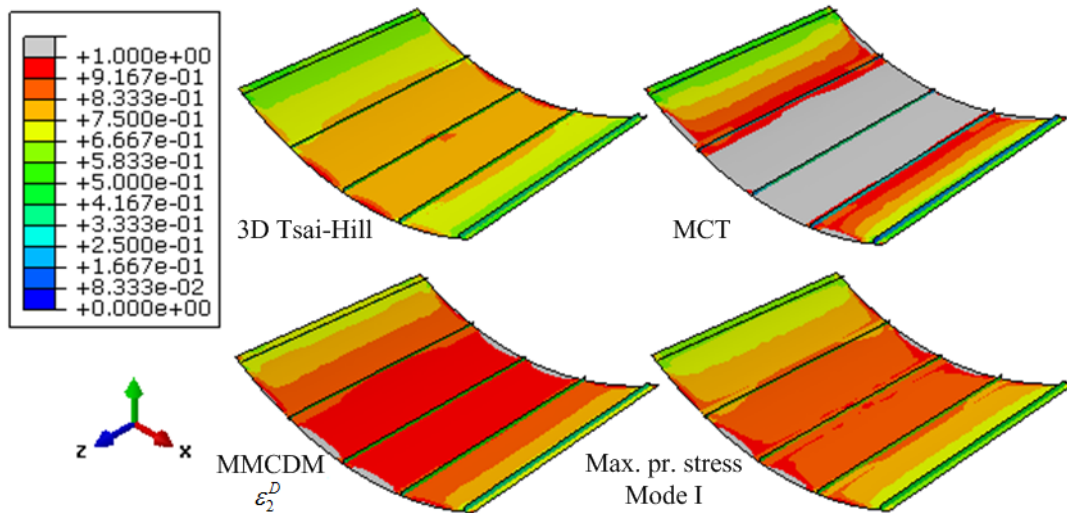
Figure 5.2: Maximal over-the-thickness values of micromechanical matrix failure criteria.

Figures 5.2 – 5.5 show results obtained by the two-scale analysis on the Silenka GFRP composite panel. As explained in Section 2.6, only maximal subcell values of micromechanical failure criteria within the unit cell have been stored as SDV and visualised in Figures 5.2 and 5.4. Figure 5.2 shows the maximal over-the-thickness SDVs related to micromechanical matrix failure criteria.

The conclusions obtained from the micromechanical failure analyses performed using the standalone HFGMC application in Section 3.5 have also been observed in the multiscale application. Therefore, the MCT criterion predicts damage initiation at the
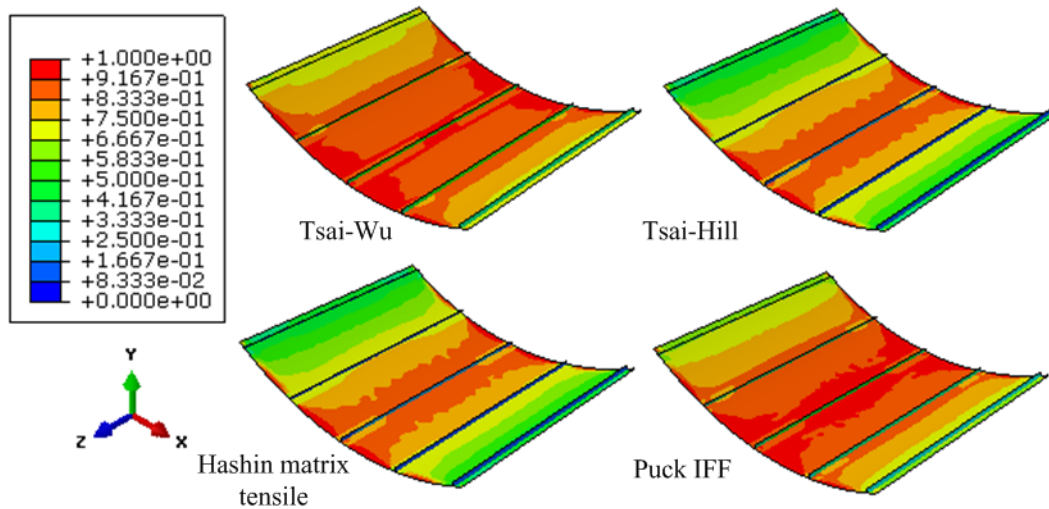
Figure 5.3: Maximal over-the-thickness values of ply-level failure criteria.

lowest loading, predicting microdamage mechanisms in the largest part of the composite structure, followed closely by the ε_2^D damage strain as the failure initiation criterion employed in the MMCDM theory.

As opposed to the MCT criterion, the 3D Tsai-Hill criterion as the least conservative micromechanical failure theory, predicts damage initiation in a significantly smaller part of the composite panel. The criterion tends to underestimate damage initiation compared even to the evaluated ply-level failure theories.

For the comparison with the micromechanical failure theories, Figure 5.3 shows
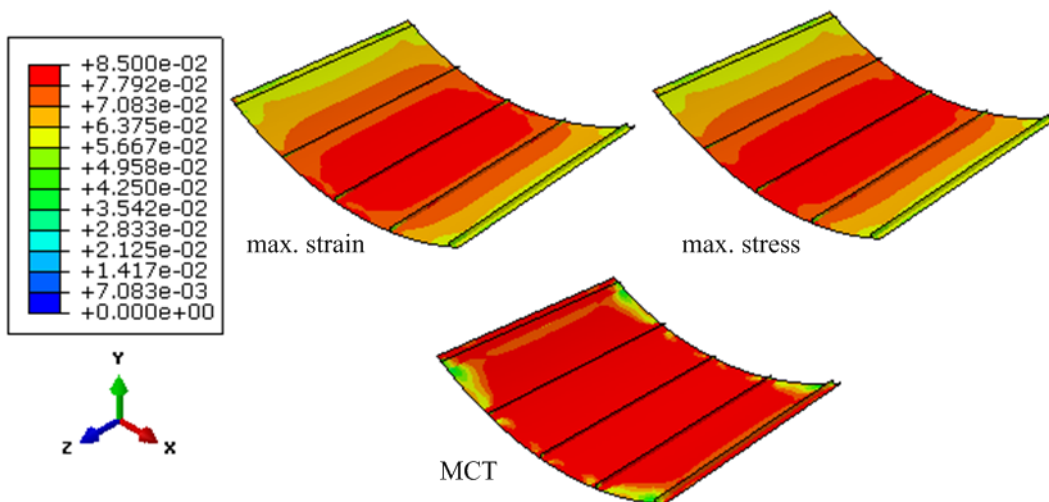
Figure 5.4: Maximal over-the-thickness values of micromechanical fibre failure criteria.
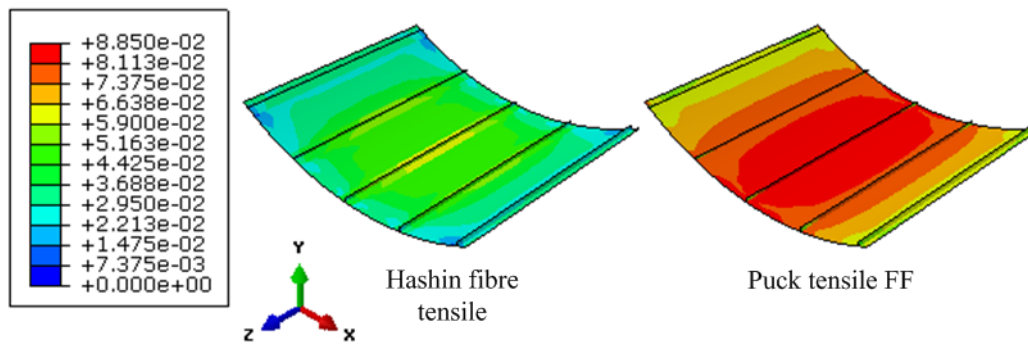
Figure 5.5: Maximal over-the-thickness values of ply-level fibre failure criteria.

the distribution of maximal over-the-thickness values of the ply-level failure theories associated with matrix failure. As shown, the micromechanical MCT and MMCDM damage initiation criteria (in Figure 5.2) indicate damage onset in larger parts of the composite panel compared to all evaluated ply-level failure criteria. Contours of the Mode I maximal principal stress criterion (in Figure 5.2) are similar to the ply-level Tsai-Wu, Tsai-Hill and Hashin matrix tensile criteria, but are less conservative compared to Puck's failure theory.

Figures 5.4 and 5.5 show differences between the micromechanical and ply-level fibre failure criteria. Fibre failure has not been initiated for the particular load case analysed in this benchmark example, as predicted by micromechanical as well as by the ply-level failure criteria. Contours of the Puck ply-level criterion and micro level maximal stress and maximal strain failure criteria agree very well. The MCT criterion predicts significantly higher fibre failure indexes compared to all other fibre failure criteria analysed in this work. Although the MCT fibre failure criterion in this load case is still far from the critical value (maximal value is approximately 0.15), fibre failure at an increased tensile loading would have been indicated by the MCT criterion at a significantly lower loading compared to other micromechanical as well as the ply-level failure criteria.

The magnitude of the tensile loading for the load case on the T300/914 composite panel has been increased to a nodal loading of 5700 N, resulting in a total force of 501.6 kN. The T300/914 constituent properties employed in this benchmark analysis have been provided in Table 4.3, whereas the strength properties employed in the prediction of the ply-level failure theories are shown in Table 5.3.

Table 5.3: T300/914 strength properties and parameters for Puck's failure criterion after [Lachaud et al., 1997], [Puck et al., 2002].

X_t [MPa]	X_c [MPa]	Y_t [MPa]	Y_c [MPa]	S [MPa]
1520.	1520.	60.	246.	95.
p_{12}^t [−]	p_{12}^c [−]	p_{23}^t [−]	p_{23}^c [−]	
0.3	0.35	0.27	0.23	

Figure 5.6 shows the contours of maximal over-the-thickness values of micromechanical failure criteria for the CFRP load case. As shown by the comparison with ply-level criteria in Figure 5.7, the evaluated micromechanical failure theories are in this load case more conservative compared to the ply-level failure theories. Good agreement of the MCT and the MMCDM ε_2^D damage strain has been observed, while the results of the 3D Tsai-Hill criterion match with the contours of the Mode I maximal principal stress criterion. The contours of the MMCDM ε_2^D damage strain are approximately equal to the MCT results. Therefore, contours of the ε_1^D are shown in Figure 5.6. In contrast to the Silenka GFRP load case, microdamage onset has been predicted in the integration points located on the stringer reinforcements by all evaluated micromechanical failure theories.
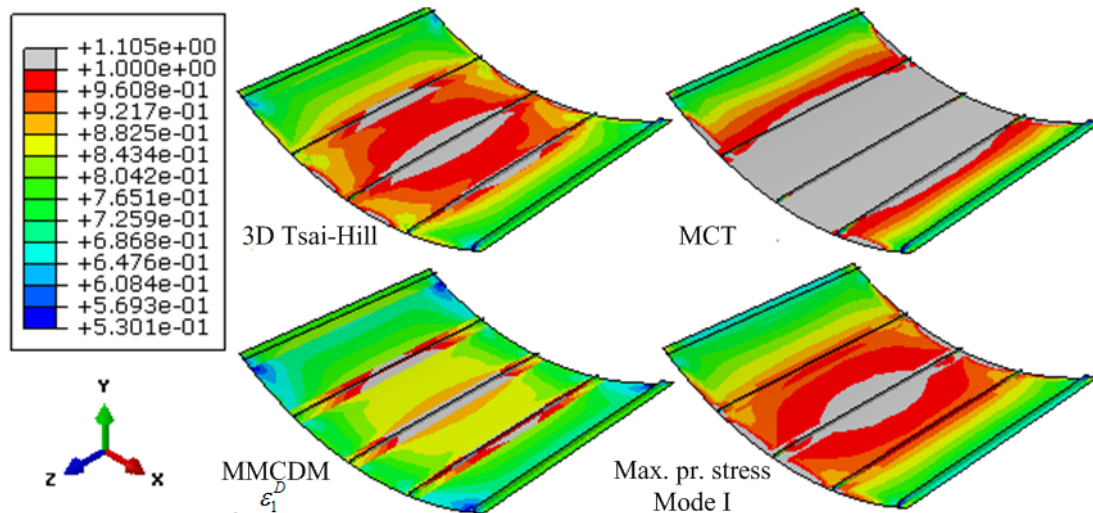
Figure 5.6: Maximal over-the-thickness values of micromechanical failure criteria, CFRP load case.

Figure 5.7 shows the relevant Puck IFF and Hashin matrix tensile criteria. The Tsai-Wu and Tsai-Hill criteria predict results similar to the Hashin's criterion and are

therefore not shown in Figure 5.7. Fibre failure has also not been initiated in this load case, which is predicted by the ply-level as well as by the micromechanical failure criteria. The MCT fibre failure criterion indicates the highest values (peak value is 0.84) whereas maximal values of the rest of ply-level and the micromechanical fibre failure criteria are approximately 0.5.
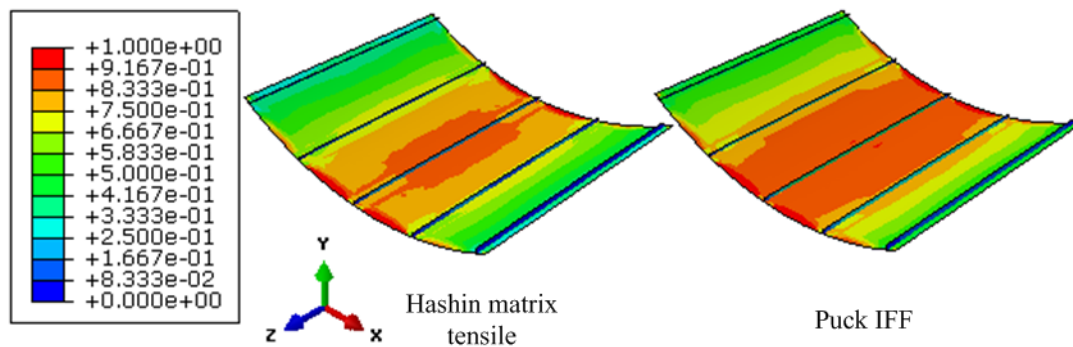
Figure 5.7: Maximal over-the-thickness values of Hashin and Puck ply-level matrix failure criteria, CFRP load case.

The evaluation of micromechanical matrix failure criteria revealed that the MCT and MMCDM matrix damage initiation criteria agree very well. The MCT criterion is the most conservative of the evaluated failure theories, particularly for prediction of fibre failure.

The 3D Tsai-Hill criterion indicates failure initiation at significantly higher stress values. The results for the 3D Tsai-Hill criterion agree very well with homogenised failure criteria while the MCT and MMCDM damage strains indicate failure initiation at lower stress states compared to the ply-level failure criteria. Comparison of the micromechanical maximal stress and maximal strain failure criteria shows good agreement with ply-level fibre failure theories while the MCT fibre failure criterion indicates higher values of failure indexes.

Different conclusions have been obtained for the GFRP and the CFRP load case indicating that there is no straightforward conclusion on which ply-level failure criterion should be used in the adaptive multiscaling approach. The choice depends on the particular composite material and application.

5.3   Numerical bird strike modelling technique in Abaqus/Explicit

A short overview of the employed numerical birdstrike damage prediction approach has been presented in this Section. Birdstrikes belong to the group of soft body impacts as the extreme stresses, generated in the impacting material, greatly exceed the strength of the impacting material leading to a fluid-like behaviour of the impactor. Consequently, several numerical obstacles have to be appropriately accounted for in the soft body impact simulation as to obtain a reliable prediction of the induced damage in the impacted structure. Modelling of the extreme deformations of the bird material during impact and the load transfer on the impacted structure are two major difficulties in the numerical soft body impact modelling approaches.

The impacting forces are governed by the impactor material constitutive model. Equation of state (EOS) material models have been employed in the numerical bird impactor replacement models. Only the most relevant features of the numerical soft body impact modelling, which have been implemented in the impact analyses in this Chapter, have been presented in this Section. The Abaqus built-in Mie-Grüneisen EOS has been used for the impact analyses in this Thesis. The Mie-Grüneisen equation (also known as $Us - Up$ EOS), describes a linear relationship between the shock and particle velocities as

$$U_\mathrm{S} = c_0 + sU_\mathrm{P}, \tag{5.1}$$

where c_0 is the speed of sound in the material, s is a material constant, while U_S and U_P are the shock and particle velocities, respectively. The final form of pressure to density relation has been determined by

$$p = \frac{\rho_0 c_0^2 \eta}{(1 - s\eta)^2} \left(1 - \frac{\Gamma_0 \eta}{2}\right) + \Gamma_0 \rho_0 U_m, \tag{5.2}$$

where $\eta = 1 - \rho_0/\rho$ is the nominal volumetric compressive strain, Γ_0 is a material constant and U_m is the internal energy per unit mass. In order to define Mie-Grüneisen EOS material in Abaqus, four material properties need to be specified - ρ_0, c_0 , Γ_0 and s. The

EOS parameters employed in the soft body impact analyses in this Thesis have been provided in Table 5.4.

Table 5.4: Mie-Grüneisen EOS parameters, after [Chizari et al., 2009].

ρ_0 [kg/m^3]	c_0 [m/s]	Γ_0 [-]	s [-]
1010.	1480.	0.	0.

Validation of the EOS bird material model has been performed by comparing Hugoniot and stagnation pressures developed in an impact on a rigid target at the velocity of 116 m/s normal to the plate. The time-dependent pressure values obtained with the Mie-Grüneisen EOS have been shown in Figure 5.8. The stages denoted by A, B and C in Figure 5.8 indicate the three distinct pressure stages in the soft body impact. These phases have been also observed in the experimental gas gun experiments. A denotes the short initial stage at which extreme pressure values have been generated, where the peak pressure value is known as Hugoniot pressure. B is the pressure release stage while C is the stagnation pressure stage, characterised by significantly lower and constant pressure values.
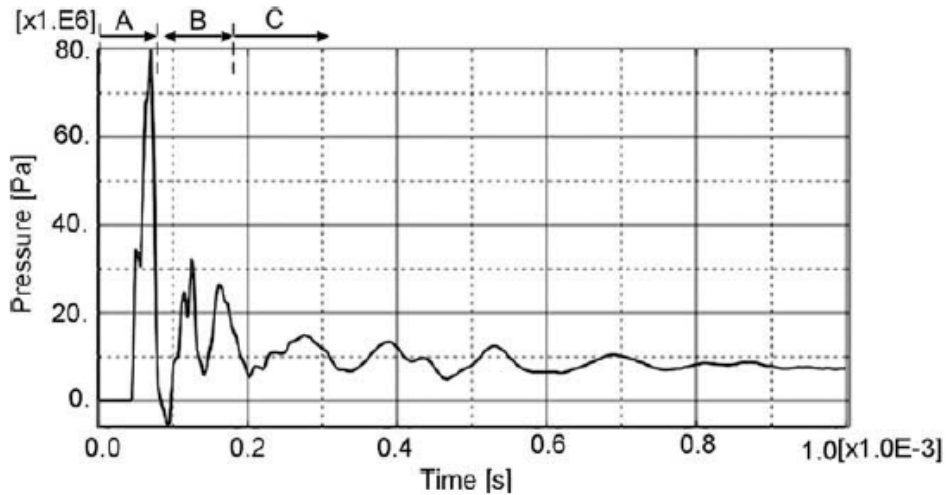
Figure 5.8: Pressure time history predicted by the Mie-Grüneisen EOS and properties defined in Table 5.4.

The theoretical value of Hugoniot pressure at the impact velocity of 116 m/s is 93.6 MPa. Theoretical values of stagnation pressures for the 116 m/s impact reach the value of 6.3 MPa. As illustrated in Figure 5.8, the numerical bird model obtains

acceptable values of Hugoniot pressure (approximately 80 MPa) and stagnation pressure (approximately 7 MPa), while the pressure time history resembles results of the EOS with porosity effects included, as shown in [Ivančević and Smojver, 2011]. Deformation of the soft body impactor in the 116 m/s impact on a rigid plate is shown in Figure 5.9.
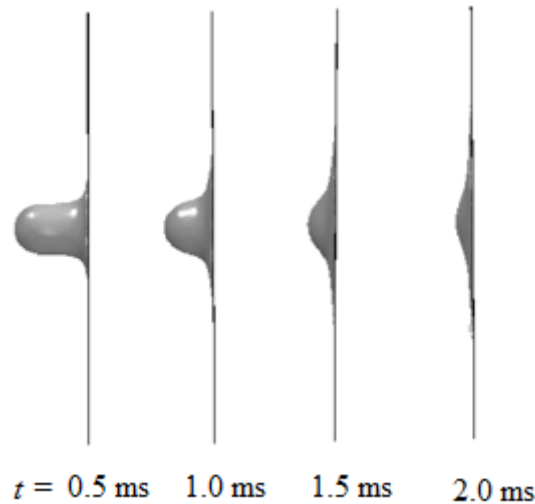
Figure 5.9: Deformation of the Eulerian impactor at 116 m/s on a rigid plate during 2 ms with a time step of 0.5 ms.

The numerical soft body impact analyses (as shown e.g. in Figure 5.9) have in this Thesis been performed by employing the Coupled Eulerian Lagrangian (CEL) approach. Application of the CEL method in the bird strike simulations allows the impactor to be modelled as Eulerian material while the impacted structure is represented by standard Lagrangian finite elements. Utilisation of this technique avoids numerical difficulties associated with Lagrangian bird models as there are no restrictions on the Eulerian material deformation. Benefits of the CEL in the numerical investigation of soft body impact have been thoroughly described in e.g. [Ivančević and Smojver, 2011].

The Eulerian finite element model in CEL analyses is represented by a stationary cube containing multi-material EC3D8R volume elements, which may be completely or partially occupied by the Eulerian material, after [Abaqus, 2010]. The Eulerian material is able to move through the stationary mesh and interact with the Lagrangian structure. The ratio by which the EC3D8R elements are occupied with bird material is the Eulerian Volume Fraction (EVF). Entirely filled elements have the EVF equal to one, whereas completely void elements have EVF values equal to zero. The EVF parameters have

been employed in post-processing as to visualise the Eulerian material.

There are two significant restrictions on the dimensions and mesh size of the Eulerian model in CEL analyses. The loss of Eulerian material through the outer boundaries of the Eulerian mesh may lead to a decrease in kinetic energy and could, under some conditions, lead to numerical instabilities. As to avoid these problems, the size of the volume enclosing Eulerian elements must be sufficiently large, as shown in Figure 5.11. The second restriction is related to the mesh size of the Eulerian finite element model. A very fine mesh of the Eulerian grid is necessary to efficiently capture the contact between Eulerian material surfaces and Lagrangian elements in order to prevent physically unacceptable penetration of the bird material through the target finite element mesh.

5.4 Soft body impact - numerical model and experimental results

Parameters of the numerical soft body impact analyses have been defined as to simulate the available experimental results. Experimental data of low-velocity impact on composite structures is widely available in the literature. On the other hand, experimental impact testing in the medium velocity range, which is of interest for bird strike simulations, is rather limited and only a small number of references provide results of such impacts on composite structures. The structural response caused by a soft body impact is specific as the impacting forces have been spread over a wide area. Therefore, gas gun experimental set-up and the results provided in [Hou and Ruiz, 2007] have been employed as references for the numerical multiscale damage prediction methodology in this Thesis.

The experimental work in [Hou and Ruiz, 2007] investigates the impact behaviour of unidirectional and woven composite plates impacted by soft body projectiles in the velocity range from 200 to 330 m/s. Unfortunately, the published results provide only visual observation and description of the induced damage in the composite plates. Therefore, emphasis in the validation of the multiscale methodology has been set on the comparison with the ply-level composite failure criteria and the Abaqus built-in progressive damage model for composite materials as described in Sections 3.2 and 3.3. The HFGMC micromechanical model employed in this Thesis is applicable only for unidirectional composites. As reported in [Hou and Ruiz, 2007], the unidirectional
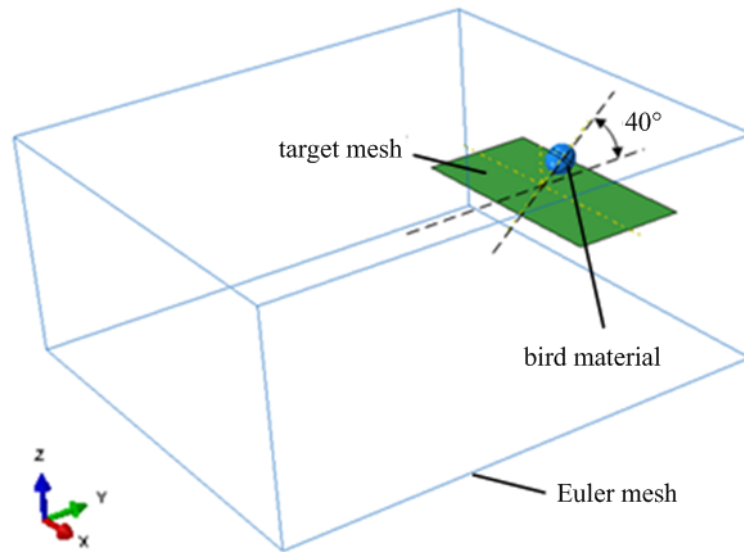
Figure 5.10: CEL numerical model for impact simulations.

composite plates had lower threshold velocities compared to the woven composite plates.

The experimental results provided in [Hou and Ruiz, 2007] have been also employed in the preceding research as to validate the bird strike damage prediction methodology. Results of these analyses have been published in e.g. [Smojver and Ivančević, 2011] and [Ivančević and Smojver, 2011]. The FE model employed in these analyses has also been used in the multiscale analyses in this Thesis. The composite plate employed for validation of the methodology in this Thesis is 3 mm thick and consists of 21 CFRP T300/914 layers with a $[(0/90)_5\bar{0}]_S$ layup. Dimensions of the composite plate are 216 x 102 mm, with one end clamped on the shorter edge with a 25 mm wide clamp.

The mechanical properties of the CFRP T300/914 unidirectional plies have not been specified in [Hou and Ruiz, 2007]. Therefore, these properties have been taken from [Lachaud et al., 1997] and are provided in Table 5.5. These properties have been employed in the validation of the birdstrike damage prediction methodology in the preceding research, as previously explained.

The initial velocity vector in the gas gun experiment is deflected by 40° with respect to the plate plane. The diameter of the gelatine projectile has been defined as 25 mm while the mass of the impactor is 10 g. The impactor has been modelled by the CEL formulation, as explained in Section 5.3. Figure 5.10 shows the FE numerical model and the initial position of the Eulerian impactor with regard to the plate and the volume
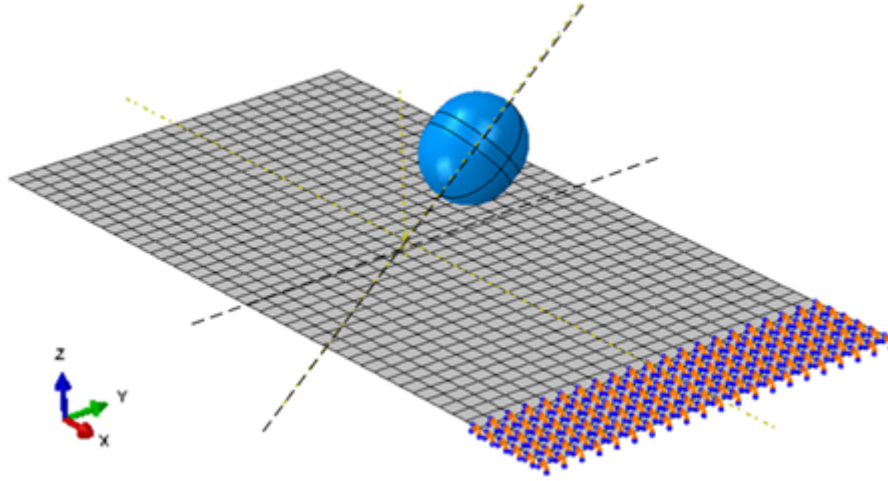
Figure 5.11: FE model - initial and boundary conditions.

Table 5.5: Mechanical properties of CFRP T300/914, after [Lachaud et al., 1997], with p parameters for Puck failure criterion [Puck et al., 2002].

$\rho\,[\mathrm{kg/m^3}]$	$E_1[\mathrm{GPa}]$	$E_2\,[\mathrm{GPa}]$	$G_{12}\,[\mathrm{GPa}]$	$\nu_{12}\,[\text{-}]$
1600.	138.	9.	4.8	0.32
$X_t\,[\mathrm{MPa}]$	$X_c\,[\mathrm{MPa}]$	$Y_t\,[\mathrm{MPa}]$	$Y_c\,[\mathrm{MPa}]$	$S\,[\mathrm{MPa}]$
1520.	1520.	60.	246.	95.
$p_{12}^t\,[-]$	$p_{12}^c\,[-]$	$p_{23}^t\,[-]$	$p_{23}^c\,[-]$	
0.3	0.35	0.27	0.23	

containing the Eulerian finite elements. The size of the cube containing 487,920 Eulerian elements is 0.45 x 0.4 x 0.2 m. The dimensions of the Eulerian model have been selected based on the limitations explained in Section 5.3.

The composite plate finite element model with initial and boundary conditions has been shown in Figure 5.11. The finite element composite plate model consists of 860 conventional shell elements while the bird model has been modelled by the CEL formulation. As the exact shape of the substitute bird has not been possible to determine, it has been approximated to resemble the conventional shape used in the numerical bird strike simulation as a cylinder with hemispherical ends.

The described numerical model has been employed in all soft body impact analyses performed in this Thesis, whereas parameters of the model have been varied as to simulate different impact cases. Therefore, in addition to the impact on the T300/914

plates, multiscale analyses have also been performed on Silenka GFRP plates as to enable application of the available in-situ properties and parameters of the damage model for this material. The same cross-ply layup has been assumed in these analyses, whereas the impacting velocities have been reduced to 100 m/s as to account for the differences in the mechanical properties of CFRP and GFRP composite plies.

5.5 Validation of micromechanical failure criteria in impact analyses

The multiscale method has been employed in this Section in dynamic impact simulations. Results of the evaluation in this Section have been published in [Ivančević and Smojver, 2014], as part of the methodology development phase in this Thesis. Similarly to the approach employed in Section 5.2, micromechanical damage initiation theories have been evaluated in this Section against the ply-level failure theories defined in Section 3.2.

Table 5.6: T300/914 constituent properties, after [Soden et al., 1998] and [Mayes and Hansen, 2004].

T300 fibre properties				
E [GPa]	ν [-]	X_ε^T [-]	X_ε^C [-]	S_{12f} [MPa]
230.	0.3	0.01086	0.00869	105.
914 matrix properties				
E [GPa]	ν [-]	$X_\varepsilon^T = Y_\varepsilon^T = Z_\varepsilon^T$ [-]	$X_\varepsilon^C = Y_\varepsilon^C = Z_\varepsilon^C$ [-]	$S_\varepsilon = Q_\varepsilon = R_\varepsilon$ [-]
4.	0.35	0.01875	0.03750	0.04725
T300/914 homogenised properties				
E_1 [GPa]	E_2 [GPa]	G_{12} [GPa]	ν_{12} [-]	ν_{23} [-]
138.473	20.344	5.869	0.314	0.257

As the purpose of the analyses in this Section has been the comparison of micromechanical damage initiation theories, degradation of mechanical properties has been neglected throughout the simulations. Therefore, the micromechanical analyses have been performed employing the constituent properties defined in [Soden et al., 1998], which are summarised in Table 5.6. Results of the analyses in which the in-situ properties with applied micromechanical progressive damage models have been employed are presented in Section 5.6.
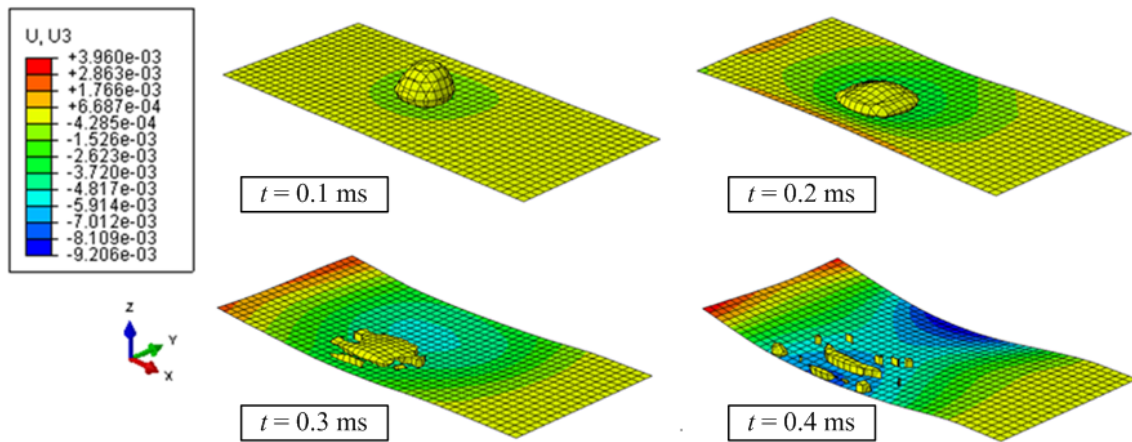
Figure 5.12: Visualisation of the impact event. The contours show displacements in the z direction [m].

The initial conditions for the presented analysis have been defined by 200 m/s velocity of the bird material, as for this loading condition no significant damage has been observed in the gas gun experiments in [Hou and Ruiz, 2007]. As discussed in Section 5.4, the impact point is located at the centre of the unclamped part of the composite plate. A total time of 1.2 ms has been simulated in this analysis.

The impact event and bird material deformation have been shown in Figure 5.12. The contours visualise the displacements in the z direction, which is perpendicular to the composite plate. The visualisation of the EOS material motion through the Eulerian finite element mesh in Figure 5.12 has been achieved using the Eulerian Volume Fractions equal to 0.6, as explained in Section 5.3. The results demonstrate the ability of the numerical bird model to replicate the very high deformations of the soft body impactor.

As demonstrated by the comparison of failure initiation criteria in the tensile loading case in Section 5.2, the Puck's failure initiation criterion for matrix damage (IFF failure) predicts damage onset in a similar part of the FE model in which the micromechanical failure theories, calculated by HFGMC, indicate microdamage initiation. Therefore, in order to enhance the computational aspects of the developed methodology, results of the macroscopic Puck's criterion have been employed as to initiate micromechanical computations.

Puck's criterion has been selected for the purpose of initiation of micromechanical calculations due to outstanding performance in the World Wide Failure Exercise. Consequently, the computationally intensive micromechanical calculations have been

omitted for parts of the macroscopic finite element model which are not loaded and, therefore, no damage processes are expected in the relevant FE integration points. The micromechanical computations in the results presented in this Section have been initiated for integration points in which the macroscopic stress state resulted in FF or IFF criterion values above 0.1. This conservative value of the Puck failure model has been selected as the applied loading rate is in the 200 m/s is very high, causing large discrepancies between the micromechanical failure theories and the Puck failure initiation theory.

The 40×40 single-fibre HFGMC model has been employed in the analyses in this Section. The fibre volume fraction of the evaluated composite material is 60%. The orthotropic mechanical properties of the homogenised composite ply have been calculated by the HFGMC model. The constituent properties employed in this analysis have been provided in Table 5.6 with the homogenised composite properties of the T300/914 composite material, as calculated by the micromechanical model. Properties necessary for the calculation of the ply-level failure criteria have been taken from [Soden et al., 1998] and [Puck et al., 2002]. Table 5.5 summarises the ply-level strength properties employed for the calculation of the ply-level failure criteria.
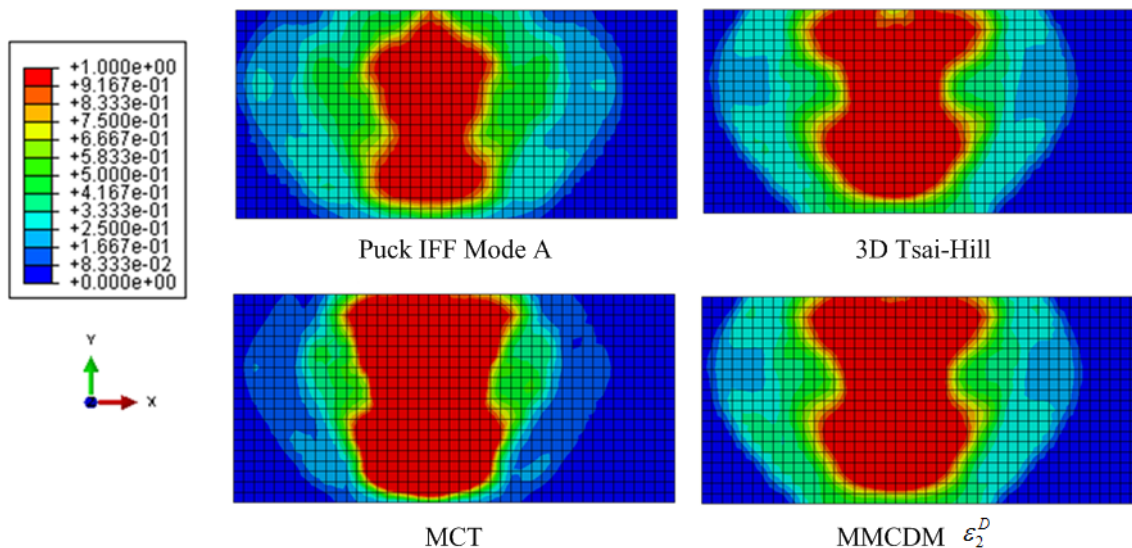
Figure 5.13: Comparison of the Puck IFF Mode A criterion and the micromechanical matrix failure theories (maximal over-the-thickness values are shown at $t = 0.1$ ms).

Comparison of the micromechanical failure criteria and ply-level failure criteria has been done using the Puck failure model. As explained in Section 2.6, the SDVs associated with micromechanical failure theories visualise maximal values of the criteria within the

unit cell. Figure 5.13 shows comparison of the failure criteria related to matrix failure at $t = 0.1$ ms. The clamped end of the composite plate is located on the right side of the images in Figures 5.13 - 5.15. Although only approximately half of the impacting material has actually impacted the plate (shown by the upper left image in Figure 5.12), all evaluated failure criteria predict initiation of damage processes in a very large part of the composite plate.
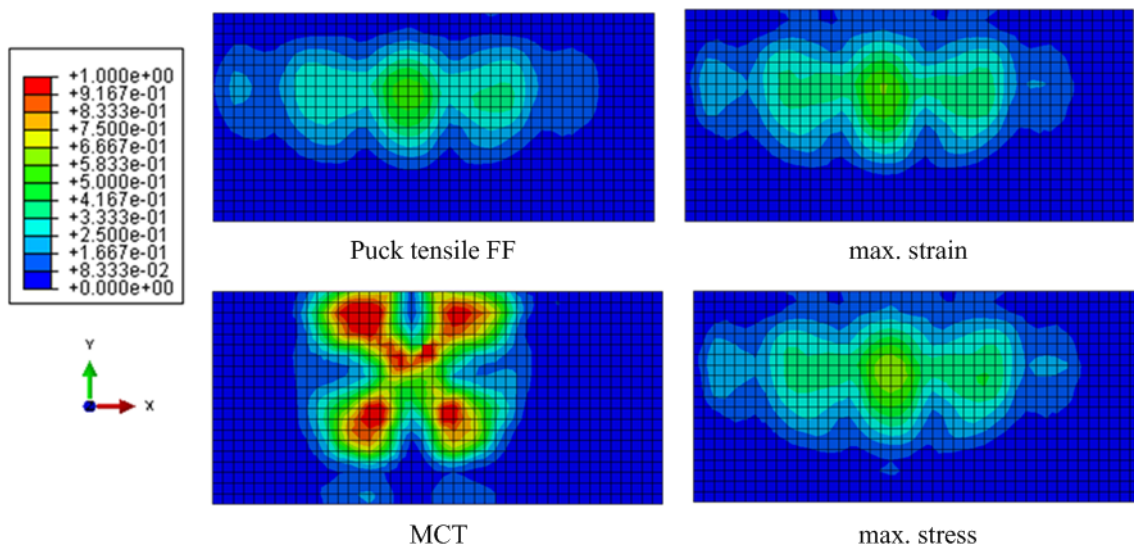
Figure 5.14: Comparison of the Puck tensile fibre failure and the micromechanical fibre failure theories (maximal over-the-thickness values are shown at $t = 0.1$ ms).

The shapes and sizes of the failed part of the composite plate, in which failure criteria predict failure initiation, agree very well for the evaluated micromechanical matrix failure theories. However, the MCT criterion predicts damage initiation in the largest area of the impacted composite plate. The predicted portions of the plate in which micromechanical failure criteria indicate damage processes at the considered time step ($t = 0.1$ ms) are slightly larger compared to the Puck's Mode A criterion.

At $t = 0.1$ ms, fibre failure has not been predicted by the evaluated failure criteria. The comparison of criteria associated with fibre failure is shown in Figure 5.14. As illustrated, the micromechanical maximal stress and maximal strain values contours agree very well to each other and to the ply-level Puck's fibre tensile failure initiation contours. Corresponding to the matrix failure results in Figure 5.13, the MCT criterion indicates the highest values of the failure initiation criteria, which at the considered time step reaches the maximal value of 0.96.
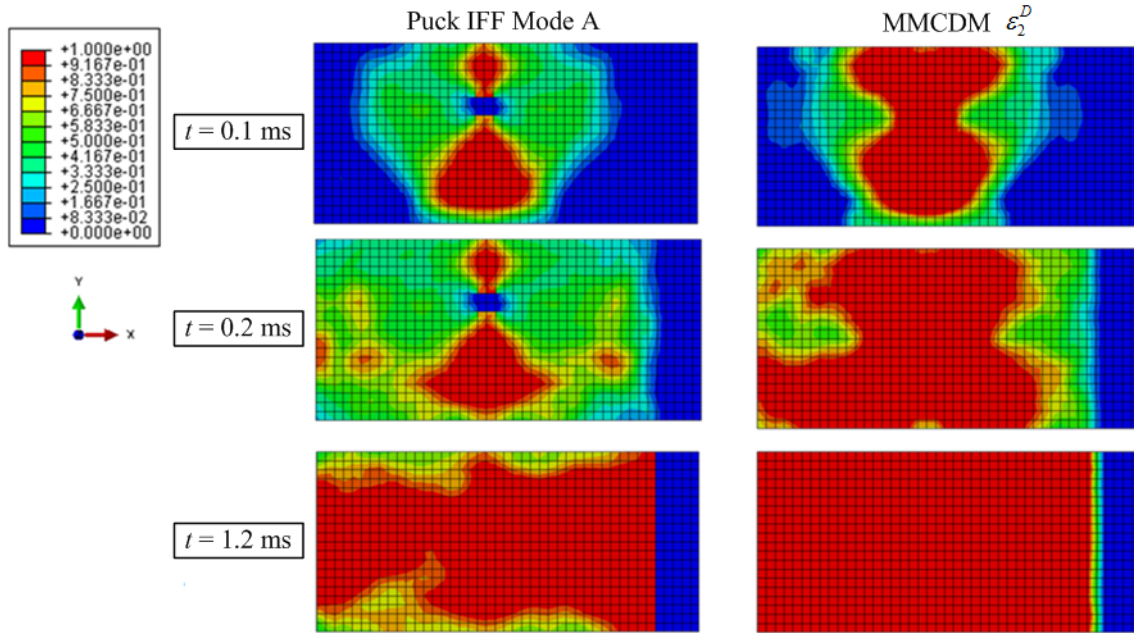
Figure 5.15: Evolution of Puck's Mode A IFF and the MMCDM ε_2^D damage strain.

Figure 5.15 shows the comparison of the time-dependent evolution of Puck's IFF Mode A criterion and the ε_2^D damage strains. The results in Figure 5.15 have been calculated at the integration points located on the composite plate side at which the soft body impacts the plate. As illustrated, the differences between the Puck's Mode A criterion and the ε_2^D damage strain increase with the progression of the analysis. The high values of Puck's failure criterion have been caused by the structural motion of the plate at later time steps. As shown in this analysis, the micromechanical as well as the ply-level failure criteria indicate significant matrix damage in the composite plate.

5.6   Multiscale impact damage analyses

The micromechanical progressive damage theories, introduced in Sections 4.2 and 4.3, have been applied in this Chapter in numerical high-velocity impact damage modelling. As explained in Section 5.4, the numerical impact prediction analyses have been performed as to replicate the experimental gas gun experiments in [Hou and Ruiz, 2007]. Therefore, the multiscale damage prediction methodology has been applied in the simulation of the 200 and 280 m/s soft body impacts on the T300/914 composite plate.

The main obstacle in the application of micromechanical progressive damage theories

is the determination of in-situ properties of the matrix which are necessary for accurate simulation of the constitutive behaviour and the damage mechanisms of the homogenised composite material, as discussed in Chapter 4. Consequently, in addition to the impact on the T300/914 CFRP plate, multiscale impact analyses have been also performed on the Silenka GFRP plates as to enable application of damage model parameters which are defined in [Bednarcyk et al., 2010] for the MMCDM model and [Pineda, 2012] for the Crack Band model. As for this impact case no experimental evidence exist in the literature, validation of the results obtained using the multiscale damage models has been performed only by comparison with the Abaqus damage model and ply-level failure criteria.

The initial motive in the methodology development has been to compare the results obtained using the MMCDM and the Crack Band damage model. However, this task has been performed only in a limited way as the damage progression method based on the Crack Band model has shown to be computationally over-expensive for the performed multiscale analyses. Consequently only limited results, obtained by application of the Crack Band damage model in the initial impact on the Silenka GFRP plate, have been shown in this Section.

The soft body impact analyses in this Chapter have been performed using the same finite element model, as explained in Section 5.4. As to model the different composite materials, parameters of HFGMC model have been adjusted in the various analyses. Additionally, the transverse shear stiffness parameter, which is required for shell element sections when used in combination with UMAT/VUMAT subroutines in Abaqus, has to be modified in the input file based on the homogenised composite mechanical properties.

All micromechanical computations in the multiscale analyses in this Section have been performed using the 30×30 unit cell model with the square unit cell morphology. Results obtained with this model presented a compromise between computational cost and fidelity of the micromechanical solution, as discussed previously. Accurate solution of the HFGMC model as a constitutive model has been ensured by reduction of the stable time increment of the explicit finite element analyses as to keep the applied strain increments below the required stability limit predicted by the standalone HFGMC application. As to provide insight into the obtained computation times, the linear analysis performed in Section 5.5 for simulation of 1.2 ms took approximately 6 hours with a stable time increment of $6. \times 10^{-7}$ s. Manual control of the stable time increment

of the explicit analysis has been necessary since the explicit FE solver is not directly linked to the micromechanical computations and only the homogenised RUC output is returned to the VUMAT subroutine, as explained in Section 2.6.

Case I: Impact on Silenka GFRP plate at 100 m/s, MMCDM damage model

Parameters of the numerical model simulating the impact on the Silenka GFRP plate have been modified as to account for the lower mechanical properties of the GFRP compared to the CFRP composite. Consequently, a lower magnitude of the initial velocity vector has been applied compared to the gas gun experiments which have been performed above 200 m/s. Therefore, an initial velocity vector with a magnitude of 100 m/s has been employed in these simulations.

Table 5.7: Homogenised properties of Silenka GFRP composite with parameters for the Abaqus damage model, after [Soden et al., 1998], [Lapczyk and Hurtado, 2007] and [Lopes et al., 2009].

E_1 [GPa]	E_2 [GPa]	ν_{12} [-]	G_{12} [GPa]	G_{13} [GPa]
45.911	16.332	0.249	5.043	5.043
G_{23} [GPa]	X_t [MPa]	X_c [MPa]	Y_t [MPa]	Y_c [MPa]
3.591	1280.	800.	40.	145.
G_{1t} [J/m^2]	G_{1c} [J/m^2]	G_{2t} [J/m^2]	G_{2c} [J/m^2]	
85000.	106300.	1000.	1000.	

Mechanical properties and parameters for the MMCDM model, employed in the multiscale analyses, have been previously provided in Tables 4.1 and 4.2, after [Bednarcyk et al., 2010]. The homogenised mechanical properties which have been employed in the Abaqus damage model analysis have been predicted by the HFGMC model and are provided in Table 5.7. In addition to the equivalent elasticity properties, Table 5.7 contains strength properties and damage model parameters for GFRP material which have been employed in the referent damage models. The strengths in Table 5.7 have been taken from [Soden et al., 1998], while damage energies for GFRP composites, as input parameters of the Abaqus damage model, have been taken from [Lapczyk and Hurtado, 2007] (matrix fracture energies) and [Lopes et al., 2009] (fibre fracture energies). The p parameters of the Puck criterion have been assumed to be equal to the values provided
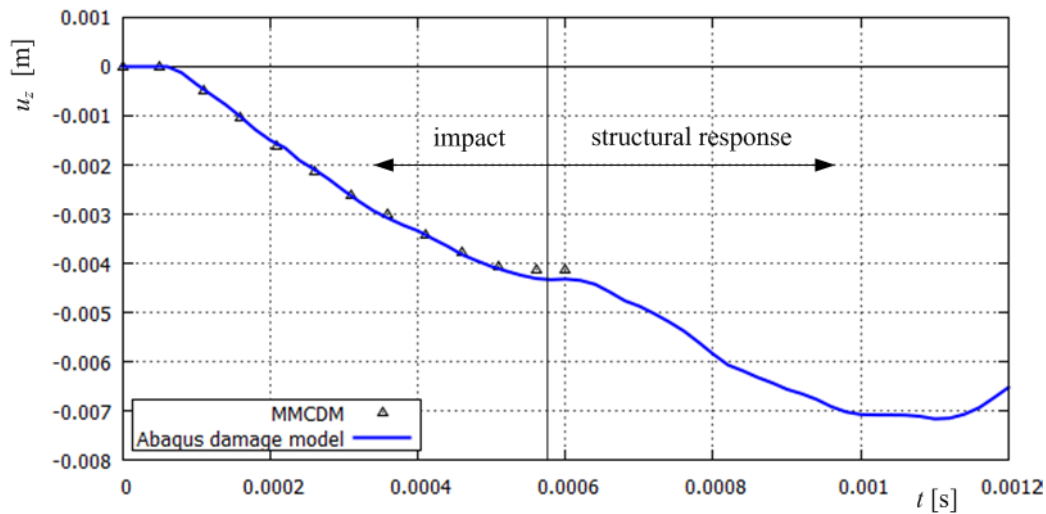
Figure 5.16: Time history of displacement of a node at the impact location - comparison of MMCDM model and Abaqus progressive damage model.

in Table 5.2.

Figure 5.16 shows comparison of the displacement time histories of a node located at the middle of the impact location, as calculated by the referent Abaqus damage model and by the multiscale analysis using the MMCDM micromechanical damage model. A total time of 1.2 ms has been analysed in the simulation using the Abaqus damage model. As shown in Figure 5.16, time-dependent nodal deflection shows an inflection point at approximately 0.6 ms. The physical interpretation of the inflection point coincides with the switch between the deflection caused by the soft body impact and the subsequent flexural structural motion of the plate. After 0.6 ms the maximal nodal deflection, as predicted by the Abaqus damage model, increases due to the structural response of the plate whereas damage in the plate is approximately constant. Damage increases only at the clamped edge of the plate due to the plate's structural response and the applied boundary conditions. The problem of isolating damage caused by the soft body impact from the damage caused by the boundary conditions at the clamped end has also been encountered in the referent experiments, as discussed in [Hou and Ruiz, 2007].

Consequently, only the first 0.6 ms have been analysed in the multiscale analyses as to keep the computation times at an acceptable level. The relative difference between the deflection predicted by the MMCDM and the referent Abaqus damage analysis at 0.6 ms is approximately 4.4%, as shown in Figure 5.16. The computation time of the multiscale analysis with the defined parameters has been approximately 24 hours on a

desktop workstation. The time increment of the explicit analysis has in these analyses been reduced to $5.\times10^{-8}$ s as to ensure the accuracy of the micromechanical analysis, as discussed in Chapter 2. The multiscale analyses have been initiated in the material points in which Puck's failure theory indicates failure indexes of 0.1, as explained in Section 5.5.
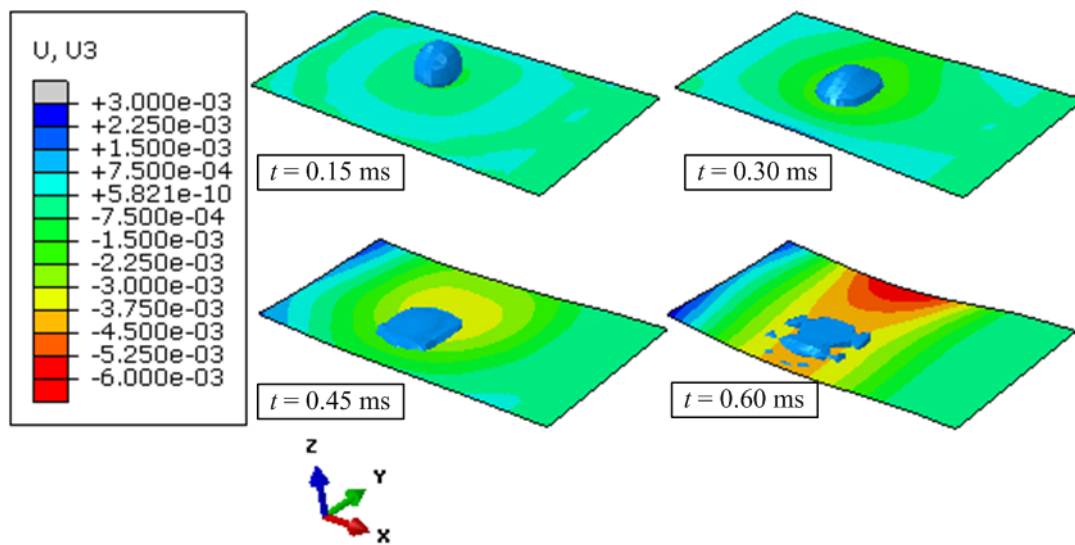
Figure 5.17: Visualisation of the 100 m/s impact event on the Silenka GFRP plate modelled with the MMCDM damage model, plate displacements in the z direction in [mm].

Figures 5.17 – 5.23 show results of the soft body impact calculated by the multiscale methodology. The clamped end of the composite plate is located on the right side in these figures. The impact event and bird material deformation for these impact conditions are shown in 5.17. The contours in Figure 5.17 visualise the displacements in the z direction, which is perpendicular to the composite plate. Results of the micromechanical failure model have been compared with results of the ply-based Puck's failure model, as this failure theory has showed excellent results in the World Wide Failure Exercise (WWFE) [Hinton et al., 2002].

As explained in Chapter 2.6, the SDVs associated with micromechanical failure criteria and damage variables show the maximal values within the RUC associated to the relevant FE material point. Damage initiation in the MMCDM theory has been predicted by the damage strains, as defined in Section 4.2. The predominant mode of failure in the analysed impact case is matrix damage initiated by the ε_2^D damage strain.

The images in Figure 5.18 show the evolution of the values of the ε_2^D damage strain
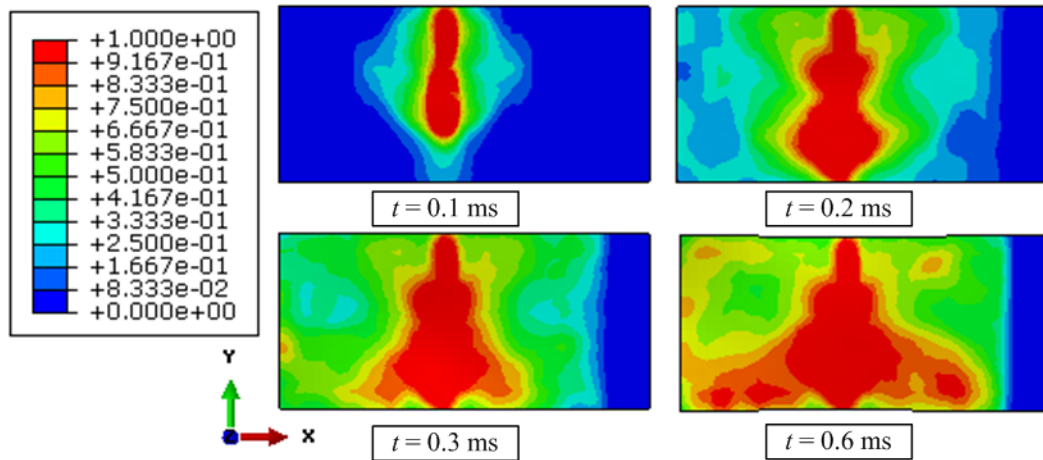
Figure 5.18: Evolution of ε_2^D damage strains in the material points at the impacted side of the composite plate.

criterion on the impacted side of the plate (referred in the following text as the "top ply"), whereas Figure 5.19 shows the evolution of damage strains on the opposite side of the impacted plate (referred as the "bottom ply" in the following text). As defined by the layup of the plate, both of these plies are aligned with the longer plate dimension ($0°$ plies).
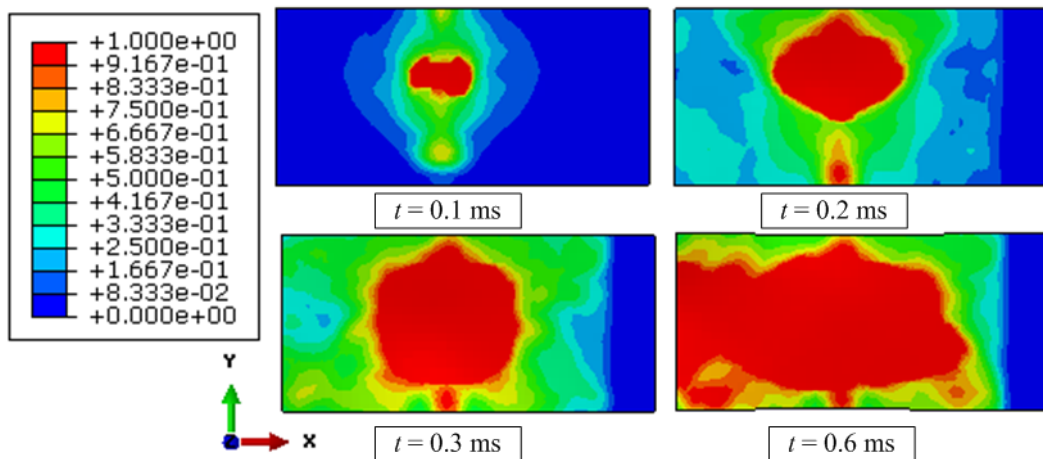
Figure 5.19: Evolution of ε_2^D damage strains in the material points located at the opposite of the impacted side of the composite plate.

As shown by the results in Figures 5.18 and 5.19, damage effects are more pronounced in the material points located at the bottom of the composite layup due to the lower damage initiation properties of the epoxy matrix in tensile loading conditions, as indicated

by the constituent properties of the Silenka GFRP material in Table 4.1.

Results of the analysis show that ε_2^D damage strain reached the highest value of the three damage strains defined in Equations 3.26 - 3.28 and predicts degradation of mechanical properties in a very large area of the composite plate. Matrix failure under ε_2^D is the primary mode of failure in this analysis while ε_1^D and ε_3^D reach lower values. Consequently, only the ε_2^D damage strains are shown in the results in this Section.
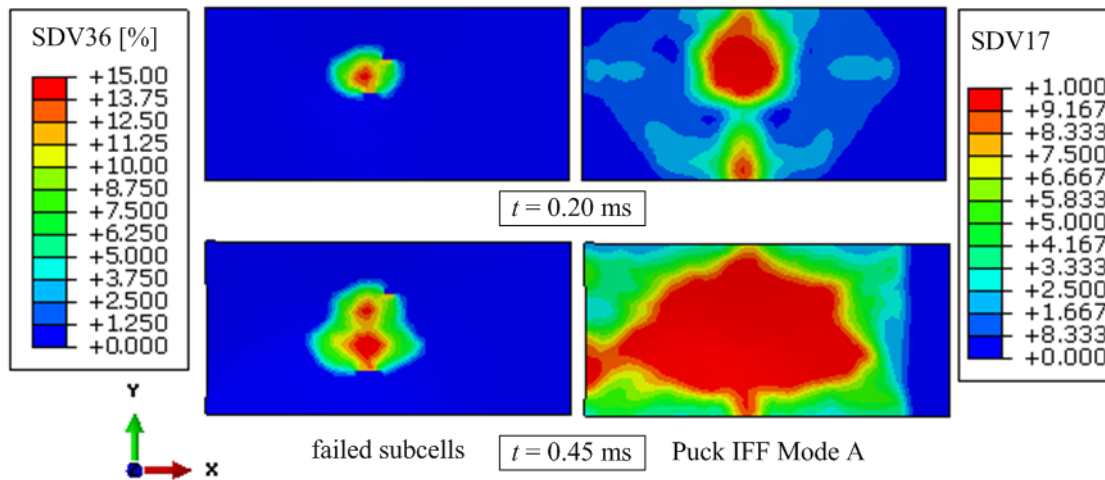
Figure 5.20: Comparison of fraction of failed matrix subcells (left-hand side images) with the Puck Mode A IFF criterion (right-hand side images) at 0.2 ms and 0.45 ms (bottom plies, 100 m/s impact on Silenka GFRP composite plate).

The results illustrated in Figure 5.20 refer to the composite plies oriented at 0° and located on the bottom side of the composite plate. The results show comparison of Puck's Mode A matrix failure criterion and the SDV visualising the number of failed subcells in the RUC, which are linked to the SDV controlling material point deletion from VUMAT.

Initially, material point failure (STATUS variable in Abaqus) has been predicted if the micromechanical model predicts transverse cracks by the critical fraction of failed matrix subcells (15%, as explained in Sections 4.4 and 4.5). As the composite material in these conditions still has considerable retained elasticity properties in the fibre direction (E_1), which contribute to the overall laminate stiffness despite the completely degraded E_2 or G_{12} components, the material point deletion approach resulted in too large displacements of the impacted plate compared to the Abaqus damage model.

Therefore, once this state has been predicted in the multiscale analyses, the state

of transverse matrix cracks has been assumed. Consequently, the HFGMC model has not been called for this particular material point in further increments. The constitutive behaviour of the material point has been governed by the very low properties which have been considered as elastic. Complete material point failure has been predicted if fibre failure occurs in the material point, which is in accordance with the material point failure approach employed in the Abaqus damage model. In order to remove an element from the analysis, this material point failure has to be predicted in all material points of the finite element.

The contours of the fractions of failed subcells agree well with the contours of the Puck inter-fibre failure criterion as shown in Figure 5.20. All material points in which failure of subcells occurs are located in the part of the composite plate in which the Puck Mode A criterion predicted initiation of inter-fibre failure.

The contours of the Mode A Puck failure criterion in Figure 5.20 closely agree with the contours of ε_2^D damage strains shown in Figure 5.18 and 5.19. This observation applies for top and bottom sides of the composite plate as shown in these Figures.
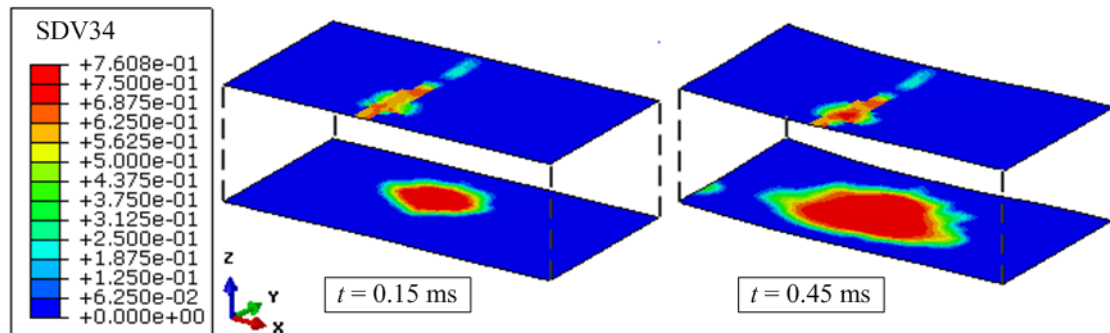
Figure 5.21: Comparison of D_2^T damage parameters at the top and bottom material points at 0.15 ms and 0.45 ms.

Contours of the damage parameters of the D_2^T damage variable in the top and bottom composite plies are shown in Figure 5.21. The damage parameter values do not have to reach 1 as to indicate subcell failure, as discussed in Section 4.2. The contours of the damage parameters in Figure 5.21 also resemble the results of the Mode A Puck criterion as shown in Figure 5.20.

Figure 5.22 shows contours of the matrix tensile damage variable calculated by the referent analysis performed with the Abaqus progressive damage model. Comparison of the sizes and shapes of the matrix damage predicted by the multiscale model in Figure
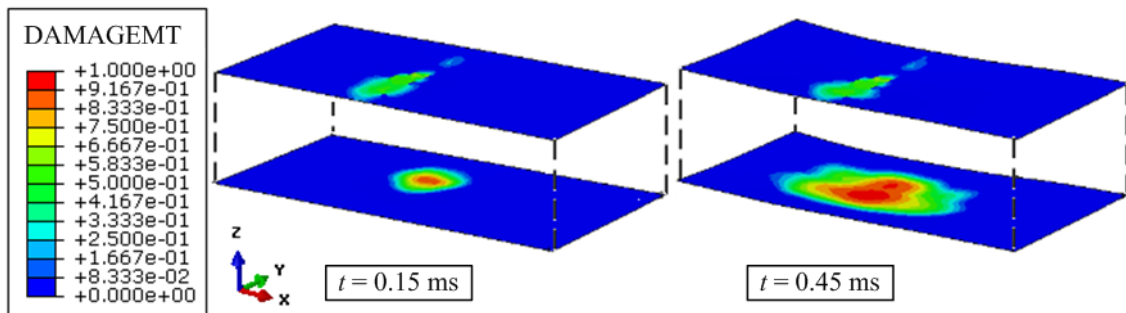
Figure 5.22: Matrix damage variable calculated by the Abaqus progressive damage model in the top and bottom material points at 0.15 ms and 0.45 ms.

5.21 with the matrix damage predicted by the Abaqus model in Figure 5.22 shows that the micromechanical model predicts approximately the same extent of damage in the composite plies. A distinction between the physical interpretation of the results shown in Figures 5.21 and 5.22 is that the damage parameters in the multiscale model refer to the maximal subcell value in the relevant unit cell, whereas the damage parameters in the Abaqus progressive damage model refer to the homogenised composite ply material properties.
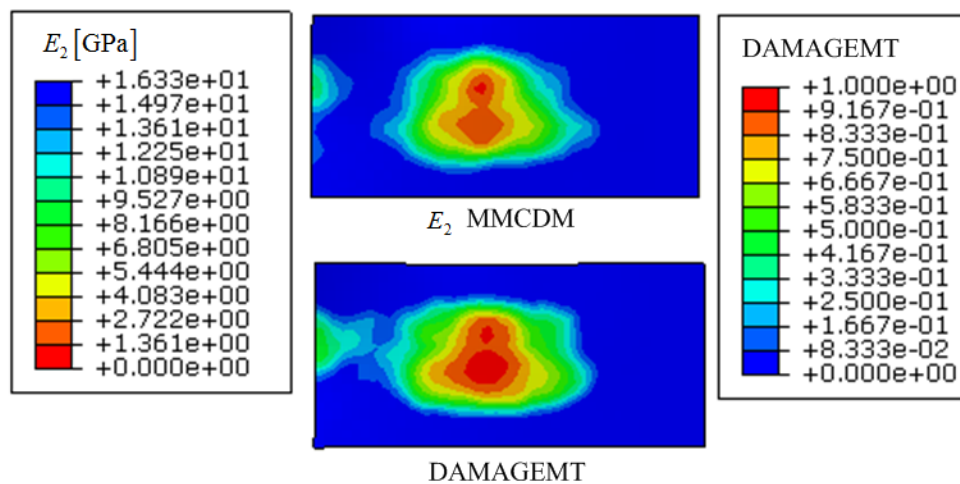
Figure 5.23: Comparison of E_2 elasticity component with the Abaqus matrix tensile damage variable (DAMAGEMT) at $t = 0.6$ ms (bottom plies, 100 m/s impact on Silenka GFRP composite plate).

Homogenisation over the RUC with damaged elasticity properties results in the damaged elasticity components. As to further illustrate the damage effects predicted by the MMCDM model and the Abaqus damage model, Figure 5.23 shows comparison of

the E_2 homogenised elasticity component predicted by HFGMC and MMCDM model with the matrix tensile damage variable (DAMAGEMT) at $t = 0.6$ ms. As shown in Figures 5.22 and 5.23, good correlation between the applied damage models exist.

Comparison of the micromechanical fibre failure initiation theories and the Puck's fibre failure criteria is shown in Figure 5.24. Although the impact caused severe matrix damage, fibre failure has not been predicted to occur in the analysis by any of the evaluated failure theories. The Puck's ply-level fibre failure criteria reach maximal values of 0.379, whereas the micromechanical maximal stress and maximal strain in fibre direction criteria, predicted by HFGMC, reached approximately the same value. Values of the Puck criteria indicate that the compressive failure criteria take higher values compared to the tensile values. This effect is not visible in the micromechanical max. stress and max.strain criteria as the SDVs associated with the micromechanical failure criteria do not distinguish between the tensile and compressive failure modes.
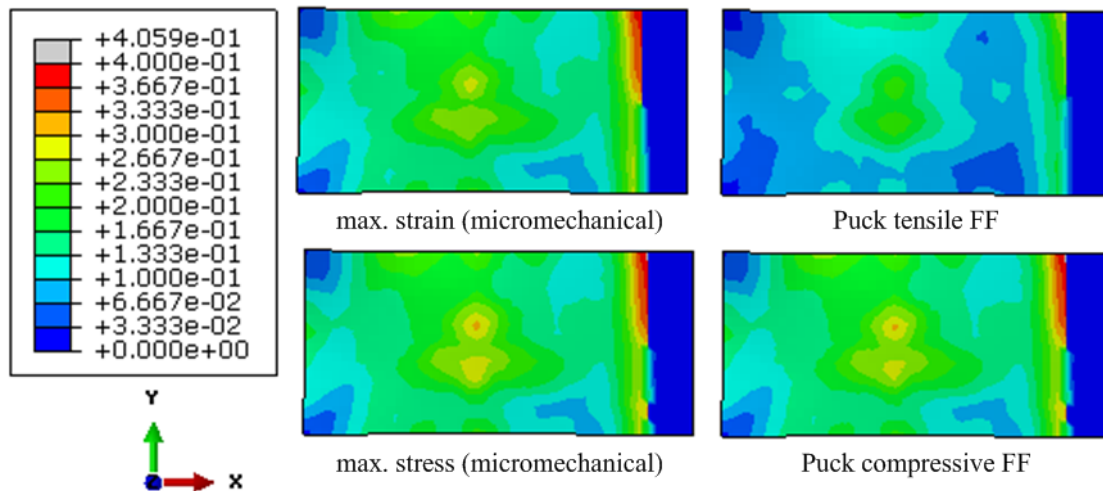
Figure 5.24: Comparison of maximal over-the-thickness values of max. stress and max. strain in fibre direction criteria and Puck's fibre criteria at $t = 0.6$ ms.

Case II: Impact on Silenka GFRP plate at 100 m/s, Crack Band damage model

The multiscale simulation of the soft body impact on the GFRP plate has been also simulated using the micromechanical Crack Band damage model. The employed Crack Band damage model parameters for the Silenka GFRP composite, which have been defined in [Pineda, 2012], are summarised in Table 4.5. The multiscale application of

the Crack Band micromechanical progressive degradation theory showed to be computationally extremely demanding, preventing application in the multiscale impact analyses considering the available computer hardware.

The degraded computational performance has been caused by the computational operations employed for transformation of the subcell elasticity, stress and strain tensors from the subcell to the principal stress coordinate system, as explained in Section 4.3. Consequently, the computational performance of HFGMC employing the Crack Band theory is approximately three times lower compared to the application of the MMCDM model. Therefore, only 0.2 ms have been analysed using the Crack Band damage model. However, the 100 m/s impact caused extensive matrix damage in a relatively large part of the impacted plate after 0.2 ms, as shown in the analysis performed using the MMCDM theory. Consequently, sufficient information have been provided as to enable comparison of the results obtained by the micromechanical Crack band damage model with the MMCDM results and the ply-level failure models.
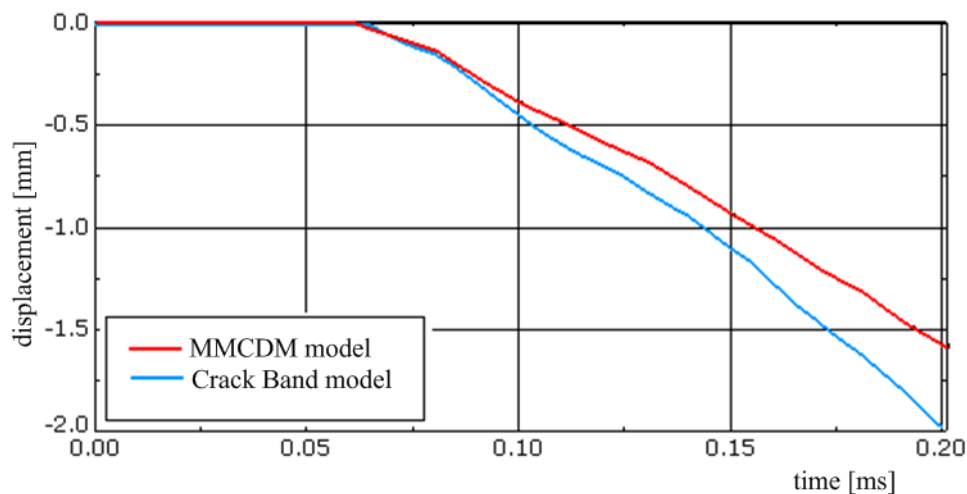
Figure 5.25: Comparison of displacements of the node at impact location predicted by the MMCDM and Crack Band damage models.

Figure 5.25 shows the comparison of the time histories of nodal displacements in the direction perpendicular to the plate, predicted by the two evaluated micromechanical damage models, for a node at the impact location. The discrepancies between the nodal displacements indicate differences between the results of the two damage modelling approaches. As shown, more extensive damage has been predicted by the Crack Band model.

Figure 5.26 shows the evolution of the Mode I maximal principal stress criterion in this impact case at 0.1, 0.15 and 0.2 ms in the top and bottom composite plies. As shown, the criterion predicts damage onset in both composite plies. As opposed to the MMCDM damage model, the Mode I criterion predicts damage onset in a large part of the plate predicted at the material points in the top composite plies.
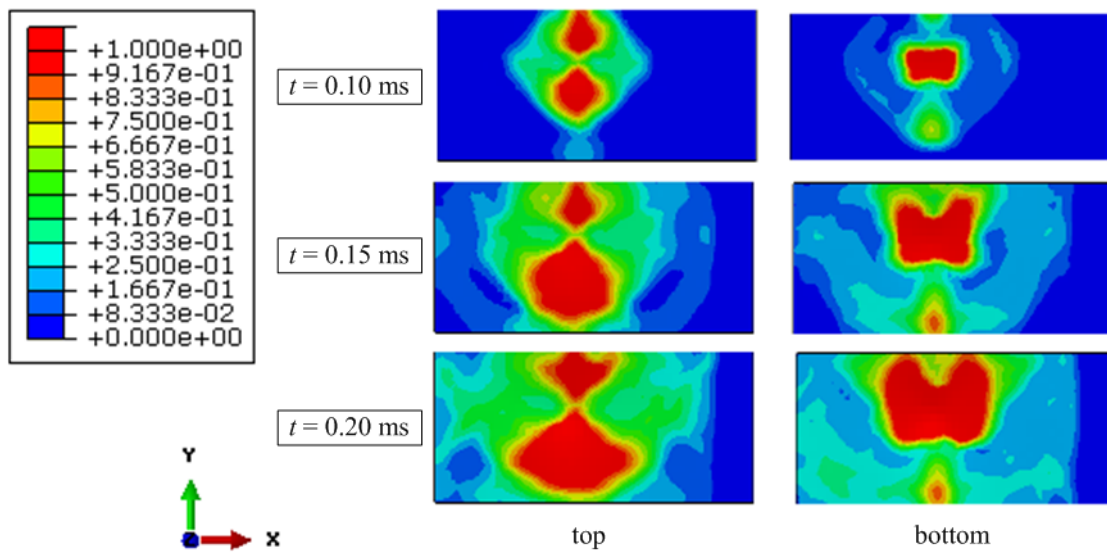
Figure 5.26: Evolution of Mode I maximal principal stress damage initiation criterion for the composite plies located at the top and bottom of the composite laminate.

Figure 5.27 shows the comparison of the fraction of failed subcells for composite plies at the top and bottom of the plate, as predicted by the Crack Band model. For comparison, the contours of failed subcells predicted by the MMCDM criterion at $t = 0.2$ ms in the bottom ply are shown in Figure 5.27. Results for the impacted side of the plate predicted by the MMCDM theory are not shown in Figure 5.27 as no subcells have failed for this material points, which is a significant difference regarding the results predicted by the two evaluated micromechanical damage theories.

Compared to the MMCDM model and to the Abaqus damage model, the micromechanical Crack Band damage model results in the more extensive damage and subcell failure prediction. The difference is particularly noticeable in the composite plies located at the top of the composite laminate. These differences have been caused by the erroneous behaviour in the in-plane shear and transverse compressive load cases, as discussed in Chapter 4.5.
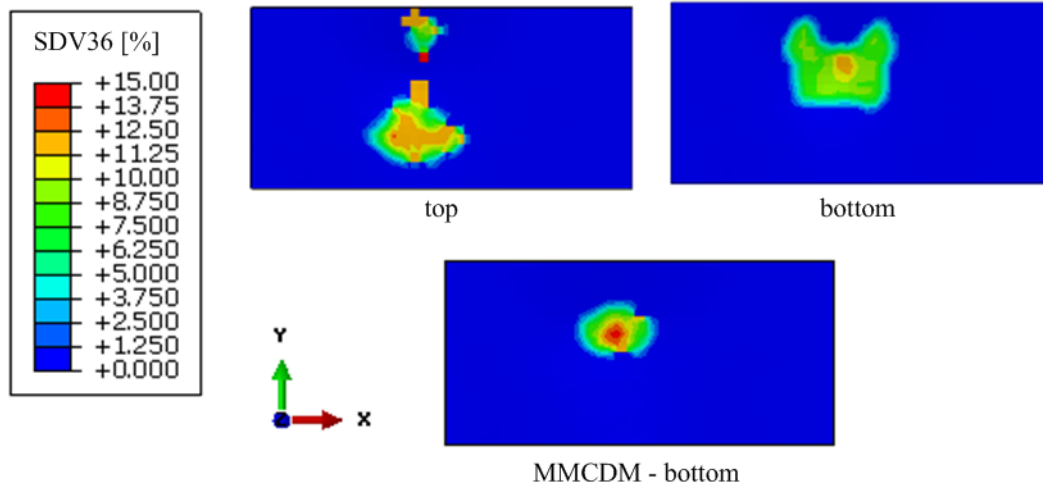
Figure 5.27: Comparison of the fractions of failed matrix subcells for the top and bottom composite plies as predicted by the Crack Band model and the MMCDM theory at $t = 0.2$ ms.

Case III: Impact on T300/914 plate at 200 m/s, MMCDM damage model

Results of the ply-level failure analyses using the Abaqus damage model indicate that simulation of 0.4 ms is necessary for the prediction of the final state of damage in the 200 m/s impact on the T300/914 composite. The ply-level properties for application of the Abaqus damage initiation model and the Puck failure theory have been provided in Table 5.5. Properties of the Abaqus damage model have been assumed to be equal to the values presented in Table 5.7. The T300/914 elasticity components and ply strengths have been taken from [Lachaud et al., 1997]. These properties have been employed with the Abaqus damage model as to validate the bird strike damage prediction methodology in the previous research phase, as explained in Section 5.4.

Constituent elasticity properties of the T300/914 composite are defined in Table 4.3. Parameters of the MMCDM model, employed in the impact analyses are summarised in Table 5.8. The employed damage initiation strains differ from the values in Table 4.3 as to account for the higher ply strength properties provided in [Lachaud et al., 1997] compared to the values provided in [Soden et al., 1998]. Validation of the MMCDM damage model parameters for the T300/914 composite has been performed in Section 4.4.

Accuracy of the micromechanical computations has been ensured by application of

Table 5.8: T300/914 MMCDM damage model properties employed in the impact analyses.

Damage initiation strains [-]			
$X_\varepsilon^T = Y_\varepsilon^T = Z_\varepsilon^T$	$X_\varepsilon^C = Y_\varepsilon^C = Z_\varepsilon^C$	$S_\varepsilon = Q_\varepsilon = R_\varepsilon$	
0.012	0.036	0.041	
Post-damage slope parameters [-]			
$A^T = 0.70$	$A^C = 1.0$	$B^T = 1.10$	$B^C = 1.0$
Scaling parameters [-]			
$b_{ii}^T = b_{ii}^C = 1.32$		$b_{4i} = b_{5i} = b_{6i} = 0.50$	

a time increment of 1.5×10^{-8} s in the 200 m/s impact analysis. The computational time of the multiscale analysis has been approximately 24 hours. The impact event with contours of the plate displacements in the z direction is shown in Figure 5.28. As shown, the analysed total time of 0.4 ms has been sufficient as to simulate the soft body impact at 200 m/s.
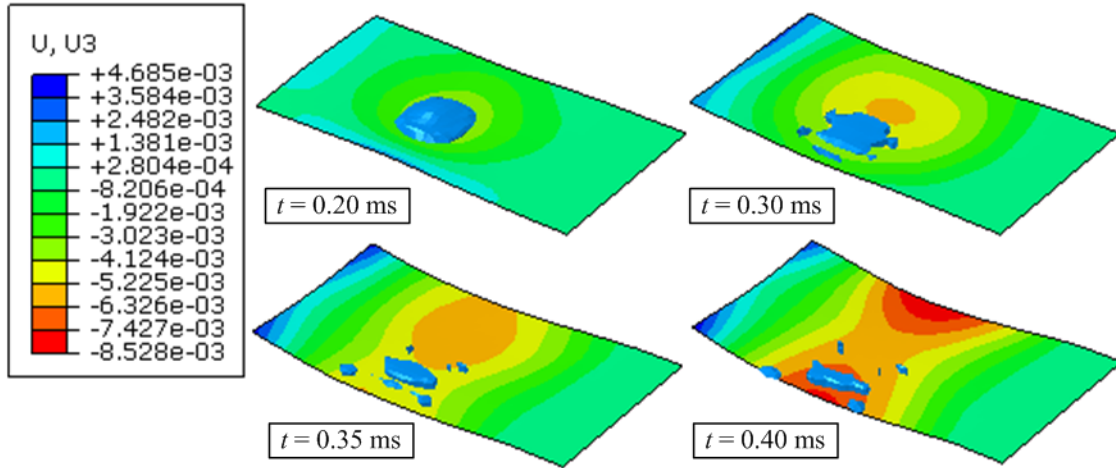
Figure 5.28: 200 m/s impact event on T300/914 plate, contours show displacements in z direction, [m].

The threshold velocity in the experiments, above which damage becomes apparent in the T300/914 unidirectional CFRP plates, is approximately 190 m/s according to [Hou and Ruiz, 2007]. Visual inspection of the damage at 200 m/s revealed only damage at the clamped edge of the plate.

The damage strains, as micromechanical failure initiation criteria in the MMCDM theory, indicate damage initiation at the subcell level at the material points located in bottom as well as in the top composite plies. Visualisation of the evolution of ε_2^D
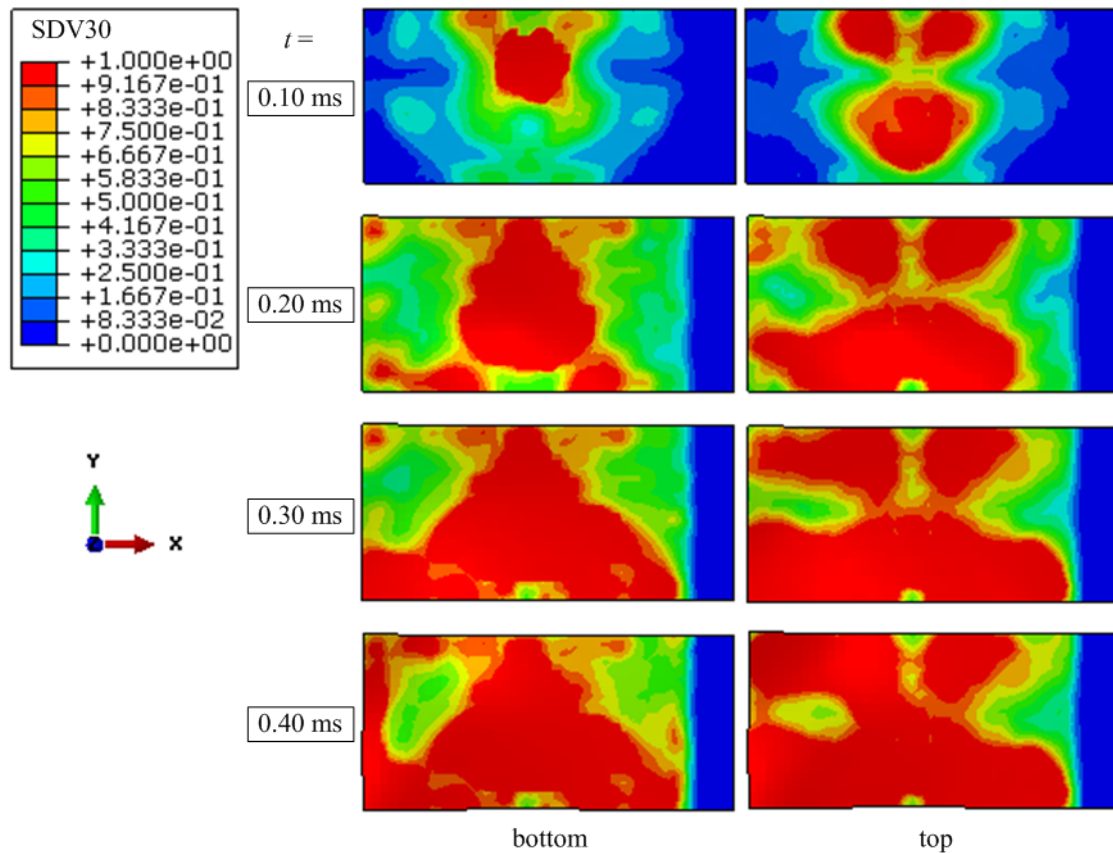
Figure 5.29: Evolution of the ε_2^D damage strain at the 200 m/s impact on the T300/914 composite plate.

damage strain for the two composite plies at opposite plate sides is shown in Figure 5.29. As indicated by the high values of the damage strains, nonlinear effects at the subcell level have been initiated in large parts of the plate. The multiscale analyses with the MMCDM damage model indicate that the 200 m/s impact causes significant matrix damage in the composite plate. These results are supported by the results of the Abaqus damage model, as shown in Figure 5.32.

The extent of damage is shown by visualisation of the SDV showing maximal subcell D_2^T damage parameters in Figure 5.30 at 0.2 and 0.4 ms. As demonstrated by the results in this Figure, damage effects are more pronounced in the composite plies at the bottom of the plate. Damage effects have been predicted only in the composite plies located near the top and bottom sides of the plate. For the 90° ply next to the top composite plate (second ply in the layup), matrix damage effects at the clamped plate edge are also pronounced, as shown in the bottom image in Figure 5.30.
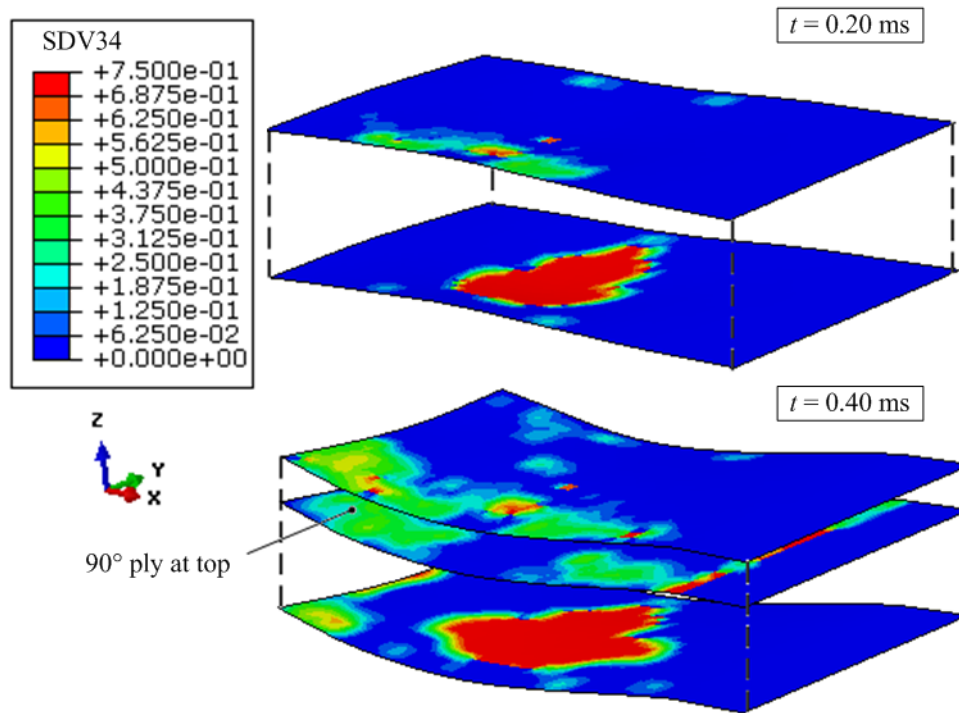
Figure 5.30: Distribution of D_2^T damage parameter at $t = 0.2$ ms and $t = 0.4$ ms, 200 m/s impact on the T300/914 plate.
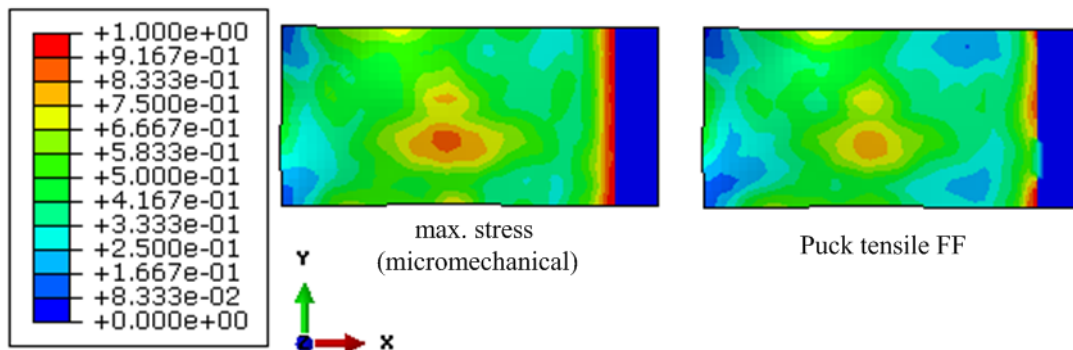
Figure 5.31: Comparison of fibre failure criteria at $t = 0.4$ ms.

Figure 5.31 shows comparison of the micromechanical maximal stress in fibre direction criterion and the Puck's tensile fibre failure criterion at $t = 0.4$ ms, as predicted by the material points in the bottom composite ply. The fibre failure criteria indicate damage onset in several 0° plies at the clamped plate end. As previously explained, this effect has been caused by the structural response of the plate.

Schematic representation of the visually observed impact damage is shown in Figure
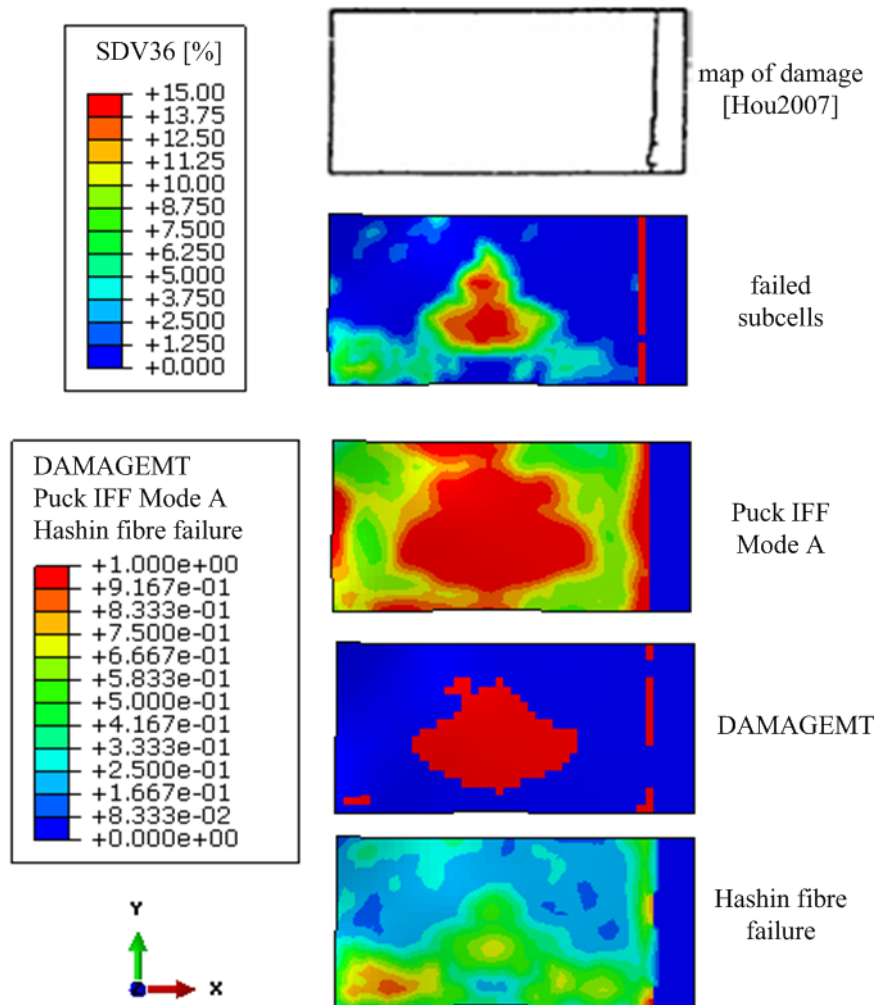
Figure 5.32: Comparison of the numerical results with the visually observed damage map provided in [Hou and Ruiz, 2007] for the 200 m/s impact on the T300/914 plate.

5.32 (image at the top), after [Hou and Ruiz, 2007]. The final state of damage in the bottom composite plies, as predicted by the MMCDM model, Puck failure theory (Mode A IFF) and the Abaqus damage model have been shown in this image. As shown, extensive matrix damage has been predicted by all failure theories. The MMCDM results presented in Figure 5.32 refer to the fractions of failed matrix subcells.

The result designated as DAMAGEMT shows the matrix tensile damage variable as predicted by the Abaqus damage model. These contours agree relatively good to the fractions of failed subcells predicted by the MMCDM model. The failed subcells at the clamped edge of the plate have been caused by fibre failure, as shown in Figure 5.31.

In addition to the matrix damage, fibre failure has been predicted by the multiscale analysis as shown in Figure 5.31. The Hashin fibre tensile failure initiation criterion predicts fibre failure in only limited area at the clamped plate edge, as shown in Figure 5.32.

Although C-scan images have been provided in [Hou and Ruiz, 2007] for some impact cases (mostly for woven composites), only visual observation of the impact damage has been provided for the T300/914 impacts. The C-scans would be very useful for the validation of the numerical damage prediction methodology, using the locations and sizes of the detected matrix cracks and delaminations as references for validation and calibration of the damage models. As an example of C-scan images provided in [Hou and Ruiz, 2007], Figure 5.33 shows the size and form of matrix damage/delamination observed on the CIBA-Geigy 1238-IMS (unidirectional CFRP composite) plate impacted at velocity 220 m/s by a 10 g projectile. Figure 5.33 provides indicative information of the damage which could be expected from the analysed soft body impact.

Figure 5.33: C-scan image for CIBA-Geigy 1238-IMS plate impacted at velocity 220 m/s by a 10 g projectile, after [Hou and Ruiz, 2007].

Case IV: Impact on T300/914 plate at 280 m/s, MMCDM damage model

Simulation of the 280 m/s impact has been performed employing a time step of $1. \times 10^{-8}$ s for the explicit analysis. The extreme loading conditions initiate damage processes in a very large part of the composite plate throughout the analysis, causing long computation times. The computational time for multiscale analysis has been approximately 48 hours in which only 0.275 ms of the impact event has been analysed employing the multiscale approach.

Results of the experimental gas gun impact at 280 m/s indicate that the soft body

impact resulted in complete perforation of the composite plate with fibre failure, matrix cracking and delamination damage modes, after [Hou and Ruiz, 2007]. Again, only visual inspection of the damaged state at the end of the experiment has been provided in [Hou and Ruiz, 2007], since visual inspection has been considered sufficient to characterise the extent of damage.
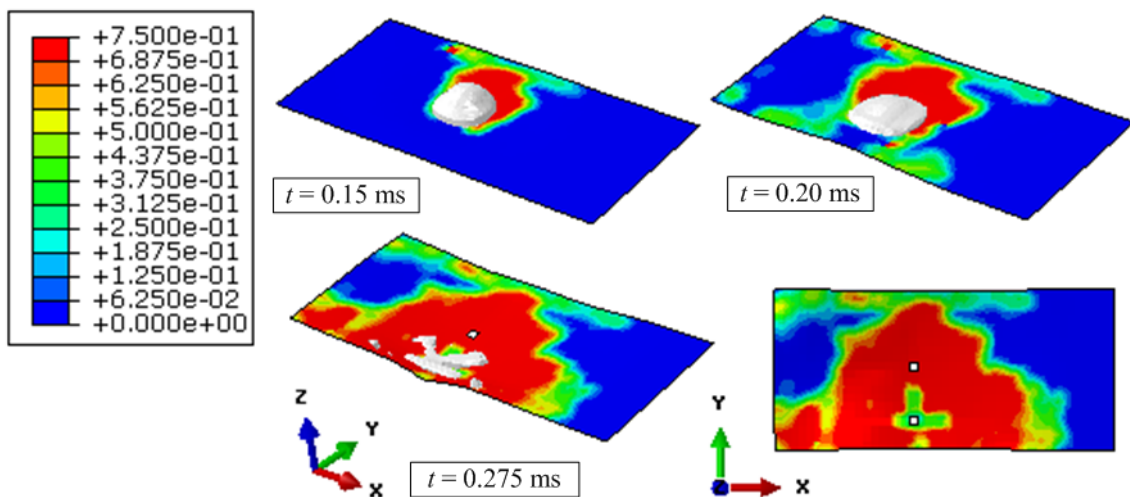
Figure 5.34: Impact event at 280 m/s, D_2^T damage variables in the bottom ply.

The impact event, as simulated by the multiscale analysis, is shown in Figure 5.34. The contours in this Figure show evolution of the SDV of the subcell D_2^T damage variables at three time steps of the analysis. The contours in the results presented in Figure 5.34 refer to the values calculated at the material points located in the bottom composite plies.

In contrast to the previous two load cases (100 m/s impact on Silenka GFRP and 200 m/s impact on T300/914 plate), the micromechanical analysis, as well as the Puck ply-based model and the Abaqus damage model, predict fibre failure in the composite plate. Fibre failure has in this load case not been caused by the structural response, as this failure mode occurs at the impact location and not just at the clamped plate edge.

Plate perforation has been predicted by the model if all through-thickness STATUS variables in the finite element indicate material point failure. This state has been predicted by the fibre failure condition, as explained earlier in this Section. The material point failure has been controlled by the fibre failure modes, whereas energy dissipation caused by fibre failure modes has not been included in the micromechanical model. As a

consequence, the multiscale methodology predicts perforation of the plate at an earlier time. The first finite element is removed from the analysis at approximately 0.16 ms, whereas the Abaqus damage model has predicted this state at approximately 0.2 ms. The process is continued further to the final state as shown in Figure 5.34.
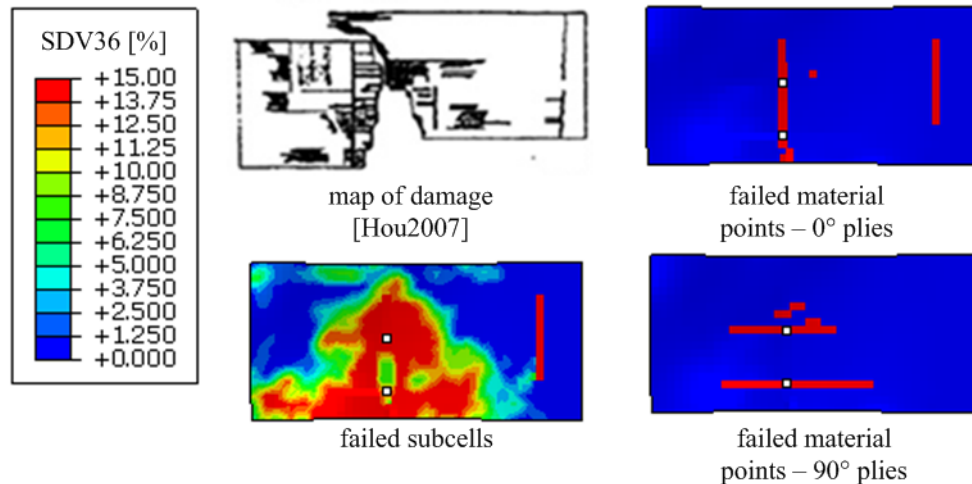
Figure 5.35: Comparison of damage predicted by the MMCDM model with experimental evidence for the 280 m/s impact on the T300/914 composite plate.

Comparison of the final damage state, predicted by the MMCDM model, and schematic representation of the experimentally observed damage, as provided in [Hou and Ruiz, 2007], is shown in Figure 5.35. Only two finite elements have been removed from the analysis indicating that the multiscale analysis does not predict complete perforation of the plate in this analysis. However, contours of the fractions of the failed matrix subcells (as shown in Figure 5.35 for the bottom composite ply) resemble the visually observed damage contours from the gas gun experiment. The contours of the failed material points (fibre failure) for the 0° and 90° plies at the bottom of the composite plate are also shown in Figure 5.35. Similar contours have been predicted in all of the through-thickness plies in the layup.

More information about the experimental plate deflections is required for the adjustment of the numerical models for the enhancement of the numerical impact damage prediction methodology. So far, experimental data provided in the literature are very limited, as discussed in Section 5.4.

The Abaqus damage model also predicts very large extent of damage in the plate. However, only one element has reached the criterion for element failure in the analysis.
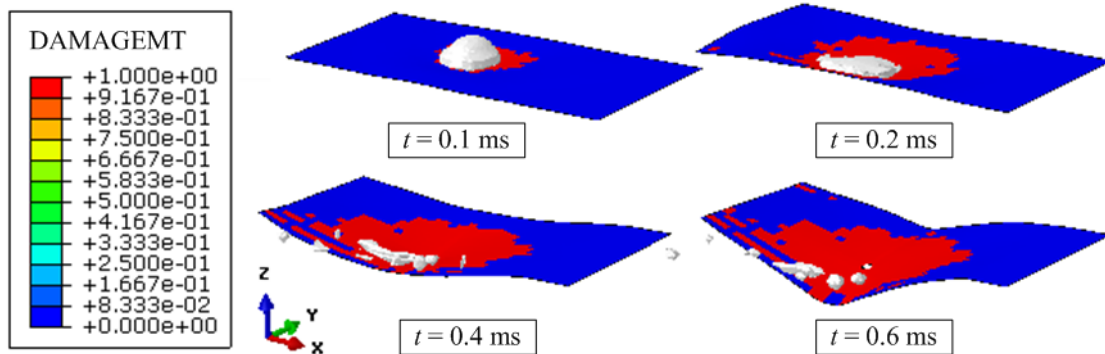
Figure 5.36: Visualisation of the impact event at 280 m/s, predicted by the Abaqus damage model.

Visualisation of the impact event is shown in Figure 5.36. The contours in this image visualise the matrix tensile damage variable. Despite the extensive damage predicted by the model, only one finite element has been removed from the analysis, causing nonphysical response of the plate at later time steps, which could be attributed to plate perforation. This conclusion indicates that a total time of approximately 0.6 ms should be analysed as to predict the plate perforation.

5.7   Conclusion

Evaluation of the micromechanical against the ply-level failure theories showed that the selection of the ply-level failure criteria employed as to initiate the micromechanical computation in multiscale analyses is not straightforward, as conclusions obtained from the analyses on the GFRP composite differ from those obtained from the CFRP composite. Results of the evaluation have been determined by interactions between several factors as for example differences in the relevant failure theories, employed constituent properties and parameters of the micromechanical model (e.g. unit cell morphology).

Complete compliance with experimental results is difficult to obtain as numerical prediction of complex phenomena, e.g. perforation of composite plates, is a highly difficult task. The results of applied multiscale damage prediction methodology, where the damage parameters reach maximal values predicting matrix cracks in location where the plate broke into two halves in the experiment, indicate that the physical phenomenon has been modelled with acceptable accuracy. Very good comparison of the contours of failed subcells (indicating matrix cracks) and the Puck's mode A inter-fibre failure mode

has been observed in the performed multiscale analysis. Good agreement between the multiscale analyses employing the MMCDM theory with the Abaqus built-in progressive damage model has also been achieved in the analyses. The multiscale application of the Crack Band damage model showed to be computationally too demanding for the numerical multiscale analyses performed within this Chapter considering the available computer resources.

There are several possible sources of discrepancies between experimental results and numerical composite failure prediction approaches. The numerical analysis of progressive damage and failure of composite materials is extremely demanding while the exact mechanical properties have to be known and applied to the numerical model as to obtain reliable solutions. This statement applies for micromechanical scale as well as for the structural level. However, as discussed in e.g. [Ng et al., 2010], the procedures for the prediction of the in-situ properties, which are required for accurate micromechanical analyses as to predict the composite behaviour, are very exhaustive.

Furthermore, strain rate effects have to be included in the composite constitutive behaviour as to accurately simulate the structural response in high-velocity impact load cases. The effect of elevated strain rates on the composite properties has been discussed in the following Chapter, where the HFGMC micromechanical model has been employed in the prediction of the homogenised composite properties at elevated strain rates.

6 | Modelling of strain rate effects using HFGMC

6.1 Introduction

Epoxy-based composite materials exhibit significant strain-rate dependence of mechanical properties, which have been caused by the epoxy matrix strain rate dependency. These effects have been neglected in the high-velocity impact analyses in Section 5.6 due to complexities encountered in the determination of micromechanical damage models properties, as explained in Chapter 4. Results of the obtained numerical analyses in Section 5.6 indicate that, compared with the available experimental results, more severe damage has been predicted by the multiscale methodology as well as by the ply-level failure and damage models.

Therefore, the HFGMC model has in this Chapter been employed as to predict the mechanical properties of epoxy-based composite plies at the elevated strain rates. The structural response in the high-velocity impact loading has been undoubtedly influenced by the strain rate effects, causing differences between experimental and numerical results.

Numerical crashworthiness analyses of aeronautical and automotive structures are becoming increasingly attractive for the industry. Consequently, advanced numerical approaches have been employed in the simulation of crashworthiness problems in the aviation industry in e.g. [Georgiadis et al., 2007], [Guida et al., 2008], whereas the ability to withstand critical crash situations has become the key design criterion in automotive structures in which composite materials have been extensively employed, after [Körber, 2010].

The high strain rate effects on mechanical properties are usually neglected in numerical investigations of high-velocity impact on composite structures, as in e.g. [Georgiadis

et al., 2007], [Guida et al., 2008]. This simplification can be attributed to difficulties with experimental procedures employed in the prediction of the strain rate dependent composite materials properties. Since the static strength and elasticity properties are generally lower compared to the dynamic values, application of rate-insensitive properties in the design and sizing of dynamically loaded structures results in excessive structural weight. However, these results are conservative, as structural failure would occur at higher loadings than predicted. A possible explanation of the higher dynamic mechanical properties is that damage evolution occurring at high strain rates allows insufficient time for damage processes to accumulate in the material resulting in higher mechanical properties, as suggested in [Eskandari and Nemes, 1999].

The high strain rate effects modelling approach in this Thesis followed the method employed in e.g. [Goldberg et al., 2003a], [Zheng, 2006], [Guedes et al., 2005], where a viscoplastic constitutive model has been used for modelling matrix nonlinearity in a strength of materials based micromechanical model. Additionally, the effect of elevated strain rates on the elasticity properties has been modelled using an exponential law defined in the literature for epoxy matrices. The generally accepted assumption in the high strain rate composites modelling, employed also in this Thesis, is that only the matrix constituent is the source of nonlinear behaviour of the composite material, whereas the fibre has been assumed to be strain rate insensitive. The results of this approach have been validated with available Split Hopkinson Pressure Bar (SHPB) experimental results, provided in [Goldberg et al., 2003a] and [Zheng, 2006], where experimental results of the composite, as well as the neat matrix nonlinear behaviour at several strain rates, have been provided.

6.2   Experimental evidence of rate dependent properties

A typical strain rate dependent stress-strain curve, as observed in the experimental testing, is shown in Figure 6.1 for the PR520 epoxy resin, after [Goldberg et al., 2003a]. The general observation of the high strain rate effects on the mechanical properties of epoxy matrices is an increase in elastic modulus and strength while the failure strain decreases at increased strain rates. Furthermore, the failure mode changes from ductile failure to brittle failure.
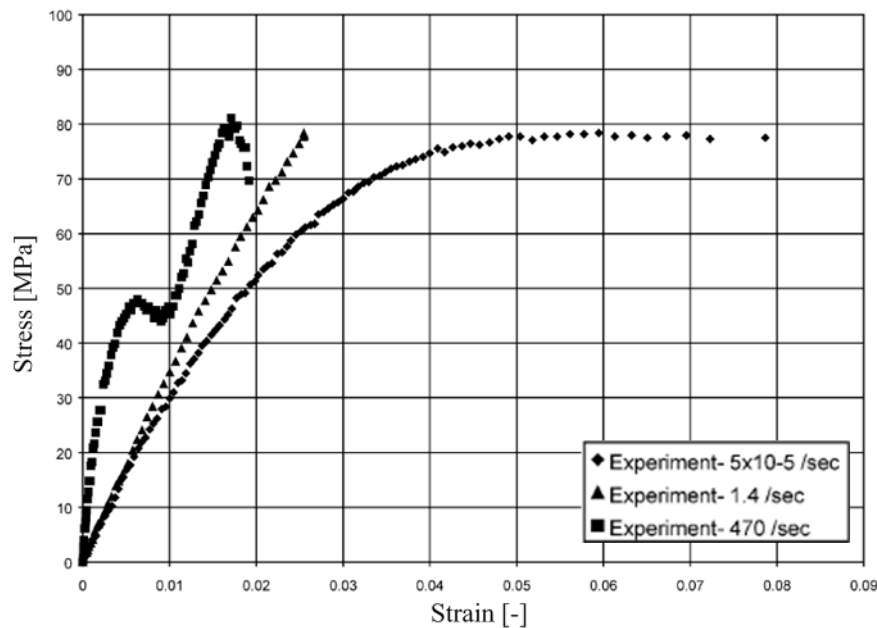
Figure 6.1: Experimental tensile stress–strain curves for the PR520 resin at three different strain rates, after [Goldberg et al., 2003a].

High strain rate experimental tests on the fibres (when not used in reinforced matrices) are very scarce in the literature. The published results indicate that carbon fibres are strain rate insensitive, whereas glass and Kevlar fibres show limited strain rate dependency, after [Körber, 2010], [Zheng, 2006].

The observations on the strain rate dependency of the composite material are not straightforward as it has been the case for the matrix material, as concluded in [Jacob et al., 2004]. In most cases, this influence is in accordance with the previously described effect on the matrix behaviour. However, deviations from these conclusions have been reported throughout the literature. For example, a decreasing elasticity modulus at very high strain rates for the PANEX 33/DA4518U (CFRP) composite laminates has been observed in [Hosur et al., 2001], as shown in Figure 6.2. The decrease in elasticity modulus at higher strain rates in this reference (162 and 817 s^{-1} in Figure 6.2) has been caused by an increase of temperature in the sample resulting in decreased elasticity properties. In addition, in this reference, an increase of temperature of 100°C has been measured at strain rates of 1500 s^{-1}. An extensive literature survey on strain rate effects on composite materials is presented in e.g. [Jacob et al., 2004].

Maximal strain rate values of interest for research in this Thesis are 200-300 s^{-1},
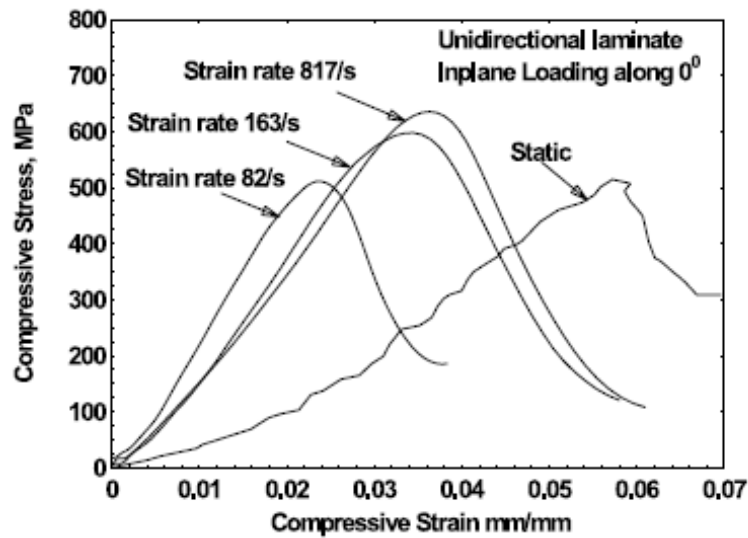
Figure 6.2: Strain rate effects in compressive loading on unidirectional PANEX 33/DA4518U laminate along the fibre direction, after [Hosur et al., 2001].

which have been observed in the bird strike numerical analyses on leading edge devices, as discussed in Section 5.4. Consequently, the decrease of elasticity properties at extremely high strain rates has not been considered in this Thesis.

Micromechanical analyses are especially suitable for modelling of the high strain rate dependent material nonlinearities in composite materials. In these approaches, it is assumed that the nonlinear effects at elevated strain rates have been caused only by the matrix constituent, whereas the fibre constitutive model is rate independent. Since the constitutive theories within micromechanical models are applied at the constituent level, the nonlinear strain rate dependent response of the composite materials can be predicted based on the experimentally observed behaviour of its constituents.

6.3   Modelling of strain rate dependence

Several viscoelastic and viscoplastic constitutive models have been employed as to model strain rate dependence of polymeric matrices in the literature. Examples for viscoplasticity theory application on composite materials are provided in e.g. [Goldberg et al., 2003a], [Guedes et al., 2005], [Fish and Shek, 1998], [Zheng, 2006].

Modelling of strain rate dependence of composites has been performed in this Thesis employing the modified Bodner-Partom viscoplasticity model, after [Goldberg et al.,

2003a], as a constitutive model for matrix subcells in the HFGMC micromechanical model. The Bodner-Partom and similar models have been developed for metallic materials to analyse the viscoplastic deformation of metals at temperatures at increased temperatures. Application of these models on polymeric materials has been justified by phenomenological similarities in the deformation mechanisms of polymers and metals as matrix microcracking, which causes the nonlinear composite behaviour, leads to apparent plasticity, after [Ng et al., 2010]. Although the micromechanical mechanisms which cause nonlinearities are fundamentally different for composites and metals, the plasticity theories provide mathematical frameworks which can be also applied to composite materials.

The research in this Thesis is focused on epoxy matrices as these polymeric materials are most widely used in aeronautical composite structures. Temperature effects have been neglected in this analysis since the experimentally obtained results in the available literature refer to data obtained at room temperature. However, as indicated in e.g. [Hosur et al., 2001], the influence of temperature on the nonlinear response is critical. Consequently, these effects should be implemented into the model in order to obtain a physically accurate model.

The original Bodner-Partom viscoplasticity model has been modified in [Goldberg et al., 2003a] as to include the effects of hydrostatic stress, which are essential for polymers, as they show increased elastic properties and yield stresses at higher hydrostatic stresses. Consequently, higher compressive strengths compared to the tensile values have been observed in the experiments, after [Zheng, 2006]. Therefore, the original Bodner-Partom model has been modified by the addition of a hydrostatic stress term in the definition of the effective stress as to include the hydrostatic stress effects.

The Bodner-Partom theory is based on the small strain and strain additivity assumption. Therefore, the total strain rate can be written as the sum of elastic and inelastic strain rates

$$\dot{\epsilon}_{ij} = \dot{\epsilon}_{ij}^{El} + \dot{\epsilon}_{ij}^{In}. \tag{6.1}$$

Additionally, the inelastic strain rate is governed by the plastic flow law, which defines the direction of plastic straining

$$\dot{\varepsilon}_{ij}^{In} = \lambda \frac{\partial f}{\partial \sigma_{ij}}, \qquad \dot{\varepsilon}_{kk}^{In} = 0, \tag{6.2}$$

where f is the flow potential and λ is the scalar rate function, after [Gilat et al., 2005].

The inelastic strain rate in the modified Bodner Partom model depends on the stress deviator s_{ij}, the second invariant of the stress deviator J_2 and the isotropic stress state variable Z

$$\dot{\varepsilon}_{ij}^{In} = D_0 \exp\left[-\frac{1}{2}\left(\frac{Z}{\sigma_e} \right)^{2n} \right] \left(\frac{s_{ij}}{\sqrt{J_2}} \right). \tag{6.3}$$

σ_e in Equation 6.3 is the effective stress, which has been modified as to include the hydrostatic stress effects

$$\sigma_e = \sqrt{3J_2} + \alpha\sigma_{kk}. \tag{6.4}$$

The hydrostatic effects have been included in the inelastic potential function by means of the term $\alpha\sigma_{kk}$ in Equation 6.4, where α is the hydrostatic stress state variable. Contrary to the original Bodner-Partom model, the mean inelastic strain rate is not equal to zero, since hydrostatic stresses contribute to the inelastic strain rate, after [Goldberg et al., 2003a]. D_0 in Equation 6.3 is a material constant defining the maximal inelastic strain rate in the experiments whereas n represents a material parameter which determines the rate dependence of the material.

Z, as the internal stress variable, presents the resistance to molecular flow in the polymeric material. A further difference between the original Bodner-Partom model and the modification introduced in [Goldberg et al., 2003a], is that evolution equations of the internal stress and the hydrostatic stress state variables have been modified as to dependent on the effective inelastic strain rate instead of the inelastic work rate. This modification has been introduced due to significant simplifications in the material characterisation, according to [Goldberg et al., 2003c]. Consequently, the evolution of the internal stress variable has been determined as

$$\dot{Z} = q(Z_1 - Z)\dot{e}_e^{In}, \tag{6.5}$$

whereas the evolution of the hydrostatic stress state variable is defined in a similar way as

$$\dot{\alpha} = q(\alpha_1 - \alpha)\dot{e}_e^{In}. \tag{6.6}$$

In the evolution equations (Equations 6.5 and 6.6), q is the material constant representing the hardening variable, whereas Z_1 and α_1 represent maximal values of the internal stress and hydrostatic stress internal variables, respectively.

The form of the inelastic strain rate defined by Equation 6.3, along with the evolution equations of the internal state variables Z and α assures low values of inelastic strain rate at low effective stress levels, followed by exponential growth and constant values of inelastic strain rate at high values of effective stress [Bodner, 2001]. Initial values of Z and α are defined by the constants α_0 and Z_0. The equivalent inelastic strain rate in Equations 6.5 and 6.6 is defined as

$$\dot{e}_e^{In} = \sqrt{\frac{2}{3}\dot{e}_{ij}^{In}\dot{e}_{ij}^{In}}, \tag{6.7}$$

where

$$\dot{e}_{ij}^{In} = \dot{\varepsilon}_{ij}^{In} - \frac{\dot{\varepsilon}_{ii}^{In}}{3}. \tag{6.8}$$

The viscoplastic model proposed in [Goldberg et al., 2003a] assumes a constant strain rate for the strain-driven simulation of the constitutive equations. A limitation of this approach is that the elasticity tensor is assumed to be constant for the evaluated strain rate. An improvement to this model has been employed in [Zheng, 2006], as explained in Chapter 6.5.

6.4   Implementation into HFGMC

Modelling of strain rate effects has been performed in this Thesis by application of the modified Bodner-Partom theory in the matrix subcell constitutive laws within the HFGMC model. The micromechanical strain rate dependence modelling followed the method developed in e.g. [Goldberg et al., 2003a], [Goldberg et al., 2003c], where

the described constitutive model has been implemented into a strength of materials micromechanical model to simulate composite strain rate dependent behaviour.

According to [Bansal and Pindera, 2006], the system of equations in the reformulated HFGMC model in the case of inelastic strains in the unit cell has been obtained in the form

$$\bar{\varepsilon}^{(\beta,\gamma)} = \mathbf{A}^{(\beta,\gamma)} : \bar{\varepsilon} + \mathbf{D}^{(\beta,\gamma)}, \tag{6.9}$$

where the vector $\mathbf{D}^{(\beta,\gamma)}$ contains the thermal and inelastic strain components. The values in this vector have been obtained by the HFGMC systems of equations (Equations 2.28 and 2.29) at each load increment by employing Mendelson's method of successive iterations within the classical incremental plasticity [Bansal and Pindera, 2006]. In this method, which is based on the modified Prandtl-Reuss flow rule, the plastic strain increments have been calculated in terms of total strain deviators for improved convergence and robustness.

The implementation of Bodner-Partom equations in this Thesis is intended to be used with explicit numerical codes. Therefore, the solutions of the localisation equations are solved in the incremental form, where the new state of micromechanical strain tensor in the β, γ subcell has been predicted as

$$\varepsilon_{new}^{(\beta,\gamma)} = \varepsilon_{old}^{(\beta,\gamma)} + \Delta\varepsilon^{(\beta,\gamma)}. \tag{6.10}$$

The incremental change of subcell strain state, as predicted by the HFGMC localisation equation in Equation 6.9, has been split into elastic and inelastic parts, according to the strain additivity assumption in Equation 6.1, after [Ambroziak, 2007]

$$\Delta\varepsilon^{(\beta,\gamma)} = \Delta\varepsilon_{El}^{(\beta,\gamma)} + \Delta\varepsilon_{In}^{(\beta,\gamma)}. \tag{6.11}$$

The modified Bodner-Partom equations have been applied in each of the matrix subcells of the HFGMC model. Evolution of the strain and stress states in each subcell has been calculated by integration of the modified Bodner-Partom equations defined in Section 6.3. Several numerical integration schemes have been employed in the literature to integrate the system of Equations 6.3, 6.5 and 6.6. The Forward Euler integration scheme and Runge-Kutta 4 integration schemes have been employed in the literature as to integrate viscoplasticity theories for explicit FE solvers [Goldberg et al., 2003a],

[Taibei et al., 2005], whereas an implicit numerical scheme for the implementation of the Bodner-Partom viscoplastic model has been derived in [Andersson, 2003].

As the methodology developed within this Thesis is intended for application within explicit FE codes, the computational cost of the implementation of the Bodner-Partom model has been considered a critical factor. After validation of several integration schemes, the Forward Euler algorithm has been selected for the implementation of the viscoplasticity model into the HFGMC standalone application, based on the better computational properties and the acceptably accurate solutions obtained for small load increments.

In addition to the viscoplastic nonlinear behaviour, a simple damage model has been introduced into the constitutive model of matrix subcells as to improve modelling of the composite nonlinear behaviour at elevated strains. The employed damage model relates the damage law and the equivalent plastic strain, as suggested in [Du Bois et al., 2006] and [Zheng, 2006]. The damage law is based on the assumption that matrix microcracks have been formed in the composite at higher strains, consequently degrading the elastic properties. The effective mechanical properties have been modelled in the employed approach based on the current effective plastic strain e_e^{In} as

$$d = 1 - \exp\left(-C_1 e_e^{In}\right), \tag{6.12}$$

where d is the isotropic damage variable. The coefficient C_1 is the only variable in the described damage model and should also depend on the applied strain rate, after [Zheng, 2006]. The values used in the analyses performed in this reference for the IM7/977-2 composite are 100 for the low and intermediate strain rates and 120 for the high strain rate results. The results in this Chapter for the composite behaviour have been obtained using C_1 equal to 150. The stress increment in the combined viscoplastic and damaging material has been expressed in vector form as

$$\dot{\boldsymbol{\sigma}}^{(\beta,\gamma)} = \mathbf{C}^* : \dot{\boldsymbol{\varepsilon}}_{El}^{(\beta,\gamma)} = (1-D)\,C : (\dot{\boldsymbol{\varepsilon}} - \dot{\boldsymbol{\varepsilon}}_{In})^{(\beta,\gamma)}, \tag{6.13}$$

where $\mathbf{C}^*$ is the effective elasticity tensor according to standard continuum damage mechanics theory [Voyiadjis and Kattan, 1999].

6.5   Strain rate effect on elasticity properties

Epoxy matrices show an increase in elastic properties at elevated strain rates, as emphasized in the introduction to this Chapter. The effect of increased strain rates on the elasticity properties of epoxy matrices has been modelled using the relation

$$E = E_0 \left(1 + C \log \frac{\dot{\varepsilon}}{\dot{\varepsilon}_{ref}} \right), \tag{6.14}$$

as suggested in [Hufenbach et al., 2013] and [Zheng, 2006]. According to Equation 6.14, the elastic modulus at increased strain rates depends on the current effective strain rate $\dot{\varepsilon}$, calculated as

$$\dot{\varepsilon} = \sqrt{\frac{2}{3} \left[(\dot{\varepsilon}_{11} - \dot{\varepsilon}_m)^2 + (\dot{\varepsilon}_{22} - \dot{\varepsilon}_m)^2 + (\dot{\varepsilon}_{33} - \dot{\varepsilon}_m)^2 + 2\dot{\varepsilon}_{12}^2 + 2\dot{\varepsilon}_{23}^2 + 2\dot{\varepsilon}_{13}^2 \right]}, \tag{6.15}$$

where $\dot{\varepsilon}_m$ is the mean strain rate defined as

$$\dot{\varepsilon}_m = \frac{\dot{\varepsilon}_{ii}}{3}, \quad i = 1, 2, 3, \tag{6.16}$$

after [Zheng, 2006]. The reference elastic modulus in Equation 6.14, E_0, has been obtained for quasi-static loading conditions while the scaling parameter C is a material property. The referent effective strain rate $\dot{\varepsilon}_{ref}$ is the strain rate at which the quasi-static properties have been obtained. The value of the referent effective strain rate has been set to 1.0 s^{-1}, since the strain rate effects on the elasticity properties can be neglected below this threshold value. Values of the scaling parameters for the PR520 and 977-2 epoxy matrices, which have been evaluated in this study, along with the relevant quasi-static elasticity properties, are shown in Table 6.1, after [Zheng, 2006].

Table 6.1: Strain rate effect on epoxy matrix elasticity properties, after [Zheng, 2006].

	E_0 [GPa]	ν [$-$]	C [$-$]
PR520	3.24	0.38	0.195
977-2	3.20	0.40	0.166

Figures 6.3 and 6.4 show the comparison of the strain rate dependent elasticity properties, predicted by Equation 6.14 using properties defined in Table 6.1, with the

strain rate dependent values of elastic moduli provided in [Goldberg et al., 2003a] and [Goldberg et al., 2003c] for the PR520 and 977-2 matrices. These values, which have been employed in the relevant references in micromechanical analyses as to match experimentally obtained mechanical properties of epoxy composites at three strain rate levels, are summarised in Table 6.2.
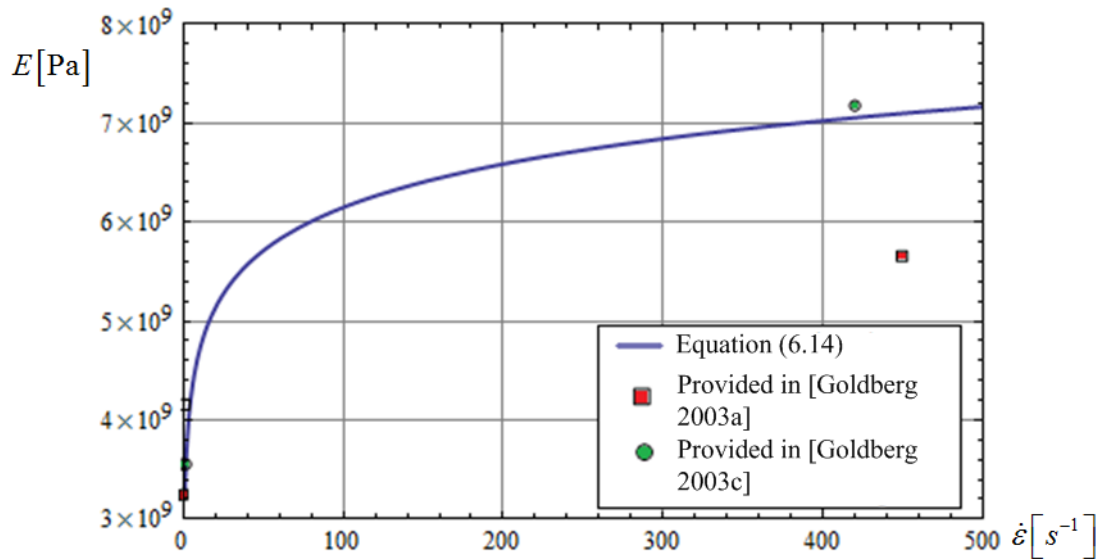
Figure 6.3: PR520 resin elasticity modulus strain rate dependence - comparison of Equation 6.14 with values provided in [Goldberg et al., 2003a] and [Goldberg et al., 2003c].

As shown in Figures 6.3 and 6.4, the problem in the evaluation of the strain rate dependence of elasticity properties emerges due to insufficient data on the experimentally observed properties. Only three data points, referring to elastic properties at the different strain rate levels, have been provided in the references as shown by the values in Table 6.2. The low and intermediate strain rates are very close to each other while no values have been provided for the intermediate strain rates which would provide more information about the strain rate dependence of the elasticity properties.

A comprehensive experimental study, including a wider range of strain rate levels would be necessary to validate the scaling parameters C. However, experimental data regarding these effects are very limited in the open literature while the references cited in this Chapter belong to the most comprehensive resources of epoxy-based composite strain rate dependent properties.

Figure 6.4 shows validation of elasticity properties for the 977-2 matrix. Along with the curve representing Equation 6.14 with parameters for the 977-2 matrix defined in
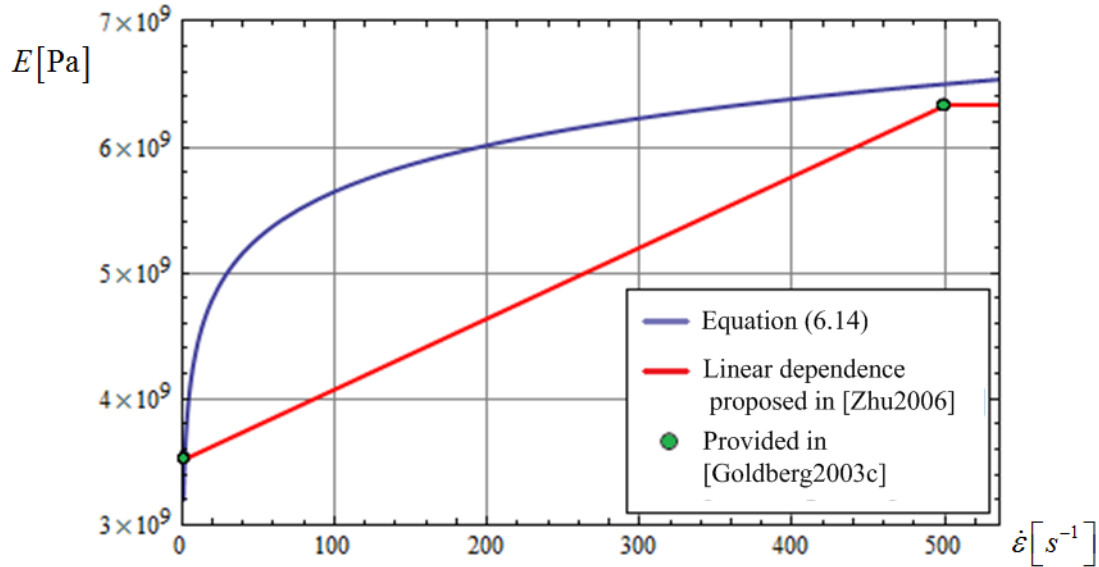
Figure 6.4: 977-2 resin elasticity modulus strain rate dependence.

Table 6.1, a linear relationship between the effective strain rate and the elastic modulus, as suggested in [Zhu et al., 2006], has been plotted in Figure 6.4. As shown in the following Section, the approximation of elastic properties using Equation 6.14 along with the Bodner-Partom viscoplasticity model results in good approximation of the experimentally observed epoxy matrix behaviour.

Table 6.2: Experimentally observed elastic moduli of PR520 and 977-2 matrices, after [Goldberg et al., 2003a] and [Goldberg et al., 2003c].

PR520 [Goldberg et al., 2003a]		PR520 [Goldberg et al., 2003c]		977-2 [Goldberg et al., 2003c]	
$\dot{\varepsilon}\,[s^{-1}]$	$E\,[\text{GPa}]$	$\dot{\varepsilon}\,[s^{-1}]$	$E\,[\text{GPa}]$	$\dot{\varepsilon}\,[s^{-1}]$	$E\,[\text{GPa}]$
$1.\times 10^{-5}$	3.24	$7.\times 10^{-5}$	3.54	$9.\times 10^{-5}$	3.52
1.4	4.15	1.76	3.54	1.9	3.52
450.	5.65	420.	7.18	500.	6.33

6.6 Modelling of epoxy composite strain rate nonlinearities

Several forms of the modified Bodner-Partom theory, which include the hydrostatic effects, have been employed in the literature. Additionally, several sets of material

Table 6.3: Properties of the modified Bodner-Partom viscoplasticity model for PR520 and 977-2 matrices, after [Zheng, 2006] and [Goldberg et al., 2003b].

	D_0 [MPa]	q [-]	n [-]	Z_0 [MPa]	Z_1 [MPa]	α_0[-]	α_1[-]
PR520	1×10^6	247.42	0.92	402.53	766.73	0.983	0.209
977-2	1×10^6	101.00	0.73	380.00	1546.00	0.223	0.201

parameters for the evaluated matrices have been used in these viscoplasticity models. Therefore, validation of the modified Bodner-Partom theory implementation, defined by Equations 6.3 - 6.6 and employing material properties in Table 6.3, has been performed by comparison with available experimental data of the neat epoxy matrix nonlinear behaviour. Table 6.3 summarises the parameters for the modified Bodner-Partom model employed in this Thesis. These parameters have been taken from [Zheng, 2006] for PR520 matrix and from [Goldberg et al., 2003b] for the 977-2 matrix. The elastic properties of the matrix subcells in these analyses have been obtained using Equation 6.14 with properties defined in Table 6.1.
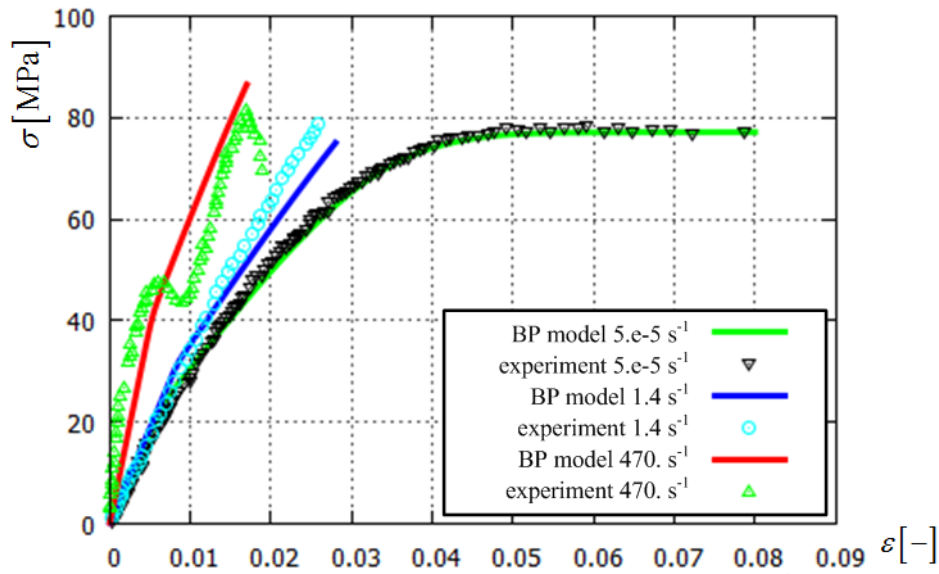
Figure 6.5: Tensile loading of PR520 resin, comparison with experimental results provided in [Goldberg et al., 2003a].

Figure 6.5 shows comparison of the Bodner-Partom viscoplasticity model in tensile loading with experimental values provided in [Goldberg et al., 2003a]. The application of the Bodner-Partom model with the defined parameters presents an overall good approximation of the experimental results, as shown in Figure 6.5.

Shear loading of the PR520 matrix at three strain rate regimes is shown in Figure 6.6. Results of the viscoplasticity model, along with the experimental data are shown in this Figure. The model slightly overestimates the shear modulus at the quasi-static loading rate. The intermediate loading regime is accurately modelled until softening in the experimental results occurs. This effect is even more pronounced for the highest rate of loading, where the influence of different elasticity modulus (as shown in Figure 6.3) becomes apparent. The C scaling parameter for the PR520 matrix (defined in Table 6.1) should be modified as to achieve better correlation with the experimental results in the high strain rate loading regime.
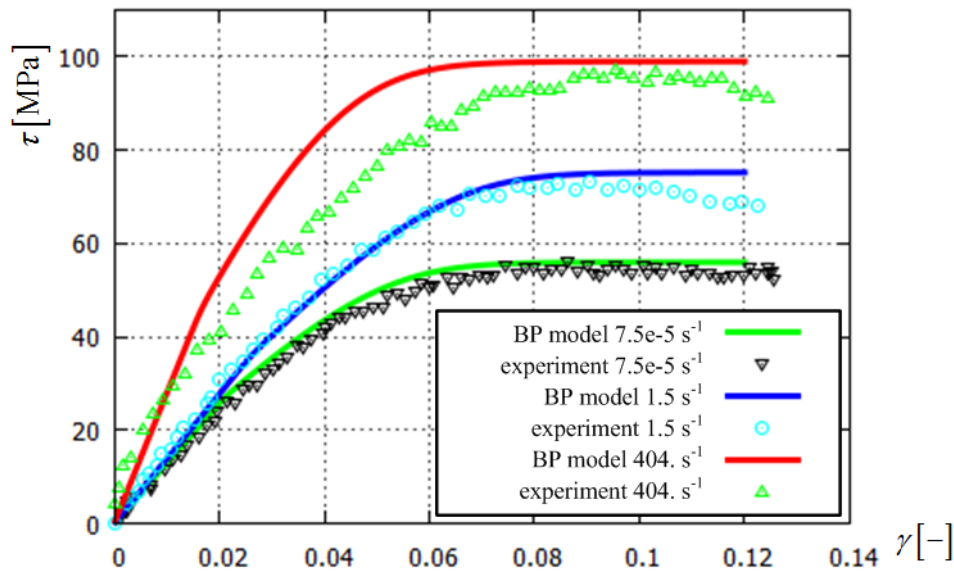
Figure 6.6: Shear loading of PR520 resin, comparison with experimental results provided in [Goldberg et al., 2003a].

Results for tensile loading of the 977-2 are shown in Figure 6.7. As shown, matching of the experimental results is better, compared to the results obtained for the PR520 matrix. Figure 6.8 shows results for shear loading of the 977-2 matrix. As indicated, the correlation with experimental results is very good for the high and intermediate strain rates, whereas the model slightly underestimates the experimental data for the lowest strain rate.

The experimental results in Figures 6.7 and 6.5 show highly nonlinear behaviour in the highest strain rate regimes for both evaluated matrices. The oscillations and very high elastic modulus at the beginning of the loading have been caused by stress waves
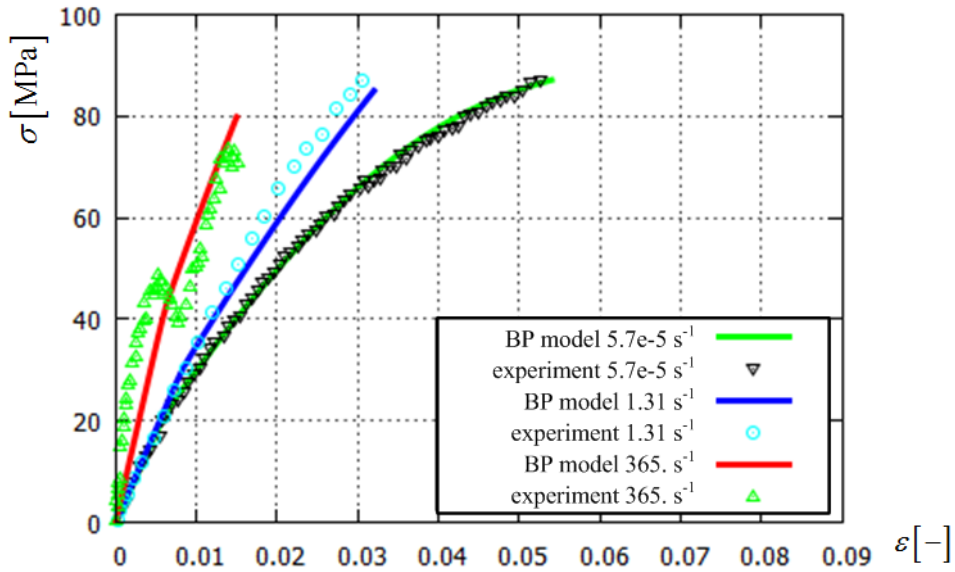
Figure 6.7: Tensile loading of 977-2 resin, comparison with experimental results provided in [Zheng, 2006].

resulting from the specimen geometry, as discussed in [Goldberg et al., 2003b].

The HFGMC micromechanical model has been applied to modelling of the strain rate dependent nonlinear behaviour of the IM7/977-2 composite. Validation of the results has been performed by comparison with the experimental results provided in [Goldberg
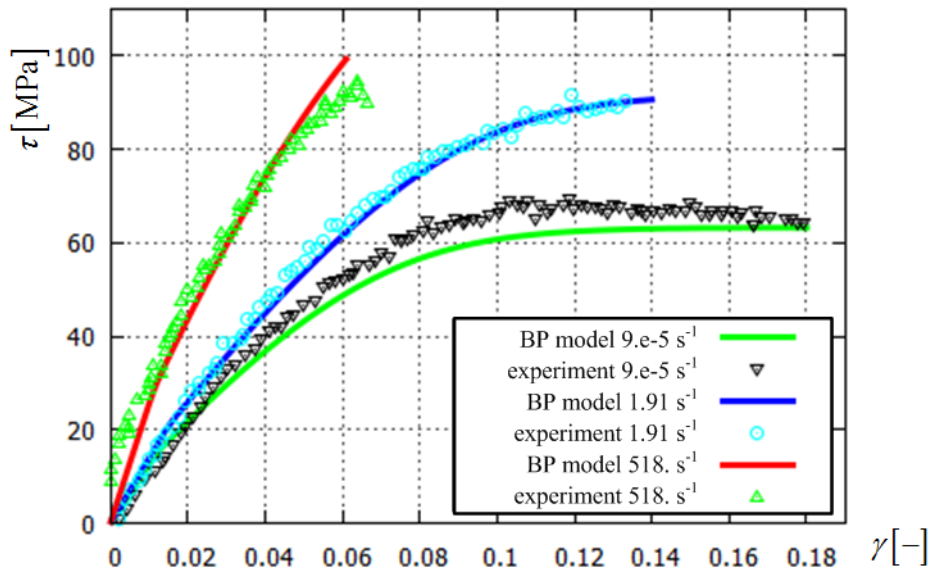
Figure 6.8: Shear loading of 977-2 resin, comparison with experimental results provided in [Zheng, 2006].

et al., 2003c]. The micromechanical model employed in the investigation of strain rate effects is the unit cell with a single fibre in the RUC centre, discretized employing 30 × 30 subcells.

Figure 6.9 shows results of tensile loading of 90° IM7/977-2 composite specimen at three strain rate regimes. The experimental results show slight nonlinearities in the quasi-static and intermediate strain rate regime, which is accurately captured by the model. However, the high strain rate response shows significant nonlinearities in the response which cause large discrepancies between the experimental results and the micromechanical analysis. The largest discrepancies, in this case, occur at the start of the loading, where the elastic properties of the homogenised material, calculated by HFGMC, underestimate the slope of the experimentally observed stiffness. A similar mismatch of the elastic properties has been also found in the results presented in [Goldberg et al., 2003c], where this effect has been attributed to inaccurate measurement caused by the specimen geometry which is also present in the neat matrix tensile experimental testing of the 977-2 matrix, as shown in Figure 6.7.

Figure 6.10 shows the shear response of the 90° lamina for intermediate and high strain rate loading. The low strain rate curve captures the experimental results, but
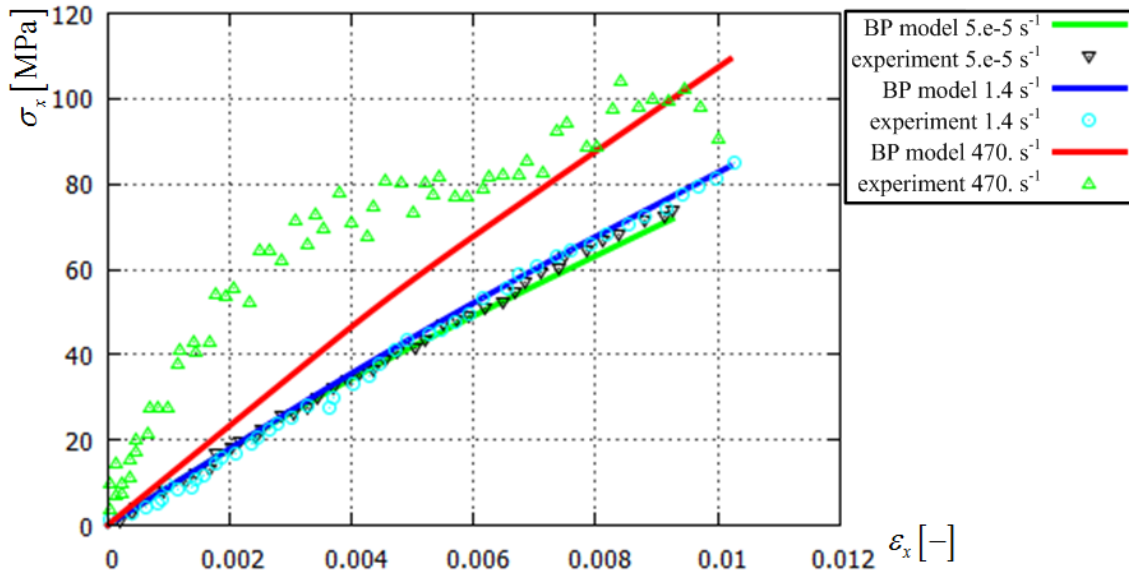
Figure 6.9: Tensile loading of 90° IM7/977-2 composite specimen - comparison of HFGMC results with experimental results provided in [Goldberg et al., 2003c] for three different strain rates.

starts do deviate from these values at shear strains above 0.4%. As shown in Figure 6.8, application of the employed viscoplasticity model on the shear response predicted for the neat matrix has also resulted in relatively large discrepancies with the experimental results. The conclusion for the results obtained at high strain rate loading is similar to the observation obtained with the tensile loading of the 90° specimen, as the initial slope of experimental results is mismatched by the model, whereas better correlation has been observed at higher strains.
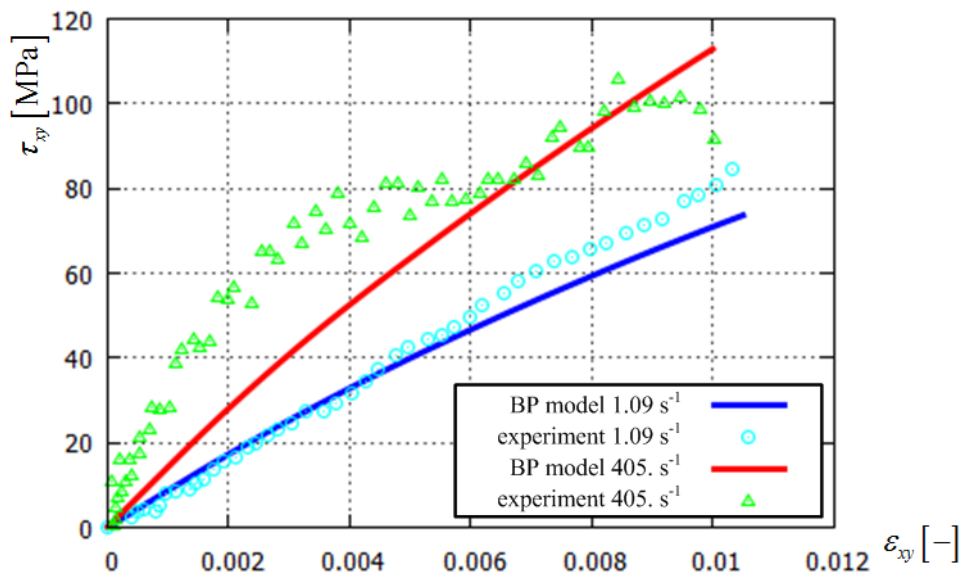
Figure 6.10: Shear loading of 90° IM7/977-2 composite ply - comparison of HFGMC results with experimental results provided in [Zheng, 2006] for intermediate and high strain rates.

Figure 6.11 shows the results for tensile loading of the 45° specimen. As shown, the model captures the experimental data reasonably well. Correlation with experimental results is better at lower strains the three strain rate regimes. However, the predicted composite response in the intermediate strain rate regime shows the largest discrepancies with experimental results which is evident even at very small strains leading to the conclusion that the composite elastic properties have been overestimated by the model.

6.7   Conclusion

Results in this Chapter showed the application of the HFGMC micromechanical analyses in the prediction of composite properties at high strain rates. Matrix nonlinear
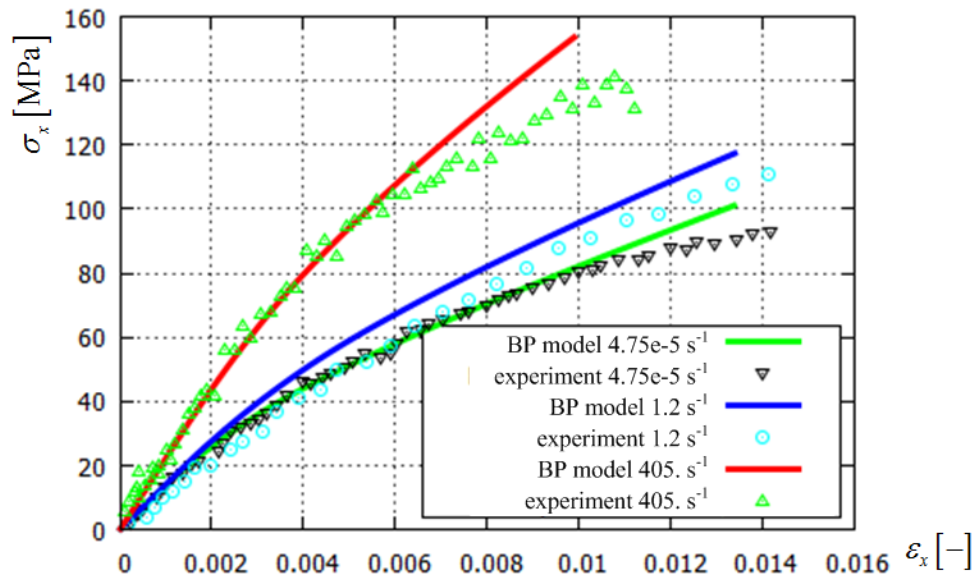
Figure 6.11: Tensile loading of 45° IM7/977-2 composite ply - comparison of HFGMC results with experimental results [Goldberg et al., 2003c] for low, intermediate and high strain rates.

behaviour, as well as rate dependence of the elastic modulus, have been included in the model for prediction of the composite response at elevated strain rates. Validation of the results has been performed by comparison with available experimental results for the IM7/977-2 composite, showing that the strain rate effects have been modelled with reasonable accuracy.

However, experimental investigations, which could be employed in the further validation of the methodology are very limited in the open literature. High strain rate testing of more complex composite laminates, composed of several differently oriented plies, are well represented in the literature. Yet, details about the nonlinear behaviour of the constituents, which are necessary for the micromechanical model have not been provided in these studies. Furthermore, the conclusions obtained from the experimental testing are often contradicting. The methodology developed in this Thesis is based on application of constituent-based constitutive modelling at the micromechanical level. Therefore, data of the nonlinear behaviour of epoxy matrices as well as the composite plies based on these matrices are necessary for validation of the micromechanical analyses.

7 | Conclusion

The HFGMC micromechanical model has been employed in this Thesis in the development of a multiscale methodology which enables application of microstructural damage and failure theories in structural scale analyses. The intent of the developed methodology is to model impact damage in composite structures, with the aim of the application on advanced composite structures in further research. The computational framework for the further research has been developed in this Thesis. Important aspects for application in the impact analyses, as e.g. computational performance and the micromechanical damage modelling approach, have been evaluated in this Thesis.

Micromechanical damage theories enable modelling of the structural failure processes at a more fundamental level compared to the homogenised approaches. As to account for the microstructural damage effects, several micromechanical failure criteria have been evaluated throughout this research. As shown in Section 3.5, significant discrepancies exist in the results obtained by application of the different failure theories. Furthermore, the obtained results indicated that the application of micromechanical progressive damage models is necessary as to model the microdamage mechanisms causing pre-peak nonlinearities.

Micromechanical damage mechanisms have been modelled by implementation of the MMCDM and Crack Band micromechanical damage models into the developed multiscale methodology. Validation of the micromechanical damage initiation and failure models has been performed by comparison with available experimental results. Consequently, conclusions obtained by the standalone HFGMC application regarding the microstructural damage effects on the homogenised composite response have been

employed in the physical interpretation of the multiscale analyses results.

The MMCDM model enables modelling of the microstructural damage mechanisms in epoxy-based unidirectional composite materials allowing modelling of the multiaxial character of composite damage modes. Consequently, application of the model in the multiscale framework enables more accurate modelling over the previous applications of micromechanical failure criteria in multiscale damage approaches, where instantaneous subcell degradation damage models have been employed, as explained in Section 4.1.

Evaluation of the micromechanical damage models showed that the damage initiation criterion employed in the Crack Band damage model should be modified as to enable prediction of the composite homogenised response due to in-plane shear loading. Further research will be focused on application of the Crack Band damage model as it enables modelling of damage in more complex RUCs, which is a necessity for modelling of the advanced composite materials.

The importance of computational efficiency of the micromechanical model has been shown in the multiscale impact simulations in Chapter 5.6. Although the FE model applied in the impact analyses is relatively small, application of the multiscale approach transforms the numerical model into a computationally very demanding problem. The analyses have been performed on a desktop workstation with an average computation time of 24 hours (depending on a large number of variables, e.g. on the discretization refinement of the micromechanical model, as well as on the particular damaging case).

The developed multiscale methodology has been applied to FE models representing structural items of composite aeronautical structures. A stringer-reinforced composite panel with realistic dimensions and ply lay-up has been analysed in Section 5.2, whereas a soft body impact on a simple composite plate has been analysed in Sections 5.5 and 5.6. These aeronautical structures transform into very large numerical models when the multiscale framework is applied. Analysis of engineering problems (e.g. complex aircraft structural components) using the developed multiscale methodology could be efficiently performed by application of the multiscale VUMAT material only to the part of the structure in which damage is expected, as e.g. in [Moncada, 2012]. The limitation on the size of the numerical model, measured in the number of material points at which the multiscale framework has been applied, emerges from the standpoint of computational efficiency as well as from the employed hardware (e.g. available RAM memory).

Application of micromechanical models in the damage modelling of composite struc-

tures enables improvement in the prediction of the in-plane failure process of the composite material, as it enables insight into the actual processes within the heterogeneous material. However, an essential requirement for the accurate application of micromechanical damage modelling theories is the determination of accurate in-situ mechanical properties of the constituents. Consequently, the multiscale analyses have been performed in this Thesis on the Silenka GFRP and T300/914 composites. Experimental evidence of these composites is well documented in the literature, as they have been part of the WWFE.

The structural scale application of the MMCDM model shows that the model predicts the failure modes of the impacted plate reliably. Good correlation with the Puck's failure theory and the Abaqus built-in progressive damage model have been observed. However, more detailed structural scale experimental data is necessary as to further validate the multiscale methodology. A very close match of the Puck's failure initiation theory and the results predicted by micromechanical damage model has been observed in the multiscale applications. Consequently, the ply-level Puck failure theory has been employed in the developed multiscale methodology as to initiate micromechanical computations.

A possible source of the discrepancies between the numerically predicted impact damage (multiscale, as well as homogenised) and the experimental results in [Hou and Ruiz, 2007] is the effect of the increased strain rate on the composite properties. Fibre reinforced epoxy matrices show a significant rate dependence of the mechanical properties as shown in Chapter 6. This effect has been modelled in this Thesis using the modified Bodner-Partom viscoplasticity model for the matrix constituent. Although the constitutive model replicates the strain rate dependent nonlinearities of the neat epoxy matrices, additional damage effects have to be included in the HFGMC micromechanical model as to replicate the nonlinear behaviour of the homogenised composite material at higher strain states, which is in accordance with similar studies of composite strain rate effects, as e.g. [Zheng, 2006], [Taibei et al., 2002]. The employed approach for modelling of strain rate dependent elasticity properties results in overall acceptable results considering the scatter of available experimental results.

7.1   Original scientific contribution

1. The developed multiscale methodology has been applied at relatively large and complex numerical models. The contribution in this context is the comparison of the

micromechanical damage initiation and failure models with ply-level failure initiation theories, which have been employed as to initiate the micromechanical computations in the structural scale analyses, enabling computationally efficient multiscale analyses.

2. Validation of the applied micromechanical failure criteria and damage models has been performed by

i) comparison of the models with available experimental results provided in the WWFE,

ii) comparison of the micromechanical failure initiation models with ply-level failure criteria at the structural level and by

iii) application of the damage theories at the micromechanical level to model damage and failure at the structural scale.

Compared to similar multiscale impact damage analyses, where GMC micromechanical models have been used, the more advanced HFGMC model has been employed in this Thesis. Furthermore, the more refined damage models have been applied in the micromechanical analyses, which enable modelling of the microdamage mechanisms in the pre-peak regime.

3. The study of strain rate problems has been performed in this Thesis by implementation of the modified Bodner-Partom viscoplasticity model into the HFGMC micromechanical model. In addition to the viscoplastic constitutive model, a model which predicts the elasticity properties of the matrix at elevated strain rates has been employed as to account for the strain rate dependent elastic properties of the composite material. The scientific contribution in this part of the Thesis consists of the successful implementation of the strain rate dependent theory for epoxy-based composites into HFGMC, enabling accurate modelling of the homogenised composite materials at high strain rates. The results of the model have been compared with the experimental evidence of strain rate dependent nonlinearity of the IM7/977-2 composite.

7.2 Recommendations for further research

Failure and damage of composite structures can be accurately modelled with homogenised theories. However, micromechanical models enable modelling of microstructural phenomena which cannot be considered using homogenised approaches. Examples of these applications are the self-healing materials and other advanced composite materi-

als. Consequently, the developed methodology could be regarded as the initial research phase towards the development of a multiscale modelling approach for advanced composite materials, in which the micromechanical failure theories have been evaluated and validated in the multiscale framework.

Further validation of the micromechanical damage and failure models could be performed by addition of lamination theory to the standalone HFGMC micromechanical model as to simulate failure curves of more complex composite layups.

The simplified damage model, employed in the modelling of strain rate effects in this Thesis, which employs an isotropic damage variable, can only marginally be applied in the micromechanical modelling of composite materials under different loading conditions, as discussed in Section 4.2. Therefore, further research should be focused on the evaluation of the micromechanical failure theories, evaluated in this Thesis, in the high strain rate loading regime. The strain rate micromechanical methodology, developed in this Thesis, could be employed in the initial phase of the further research.

The damage and failure mechanisms under high strain rates are not entirely understood. The main obstacle to the application of the micromechanical damage modelling approach employed in this Thesis emerges from the availability of the experimental data which are necessary for validation of the methodology. Consequently, further research should be performed concurrently with experimental high strain rate investigations as to validate the obtained results.

A | Appendix

The elements of the (β, γ) axial stiffness matrix, in Equation 2.21, have been defined in [Bansal and Pindera, 2006] as

$$L_{11}^{(\beta,\gamma)} = L_{22}^{(\beta,\gamma)} = \frac{C_{66}^{(\beta,\gamma)}}{h_\beta} \left(4 - 3\frac{C_{66}^{(\beta,\gamma)}}{\bar{C}_{11}^{(\beta,\gamma)}} \right),$$

$$L_{12}^{(\beta,\gamma)} = L_{21}^{(\beta,\gamma)} = \frac{C_{66}^{(\beta,\gamma)}}{h_\beta} \left(2 - 3\frac{C_{66}^{(\beta,\gamma)}}{\bar{C}_{11}^{(\beta,\gamma)}} \right),$$

$$L_{13}^{(\beta,\gamma)} = L_{14}^{(\beta,\gamma)} = L_{23}^{(\beta,\gamma)} = L_{24}^{(\beta,\gamma)} = -\frac{3C_{55}^{(\beta,\gamma)}C_{66}^{(\beta,\gamma)}h_\beta}{\bar{C}_{11}^{(\beta,\gamma)}l_\gamma^2},$$

$$L_{31}^{(\beta,\gamma)} = L_{32}^{(\beta,\gamma)} = L_{41}^{(\beta,\gamma)} = L_{42}^{(\beta,\gamma)} = -\frac{3C_{55}^{(\beta,\gamma)}C_{66}^{(\beta,\gamma)}}{\bar{C}_{11}^{(\beta,\gamma)}l_\gamma},$$

$$L_{33}^{(\beta,\gamma)} = L_{44}^{(\beta,\gamma)} = \frac{C_{55}^{(\beta,\gamma)}}{l_\gamma} \left(4 - 3\frac{h_\beta^2 C_{55}^{(\beta,\gamma)}}{l_\gamma^2 \bar{C}_{11}^{(\beta,\gamma)}} \right),$$

$$L_{34}^{(\beta,\gamma)} = L_{43}^{(\beta,\gamma)} = \frac{C_{55}^{(\beta,\gamma)}}{l_\gamma} \left(2 - 3\frac{h_\beta^2 C_{66}^{(\beta,\gamma)}}{l_\gamma^2 \bar{C}_{11}^{(\beta,\gamma)}} \right),$$

whereas the nonzero elements in the transversal subcell stiffness matrix in Equation 2.22 are

$$K_{11}^{(\beta,\gamma)} = K_{22}^{(\beta,\gamma)} = \frac{C_{22}^{(\beta,\gamma)}}{h_\beta} \left(4 - 3\frac{C_{22}^{(\beta,\gamma)}}{\bar{C}_{22}^{(\beta,\gamma)}} \right),$$

$$K_{12}^{(\beta,\gamma)} = K_{21}^{(\beta,\gamma)} = \frac{C_{22}^{(\beta,\gamma)}}{h_\beta} \left(2 - 3\frac{C_{22}^{(\beta,\gamma)}}{\bar{C}_{22}^{(\beta,\gamma)}} \right),$$

$$K_{15}^{(\beta,\gamma)} = K_{16}^{(\beta,\gamma)} = K_{25}^{(\beta,\gamma)} = K_{26}^{(\beta,\gamma)} = -\frac{3C_{22}^{(\beta,\gamma)}C_{44}^{(\beta,\gamma)}h_\beta}{\bar{C}_{22}^{(\beta,\gamma)}l_\gamma^2} \; ,$$

$$K_{17}^{(\beta,\gamma)} = -K_{18}^{(\beta,\gamma)} = -K_{27}^{(\beta,\gamma)} = K_{28}^{(\beta,\gamma)} = \frac{C_{23}^{(\beta,\gamma)}}{l_\gamma} \; ,$$

$$K_{33}^{(\beta,\gamma)} = K_{44}^{(\beta,\gamma)} = \frac{C_{44}^{(\beta,\gamma)}}{h_\beta} \left(4 - 3\frac{l_\gamma^2 C_{44}^{(\beta,\gamma)}}{h_\beta^2 \bar{C}_{33}^{(\beta,\gamma)}} \right) \; ,$$

$$K_{34}^{(\beta,\gamma)} = K_{43}^{(\beta,\gamma)} = \frac{C_{44}^{(\beta,\gamma)}}{h_\beta} \left(2 - 3\frac{l_\gamma^2 C_{44}^{(\beta,\gamma)}}{h_\beta^2 \bar{C}_{33}^{(\beta,\gamma)}} \right) \; ,$$

$$K_{35}^{(\beta,\gamma)} = -K_{36}^{(\beta,\gamma)} = -K_{45}^{(\beta,\gamma)} = K_{46}^{(\beta,\gamma)} = \frac{C_{44}^{(\beta,\gamma)}}{l_\gamma} \; ,$$

$$K_{37}^{(\beta,\gamma)} = K_{38}^{(\beta,\gamma)} = K_{47}^{(\beta,\gamma)} = K_{48}^{(\beta,\gamma)} = -\frac{3C_{33}^{(\beta,\gamma)}C_{44}^{(\beta,\gamma)}}{\bar{C}_{33}^{(\beta,\gamma)}h_\beta} \; ,$$

$$K_{51}^{(\beta,\gamma)} = K_{52}^{(\beta,\gamma)} = K_{61}^{(\beta,\gamma)} = K_{62}^{(\beta,\gamma)} = -\frac{3C_{22}^{(\beta,\gamma)}C_{44}^{(\beta,\gamma)}}{\bar{C}_{22}^{(\beta,\gamma)}l_\gamma} \; ,$$

$$K_{53}^{(\beta,\gamma)} = -K_{54}^{(\beta,\gamma)} = -K_{63}^{(\beta,\gamma)} = K_{64}^{(\beta,\gamma)} = \frac{C_{44}^{(\beta,\gamma)}}{h_\beta} \; ,$$

$$K_{55}^{(\beta,\gamma)} = K_{66}^{(\beta,\gamma)} = \frac{C_{44}^{(\beta,\gamma)}}{l_\gamma} \left(4 - 3\frac{h_\beta^2 C_{44}^{(\beta,\gamma)}}{l_\gamma^2 \bar{C}_{22}^{(\beta,\gamma)}} \right) \; ,$$

$$K_{56}^{(\beta,\gamma)} = K_{65}^{(\beta,\gamma)} = \frac{C_{44}^{(\beta,\gamma)}}{l_\gamma} \left(2 - 3\frac{h_\beta^2 C_{44}^{(\beta,\gamma)}}{l_\gamma^2 \bar{C}_{22}^{(\beta,\gamma)}} \right) \; ,$$

$$K_{71}^{(\beta,\gamma)} = -K_{72}^{(\beta,\gamma)} = -K_{81}^{(\beta,\gamma)} = K_{82}^{(\beta,\gamma)} = \frac{C_{23}^{(\beta,\gamma)}}{h_\beta} \; ,$$

$$K_{73}^{(\beta,\gamma)} = K_{74}^{(\beta,\gamma)} = K_{83}^{(\beta,\gamma)} = K_{84}^{(\beta,\gamma)} = -\frac{3C_{33}^{(\beta,\gamma)}C_{44}^{(\beta,\gamma)}l_\gamma}{\bar{C}_{33}^{(\beta,\gamma)}h_\beta^2} \; ,$$

$$K_{77}^{(\beta,\gamma)} = K_{88}^{(\beta,\gamma)} = \frac{C_{33}^{(\beta,\gamma)}}{l_\gamma} \left(4 - 3\frac{C_{33}^{(\beta,\gamma)}}{\bar{C}_{33}^{(\beta,\gamma)}} \right) \; ,$$

$$K_{78}^{(\beta,\gamma)} = K_{87}^{(\beta,\gamma)} = \frac{C_{33}^{(\beta,\gamma)}}{l_\gamma} \left(2 - 3\frac{C_{33}^{(\beta,\gamma)}}{\bar{C}_{33}^{(\beta,\gamma)}} \right) \; .$$

The $\bar{C}$ components in these relations have been defined in Equation 2.17. The relations for the assembly of the axial global system of equations, in Section 2.4, after [Bansal and Pindera, 2006] are

$$L_{12}^{(\beta,\gamma)} \bar{u}_1^{'2(\beta,\gamma)} + (L_{11}^{(\beta,\gamma)} + L_{22}^{(\beta+1,\gamma)}) \bar{u}_1^{'2(\beta+1,\gamma)} + L_{21}^{(\beta+1,\gamma)} \bar{u}_1^{'2(\beta+2,\gamma)} + L_{14}^{(\beta,\gamma)} \bar{u}_1^{'3(\beta,\gamma)} +$$

$$L_{13}^{(\beta,\gamma)} \bar{u}_1^{'3(\beta,\gamma+1)} + L_{24}^{(\beta+1,\gamma)} \bar{u}_1^{'3(\beta+1,\gamma)} + L_{23}^{(\beta+1,\gamma)} \bar{u}_1^{'3(\beta+1,\gamma+1)} = 2\left(C_{66}^{(\beta+1,\gamma)} - C_{66}^{(\beta,\gamma)}\right) \bar{\varepsilon}_{12},$$

$$L_{32}^{(\beta,\gamma)} \bar{u}_1^{'2(\beta,\gamma)} + L_{31}^{(\beta,\gamma)} \bar{u}_1^{'2(\beta+1,\gamma)} + L_{42}^{(\beta,\gamma+1)} \bar{u}_1^{'2(\beta,\gamma+1)} + L_{41}^{(\beta,\gamma+1)} \bar{u}_1^{'2(\beta+1,\gamma+1)} + L_{34}^{(\beta,\gamma)} \bar{u}_1^{'3(\beta,\gamma)}$$

$$+ \left(L_{33}^{(\beta,\gamma)} + L_{44}^{(\beta,\gamma+1)}\right) \bar{u}_1^{'3(\beta,\gamma+1)} + L_{43}^{(\beta,\gamma+1)} \bar{u}_1^{'3(\beta,\gamma+2)} = 2\left(C_{55}^{(\beta,\gamma+1)} - C_{55}^{(\beta,\gamma)}\right) \bar{\varepsilon}_{13},$$

whereas the global transversal system of equations has been assembled as

$$K_{12}^{(\beta,\gamma)} \bar{u}_2^{'2(\beta,\gamma)} + \left(K_{11}^{(\beta,\gamma)} + K_{22}^{(\beta+1,\gamma)}\right) \bar{u}_2^{'2(\beta+1,\gamma)} + K_{21}^{(\beta+1,\gamma)} \bar{u}_2^{'2(\beta+2,\gamma)} + K_{16}^{(\beta,\gamma)} \bar{u}_2^{'3(\beta,\gamma)} +$$

$$K_{15}^{(\beta,\gamma)} \bar{u}_2^{'3(\beta,\gamma+1)} + K_{26}^{(\beta+1,\gamma)} \bar{u}_2^{'3(\beta+1,\gamma)} + K_{25}^{(\beta+1,\gamma)} \bar{u}_2^{'3(\beta+1,\gamma+1)} + K_{18}^{(\beta,\gamma)} \bar{u}_3^{'3(\beta,\gamma)} +$$

$$K_{17}^{(\beta,\gamma)} \bar{u}_3^{'3(\beta,\gamma+1)} + K_{28}^{(\beta+1,\gamma)} \bar{u}_3^{'3(\beta+1,\gamma)} + K_{27}^{(\beta+1,\gamma)} \bar{u}_3^{'3(\beta+1,\gamma+1)}$$

$$= \left(C_{12}^{(\beta+1,\gamma)} - C_{12}^{(\beta,\gamma)}\right) \bar{\varepsilon}_{11} + \left(C_{22}^{(\beta+1,\gamma)} - C_{22}^{(\beta,\gamma)}\right) \bar{\varepsilon}_{22} + \left(C_{23}^{(\beta+1,\gamma)} - C_{23}^{(\beta,\gamma)}\right) \bar{\varepsilon}_{33},$$

$$K_{34}^{(\beta,\gamma)} \bar{u}_3^{'2(\beta,\gamma)} + \left(K_{33}^{(\beta,\gamma)} + K_{44}^{(\beta+1,\gamma)}\right) \bar{u}_3^{'2(\beta+1,\gamma)} + K_{43}^{(\beta+1,\gamma)} \bar{u}_3^{'2(\beta+2,\gamma)} + K_{36}^{(\beta,\gamma)} \bar{u}_2^{'3(\beta,\gamma)} +$$

$$K_{46}^{(\beta+1,\gamma)} \bar{u}_2^{'3(\beta+1,\gamma)} + K_{35}^{(\beta,\gamma)} \bar{u}_2^{'3(\beta,\gamma+1)} + K_{45}^{(\beta+1,\gamma)} \bar{u}_2^{'3(\beta+1,\gamma+1)} + K_{38}^{(\beta,\gamma)} \bar{u}_3^{'3(\beta,\gamma)} +$$

$$K_{48}^{(\beta+1,\gamma)} \bar{u}_3^{'3(\beta+1,\gamma)} + K_{37}^{(\beta,\gamma)} \bar{u}_3^{'3(\beta,\gamma+1)} + K_{47}^{(\beta+1,\gamma)} \bar{u}_3^{'3(\beta+1,\gamma+1)} = 2\left(C_{44}^{(\beta+1,\gamma)} - C_{44}^{(\beta,\gamma)}\right) \bar{\varepsilon}_{23},$$

$$K_{52}^{(\beta,\gamma)} \bar{u}_2^{'2(\beta,\gamma)} + K_{51}^{(\beta,\gamma)} \bar{u}_2^{'2(\beta+1,\gamma)} + K_{62}^{(\beta,\gamma+1)} \bar{u}_2^{'2(\beta,\gamma+1)} + K_{61}^{(\beta,\gamma+1)} \bar{u}_2^{'2(\beta+1,\gamma+1)} + K_{54}^{(\beta,\gamma)} \bar{u}_3^{'2(\beta,\gamma)} +$$

$$K_{53}^{(\beta,\gamma)} \bar{u}_3^{'2(\beta+1,\gamma)} + K_{64}^{(\beta,\gamma+1)} \bar{u}_3^{'2(\beta,\gamma+1)} + K_{63}^{(\beta,\gamma+1)} \bar{u}_3^{'2(\beta+1,\gamma+1)} + K_{56}^{(\beta,\gamma)} \bar{u}_2^{'3(\beta,\gamma)} +$$

$$\left(K_{55}^{(\beta,\gamma)} + K_{66}^{(\beta,\gamma+1)}\right) \bar{u}_2^{'3(\beta,\gamma+1)} + K_{65}^{(\beta,\gamma+1)} \bar{u}_2^{'3(\beta,\gamma+2)} = 2\left(C_{44}^{(\beta,\gamma+1)} - C_{44}^{(\beta,\gamma)}\right) \bar{\varepsilon}_{23},$$

$$K_{72}^{(\beta,\gamma)} \bar{u}_2^{'2(\beta,\gamma)} + K_{71}^{(\beta,\gamma)} \bar{u}_2^{'2(\beta+1,\gamma)} + K_{82}^{(\beta,\gamma+1)} \bar{u}_2^{'2(\beta,\gamma+1)} + K_{81}^{(\beta,\gamma+1)} \bar{u}_2^{'2(\beta+1,\gamma+1)} +$$

$$K_{74}^{(\beta,\gamma)} \bar{u}_3^{'2(\beta,\gamma)} + K_{73}^{(\beta,\gamma)} \bar{u}_3^{'2(\beta+1,\gamma)} + K_{84}^{(\beta,\gamma+1)} \bar{u}_3^{'2(\beta,\gamma+1)} + K_{83}^{(\beta,\gamma+1)} \bar{u}_3^{'2(\beta+1,\gamma+1)} +$$

$$K_{78}^{(\beta,\gamma)} \bar{u}_3^{'3(\beta,\gamma)} + \left(K_{77}^{(\beta,\gamma)} + K_{88}^{(\beta,\gamma+1)}\right) \bar{u}_3^{'3(\beta,\gamma+1)} + K_{87}^{(\beta,\gamma+1)} \bar{u}_3^{'3(\beta,\gamma+2)}$$

$$= \left(C_{13}^{(\beta,\gamma+1)} - C_{13}^{(\beta,\gamma)}\right) \bar{\varepsilon}_{11} + \left(C_{23}^{(\beta,\gamma+1)} - C_{23}^{(\beta,\gamma)}\right) \bar{\varepsilon}_{22} + \left(C_{33}^{(\beta,\gamma+1)} - C_{33}^{(\beta,\gamma)}\right) \bar{\varepsilon}_{33}.$$

Biography

<u>Personal data:</u>	Darko Ivančević was born on November 05, 1984 in Vukovar, Croatia. He attended primary school in Germany, Bjelovar and Ilok. He gained secondary education at the Vukovar Gymnasium. In 2003, he enroled in the Study of Aeronautical Engineering at the Faculty of Mechanical Engineering and Naval Architecture (FMENA), University of Zagreb. He is fluent in English and German.
<u>Education:</u>	
2009-2015	PhD student at Faculty of Mechanical Engineering and Naval Architecture, University of Zagreb
2008	Master Degree in Aeronautical Engineering
2003-2008	Undergraduate and graduate studies in Aeronautical Engineering at the Faculty of Mechanical Engineering and Naval Architecture, University of Zagreb
<u>Employment:</u>	
since 2009	Research assistant at the Department of Aeronautical Engineering, Faculty of Mechanical Engineering and Naval Architecture, University of Zagreb
<u>Associations:</u>	
	Croatian Society of Mechanics
<u>Awards:</u>	
2008	Medal of FMENA for achievement during studies
2005, 2006 and 2007	"Davorin Bazjanac" Award
<u>List of publications:</u>	http://bib.irb.hr/lista-radova?autor=316916&lang=EN

Životopis

Osobni podaci:

Darko Ivančević je rođen 5.11.1984. u Vukovaru. Osnovnu školu pohađao je u Njemačkoj, Bjelovaru i Iloku. Srednjoškolsko obrazovanje stekao je u Gimnaziji Vukovar. Studij zrakoplovstva na Fakultetu strojarstva i brodogradnje Sveučilišta u Zagrebu upisuje 2003. godine. Aktivno se služi engleskim i njemačkim jezikom.

Obrazovanje:

2009. - 2015.

Student na poslijediplomskom studiju Fakulteta strojarstva i brodogradnje, Sveučilišta u Zagrebu.

2008.

Magistar inženjer zrakoplovnog inženjerstva.

2003. - 2008.

Preddiplomski i diplomski studij zrakoplovstva na Fakultetu strojarstva i brodogradnje, Sveučilišta u Zagrebu.

Zaposlenja:

2009. -

Znanstveni novak na Zavodu za zrakoplovstvo, Fakulteta strojarstva i brodogradnje, Sveučilišta u Zagrebu.

Članstva:

Hrvatsko Društvo za Mehaniku

Nagrade:

2008.

Medalja Fakulteta strojarstva i brodogradnje Sveučilišta u Zagrebu za uspjeh tijekom studija.

2005., 2006. i 2007.

Nagrade ”Davorin Bazjanac” za uzoran uspjeh na prvoj, drugoj i trećoj godini preddiplomskog studija.

Popis publikacija:

http://bib.irb.hr/lista-radova?autor=316916

Bibliography

Abaqus (2010). *Abaqus Analysis User's Manual.* Dassault Systémes Simulia Corp., Providence RI.

Aboudi, J. (1988). Constitutive equations for elastoplastic composites with imperfect bonding. *International Journal of Plasticity*, 4(2):103–125.

Aboudi, J. (1995). Micromechanical analysis of thermo-inelastic multiphase short-fiber composites. *Composites Engineering*, 5(7):839–850.

Aboudi, J., Arnold, S. M., and Bednarcyk, B. A. (2012). *Micromechanics of composite materials, a generalized multiscale analysis approach.* Butterworth-Heinemann.

Aboudi, J., Pindera, M.-J., and Arnold, S. (2003). Higher-order theory for periodic multiphase materials with inelastic phases. *International Journal of Plasticity*, 19(6):805–847.

Aboudi, J., Pindera, M.-J., and Arnold, S. M. (1999). Higher-order theory for functionally graded materials. *Composites Part B: Engineering*, 30(8):777–832.

Aboudi, J. and Ryvkin, M. (2012). The effect of localized damage on the behavior of composites with periodic microstructure. *International Journal of Engineering Science*, 52:41–55.

Ambroziak, A. (2007). A pplication of elasto-viscoplastic Bodner-Partom constitutive equations in finite element analysis. *Computer Assisted Mechanics and Engineering Sciences*, 14:405–429.

Andersson, H. (2003). An implicit formulation of the Bodner-Partom constitutive equations. *Computers and Structures*, 81:1405–1414.

Arnold, S. M., Bednarcyk, B. A., and Aboudi, J. (2004). Comparison of the computational efficiency of the original versus reformulated High Fidelity Generalized Method of Cells. NASA/TM 2004-213438, 2004, NASA Glenn Research Center.

Arnold, S. M., Pindera, M.-J., and Wilt, T. E. (1996). Influence of fiber architecture on the inelastic response of metal matrix composites. *International Journal of Plasticity*, 5(7):839–850.

Bansal, Y. and Pindera, M.-J. (2002). Efficient reformulation of the thermoelastic Higher-Order Theory for FGMs. NASA/CR - 2002-211909, NASA Glenn Research Center.

Bansal, Y. and Pindera, M.-J. (2005). A second look at the Higher-Order Theory for periodic multiphase materials. *Journal of Applied Mechanics*, 72:177–195.

Bansal, Y. and Pindera, M.-J. (2006). Finite-volume direct averaging micromechanics of heterogeneous materials with elastic-plastic phases. *International Journal of Plasticity*, 22(5):775–825.

Barbero, E., Cosso, F., Roman, R., and Weadon, T. (2013). Determination of material parameters for Abaqus progressive damage analysis of E-glass epoxy laminates. *Composites Part B: Engineering*, 46:211–220.

Bažant, Z. P. and Cedolin, L. (2010). *Stability of structures: elastic, inelastic, fracture and damage theories.* World Scientific Publishing Company.

Bednarcyk, B. A., Aboudi, J., and Arnold, S. M. (2010). Micromechanics modeling of composites subjected to multiaxial progressive damage in the constituents. *AIAA Journal*, 48(7):1367 – 1378.

Bednarcyk, B. A. and Arnold, S. M. (2009). *Advances in mathematical modeling and experimental methods for materials and structures*, volume 168 of *Solid Mechanics and Its Applications*, chapter Aboudi's micromechanics theories applied to multiscale analysis of composites, pages 1–14. Springer Science+Business Media B.V. 2010.

Bednarcyk, B. A., Arnold, S. M., Aboudi, J., and Pindera, M.-J. (2004). Local field effects in titanium matrix composites subject to fiber-matrix debonding. *International Journal of Plasticity*, 20(8-9):1707–1737.

Bodner, S. R. (2001). *Handbook of Materials Behavior Models*, volume 71, chapter An Outline of the Bodner-Partom (B-P) Unified Constitutive Equations for Elastic-Viscoplastic Behavior, pages 349–357. Academic Press.

Calvacante, M. A. and Marques, S. P. (2014). Homogenization of periodic materials with viscoelastic phases using the generalized FVDAM theory. *Computational Materials Science*, 87:43–53.

Calvacante, M. A., Marques, S. P., and Pindera, M.-J. (2008). Computational aspects of the parametric finite-volume theory for functionally graded materials. *Computational Materials Science*, 44:422–438.

Camanho, P., Maimi, P., and Davila, C. (2007). Prediction of size effects in notched laminates using continuum damage mechanics. *Composites Science and Technology*, 67:2715–2727.

Chizari, M., Barrett, L., and Al-Hassani, S. (2009). An explicit numerical modelling of the water jet tube forming. *Computational Materials Science*, 45:378–384.

Degenhardt, R., Kling, A., Rohwer, K., Orifici, A. C., and Thomson, R. S. (2008). Design and analysis of stiffened composite panels including post-buckling and collapse. *Computers and Structures*, 86:919–929.

Du Bois, P., Kolling, S., Koesters, M., and Frank, T. (2006). Material behaviour of polymers under impact loading. *International Journal of Impact Engineering*, 32:725–740.

Eskandari, H. and Nemes, J. (1999). Application of a damage model for high rate deformation of composite structures. In *Proceedings of the 12th International Conference on Composite Materials - ICCM12*.

Fish, J. and Shek, K. (1998). Computational plasticity and viscoplasticity for composite materials and structures. *Composites Part B: Engineering*, 29(5):613–619.

Fish, J. and Shek, K. (2000). Multiscale analysis of composite materials and structures. *Composites Science and Technology*, 60:2547–2556.

Freed, Y. and Aboudi, J. (2009). Micromechanical prediction of the two-way shape memory effect in shape memory alloy composites. *International Journal of Solids and Structures*, 46(7-8):1634–1647.

Gan, H., Orozco, C. E., and Herakovich, C. T. (2000). A strain-compatible method for micromechanical analysis of multi-phase composites. *International Journal of Solids and Structures*, 37:5097–5122.

Georgiadis, S., Gunnion, A., Thomson, R., and Cartwright, B. (2007). Bird-strike simulation for certification of the Boeing 787 composite moveable trailing edge. *Composite Structures*, 86:258–268.

Gilat, A., Goldberg, R. K., and Roberts, G. D. (2005). Strain rate sensitivity of epoxy resin in tensile and shear loading. NASA/TM-2005-213595, NASA Glenn Research Center.

Goldberg, R. K., Roberts, G., and Gilat, A. (2003a). Incorporation of mean stress effects into the micromechanical analysis of the high strain rate response of polymer matrix composites. *Composites Part B: Engineering*, 34(2):151–165.

Goldberg, R. K., Roberts, G. D., and Gilat, A. (2003b). Anayltical modeling of the high strain rate deformation of polymer matrix composites. In *44th AIAA/ASME/ASCE/AHS/ASC Structures, Structural Dynamics, and Materials Conference*.

Goldberg, R. K., Roberts, G. D., and Gilat, A. (2003c). Implementation of an associative flow rule including hydrostatic stress effects into the high strain rate deformation analysis of polymer matrix composites. NASA/TM-2003-212382, NASA Glenn Research Center.

Guedes, R., Vaz, M., Ferreira, F., and Morals, J. (2005). Response of CFRP laminates under high strain rate compression until failure. *Science and Engineering of Composite Materials*, 12:145–151.

Guida, M., Marulo, F., Meo, M., and Riccio, M. (2008). Analysis of bird impact on a composite tailplane leading edge. *Applied Composite Materials*, 15:241 – 257.

Guida, M., Marulo, F., Meo, M., and Russo, S. (2013). Certification by birdstrike analysis on C27J fullscale ribless composite leading edge. *International Journal of Impact Engineering*, 54:105–113.

Haj-Ali, R. and Aboudi, J. (2009). Nonlinear micromechanical formulation of the High Fidelity Generalized Method of Cells. *International Journal of Solids and Structures*, 46:2577–2592.

Haj-Ali, R. and Aboudi, J. (2012). Discussion paper: Has renaming the High Fidelity Generalized Method of Cells been justified. *International Journal of Solids and Structures*, 49:2051–2058.

Herakovich, C. T. (1998). *Mechanics of fibreous composites*. John Wiley & Sons, Inc.

Hinton, M., Kaddour, A., and Soden, P. (2002). A comparison of the predictive capabilities of current failure theories for composite laminates, judged against experimental evidence. *Composites Science and Technology*, 62(12-13):1725–1797.

Hinton, M., Kaddour, A., and Soden, P. (2004). A further assessment of the predictive capabilities of current failure theories for composite laminates: comparison with experimental evidence. *Composites Science and Technology*, 64(3-4):549–588.

Hosur, M., Alexander, J., Vaidya, U., and Jeelani, S. (2001). High strain rate compression response of carbon/epoxy laminate composites. *Composite Structures*, 52:405–417.

Hou, J. and Ruiz, C. (2007). Soft body impact on laminated composite materials. *Composites Part A: Applied Science and Manufacturing*, 38:505–515.

Hufenbach, W., Langkamp, A., Gude, M., Ebert, C., Hornig, A., Nitschke, S., and Böhm, H. (2013). Characterisation of strain rate dependent material properties of textile reinforced thermoplastics for crash and impact analysis. *Procedia Materials Science*, 2:204–211.

Hyer, M. (2009). *Stress Analysis of Fiber-Reinforced Composite Materials*. DEStech Publications.

Ivančević, D. and Smojver, I. (2011). Hybrid approach in bird strike damage prediction on aeronautical composite structures. *Composite Structures*, 94(1):15–23.

Ivančević, D. and Smojver, I. (2014). Multiscale modeling of high velocity impact damage on composite structures. In *Proceedings of the 2014 SIMULIA Community Conference*.

Jacob, G., Starbuck, M., Fellers, J., Simunovic, S., and Boeman, R. (2004). Strain rate effects on the mechanical properties of polymer composite materials. *Journal of Applied Polymer Science*, 94:296–301.

Jirasek, M. (2011). *Numerical modeling of concrete cracking*. Springer Wien New York.

Kassapoglou, C. (2010). *Design and analysis of composite structures with applications to aerospace structures*. John Wiley & Sons, Ltd.

Khatam, H. and Pindera, M.-J. (2009). Parametric finite-volume micromechanics of periodic materials with elastoplastic phases. *International Journal of Plasticity*, 25(7):1386–1411.

Kollar, L. P. and Springer, G. S. (2003). *Mechanics of composite structures*. Cambridge University Press.

Körber, H. (2010). *Mechanical response of advanced composites under high strain rates*. PhD thesis, Faculdade de Engenharia da Universidade do Porto.

Kurnatowski, B., Chatiri, M., and Matzenmiller, A. (2012). Multi-scale analysis of fibre reinforced structures. In Eberhardsteiner, J., Böhm, H. J., and Rammerstorfer, F. G., editors, *Proceedings of 6th European Congress on Computational Methods in Applied Sciences and Engineering - ECCOMAS 2012*.

Kurnatowski, B. and Matzenmiller, A. (2012). Coupled twoscale analysis of fiber reinforced composite structures with microscopic damage evolution. *International Journal of Solids and Structures*, 49(18):2404–2417.

Lachaud, F., Lorrain, B., Michel, L., and Barriol, R. (1997). Experimental and numerical study of delamination caused by local buckling of thermoplastic and thermoset composites. *Composites Science and Technology*, 58:727–733.

Lapczyk, I. and Hurtado, J. (2007). Progressive damage modeling in fiber-reinforced materials. *Composites Part A: Applied Science and Manufacturing*, 38:2333–2341.

Lopes, C., Camanho, P. P., and Gürdal, Z. (2009). Low-velocity impact damage on dispersed stacking sequence laminates. Part II: Numerical simulations. *Composites Science and Technology*, 69:937–947.

Matzenmiller, A. and Köster, B. (2007). Consistently linearized constitutive equations of micromechanical models for fibre composites with evolving damage. *International Journal of Solids and Structures*, 44(7-8):2244–2268.

Matzenmiller, A. and Kurnatowski, B. (2009). *Advances in mathematical modeling and experimental methods for materials and structures*, volume 168 of *Solid Mechanics and Its Applications*, chapter A comparison of micromechanical models for the homogenization of microheterogeneous elastic composites, pages 57–71. Springer Science+Business Media B.V. 2010.

May, M., Nossek, M., Petrinic, N., Hiermaier, S., and Thoma, K. (2014). Adaptive multi-scale modeling of high velocity impact on composite panels. *Composites Part A: Applied Science and Manufacturing*, 58:56–64.

Mayes, J. and Hansen, A. (2004.). Composite laminate failure analysis using Multicontinuum Theory. *Composites Science and Technology*, 64:379–394.

McConnell, V. (2011). Past is prologue for composite repair. *Reinforced Plastics*, 55(6):17–21.

Moncada, A. (2012). *Advances in Micromechanics Modeling of Composites Structures for Structural Health Monitoring*. PhD thesis, Arizona State University.

Moncada, A. M., Chattopadhyay, A., Bednarcyk, B. A., and Arnold, S. M. (2008). Micromechanics-based progressive failure analysis of composite laminates using different constituent failure theories. *Journal of Reinforced Plastics and Composites*, 31:1467–1487.

Ng, W., Salvi, A., and Waas, A. M. (2010). Characterization of the in-situ non-linear shear response of laminated fiber-reinforced composites. *Composites Science and Technology*, 70:1126–1134.

Paley, M. and Aboudi, J. (1992). Micromechanical analysis of composites by the generalized cells model. *Mechanics of Materials*, 14(2):127–139.

Pimenta, S., Gutkin, R., Pinho, S. T., and Robinson, P. (2009). A micromechanical model for kink-band formation: Part II - Analytical modelling. *Composites Science and Technology*, 69(7-8):956–964.

Pindera, M.-J. and Bednarcyk, B. A. (1999). An efficient implementation of the Generalized Method of Cells for unidirectional, multi-phased composites with complex microstructures. *Composites Part B: Engineering*, 30(1):87–105.

Pindera, M.-J., Khatam, H., Drago, A., and Bansal, Y. (2009). Micromechanics of spatially uniform heterogeneous media: a critical review and emerging approaches. *Composites Part B: Engineering*, 40:349–78.

Pineda, E. J. (2012). *A novel multiscale physics-based progressive damage and failure modeling tool for advanced composite structures*. PhD thesis, University of Michigan.

Pineda, E. J., Bednarcyk, B. A., and Arnold, S. M. (2012a). Effects of subscale size and shape on global energy dissipation in a multiscale model of a fiber-reinforced composite exhibiting post-peak strain softening using Abaqus and FEAMAC. In *2012 3DS SIMULIA Community Conference Proceedings. Providence*.

Pineda, E. J., Bednarcyk, B. A., and Arnold, S. M. (2014). Achieving ICME with multiscale modeling: The effects of constituent properties and processing on the performance of laminated polymer matrix composite structures. In *55th AIAA/ASME/ASCE/AHS/SC Structures, Structural Dynamics and Materials Conference*.

Pineda, E. J., Bednarcyk, B. A., Waas, A. M., and Arnold, S. M. (2012b). Progressive failure of a unidirectional fiber-reinforced composite using the Method of Cells: discretization objective computational results. In *53rd AIAA/ASME/ASCE/AHS/ASC Structures, Structural Dynamics and Materials Conference*, Honolulu, Hawaii.

Pineda, E. J., Bednarcyk, B. A., Waas, A. M., and Arnold, S. M. (2013). On multiscale modeling using the Generalized Method of Cells: Preserving energy dissipation across disparate length scales. *CMC Computers, Materials & Continua*, 35(2):119–154.

Pineda, E. J., Waas, A. M., Bednarcyk, B. A., and Collier, C. (2009). Multiscale model for progressive damage and failure of laminated composites using an explicit finite element method. In *50th AIAA/ASME/ASCE/AHS/ASC Structures, Structural Dynamics, and Materials Conference, Palm Springs, California, 2009*.

Pinho, S. T., Robinson, P., and Iannucci, L. (2006). Fracture toughness of the tensile and compressive fibre failure modes in laminated composites. *Composites Science and Technology*, 66(13):2069–2079.

Puck, A., Kopp, J., and Knops, M. (2002). Guidelines for the determination of the parameters in Puck's action plane strength criterion. *Composites Science and Technology*, 62:371–378.

Puck, A. and Schürmann, H. (1998). Failure analysis of FRP laminates by means of physically based phenomenological models. *Composites Science and Technology*, 58(7):1045–1067.

Ryvkin, M. and Aboudi, J. (2012). Stress redistribution due to cracking in periodically layered composites. *Engineering Fracture Mechanics*, 93:225–238.

Schücker, C. (2006). *Mechanism based modeling of damage and failure in fiber reinforced polymer laminates*. PhD thesis, Institute of Lightweight Design and Structural Biomechanics Vienna University of Technology.

Schwab, M., Gager, J., and Petterman, H. (2014). Assessing material nonlinearities in large composite structures by predicting energy dissipations at the mesoscale. In *Proceedings of WCCM XI, ECCM V and ECFD VI, Barcelona 2014*.

Smilauer, V., Hoover, C., Bazant, Z., Caner, F., and Waas, A. M. (2011). Multiscale simulation of fracture of braided composites via repetitive unit cells. *Engineering Fracture Mechanics*, 78:901–918.

Smojver, I. (2007). *Mechanics of Composite Materials*. Internal script at FMENA.

Smojver, I. and Ivančević, D. (2010). Numerical simulation of bird strike damage prediction in airplane flap structure. *Composite Structures*, 92:2016–2026.

Smojver, I. and Ivančević, D. (2011). Bird strike damage analysis in aircraft structures using Abaqus/Explicit and coupled Eulerian Lagrangian approach. *Composites Science and Technology*, 71(4):489–498.

Soden, P., Hinton, M., and Kaddour, A. (1998). Lamina properties, lay-up configurations and loading conditions for a range of fibre-reinforced composite laminates. *Composites Science and Technology*, 58:1011–1022.

Sullivan, R. and Arnold, S. M. (2010). An annotative review of multiscale modeling and its application to scales inherent in the field of ICME. In *Proceedings of the symposium Models, Databases, and Simulation Tools Needed for the Realization of Integrated Computational Materials Engineering, Houston, 2010.*

Sun, C., Quinn, B., Tao, J., Oplinger, D., and William, J. (1996). Comparative evaluation of failure analysis methods for composite laminates. Technical report, FAA Technical Report.

Sun, H., Di, S., Zhang, N., and Wu, C. (2001). Micromechanics of composite materials using multivariable finite element method and homogenization theory. *International Journal of Solids and Structures*, 38:3007–3020.

Taibei, A., Yi, W., and Goldberg, R. (2002). Strain rate dependent micro-mechanical composite material model for Finite Element impact simulation. In *Proceedings of the 7th LS-DYNA Users Conference*, Detroit.

Taibei, A., Yi, W., and Goldberg, R. K. (2005). Non-linear strain rate dependent micro-mechanical composite material model for finite element impact and crashworthiness simulation. *International Journal of Non-Linear Mechanics*, 40:957–970.

Talreja, R. and Singh, C. (2007). *Multiscale modeling and simulation of composite materials and structures*, chapter Multiscale modeling for damage analysis, pages 529–578. Springer Science & Business Media.

Tang, Z. and Zhang, B. (2012). Prediction of biaxial failure envelopes for composite laminates based on Generalized Method of Cells. *Composites Part B: Engineering*, 43(3):914–925.

Verpoest, I. and Lomov, S. V. (2005). Virtual textile composites software WiseTex: Integration with micro-mechanical, permeability and structural analysis. *Composites Science and Technology*, 65:2563–2574.

Voyiadjis, G. Z. and Kattan, P. I. (1999). *Advances in Damage Mechanics: Metals and Metal Matrix Composites.* Elsevier Science.

Zheng, X. (2006). *Nonlinear strain rate dependent composite model for explicit finite element analysis.* PhD thesis, The Graduate Faculty of The University of Akron.

Zhu, L., Chattopadhyay, A., and Goldberg, R. K. (2006). Nonlinear transient response of strain rate dependent composite laminated plates using multiscale simulation. *International Journal of Solids and Structures*, 43:2602–2630.